Spectroscopic Studies of Anomalous Hydrodynamic Behaviour in Complex Fluids

David W. N. Edington

Thesis submitted for the degree of Doctor of Philosophy

Department of Physics and Astronomy

University of Edinburgh

2002

If you think... that anything like a romance is preparing for you, reader, you were never more mistaken. Do you anticipate sentiment, and poetry, and reverie? Do you expect passion, and stimulus, and melodrama? Calm your expectations, reduce them to a lowly standard. Something real, cool and solid lies before you; something unromantic as Monday morning, when all who have work wake with the consciousness that they must rise and betake themselves thereto.

Charlotte Brontë, prelude to Shirley

Songs, novels, doctoral theses, autumn festivals – all are meant to remind us of death; and not infrequently, thousands of people give their consent to that premature obituary.

Ismail Kadare, Albanian Spring

The labour we delight in physics pain.
William Shakespeare, Macbeth

Abstract

Brillouin spectroscopy probes the thermally generated pressure fluctuations (sound waves) which propagate in a material. The resulting information on sound velocity and absorption provides a fast and efficient method of monitoring high frequency ($\sim 10^9$ Hz) dynamics in the system being studied. In certain cases, structural information may also be inferred from changes in the Brillouin spectrum as a function of temperature, pressure or composition (in the case of multi-component systems). The aim of the work presented in this thesis was to integrate Brillouin spectroscopy into current soft condensed matter research projects at Edinburgh, namely (*i*) hydration in methanol–water mixtures and (*ii*) the behaviour of hard-sphere colloidal dispersions.

A Brillouin spectrometer based on a Fabry-Perot interferometer was developed and tested, resulting in a high-resolution instrument operating at variable scattering vector (exchanged momentum), temperature and pressure. The technical aspects of this work were carried out in collaboration with a colleague. Data analysis routines were designed and implemented, enabling calibrated Brillouin spectra to be produced automatically from raw experimental data. Excellent agreement with results on several materials studied in the literature confirmed the accuracy and sensitivity of the spectrometer.

The molecular details of hydration in methanol–water mixtures are of great interest due to the prototypical amphiphilic nature of the methanol molecule. The effect of deep cooling on the Brillouin spectrum across a wide range of methanol concentrations was studied in detail, resulting in the first observation of an anomalous increase in sound velocity and maximum in sound absorption at intermediate compositions. A similar effect was then found at higher temperature in aqueous tertiary butanol, and was identified in a brief survey of several other aqueous solutions. High pressure Brillouin

spectra indicate that this anomalous behaviour may also be present in pure water. It is suggested that these novel effects may be due to the presence of a relatively unperturbed water structure in the aqueous solutions studied, even at quite high solute concentration. Preliminary results from a neutron diffraction experiment performed on a 40 % by mass methanol–water mixture were consistent with this hypothesis.

Brillouin spectroscopy was also used to study the propagation of high frequency sound in monodisperse colloidal suspensions of sub-micron hard spheres. A second longitudinal sound mode was observed for scattering vectors of magnitude greater than π/d where d is the diameter of the spheres. These results are the first reproduction and extension of the pioneering work in the field, which identified the additional mode with a surface acoustic excitation, propagating between adjacent spheres via an evanescent wave in the solvent. The new results show that the second mode is extinguished at a particular scattering vector – an effect not reported previously. It is suggested that this extinction is due to the minimum in the form factor for elastic scattering from a single sphere.

Declaration

This thesis has been composed by myself and has not been submitted in any previous application for a degree. The experiments reported within were performed by me and, where indicated, in collaboration with colleagues. All data analysis and interpretation is my own work.

David W.N. Edington, May 2002.

Acknowledgements

I would like to thank my supervisors, Jason Crain and Wilson Poon, for all of their advice, patience and encouragement over the last few years. Their expertise and infectious enthusiasm was a vital contribution to many productive and enjoyable meetings and discussions.

Many of the experiments presented in this thesis would not have been possible without the technical support provided by Hugh Vass. It has been a pleasure to work with him and benefit from his practical expertise in all things spectroscopic.

Other Edinburgh colleagues have helped with my research in a number of ways. Thanks in particular to Andrew Schofield for helping with colloid preparation and Sanhita Dixit for countless discussions about what happens when water and methanol meet.

I have been fortunate to work with a number of very knowledgeable, friendly and enthusiastic people outside Edinburgh during my doctoral research. John Finney, Toshio Yamaguchi and Alan Soper were all of great help in my studies of aqueous alcohol solutions – providing access to beamtime, collaborating on x-ray and neutron experiments, and always finding time to discuss my latest Brillouin results. Thanks also to Ping Sheng at the Hong Kong University of Science and Technology, who was willing and able to cast his mind back more than ten years in order to explain the finer points of his theoretical work on sound propagation in colloids, both in person and via email.

This work was funded in full by a scholarship from the Carnegie Trust for the Universities of Scotland, who also provided support for trips to international conferences and meetings through the award of a Carnegie Research Grant. I am extremely grateful for their generosity.

Thanks to all the friends who have helped in many ways; answering stupid physics questions, making the office a nice place to be and ensuring that lunchtime was always something to look forward to.

Extra special thanks to Miranda for her enthusiasm when things went well, for keeping me going when they didn't, and most of all for the cuddles. Thank you for putting up with me.

Finally, I would like to thank my family who – despite my failure to explain what it is that I actually do every day – have given me every kind of support and encouragement during this PhD and throughout my education.

Contents

Symbols and notation

The symbols and notation listed below are used throughout this thesis. Wherever possible, conventions adopted in the light scattering and condensed matter literature have been followed. Many of these symbols are used with subscripts which will be made clear in the adjacent text. Vectors are printed in bold face.

Thermodynamic Variables

B	bulk modulus
c	speed of light *in vacuo*
c_P	specific heat at constant pressure
c_V	specific heat at constant volume
d	hard-sphere diameter of a colloidal sphere
d_c	core diameter of a colloidal sphere, excluding polymer coating
D_T	thermal diffusivity $= \kappa/\rho c_P$
D_V	longitudinal kinematic viscosity $= (\eta_v + \frac{4}{3}\eta_s)/\rho$
$\mathbf{G}$	momentum
I	intensity
$\mathbf{k}$	wavevector; magnitude is wavenumber $k = 2\pi/\lambda$
k_B	Boltzmann's constant
n	refractive index
N	particle number
P	pressure
S	entropy
$S_{\rho\rho}(\boldsymbol{q}, \omega)$	spectral density of the density autocorrelation function (dynamic structure factor)
t	time
$\mathbf{u}(\mathbf{r}, t)$	Brownian particle velocity
v_s	adiabatic sound speed
v_T	isothermal sound speed
V	volume
x	mole fraction (with subscript identifying species)
γ	specific heat ratio $\equiv c_P/c_V \equiv \chi_T/\chi_S$

Γ	linewidth (with identifying subscript)
ϵ	dielectric constant
η	viscosity (with identifying subscript)
κ	thermal conductivity
λ	wavelength
ν	frequency
ν_B	Brillouin peak frequency
$\Delta\nu_B$	Brillouin peak half-width at half height
ρ	density (mass or number depending on context)
ϕ	hard-sphere volume fraction of colloidal spheres
ϕ_c	core volume fraction of colloidal spheres, excluding polymer coating
τ	relaxation time (with subscript when required)
χ_S	adiabatic compressibility
χ_T	isothermal compressibility
ω	angular frequency $= 2\pi\nu$
ω_B	Brillouin peak angular frequency

Experimental Variables

d	plate spacing of a Fabry-Perot interferometer
$\mathcal{C}$	contrast (or extinction ratio)
$\mathcal{F}$	finesse (of a Fabry-Perot interferometer)
$\boldsymbol{q}$	scattering vector, $\lvert\boldsymbol{q}\rvert = q = (4\pi n/\lambda)\ \sin\theta/2$
R	resolving power
$\mathcal{R}$	mirror reflectivity
$\mathcal{T}$	mirror transmissivity
$(\Delta\lambda)_{BW}$	minimum resolvable wavelength bandwidth
$(\Delta\nu)_{BW}$	minimum resolvable frequency bandwidth
$(\Delta\nu)_{FSR}$	free spectral range (of a Fabry-Perot interferometer)
θ	scattering angle

Abbreviations

CPA	coherent potential approximation
DSC	differential scanning calorimetry
DOS	density of states
EPSR	empirical potential structure refinement
FP	Fabry-Perot interferometer
FSR	free spectral range (of a Fabry-Perot interferometer)
FWHH	full width at half height (of a spectral feature)
HWHH	half width at half height (of a spectral feature)
IRF	instrumental response function
LDA	low-density amorphous ice
MCA	multichannel analyser

MCT	mode-coupling theory
PHSA	poly-12-hydroxystearic acid
PMMA	polymethylmethacrylate
PMT	photomultiplier tube
RCP	random close-packed
RDF	radial distribution function
SLS	static light scattering
SNR	signal-to-noise ratio
VH	Vertical-Horizontal
VV	Vertical-Vertical

Chapter 1

Introduction

The velocity, absorption and dispersion (variation of frequency with wavevector) of sound waves in a fluid are useful indicators of the bulk dynamical properties of the medium, and in certain circumstances may be used to deduce structural information on lengthscales and timescales determined by the wavelength and frequency of the sound. Sound waves are hydrodynamic modes which modulate the dielectric constant ϵ of the material, and should therefore have an observable effect on the spectrum of scattered light since electromagnetic radiation couples to these fluctuations in ϵ.

In fact the presence of a propagating sound mode results in a pair of *Brillouin peaks* up- and down-shifted from the excitation frequency by an amount proportional to the speed of sound in the medium. The origin of this Brillouin scattering is the exchange of energy between photons in the incident laser beam and phonons in the fluid – a process analogous to Raman scattering of light due to quantised molecular energy levels. If more than one sound mode propagates in the scattering medium (e.g. transverse acoustic waves if the material supports shear) more than one pair of Brillouin peaks will be present in the spectrum.

The origin of these phonons, which exist in any material, is fluctuations in dielectric constant caused by the random thermal motion of molecules, which can be decomposed into statistically independent fluctuations in pressure and entropy. A pressure fluctuation is nothing other than a sound wave, and these random fluctuations can be thought of as a Fourier sum of sinusoidal pressure waves travelling in all directions,

with all frequencies, at the speed of sound in the material. The excitation frequency and scattering angle select the wavevector of the thermally generated sound wave which is probed in a light scattering experiment.

The scattering vectors obtained with visible light place the frequency of sound probed by Brillouin spectroscopy in the so-called 'hypersonic' ($\sim 10^9$ Hz) régime. Thus structural and thermal relaxation processes with relaxation times of $\sim 10^{-9}$ s are able to be detected using the technique, and structural units in complex fluids with sizes comparable to the acoustic wavelength $\lambda_s \sim 100$ nm may have an observable effect on the Brillouin spectrum.

Brillouin spectroscopy is therefore a valuable non-invasive (no forces are exerted – the thermal phonons are already present in a material at equilibrium) probe of high-frequency dynamics and structure in a wide range of materials. Although unable to provide the depth of information which may be obtained from modern neutron diffraction techniques, Brillouin scattering does have the advantage of being orders of magnitude less expensive and time consuming, allowing a wide range of variables to be explored, the most interesting combinations of which may then be investigated using neutrons.

The primary aim of this research project was to develop a Brillouin spectrometer for the study of soft condensed matter at variable temperature, pressure and scattering vector. Potential applications of the instrument range from simple molecular liquids to complex fluids such as colloids and gels, demanding both high performance and versatility. Great effort was therefore made to ensure that optical stability, contrast ratio and range of accessible temperatures and pressures all match or exceed the abilities of other Brillouin spectrometers described in the literature. Upon completion, the instrument was used in an attempt to contribute to two areas of ongoing research at Edinburgh: (*i*) the molecular physics of aqueous alcohol solutions, and (*ii*) the dynamics of hard-sphere colloidal suspensions.

1.1 Aqueous alcohol solutions

The physical properties of aqueous alcohol solutions have been studied extensively due to their fundamental importance and the prototypical amphiphilic properties of alcohol

molecules, but remain a focus of attention due to a relatively poor understanding of hydration and the hydrophobic interaction at the molecular level of detail. Ongoing research at Edinburgh is using advanced neutron diffraction techniques and Raman spectroscopy to reveal the molecular structure of methanol–water mixtures, with unexpected results. It seems that water and methanol do not mix homogeneously – the amphiphilic alcohol molecules and hydrogen-bonded water structure result in significant structuring, the nature of which depends on the amount of methanol in the solution. These experiments provide detailed static structural information on molecular lengthscales, but are not best suited to studying bulk dynamical properties. Brillouin spectroscopy does however probe bulk behaviour (sound velocity and absorption), and in this sense is complementary to the neutron and Raman experiments. A promising first application of the newly developed Brillouin spectrometer was therefore to look at methanol–water mixtures at room temperature as a function of concentration, in order to compare results with the recent findings of my colleagues. This was extended to investigate the effect of reducing the temperature of these solutions – very little is known about their behaviour below 0 °C. The same experiments were then performed on other aqueous solutions, and in all cases an anomalous increase in the sound velocity and absorption was observed at low temperature. Similarities with data from the literature turned our attention towards the properties of supercooled pure water, for which almost identical trends in sound velocity and absorption emerge with cooling to about -20 °C. This raises new questions about the rôle of water itself in determining the properties of aqueous solutions, as will be discussed in Chapter 4.

1.2 Colloids and other complex fluids

Colloidal suspensions (defined in the introduction to Chapter 5) are of great interest, largely due to their wide-ranging industrial, biological and technological applications. A considerable body of knowledge and expertise has been accumulated at Edinburgh over the last decade, with particular emphasis on the structure and dynamics of hard-sphere colloids. The addition of Brillouin spectroscopy to the portfolio of techniques available to the group was desirable for several reasons. Firstly, it appears that two longitudinal sound modes can propagate in a hard-sphere colloid under certain conditions – a very

surprising discovery which has received no further attention since its publication more than a decade ago. Confirmation of this finding and extension of the original research could provide valuable insights into the propagation of sound in dispersed random media – a topic of considerable fundamental and industrial importance. Secondly, a wide range of phenomena in complex fluids have been predicted which should be observable using Brillouin spectroscopy, but have not yet been confirmed due to an apparent neglect of the technique in recent years. Such predictions include acoustic bandgaps in colloidal crystals, new sound modes in polymer gels and internal modes in soft colloidal particles. The mesoscale structure present in a variety of complex fluids (such as colloidal gels, suspensions of micelles, emulsions, exotic lyotropic liquid crystal phases and many others) also suggests that interesting features may be apparent in the Brillouin spectrum upon tuning the scattering vector so that the sound waves probed have a wavelength similar to the size of the structural units.

1.3 Thesis plan

This thesis can be divided into three main parts: background, the development of experimental and analytical techniques for Brillouin spectroscopy, and the application of these in research on sound propagation in two types of soft condensed matter. The contents of each chapter may be summarised as follows:

Chapter 2 – An introduction to Brillouin spectroscopy. The physical origin of the Rayleigh-Brillouin spectrum is discussed, before outlining a mathematical derivation of the dynamic structure factor for a monatomic fluid. The effect of intramolecular relaxation on the spectrum is then considered.

Chapter 3 – The design and development of a new high-contrast Brillouin spectrometer for the study of soft condensed matter. The principles of operation of a Fabry-Perot interferometer are summarised, and its implementation as a frequency analyser for high-resolution Brillouin spectroscopy is considered. The design and use of apparatus enabling the scattering angle, temperature and pressure to be varied is then described. The development of automated data analysis routines is discussed.

Chapter 4 – Anomalous hydrodynamic behaviour is observed using the newly developed Brillouin spectrometer to investigate the speed and absorption of high-frequency sound in several aqueous solutions. The importance of hydration and hydrophobicity in determining the physical properties of aqueous alcohol solutions is emphasised, and the unusual behaviour of supercooled water is introduced. Detailed Brillouin scattering, x-ray diffraction and neutron diffraction experiments on cooled methanol–water mixtures are presented, before looking at other aqueous solutions. Brillouin peak frequencies and widths both show unexpected increases at low temperature, which is noted to be similar to findings in supercooled pure water and glass-forming systems reported in the literature. It is suggested that the anomalies in aqueous solutions are due to pre-glassy dynamics of pure water.

Chapter 5 – Brillouin scattering is used to study the propagation of sound in colloidal suspensions. Earlier research showing the existence of a second longitudinal sound mode in hard-sphere colloids is summarised, before presenting the results of new experiments which confirm and extend the original work to much smaller sphere sizes. The potential of Brillouin spectroscopy as the means of observing new physics in binary colloidal suspensions and acoustic bandgaps (predicted by theory to exist in colloidal crystals) is discussed briefly.

Chapter 6 – A short concluding chapter, restating the aims and summarising the results of Chapters 3, 4 and 5. Suggestions are given for future work based on the outcomes of the apparatus development and research programs presented in this thesis.

Chapter 2

Brillouin spectroscopy

Brillouin spectroscopy (sometimes referred to as Rayleigh-Brillouin or Mandel'shtam-Brillouin scattering) is an experimental technique originating from the interaction of light with the medium through which it propagates. As with all spectroscopic techniques, inferences about the internal properties of this medium are made by comparing incident radiation with that which has passed through and been modulated by the material.

In this chapter, we begin by introducing the physics of light scattering, before discussing the physical origin of Brillouin scattering (Sec. 2.1), and then going on to outline a mathematical derivation of the Rayleigh-Brillouin spectrum of a simple liquid (Sec. 2.2).

Although not common knowledge outside the physics community, we are surrounded by everyday phenomena whose origins lie in the scattering of light by various types of matter. The answer to the old question "Why is the sky blue?" is perhaps the most striking example, while the colour of sunsets, the operation of mirrors, and the reason why a glass of milk looks different to a glass of water are also familiar consequences of the way in which light interacts with atoms, molecules and other larger particles.

Light is scattered by changes in the refractive index n or dielectric constant $\epsilon = n^2$. An example of this is a mirror, where light is scattered (reflected) by the large difference in ϵ between the glass and the reflective silver coating. The first theoretical description of

light scattering was given by Rayleigh in 1871*, when he considered the interaction of light of wavelength λ with a non-interacting gas in which particles much smaller than λ are separated by distances much greater than λ. What he found is now known as Rayleigh's law, namely that the intensity of scattered light varies as λ^{-4}. Thus blue light with $\lambda \approx 450\,\text{nm}$ is scattered about 6 times more strongly than red light with $\lambda \approx 700\,\text{nm}$, which is the reason that sunlight scattered towards us (when we look at the sky during the day we do not look at light which has travelled in a straight line from the sun) from the Earth's atmosphere is predominantly blue. At sunset, when we are able to look at light from the sun more directly, it is low in the sky and its light must travel through a lot of air before reaching our eyes. As the sunlight propagates towards us, blue light is scattered off in all directions, leaving the orange and red parts of the spectrum to form the sunset.

In fact, Rayleigh's law is not really sufficient to explain the blue colour of the sky. He assumed that the scatterers were far apart compared to the wavelength of light, which is not valid in the atmosphere. Hence there are many scatterers within each wavelength, and one might suppose that the medium would therefore appear homogeneous on this lengthscale; scattering from individual molecules would interfere destructively apart from in the propagation direction of the light. This is evidently not the case in the atmosphere, where homogeneity is in fact destroyed by thermally generated random motion of the molecules, causing the local density to fluctuate and allowing the scattered light to be seen from the ground.

The 'blue sky' effect can also be seen by adding small amounts of milk to a glass of water illuminated by a source of white light. In pure water, very little light is scattered and the beam will be difficult to observe. When a little milk is added, a bluish haze appears, due to scattering from sub-micron particles of protein and fat in the milk. If the straight-through light beam is observed using a piece of white paper as a screen, it will appear orange or red due to the blue part of the spectrum having been removed by this scattering. If more milk is added, the liquid will become white, due to the large number of scatterers; all of the light entering the liquid is scattered, and none is transmitted. The light we see leaving the liquid therefore consists of all wavelengths

*At this point Rayleigh wrongly believed light to consist of mechanical vibrations, but in 1881 [1] obtained the same dependence on λ using Maxwell's new electromagnetic wave theory.

present in the incident beam, and the milk appears white.

Scattering from a pure liquid like the water in our milk experiment occurs due to the thermal density fluctuations discussed above. These in turn give rise to spatial and temporal fluctuations in the dielectric constant ϵ which cause light to be scattered. A theory treating light scattering from dense media was published by Einstein in 1910 [2], giving an expression for the scattered intensity which depends on $\langle(\Delta\epsilon)^2\rangle$ – the mean square fluctuation of ϵ – and again varies as λ^{-4} (see Eq. 2.1). The process is weak, with approximately one millionth of the incident light being affected [3].

Further consideration of Einstein's theory led to a surprising result; the frequency of the scattered light is altered by the thermal fluctuations, producing a characteristic spectrum which contains useful information on thermodynamic and transport properties of the scattering medium. This process is called *Brillouin scattering*, after the French physicist Léon Brillouin, who predicted the effect in 1914 [4].

The form of this spectrum can be derived by developing a hydrodynamic theory of the fluctuations and calculating the correlation functions relevant to light scattering measurements; this approach will be summarised in Sec. 2.2 below. However a great deal of insight into the origin of the effect may be gained without resorting to the full mathematical treatment, as we will now see.

2.1 Physical origin of the Rayleigh-Brillouin spectrum

According to the Einstein theory, the total intensity I of light scattered by a homogeneous medium consisting of spherically symmetric molecules is given by

$$I = I_0 \frac{\pi^2}{r^2\lambda^4} V^2 \langle(\Delta\epsilon)^2\rangle \tag{2.1}$$

where I_0 is the incident intensity, and r is the distance of the detector from the volume element V which is the source of the scattering [5]. Assuming a constant wavelength λ of incident light as is the case in a conventional experiment, the key quantity in this expression is the mean square fluctuation of the dielectric constant.

The fluctuation $\Delta\epsilon$ can be decomposed into fluctuations in pairs of statistically independent thermodynamic variables. We could choose the density $\Delta\rho$ and temperature

ΔT, but it will be more illuminating to consider the fluctuations in entropy ΔS and pressure ΔP, because this factors $\Delta\epsilon$ into propagating and non-propagating parts:

$$\Delta\epsilon = \left(\frac{\partial\epsilon}{\partial S}\right)_P \Delta S + \left(\frac{\partial\epsilon}{\partial P}\right)_S \Delta P \tag{2.2}$$

Since fluctuations in entropy and pressure are statistically independent, cross terms like $\langle(\Delta S \Delta P)\rangle$ vanish when Eq. 2.2 is squared, leaving only $\langle(\Delta S)^2\rangle$ and $\langle(\Delta P)^2\rangle$ terms to be substituted into Eq. 2.1. These fluctuations therefore contribute individually to the scattered intensity, resulting in two different spectral features.

2.1.1 Entropy fluctuations at constant pressure – the Rayleigh peak

Entropy fluctuations at constant pressure do not propagate in a normal liquid and as such scatter light without change in frequency [6]. They decay over time due to damping by thermal dissipation, resulting in frequency-broadening of the spectral feature associated with entropy fluctuations. This feature will appear centred at $\nu = \nu_0$, the frequency of the incident light, and has come to be known as the *Rayleigh peak*. The fluctuations decay according to the heat diffusion equation, and the shape of this peak will be Lorentzian with width $\Delta\omega_R$ proportional to the thermal diffusivity $D_T = \kappa/\rho c_P$, where κ is the thermal conductivity, ρ the mass density and c_P the specific heat capacity at constant pressure (see e.g. Ref. [5]). In fact this width is typically only a few MHz, which is not resolvable using a Fabry-Perot interferometer and is therefore swamped by instrumental broadening of the laser line in all of the spectra presented later in this thesis.

2.1.2 Adiabatic pressure fluctuations – the Brillouin doublet

Adiabatic pressure fluctuations *do* propagate in a liquid – as sound waves. The existence of spontaneously occurring thermally generated sound waves in a fluid is perhaps initially surprising, but arises naturally from the random thermal motion of molecules in a manner analogous to the origin of lattice vibrations (phonons) in solids.

The density, and hence local pressure, fluctuates due to random thermal motion which causes the number of molecules within a given volume to change over time. Because

they are random, the pressure fluctuations can be considered to be a Fourier sum of sinusoidal pressure waves travelling in all directions, with all frequencies, at the speed of sound in the material. The excitation frequency and scattering angle select the wavevector of the thermally generated sound wave which is probed in a light scattering experiment. In liquids, the only sound mode which can be supported is compressional (longitudinal) because of the inability of the medium to support shear stress.

Léon Brillouin noted that these pressure waves consist of successive compressions and rarefactions in the medium, making it optically inhomogeneous. These will of course be periodic in space, and therefore form something like a diffraction grating. An incoming beam of light with wavelength λ will be partially scattered at angles for which constructive interference occurs between reflections from different scattering planes: angles of incidence θ_i satisfying the Bragg condition $d = \lambda_s = 2\lambda sin\theta_i$ where λ_s is the wavelength of the sound wave and hence the pitch of the grating. This is illustrated in Fig. 2.1. The sound waves are of course propagating at the speed of sound v_s through the medium, so our 'diffraction grating' is *moving*. The scattered light will therefore be shifted in frequency by the Doppler effect, and the spectrum must have blue- and red-shifted peaks corresponding to waves travelling towards and away from the observer. These are the *Brillouin peaks* and occur at $\pm\nu_B$, a frequency equal to that of the sound wave in the scattering medium. This process is sometimes referred to as *thermal scattering*.

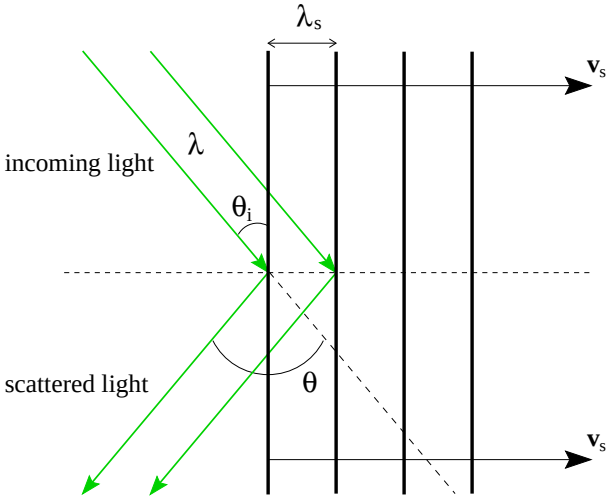

Figure 2.1: Diffraction of light from a grating moving at speed v_s, formed by thermally generated pressure waves propagating in a liquid (after Ref. [5]). θ is the scattering angle.

An alternative approach to the scattering of light by a thermally generated sound wave is to adopt the quantum mechanical description of the process as an inelastic collision between a quantum of light (a photon) and a quantum of vibrational energy (a phonon) in the liquid. Following Ref. [3] we can use this picture to calculate the frequency shift of the Brillouin peaks. If the wavevector of the thermal phonon selected by the Bragg condition for scattering at an angle θ is $\boldsymbol{q}$, then conservation of momentum requires $\boldsymbol{q} = \boldsymbol{k}_s - \boldsymbol{k}_i$, where $\boldsymbol{k}_i$ and $\boldsymbol{k}_s$ are the incident and scattered wavevectors respectively. A schematic illustration of the scattering event is shown in Fig. 2.2. The energy change in light scattering is very small, so the magnitude of the wavevector of the light before and after scattering will be the same to a good approximation; $k_i \approx k_s \equiv k = 2\pi/\lambda$, where λ is the wavelength of the light *in vacuo*. The vector diagram in Fig. 2.3 then allows us to relate the magnitude q of the wavevector of the thermal phonon probed by light of wavelength λ at a scattering angle θ. This extremely important relationship will be referred to throughout this thesis:

$$\boxed{q = \frac{4\pi n}{\lambda} \sin\theta/2} \tag{2.3}$$

where n is the refractive index of the medium.

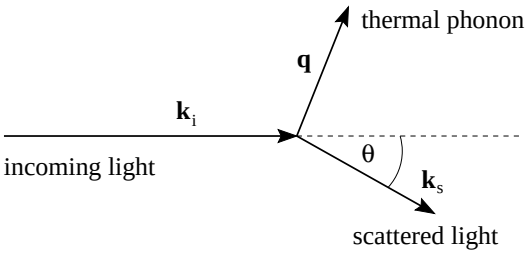

Figure 2.2: Incoming light with wavevector $\boldsymbol{k}_i$ is scattered by a thermal phonon of wavevector $\boldsymbol{q}$, resulting in scattered light with wavevector $\boldsymbol{k}_s$. The scattering angle is θ.

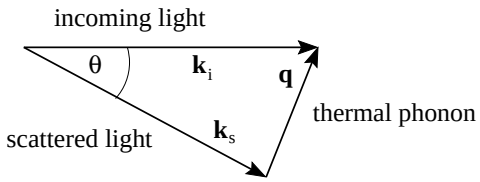

Figure 2.3: Vector diagram of the scattering event in Fig. 2.2. Since $k_i \approx k_s = k$ which becomes nk in the liquid, it follows that $q = 2nk\sin\theta/2 = \frac{4\pi n}{\lambda}\sin\theta/2$.

The thermal phonon (which can be thought of as a sound wave as described above) travels at the adiabatic speed of sound v_s, so $q = 2\pi\nu_{ph}/v_s$ where ν_{ph} is the frequency

of the phonon, and substituting into Eq. 2.3 gives

$$\nu_{ph} = \frac{2nv_s}{\lambda} \sin\theta/2 \qquad \text{or} \qquad \omega_{ph} = v_s q \tag{2.4}$$

The spectrum will therefore contain two Brillouin peaks at $\pm\nu_B = \nu_{ph}$, caused by energy being taken from or given to the photon by the phonon. The same formula could have been derived within the Doppler shift framework, with the higher frequency peak corresponding to a sound wave moving towards the detector, and the lower peak a wave going in the opposite direction. The position of the Brillouin peak can therefore be used to determine the sound velocity in a very straightforward way. In a solid (or viscoelastic liquid) there will be more pairs of Brillouin peaks corresponding to the ability of the medium to support more than one sound mode.

The frequencies of thermal phonons probed by light scattering are in the GHz range – often referred to as *hypersonic*. The sound velocity measured by Brillouin spectroscopy is therefore a high-frequency value, which may differ by a few percent from the low-frequency (MHz and below) speed depending on the properties of the liquid. This important point will be discussed further in Sec. 2.1.3.

The Brillouin peaks are broadened due to absorption of sound waves in the liquid. This dissipation is due to viscosity and thermal conduction (these contributions will be evaluated in Sec. 2.2.1.3). If the phonon lifetime is τ, the half width at half height (HWHH) $\Delta\omega_B = 2\pi\Delta\nu_B$ will be given by $1/\tau$. The absorption coefficient per unit distance α may also be measured using the Brillouin peak; $\Delta\omega_B = \alpha v_s$ [5].

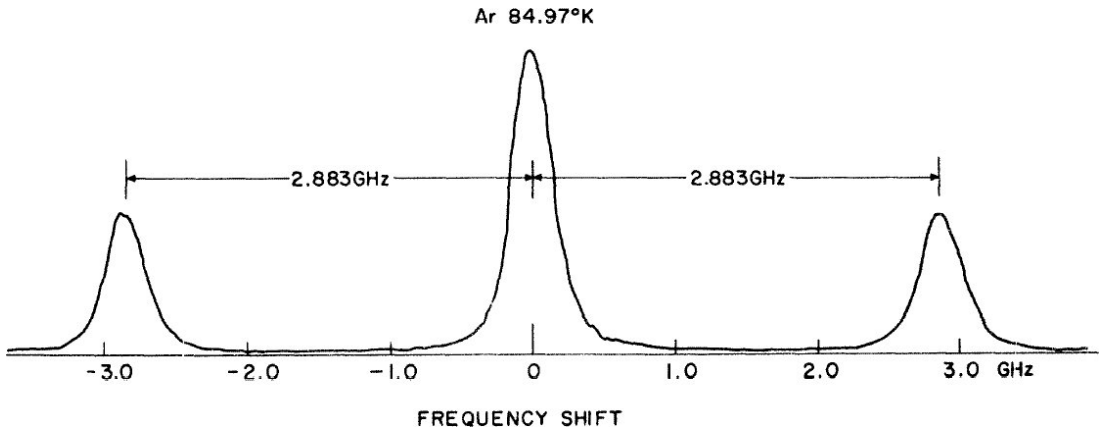

Figure 2.4: Brillouin spectrum of liquid argon at 84.97 K. λ = 514.5 nm, θ = 90° [7].

A typical Rayleigh-Brillouin spectrum of a simple monatomic fluid (liquid argon) is shown in Fig. 2.4, reproduced from an early paper by Fleury & Boon [7]. The features which have been discussed above are apparent; the central Rayleigh peak flanked by a pair of Brillouin peaks shifted in frequency by a few GHz. The spectrum shown is artificially broadened by the resolving instrument (a Fabry-Perot interferometer in this case). In order to extract the true linewidths, the response function of the interferometer could be deconvoluted. This will be discussed in Sec. 3.1.2.3 below. The refractive index of argon is $n = 1.2319$ at this temperature [7], hence the magnitude of the scattering vector $q = 0.0213\,\mathrm{nm}^{-1}$ (calculated using Eq. 2.3). Eq. 2.4 can then be used to find the hypersonic sound velocity, $v_s = 850\,\mathrm{ms}^{-1}$ using the observed Brillouin shift $\nu_B = 2.883\,\mathrm{GHz}$.

2.1.3 Sound propagation in liquids

As we have now seen, the Brillouin spectrum is directly related to the existence of adiabatic sound waves in the scattering medium. It will therefore be useful to look at some of the properties of sound propagation in liquids. An excellent review of the theory of sound in fluids can be found in Chapter 8 of Ref. [8].

A longitudinal adiabatic sound wave in a liquid will move with speed

$$v_s = \sqrt{\frac{B}{\rho}} = \sqrt{\frac{1}{\chi_S\,\rho}} \tag{2.5}$$

where B is the bulk modulus, equal to the inverse of χ_S, the adiabatic compressibility. This has the usual form of a sound velocity; the square root of an elasticity term over an inertia. Substituting the isothermal compressibility χ_T for χ_S would give the isothermal sound speed v_T, but as the pressure fluctuations which result in Brillouin peaks are adiabatic, it will be the adiabatic value v_s which is used in this thesis. The two quantities are related: $v_s^2 = \gamma v_T^2$ where γ is the ratio of specific heats.

Typical sound speeds in simple liquids at room temperature range from $900\,\mathrm{ms}^{-1}$ to $1400\,\mathrm{ms}^{-1}$, and usually increase by about $3\,\mathrm{ms}^{-1}$ for each 1 K decrease in temperature [9].

Many people intuitively expect that increasing the density of a material should result

in a higher sound speed, but this is not the case, as can be seen from Eq. 2.5. This assumption is perhaps due to the fact that sound speed increases upon condensation of a gas into a liquid, when the density of course increases dramatically. However this is outweighed by the reduction in compressibility which accompanies the phase change.

A key quantity in determining the sound velocity is therefore the adiabatic compressibility χ_S, which is defined as

$$\chi_S = \frac{1}{\rho}\left(\frac{\partial \rho}{\partial P}\right)_S = -\frac{1}{V}\left(\frac{\partial V}{\partial P}\right)_S \tag{2.6}$$

It is a measure of the density (or volume) change which occurs when pressure is applied to the liquid, and has units of inverse pressure, Pa^{-1}. The compressibility therefore determines how readily compressions and rarefactions can be formed in the liquid, and thus how 'easy' it is for a sound wave to propagate. Interestingly, as a critical point is approached, the adiabatic compressibility diverges, so we expect the sound speed and hence Brillouin shift $\omega_B = v_s q$ to tend to zero; the Brillouin peaks will move in towards the central Rayleigh peak [10].

Sound waves in a liquid are absorbed due to the dissipation of energy by viscosity and thermal conduction. This means that the intensity of a sound wave diminishes with a characteristic lifetime which, as noted above, results in broadening of the Brillouin peak. The quantities which determine the extent of this absorption will therefore be the thermal conductivity κ and the bulk and shear viscosities η_v and η_s. The bulk viscosity may contain contributions due to dissipative relaxation processes involving intramolecular degrees of freedom or structural changes in the liquid, and will be discussed further in Sec. 2.2.3. Large thermal conductivity or viscosities will result in a heavily damped sound wave, and a large Brillouin linewidth. As stated in Sec. 2.1.2 above, the HWHH of the Brillouin peak $\Delta\omega_B = \alpha v_s = 1/\tau$, where α is the absorption coefficient per unit distance and τ is the lifetime of the thermal phonon. τ is the time taken for the intensity of the sound wave to fall to $1/e$ of its initial value, and α is defined such that the intensity falls off as $e^{-\alpha x}$, where x represents distance.

When intramolecular relaxation is present, or when the liquid has local structure, the sound velocity becomes frequency dependent (*dispersion*). At high enough frequencies, the molecules will not be able to follow the periodic rearrangements of the sound wave, and the relaxation will be frozen out. Thus a zero frequency limit v_0 and an infinite

frequency limit v_∞ can be defined, with the observed sound speed v_s lying somewhere between the two extremes. The three speeds are related according to the expression

$$\frac{v_s^2}{v_0^2} - 1 = \left(\frac{v_\infty^2}{v_0^2} - 1\right) \frac{\omega^2 \tau_r^2}{1 + \omega^2 \tau_r^2} \tag{2.7}$$

where a single relaxation time τ_r is assumed [11]. Measurement of v_0 and v_∞ therefore allows the relaxation time to be extracted from a fit to this equation. The infinite frequency speed is typically 5–10 % higher than the zero frequency value. v_0 can usually be measured in the MHz region with a conventional ultrasound experiment, but v_∞ is often inaccessible and hypersonic values from Brillouin scattering must be extrapolated to higher frequencies. In some viscous liquids, varying the temperature changes the structural relaxation time dramatically, and the transition from v_0 to v_∞ falls in a frequency range which allows the two limits to be accessed, enabling an accurate measurement of τ_r to be made (see e.g. [3]). The effects of intramolecular and structural relaxation on the Brillouin spectrum will be discussed further in Sec. 2.2.3 and Chapter 4.

When comparing sound velocities measured using light scattering techniques with the results of ultrasonic experiments, it must be recognised that there is an inherent difference between 'thermal phonons' and 'ultrasonic phonons'. In the words of Evans & Powles [12] "Brillouin scattering is not ultrasonics at hypersonic frequencies and vice versa". A light scattering experiment requires a real spatial wave to exist in the fluid from which diffraction then occurs; the scattering vector $\boldsymbol{q}$ is thus real, and the finite lifetime of the wave means that its frequency ω is complex. The opposite is true in an ultrasonic measurement, where the frequency imposed by the transducer is real and well-defined, with the wave decaying in space so that its wavenumber k is complex. As long as one is aware of the differences in phase velocities calculated using these different boundary conditions, problems of interpretation can be avoided. The issue will not arise in this thesis because no detailed comparison of Brillouin scattering with ultrasonic results is attempted.

So, to summarise our findings so far, the random thermal motion of molecules in a liquid results in the frequency of an incident beam of light being modulated to produce a spectrum of scattered light with three peaks; a central unshifted Rayleigh peak due to entropy fluctuations, and a pair of Brillouin peaks at the incident frequency $\pm\nu_B$

due to the interaction of light with random thermally generated pressure fluctuations, which can be thought of as sound waves. Without recourse to any detailed theoretical treatment, we have established the form of the Brillouin spectrum, and discussed some of the physical properties of liquids which may be revealed by the technique.

Such a qualitative approach – though extremely valuable – is not capable of identifying all of the processes which contribute to the observed spectrum. The next section therefore attempts to guide the reader through the derivation of an expression which contains *all* of the dynamical information probed by Brillouin spectroscopy, confirming and expanding the picture arrived at above.

2.2 Hydrodynamic derivation of the Rayleigh–Brillouin spectrum

Now that we have developed a degree of understanding of the Rayleigh and Brillouin peaks in the spectrum of light scattered from a liquid, it will be illuminating to consider a more systematic theoretical approach to the phenomenon. It is possible to derive an analytic expression which fully describes the spectrum by writing down conservation laws for the random thermal fluctuations introduced above, then using them to develop a set of hydrodynamic equations which can be solved to yield the density-density correlation function probed in a light scattering experiment.

The mathematical treatment presented here differs in tone from the predominantly experimental nature of this thesis, but is necessary in order to appreciate fully the hydrodynamic and thermodynamic origins of the results which will be presented in later chapters. The full expression describing the spectrum which we obtain in Sec. 2.2.1.3 may be fitted to the results of these experiments in order to extract many useful thermodynamic and transport properties of the fluid being studied.

The derivation of the spectral density $S_{\rho\rho}(\boldsymbol{q},\omega)$ (which describes the spectrum – it is the Fourier transform of the density-density correlation function) will first be described in some detail for the idealised case of a one component, monatomic hard-sphere fluid. The important extension to the case of a relaxing molecular liquid will then be discussed

in Sec. 2.2.3.

The following is an attempt to combine the complementary approaches of the invaluable books by Berne & Pecora [13] and Boon & Yip [14]. Where details have inevitably been omitted below, these works – together with the original review paper on the subject by Mountain [15] – can usually be relied upon to provide a more complete treatment. In particular, some of the more complex parts of the derivation (such as Laplace-Fourier transforms and lengthy matrix algebra) are left for the interested reader to follow in the literature; the aim of this discussion is to highlight the key stages along the route to the final expression for $S_{\rho\rho}(\boldsymbol{q}, \omega)$.

2.2.1 Pure monatomic fluid with no intramolecular relaxation

The intensity of light scattered isotropically[†] from a pure monatomic liquid is proportional to the spectral density $S_{\rho\rho}(\boldsymbol{q}, \omega)$ of the autocorrelation function of thermally generated density fluctuations [13] (sometimes referred to as the dynamic structure factor), which contains all of the dynamical information necessary to describe the functional form of the Rayleigh-Brillouin spectrum. This relationship between the dynamic structure factor and scattered intensity at a given $\boldsymbol{q}$ and ω is very important, because it allows theoretical calculations of correlation functions to be compared to the results of many types of scattering experiments. The density fluctuations which contribute to the spectrum in the hypersonic region are collective movements of many thousands of particles (in a light scattering experiment $q \sim 0.02\,\mathrm{nm}^{-1}$ which corresponds to a length of 500 Å), hence we will use the macroscopic laws of hydrodynamics and thermodynamics to derive the correlation function, which can then be Fourier transformed to give $S_{\rho\rho}(\boldsymbol{q}, \omega)$.

We will begin by establishing a set of conservation laws for the number of particles, their momentum, and energy, within a small volume of liquid whose dimensions are chosen according to the requirements of hydrodynamics. These are used to write down a set of hydrodynamic equations which are linearised, and then solved using Laplace-Fourier analysis and perturbation theory to obtain the density-density correlation function.

[†]We will neglect the contribution from depolarised (VH) scattering, which is negligible for simple liquids in the GHz region.

Note that the density considered in the following section is the *number* density of particles in a small volume. Previously, and in subsequent chapters of this thesis, the *mass* density will be more appropriate. The conventional symbol ρ is used to represent both quantities. Local densities of other variables such as the energy E and momentum $\boldsymbol{G}$ will be denoted by small case letters; e and $\boldsymbol{g}$ respectively for these examples.

2.2.1.1 Conservation equations

We will consider a fluid element of volume V and surface S with dimensions large compared to the size of a molecule, but small enough that the values of thermodynamic variables inside V are the same as at the interior reference point which defines its position in space.

Conservation of matter – the *continuity equation*
The total number of particles in this volume element V as a function of time is given by $N(t) = \int_V \mathrm{d}^3 r\, \rho(\boldsymbol{r}, t)$, where $\rho(\boldsymbol{r}, t)$ is the time-dependent local number density. By conservation of matter, the rate of change of N must be equal to the rate at which particles flow through the surface of the volume element, which is given by the divergence of this flux $\boldsymbol{\nabla} \cdot \boldsymbol{J}(\boldsymbol{r}, t)$. Hence the so-called continuity equation

$$\frac{\partial \rho(\boldsymbol{r}, t)}{\partial t} + \boldsymbol{\nabla} \cdot \boldsymbol{J}(\boldsymbol{r}, t) = 0 \tag{2.8}$$

where $\boldsymbol{J}(\boldsymbol{r}, t) = \rho(\boldsymbol{r}, t)\boldsymbol{u}(\boldsymbol{r}, t)$ denotes the flux of particle number.

This form of conservation equation is general; for any conserved extensive variable $\mathcal{A}$ with a local density $A(\boldsymbol{r}, t)$, there can be no net creation or destruction of $\mathcal{A}$ in a volume element, thus

$$\frac{\partial A(\boldsymbol{r}, t)}{\partial t} + \boldsymbol{\nabla} \cdot \boldsymbol{J}_A(\boldsymbol{r}, t) = 0 \tag{2.9}$$

with $\boldsymbol{\nabla} \cdot \boldsymbol{J}_A(\boldsymbol{r}, t)$ giving the rate of change of $\mathcal{A}$ within V due to outwards flow through the surface of the volume element [13]. Eq. 2.8 is a specific case of this general form, with the conserved extensive quantity N having a density $\rho(\boldsymbol{r}, t)$. The two remaining conservation equations can be stated in a similar manner as will be seen below.

Eq. 2.8 can be restated in a more useful way by considering the origin of changes in the particle number N within V. Since $N(t) = \int_V \mathrm{d}^3 r\, \rho(\boldsymbol{r}, t)$, the rate of change of N

with time will be given by

$$\frac{\mathrm{d}N(t)}{\mathrm{d}t} = \int_V \mathrm{d}^3 r \, \frac{\partial \rho(\boldsymbol{r}, t)}{\partial t} \tag{2.10}$$

The only process by which N can change is convection into or out of V through its surface S. The volume of fluid flowing out in this way is $\boldsymbol{u}(\boldsymbol{r}, t) \cdot \mathrm{d}\boldsymbol{S}$ where $\mathrm{d}\boldsymbol{S}$ is an element of S. Hence the number of particles flowing into V through $\mathrm{d}\boldsymbol{S}$ per unit time will be $-\rho(\boldsymbol{r}, t)\boldsymbol{u}(\boldsymbol{r}, t) \cdot \mathrm{d}\boldsymbol{S}$, and integrating this over S will give the total change in N due to convection. As there is no other contribution to $\frac{\mathrm{d}N(t)}{\mathrm{d}t}$, we can equate this integral to the right hand side of Eq. 2.10 to obtain

$$\int_V \mathrm{d}^3 r \, \frac{\partial \rho(\boldsymbol{r}, t)}{\partial t} = -\int_S \rho(\boldsymbol{r}, t)\boldsymbol{u}(\boldsymbol{r}, t) \cdot \mathrm{d}\boldsymbol{S} \tag{2.11}$$

Conservation of momentum

If we now define a momentum vector $\boldsymbol{G}(t)$ with a momentum density $\boldsymbol{g}(\boldsymbol{r}, t)$ such that $\boldsymbol{G}(t) = \int_V \mathrm{d}^3 r \, \boldsymbol{g}(\boldsymbol{r}, t)$, conservation of momentum can be expressed in the same way as for conservation of matter;

$$\frac{\partial g_i(\boldsymbol{r}, t)}{\partial t} + \nabla_j \cdot \tau_{ij}(\boldsymbol{r}, t) = 0 \qquad (i = 1, 2, 3) \tag{2.12}$$

The flux of momentum $\tau_{ij}(\boldsymbol{r}, t)$ is the j^{th} component of the flux of the i^{th} component of the momentum.

As in the case of the particle number above, we can now consider the processes which cause the momentum to change within V. Following the same argument which led to Eq. 2.11, the increase in $\boldsymbol{G}(t)$ due to convection will be $-\int_S \boldsymbol{g}(\boldsymbol{r}, t)\boldsymbol{u}(\boldsymbol{r}, t) \cdot \mathrm{d}\boldsymbol{S}$. The momentum will also change if the fluid surrounding V exerts a force $\boldsymbol{F}$. The force $\mathrm{d}\boldsymbol{F}$ acting on $\mathrm{d}\boldsymbol{S}$ can be written $\mathrm{d}\boldsymbol{F} = \boldsymbol{\sigma} \cdot \mathrm{d}\boldsymbol{S}$, defining the stress tensor $\boldsymbol{\sigma}$. Integrating $\mathrm{d}\boldsymbol{F}$ over S then gives the total force exerted on the fluid, $\boldsymbol{F} = \int_S \boldsymbol{\sigma} \cdot \mathrm{d}\boldsymbol{S}$. Appealing to the expression for $\boldsymbol{G}(t)$ above, the rate of change of momentum within V will be

$$\frac{\mathrm{d}\boldsymbol{G}(t)}{\mathrm{d}t} = \int_V \mathrm{d}^3 r \, \frac{\partial \boldsymbol{g}(\boldsymbol{r}, t)}{\partial t} \tag{2.13}$$

and we can thus equate our integrals for contributions from convection and force to the right hand side of Eq. 2.13 to obtain

$$\int_V \mathrm{d}^3 r \, \frac{\partial \boldsymbol{g}(\boldsymbol{r}, t)}{\partial t} = \int_S [\boldsymbol{\sigma}(\boldsymbol{r}, t) - \boldsymbol{g}(\boldsymbol{r}, t)\boldsymbol{u}(\boldsymbol{r}, t)] \cdot \mathrm{d}\boldsymbol{S} \tag{2.14}$$

As momentum is the product of mass and velocity, we can write $\boldsymbol{g}(\boldsymbol{r},t) = m\rho(\boldsymbol{r},t)\boldsymbol{u}(\boldsymbol{r},t)$ and substitute in the above equation such that

$$\int_V \mathrm{d}^3 r \, \frac{\partial \boldsymbol{g}(\boldsymbol{r},t)}{\partial t} = \int_S [\boldsymbol{\sigma}(\boldsymbol{r},t) - m\rho(\boldsymbol{r},t)\boldsymbol{u}(\boldsymbol{r},t)\boldsymbol{u}(\boldsymbol{r},t)] \cdot \mathrm{d}\boldsymbol{S} \tag{2.15}$$

Conservation of energy

The final conserved density we will consider is the energy density $e(\boldsymbol{r},t)$, defined such that the energy of the fluid in the volume element V is $E(t) = \int_V \mathrm{d}^3 r \, e(\boldsymbol{r},t)$. If the flux of energy is given by $\boldsymbol{J}_e(\boldsymbol{r},t)$, then conservation of energy can be written

$$\frac{\partial e(\boldsymbol{r},t)}{\partial t} + \boldsymbol{\nabla} \cdot \boldsymbol{J}_e(\boldsymbol{r},t) = 0 \tag{2.16}$$

where $\boldsymbol{\nabla} \cdot \boldsymbol{J}_e(\boldsymbol{r},t)$ is the flow of energy out of V.

As for the other conserved quantities discussed above, we can recast this relation into a more useful form by considering the processes which contribute to changes of energy within V. There will once again be a contribution due to convection, as well as work done on V by the fluid outside and heat diffusion from the surroundings. In the same way as for conservation of matter and momentum, the increase in $E(t)$ due to convection from outside V will be $-\int_S e(\boldsymbol{r},t)\boldsymbol{u}(\boldsymbol{r},t) \cdot \mathrm{d}\boldsymbol{S}$. The work done per unit time on $\mathrm{d}\boldsymbol{S}$ by $\mathrm{d}\boldsymbol{F}$ is $\boldsymbol{u}(\boldsymbol{r},t) \cdot \mathrm{d}\boldsymbol{F} = \boldsymbol{u}(\boldsymbol{r},t) \cdot \boldsymbol{\sigma}(\boldsymbol{r},t) \cdot \mathrm{d}\boldsymbol{S}$, since $\mathrm{d}\boldsymbol{F} = \boldsymbol{\sigma}(\boldsymbol{r},t) \cdot \mathrm{d}\boldsymbol{S}$. The work done on V per unit time is therefore $\int_S \boldsymbol{u}(\boldsymbol{r},t) \cdot \boldsymbol{\sigma}(\boldsymbol{r},t) \cdot \mathrm{d}\boldsymbol{S}$. The heat diffusing into $\mathrm{d}\boldsymbol{S}$ from the surroundings per unit time is $-\boldsymbol{Q}(\boldsymbol{r},t) \cdot \mathrm{d}\boldsymbol{S}$ where $\boldsymbol{Q}(\boldsymbol{r},t)$ is the flux of heat due to diffusion, giving a total increase of heat in V of $-\int_S \boldsymbol{Q}(\boldsymbol{r},t) \cdot \mathrm{d}\boldsymbol{S}$ per unit time. Appealing to the expression for $E(t)$ above, the rate of change of energy within V can be written

$$\frac{\mathrm{d}E(t)}{\mathrm{d}t} = \int_V \mathrm{d}^3 r \, \frac{\partial e(\boldsymbol{r},t)}{\partial t} \tag{2.17}$$

and we can equate our integrals for the contributions from convection, work done and heat diffusion to the right hand side to get

$$\int_V \mathrm{d}^3 r \, \frac{\partial e(\boldsymbol{r},t)}{\partial t} = \int_S [\boldsymbol{u}(\boldsymbol{r},t) \cdot \boldsymbol{\sigma}(\boldsymbol{r},t) - e(\boldsymbol{r},t)\boldsymbol{u}(\boldsymbol{r},t) - \boldsymbol{Q}(\boldsymbol{r},t)] \cdot \mathrm{d}\boldsymbol{S} \tag{2.18}$$

The three conservation laws

We now have three expressions for conservation of matter, momentum and energy densities, all of which equate a volume integral to a surface integral. We can appeal

to Gauss's theorem (also called the divergence theorem) [16] to convert the surface integrals to volume integrals, resulting in a major simplification of these conservation laws. Taking the expression for conservation of matter (Eq. 2.11) as an example, applying Gauss's theorem to the right hand side gives

$$-\int_S \rho(\boldsymbol{r},t)\boldsymbol{u}(\boldsymbol{r},t)\cdot \mathrm{d}\boldsymbol{S} = -\int_V \mathrm{d}^3\boldsymbol{r}\,\boldsymbol{\nabla}\cdot\rho(\boldsymbol{r},t)\boldsymbol{u}(\boldsymbol{r},t) \tag{2.19}$$

Hence Eq. 2.11 can be restated as

$$\int_V \mathrm{d}^3\boldsymbol{r}\left[\frac{\partial\rho(\boldsymbol{r},t)}{\partial t}+\boldsymbol{\nabla}\cdot\rho(\boldsymbol{r},t)\boldsymbol{u}(\boldsymbol{r},t)\right]=0 \tag{2.20}$$

and since V is arbitrary, it follows that the integrand must be equal to zero, resulting in a final statement of the conservation of matter;

$$\boxed{\frac{\partial\rho(\boldsymbol{r},t)}{\partial t}+\boldsymbol{\nabla}\cdot\rho(\boldsymbol{r},t)\boldsymbol{u}(\boldsymbol{r},t)=0} \tag{2.21}$$

In the same manner, application of Gauss's theorem to the right hand sides of Eqs. 2.15 and 2.18 results in concise statements of conservation of local momentum density

$$\boxed{\frac{\partial\boldsymbol{g}(\boldsymbol{r},t)}{\partial t}+\boldsymbol{\nabla}\cdot[m\rho(\boldsymbol{r},t)\boldsymbol{u}(\boldsymbol{r},t)\boldsymbol{u}(\boldsymbol{r},t)-\boldsymbol{\sigma}(\boldsymbol{r},t)]=0} \tag{2.22}$$

and energy density

$$\boxed{\frac{\partial e(\boldsymbol{r},t)}{\partial t}+\boldsymbol{\nabla}\cdot[\boldsymbol{Q}(\boldsymbol{r},t)+e(\boldsymbol{r},t)\boldsymbol{u}(\boldsymbol{r},t)-\boldsymbol{u}(\boldsymbol{r},t)\cdot\boldsymbol{\sigma}(\boldsymbol{r},t)]=0} \tag{2.23}$$

respectively.

2.2.1.2 The linearised equations of hydrodynamics

Now that we have established conservation laws for the local densities of matter, momentum and energy, we can proceed with our calculation of the Brillouin spectrum by establishing a set of hydrodynamic equations, which when solved yields the spectral density function which describes the spectrum.

The conservation laws alone are not enough to allow us to obtain these hydrodynamic equations. They must be used in conjunction with *constitutive relations* which relate fluxes to densities; they then form a closed set of equations which may be solved.

Constitutive relations

Comparing the three conservation equations 2.21, 2.22 and 2.23 with Eqs. 2.8, 2.12

and 2.16 respectively allows us to relate the fluxes of particle number, momentum and energy with their corresponding local densities to give a set of constitutive relations;

$$\boldsymbol{J}(\boldsymbol{r},t) = \rho(\boldsymbol{r},t)\,\boldsymbol{u}(\boldsymbol{r},t) \tag{2.24a}$$

$$\tau_{ij}(\boldsymbol{r},t) = m\rho(\boldsymbol{r},t)\,u_i(\boldsymbol{r},t)\,u_j(\boldsymbol{r},t) - \sigma_{ij}(\boldsymbol{r},t) \tag{2.24b}$$

$$\boldsymbol{J}_e(\boldsymbol{r},t) = e(\boldsymbol{r},t)\,\boldsymbol{u}(\boldsymbol{r},t) + \boldsymbol{Q}(\boldsymbol{r},t) - \boldsymbol{u}(\boldsymbol{r},t)\cdot\boldsymbol{\sigma}(\boldsymbol{r},t) \tag{2.24c}$$

Our next task is to expand the momentum and energy fluxes by substituting explicit expressions for $\tau_{ij}(\boldsymbol{r},t)$, $\boldsymbol{Q}(\boldsymbol{r},t)$ and $e(\boldsymbol{r},t)$ into Eqs. 2.24b and 2.24c.

The stress tensor $\sigma_{ij}(\boldsymbol{r},t)$ defined above can be split into two components – a pressure term $p\delta_{ij}$ and a viscous shear term $\sigma'_{ij}(\boldsymbol{r},t)$;

$$\sigma_{ij}(\boldsymbol{r},t) = -p\delta_{ij} + \sigma'_{ij}(\boldsymbol{r},t) \tag{2.25}$$

The viscous term is given by the Newtonian stress tensor

$$\sigma'_{ij} = \eta_s[\nabla_i u_j + \nabla_j u_i - \tfrac{2}{3}\boldsymbol{\nabla}\cdot\boldsymbol{u}\delta_{ij}] + \eta_v\boldsymbol{\nabla}\cdot\boldsymbol{u}\delta_{ij} \tag{2.26}$$

where η_s is the shear viscosity and η_v is the bulk viscosity. The velocity gradients enter the expression because the flux of momentum due to viscous processes is proportional to their magnitude. That is, $\sigma'_{ij}(\boldsymbol{r},t)$ represents a diffusion of momentum from regions of high momentum to regions of low momentum. Substituting the Newtonian stress tensor into Eq. 2.25, and then into Eq. 2.24b results in our final constitutive relation for the flux of momentum;

$$\boxed{\tau_{ij} = m\rho u_i u_j + p\delta_{ij} - \eta_s(\nabla_i u_j + \nabla_j u_i - \tfrac{2}{3}\boldsymbol{\nabla}\cdot\boldsymbol{u}\delta_{ij}) - \eta_v\boldsymbol{\nabla}\cdot\boldsymbol{u}\delta_{ij}} \tag{2.27}$$

where the dependence on $\boldsymbol{r}$ and t specified in earlier equations is implied.

We now deal with the constitutive relation for the energy flux $\boldsymbol{J}_e(\boldsymbol{r},t)$. The energy density $e(\boldsymbol{r},t)$ in Eq. 2.24c can be split into a kinetic contribution and a local *internal* energy density $e'(\boldsymbol{r},t)$;

$$e(\boldsymbol{r},t) = \tfrac{1}{2}m\rho(\boldsymbol{r},t)u^2(\boldsymbol{r},t) + e'(\boldsymbol{r},t) \tag{2.28}$$

and the diffusive heat flux $\boldsymbol{Q}$ can then be expanded using Fourier's law

$$\boldsymbol{Q} = -\kappa \boldsymbol{\nabla} T \tag{2.29}$$

where κ is the thermal conductivity and $\boldsymbol{\nabla} T$ is the temperature gradient in the fluid. Substituting these two expressions into Eq. 2.24c gives an expanded constitutive relation for $\boldsymbol{J}_e(\boldsymbol{r}, t)$;

$$\boxed{\boldsymbol{J}_e = (\tfrac{1}{2} m \rho u^2 + e')\boldsymbol{u} - \kappa \boldsymbol{\nabla} T - \boldsymbol{u} \cdot \boldsymbol{\sigma}} \tag{2.30}$$

in which Eqs. 2.25 and 2.26 may be used to substitute for $\boldsymbol{\sigma}(\boldsymbol{r}, t)$ when required.

The linearised equations of fluid dynamics

We now have a set of conservation equations and corresponding constitutive relations which can be combined to give a set of fluid dynamic equations. In order to simplify matters, these equations can be linearised, taking advantage of the assumption that thermodynamic fluctuations are small in our system.

Each of the seven variables ρ, $\boldsymbol{u}$, e, p and T on which our set of equations depends can be written as a sum of a constant equilibrium value and a small fluctuation around this equilibrium. For a variable x we write $x(\boldsymbol{r}, t) = x_0 + x_1(\boldsymbol{r}, t)$, where x_0 is the equilibrium value and $x_1(\boldsymbol{r}, t)$ is the fluctuation. In order to linearise the conservation equations and constitutive relations, we substitute $\rho(\boldsymbol{r}, t) = \rho_0 + \rho_1(\boldsymbol{r}, t)$ and so on, then neglect any terms which are higher than first order in the fluctuations. Thus terms such as u_1^2 and $\boldsymbol{u}_1 \rho_1$ will disappear. It should also be noted that, since the bulk fluid is at rest in our frame of reference, $\boldsymbol{u}_0 = 0$. Applying this linearisation procedure and substituting the constitutive relations (Eqs. 2.27, 2.30) into the conservation laws (Eqs. 2.21, 2.22) results in our first statement of the linearised equations of fluid mechanics [13, 14];

$$\frac{\partial \rho_1(\boldsymbol{r}, t)}{\partial t} = -\rho_0 \boldsymbol{\nabla} \cdot \boldsymbol{u}_1(\boldsymbol{r}, t) \tag{2.31a}$$

$$m\rho_0 \frac{\partial \boldsymbol{u}_1(\boldsymbol{r}, t)}{\partial t} = -\boldsymbol{\nabla} p_1(\boldsymbol{r}, t) + \eta_s \nabla^2 \boldsymbol{u}_1(\boldsymbol{r}, t) + \left(\eta_v + \tfrac{1}{3}\eta_s\right) \boldsymbol{\nabla}(\boldsymbol{\nabla} \cdot \boldsymbol{u}_1(\boldsymbol{r}, t)) \tag{2.31b}$$

$$\frac{\partial e_1(\boldsymbol{r}, t)}{\partial t} = \kappa \nabla^2 T_1(\boldsymbol{r}, t) - (e_0 + p_0) \boldsymbol{\nabla} \cdot \boldsymbol{u}_1(\boldsymbol{r}, t) \tag{2.31c}$$

The latter equation can also be expressed as a function of the entropy fluctuation s_1 by eliminating $\boldsymbol{\nabla} \cdot \boldsymbol{u}_1$ [13];

$$T_0 \frac{\partial s_1(\boldsymbol{r}, t)}{\partial t} = \kappa \nabla^2 T_1(\boldsymbol{r}, t) \tag{2.31d}$$

As they stand, these linearised equations cannot be solved, as there are only five equations (in ρ_1, $\boldsymbol{u}_1$ and s_1) containing seven unknowns. The final step in our derivation of a soluble set of hydrodynamic equations is to eliminate a statistically independent pair of these variables. This can be done by assuming that the system is in local equilibrium, then appealing to the thermodynamic equations of state. The most convenient variables to eliminate are pressure and entropy, using the relations [13]

$$p_1 = m v_T^2 \left(\rho_1 + \alpha \rho_0 T_1\right) \qquad\qquad s_1 = -\frac{m \rho_0 c_V}{T_0}\left[\frac{(\gamma - 1)}{\alpha \rho_0}\rho_1 - T_1\right] \tag{2.32}$$

where v_T is the isothermal speed of sound, α is the thermal expansion coefficient, c_V is the specific heat capacity at constant V, and $\gamma \equiv c_P/c_V$ is the ratio of specific heats.

Using these expressions for p_1 and s_1, Eqs. 2.31a, 2.31b and 2.31d can be reduced to the closed set of linearised hydrodynamic equations

$$\frac{\partial \rho_1(\boldsymbol{r}, t)}{\partial t} + \rho_0 \, \psi_1(\boldsymbol{r}, t) = 0 \tag{2.33a}$$

$$\frac{\partial \psi_1(\boldsymbol{r}, t)}{\partial t} + \frac{v_T^2}{\rho_0} \nabla^2 \rho_1(\boldsymbol{r}, t) + \alpha v_T^2 \nabla^2 T_1(\boldsymbol{r}, t) - D_V \nabla^2 \psi_1(\boldsymbol{r}, t) = 0 \tag{2.33b}$$

$$\frac{\partial T_1(\boldsymbol{r}, t)}{\partial t} - \frac{\gamma - 1}{\alpha \rho_0} \frac{\partial \rho_1(\boldsymbol{r}, t)}{\partial t} - \gamma D_T \nabla^2 T_1(\boldsymbol{r}, t) = 0 \tag{2.33c}$$

where $\psi_1(\boldsymbol{r}, t) = \boldsymbol{\nabla} \cdot \boldsymbol{u}_1(\boldsymbol{r}, t)$. Note that the divergence of Eq. 2.31b has been taken in order to allow the elimination of $\boldsymbol{u}_1(\boldsymbol{r}, t)$ in favour of $\psi_1(\boldsymbol{r}, t)$. $D_V \equiv (\eta_v + \frac{4}{3}\eta_s)/m\rho_0$ is the longitudinal kinematic viscosity and $D_T \equiv \kappa / m \rho_0 c_P$ is the thermal diffusivity[‡].

This coupled set of three linear partial differential equations in three unknowns $\rho_1(\boldsymbol{r}, t)$, $\psi_1(\boldsymbol{r}, t)$ and $T_1(\boldsymbol{r}, t)$ can now be solved in order to derive an expression describing the Rayleigh-Brillouin spectrum of a simple monatomic liquid.

2.2.1.3 Solving the hydrodynamic equations

There exist several excellent and complementary treatments of the solution of the above linearised hydrodynamic equations [13, 14, 15], hence the details of this rather tedious process will not be included here. Instead the key points of the most straightforward

[‡] $D_T \equiv \kappa/\rho c_P$ was stated in Sec. 2.1.1, where the mass density was used rather than the number density.

approach will be highlighted before presenting the final solution and discussing its meaning and implications for experiments.

The first step is to take the Laplace-Fourier transforms of our set of equations. For example, $\rho_1(\boldsymbol{r},t)$ is Fourier transformed to give $\rho_1(\boldsymbol{q},t) = \int \mathrm{d}^3r\, e^{i\boldsymbol{q}\cdot\boldsymbol{r}}\rho_1(\boldsymbol{r},t)$, which is then Laplace transformed to give $\tilde{\rho_1}(\boldsymbol{q},s) = \int_0^\infty \mathrm{d}t\, e^{-st}\rho_1(\boldsymbol{q},t)$, where s is the complex Laplace transform variable (not to be confused with the entropy density, also conventionally represented by s). This Laplace-Fourier transform is essentially a Fourier transform in space *and* time. This process is applied to the hydrodynamic equations 2.33, and the result is expressed in matrix form. This is then solved using normal matrix algebra to give complicated expressions for $\tilde{\rho_1}(\boldsymbol{q},s)$, $\tilde{\psi_1}(\boldsymbol{q},s)$ and $\tilde{T_1}(\boldsymbol{q},s)$.

These solutions can then be multiplied by the complex conjugate of each variable, and averaged to give a set of correlation functions for pairs of the density and temperature fluctuations, their Laplace transforms and their complex conjugates. The one in which we are interested is the density-density correlation function, as this is the dominant contribution to the light scattering spectrum (see Sec. 2.2.1). When multiplied by $\pi^{-1}S(q)$ (where $S(q) = \langle\rho_1^*(\boldsymbol{q})\rho_1(\boldsymbol{q})\rangle$ is the structure factor) this gives a complete but very complicated expression for our objective; the spectral density function $S_{\rho\rho}(\boldsymbol{q},\omega)$ which fully describes the Rayleigh-Brillouin spectrum.

All that remains now is to simplify the full spectral density function into a more tractable form which lends itself to straightforward interpretation and facilitates the fitting procedures which will be used later in this thesis to analyse experimentally measured spectra. To do this we use a perturbation technique, expanding in the small (compared to the Brillouin shift $\omega_B(q) = 2\pi\nu_B$) quantities $D_V q^2$ and $\gamma D_T q^2$. To first order in these terms, after an inverse Laplace transformation we obtain the simplified density-density correlation function

$$\begin{aligned}\frac{\langle\rho_1^*(\boldsymbol{q},0)\rho_1(\boldsymbol{q},t)\rangle}{\langle\rho_1^*(\boldsymbol{q},0)\rho_1(\boldsymbol{q},0)\rangle} &= \left(1-\frac{1}{\gamma}\right)e^{-q^2D_T|t|} \\ &+ \frac{1}{\gamma}\,e^{-q^2\Gamma|t|\cos\omega_B(q)|t|} \\ &+ \frac{1}{\gamma}\,b(q)\,e^{-q^2\Gamma|t|\sin\omega_B(q)|t|}\end{aligned} \tag{2.34}$$

where $b(q) = q(3\Gamma - D_V)/\gamma c_s$ and the quantity Γ has been identified as the classical

attenuation coefficient for sound waves in a liquid

$$\Gamma \equiv \tfrac{1}{2}\left[(\gamma-1)D_T + D_V\right] = \tfrac{1}{2}\left[\frac{(\gamma-1)\kappa}{m\rho_0 c_P} + \frac{\left(\eta_v + \frac{4}{3}\eta_s\right)}{m\rho_0}\right] \tag{2.35}$$

The Fourier transform of Eq. 2.34 results in the object of our derivation – the spectrum of density fluctuations with wavevector $\boldsymbol{q}$ in the fluid:

$$\begin{aligned} S_{\rho\rho}(\boldsymbol{q},\omega) &= \frac{1}{\pi} V\rho^2 k_B T \chi_T \left\{ \left(1-\frac{1}{\gamma}\right)\left[\frac{D_T q^2}{\omega^2 + (D_T q^2)^2}\right] \right. \\ &+ \frac{1}{\gamma}\left(\frac{\Gamma q^2}{[\omega-\omega_B(q)]^2 + [\Gamma q^2]^2} + \frac{\Gamma q^2}{[\omega+\omega_B(q)]^2 + [\Gamma q^2]^2}\right) \\ &+ \left. \frac{1}{\gamma} b(q)\left(\frac{[\omega+\omega_B(q)]}{[\omega+\omega_B(q)]^2 + [\Gamma q^2]^2} - \frac{[\omega-\omega_B(q)]}{[\omega-\omega_B(q)]^2 + [\Gamma q^2]^2}\right)\right\} \end{aligned} \tag{2.36}$$

which to a very good approximation describes the Rayleigh-Brillouin spectrum of light scattered from a pure monatomic liquid.

2.2.2 Discussion

Now that we have arrived at an expression for the dynamic structure factor $S(\boldsymbol{q},\omega)$, we can compare its predictions with the features of the Brillouin spectrum which were deduced from the existence of thermally generated sound waves in Sec. 2.1.

As indicated above, the prefactor is the $\boldsymbol{q} \to 0$ limit of the static structure factor, $S(\boldsymbol{q}) = V\rho^2 k_B T \chi_T$. The first term in the curly brackets is a Lorentzian centred on the excitation frequency ω (i.e. unshifted) with HWHH

$$\Delta\omega_R(q) = D_T q^2 = \frac{\kappa}{m\rho_0 c_P} q^2 \tag{2.37}$$

where $m\rho_0$ would be replaced by just ρ if we chose to use the mass density rather than the number density. This unshifted term is the Rayleigh peak, which we earlier found to be due to entropy fluctuations at constant pressure and are damped by heat diffusion – indeed our hydrodynamic treatment has revealed $\Delta\omega_R$ to be proportional to D_T, the thermal diffusivity.

The second line of Eq. 2.36 consists of two more Lorentzians, positioned at $\omega \pm \omega_B(q)$. Their half widths at half height are

$$\Delta\omega_B(q) \;=\; \Gamma q^2 \;=\; \tfrac{1}{2}\left[D_V + (\gamma-1)D_T\right] \;=\; \frac{1}{2}\left[\frac{\left(\eta_v + \frac{4}{3}\eta_s\right)}{m\rho_0} + \frac{\kappa\,(\gamma-1)}{m\rho_0 c_P}\right] q^2 \qquad (2.38)$$

Again, $m\rho_0$ should be replaced by ρ in order to express $\Delta\omega_B(q)$ in terms of the mass density. These are the Brillouin peaks, shifted by an amount $\omega_B(q) = v_s q$ to either side of the central Rayleigh peak. They are broadened by thermal conduction and viscosity, and are due to thermal scattering from sound waves in the liquid as discussed in Sec. 2.1.2.

The only spectral feature which we did not predict before deriving the expression for $S_{\rho\rho}(\boldsymbol{q},\omega)$ is the pair of terms on the third line of Eq. 2.36. These are S-shaped curves centred at $\pm\omega_B$ which cause an asymmetry of the Brillouin peaks and shift their position slightly towards the centre. They do not contribute to the total intensity, as their integral over ω is zero. In practice the amplitude of the asymmetric terms is extremely small relative to the Brillouin peaks and is not easily observable in experiments [14]. Their influence will therefore be neglected in this thesis.

Fig. 2.5 shows a plot of the dynamic structure factor $S_{\rho\rho}(\boldsymbol{q},\omega)$ using Eq. 2.36 with parameters chosen to reproduce approximately the Brillouin spectrum of a typical simple liquid at room temperature. The form can be seen to be identical to that of the experimentally measured spectrum of argon shown earlier in Fig. 2.4.

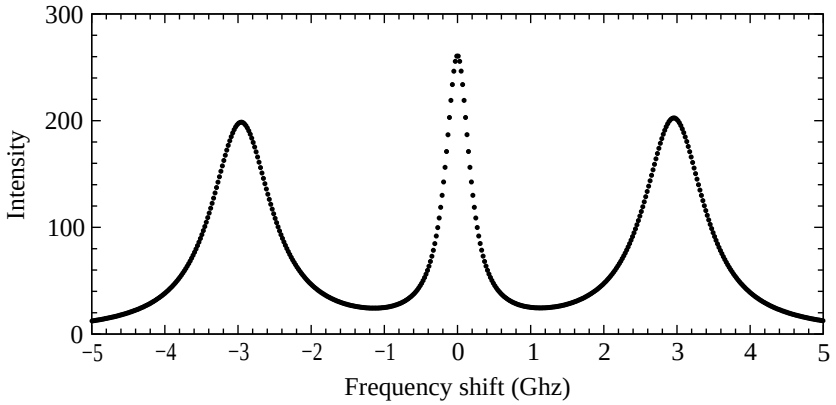

Figure 2.5: Theoretical Rayleigh–Brillouin spectrum of a pure monatomic fluid.

This theoretical spectrum can of course be fitted to experimental data using a numerical

fitting algorithm such as non-linear least squares, and this has proved very fruitful as a method of extracting high-frequency thermodynamic and transport properties of simple liquids (see e.g. Ref. [17]). The measured spectrum is broadened by the instrumental response function (IRF) of whatever type of spectrometer is used, and this must be taken into account by deconvolution of the IRF from the measured spectrum prior to fitting, or alternatively convolution of a test spectrum with the IRF which is then fitted to the raw experimental data. This will be discussed further in Sec. 3.1.2.3 below.

In principle, there are many dynamical properties of the liquid which can be extracted from such fits to measured spectra. Referring back to the expression for $S_{\rho\rho}(\boldsymbol{q},\omega)$, these are:

- *Thermodynamic properties*: ratio of specific heats γ, adiabatic sound speed v_S, acoustic attenuation coefficient Γ, isothermal compressibility χ_T
- *Transport properties*: thermal diffusivity D_T, and from this the thermal conductivity κ if one of c_V or c_P is known from another experiment, the longitudinal kinematic viscosity D_V and hence the bulk viscosity η_v if the shear viscosity η_s can be separately determined.

In fact Brillouin spectroscopy and ultrasonic attenuation are the only techniques able to measure the bulk viscosity. Measurement of the thermal diffusivity directly from the width of the Rayleigh peak is not possible in a typical Brillouin scattering experiment, because the Rayleigh width is too small to be resolved. Instruments with a much higher resolution than the Fabry-Perot interferometers used in Brillouin spectroscopy are required – a summary of suitable techniques can be found in Refs. [10] and [18]. D_T can however be obtained from the width of the Brillouin peaks using Eq. 2.38.

2.2.3 Adding relaxation: the Mountain mode

It has so far been assumed that the liquid we are dealing with is a monatomic fluid of non-interacting hard spheres. These assumptions allow Brillouin spectra of many simple liquids to be analysed with great success using Eq. 2.36, but an important extension of the treatment presented above can be made to include those *molecular* liquids in which

relaxation processes are present on the timescales measured by a Brillouin experiment. In such liquids, the density fluctuations which are probed by light scattering will be coupled to relaxing internal degrees of freedom.

The two most important types of relaxation observable in Brillouin scattering are *thermal* and *structural*. Thermal relaxation occurs when energy is transferred between the translational motion of a molecule and its internal degrees of freedom. Structural relaxation occurs in systems (e.g. highly viscous fluids, glass formers and supercooled liquids) which require a finite time to adapt structurally to local changes in density and temperature.

As will be seen below, the presence of a relaxation process results in a new contribution to the light scattering spectrum in the GHz region; a broad, unshifted fourth peak which appears as an increased background between the Rayleigh and Brillouin peaks. The existence of this was first predicted by Raymond Mountain in 1966 [19], and it has since come to be known as the 'Mountain mode'. Fitting Mountain's analytic expression for the spectrum to experimental data allows the relaxation time of the underlying process to be extracted when the additional central mode is sufficiently intense. The first experimental confirmation of the existence of the Mountain peak was soon found in a study of carbon tetrachloride, where the relaxation time is approximately 0.6 ps at ambient temperature and pressure [20].

Let us consider the case of thermal relaxation, for which the standard method of incorporating energy transfer between translational and intramolecular degrees of freedom is to generalise the bulk viscosity, η_v, to be frequency dependent, whereas before we had considered it to be constant. This results in Eq. 2.39, assuming weak translational–intramolecular coupling and a single[§] relaxation time τ_r [13].

$$\eta_v(\omega) = \eta_v + (v_\infty^2 - v_0^2)(1 + i\omega\tau_r)^{-1}\,\tau_r \tag{2.39}$$

Here η_v is the frequency-independent part of the bulk viscosity, which is due only to the translational motion of molecules and is what we considered in Sec. 2.2.1.2. The zero frequency v_0 and infinite frequency v_∞ velocities of sound appear because the presence of the internal degrees of freedom will cause dispersion, due to their inability to follow the pressure fluctuations at high frequencies (see Sec. 2.1.3). When ω is of the order of

[§]For an extension to the important case of multiple relaxation times, see Ref. [21].

τ_r^{-1}, $\eta_v(\omega)$ is highly dependent on frequency. Many molecular liquids possess thermal relaxation times $\tau_r \sim 10^{-10}\,\mathrm{s}$, which corresponds to the gigahertz frequencies probed by light scattering techniques, hence we expect information on these processes to be in principle obtainable from Brillouin spectra.

This generalised bulk viscosity is then used to derive the dynamic structure factor $S_{\rho\rho}(\boldsymbol{q},\omega)$ which describes the Rayleigh-Brillouin spectrum in the presence of thermal relaxation, following a very similar procedure to that described above for non-relaxing fluids. The full expression is very complex, and will not be reproduced here. Gornall et al. [20] compared this complete theoretical spectrum with the measured spectrum of carbon tetrachloride and found excellent agreement; a broad central background term and asymmetric Brillouin peaks being reproduced using a relaxation time of 0.64 ps, measured from the velocity dispersion curve (Eq. 2.7). $S_{\rho\rho}(\boldsymbol{q},\omega)$ can also be simplified using a perturbation expansion (as was done in the derivation for the non-relaxing case) to obtain a simplified, but still rather long formula for the spectrum, consisting of *four* Lorentzian components [14]. These are the Brillouin doublet and unshifted Rayleigh peak we have already seen in monatomic fluids, plus a new term, the relaxation (or Mountain) mode which is entirely due to intramolecular relaxation. This is unshifted, and has a width proportional to τ_r^{-1}. This width is typically quite large when $\omega\tau_r \approx 1$, resulting in the increased background visible between the central and Brillouin peaks (see Fig. 2.6). The presence of the Mountain mode produces an asymmetry in the Brillouin peaks which is not observed in non-relaxing fluids, so that the frequency of maximum intensity ω_{max} is not at the centre of the lineshape. In fact ω_{max} will be slightly less than the frequency of the thermal phonon $\omega_B = v_s q$ [17]. Hence one must be careful when attempting to extract precise values for the sound velocity and attenuation when intramolecular relaxation is present. Simply reading peak positions and widths from the spectrum will not be sufficient if precise values are required. As discussed in Sec. 2.1.3 above, the observed hypersonic sound velocity v_s will increase from v_0 to v_∞ as $1/\omega$ increases through the relaxation time τ_r according to Eq. 2.7.

The argument given above for the case of thermal relaxation can easily be adapted to deal with shear relaxation (by generalising the shear viscosity η_s) or structural relaxation (by introducing a frequency dependent longitudinal viscosity D_V). Shear relaxation will not be discussed in this thesis; the interested reader is referred to the

summary given in Ref. [14] for further details.

Structural relaxation occurs in highly viscous structured liquids, and is caused by the finite time these local structures take to respond to the rapid changes in density and temperature imposed by a high frequency sound wave. The phenomenon is closely related to the shear and bulk viscosities, and as such is strongly dependent on temperature. As the liquid is cooled, the viscosity increases and the structural relaxation time τ_s becomes longer. Structural relaxation is extremely important in supercooled liquids approaching the glass transition (see e.g. Ref. [22]), and this will be discussed further in Chapter 4. The change in τ_s can be very extreme – increasing from $\sim 10^{-11}$ s to $\sim 10^{2}$ s on cooling from the normal liquid (above its melting point) to near the glass transition [23]. The appearance of the spectrum in the presence of structural relaxation is identical to that discussed above with regard to thermal relaxation; a new central mode appears, the width of which is determined by $1/\tau_s$. When τ_s is below a certain value, the Mountain peak will be too broad to be observable in the Brillouin spectrum, and when τ_s is too large, the Mountain peak will be narrow and not resolvable. Hence structural relaxation is only observable using Brillouin spectroscopy when the relaxation time lies within a narrow window, determined by the frequency range selected for the experiment.

To illustrate the effect of a relaxation process on the Brillouin spectrum, Fig. 2.6 shows two spectra collected during the development of the Edinburgh spectrometer. When no relaxation is present, the spectrum is composed of three Lorentzians, which in the figure are well separated with the background between the central peak and the Brillouin peaks of roughly the same intensity as the background on the high-frequency side of the Brillouin peaks. When relaxation is present, the additional intensity due to the broad central Mountain mode causes the background between the peaks to increase. Looking at the relaxation spectrum in the figure, we see that the background level between the Rayleigh and the Brillouin peaks is noticeably higher than that outside the Brillouin peaks; this may be taken as a clear indicator that a relaxation process (thermal, structural or shear) takes place in the liquid being studied. If the velocity of sound is such that the Brillouin peaks overlap with the Rayleigh peak, this increased background of course no longer implies the existence of relaxation. Note also that the additional central mode causes some asymmetry on the low-frequency side of the

Brillouin peaks – another sign that a relaxation process is occurring.

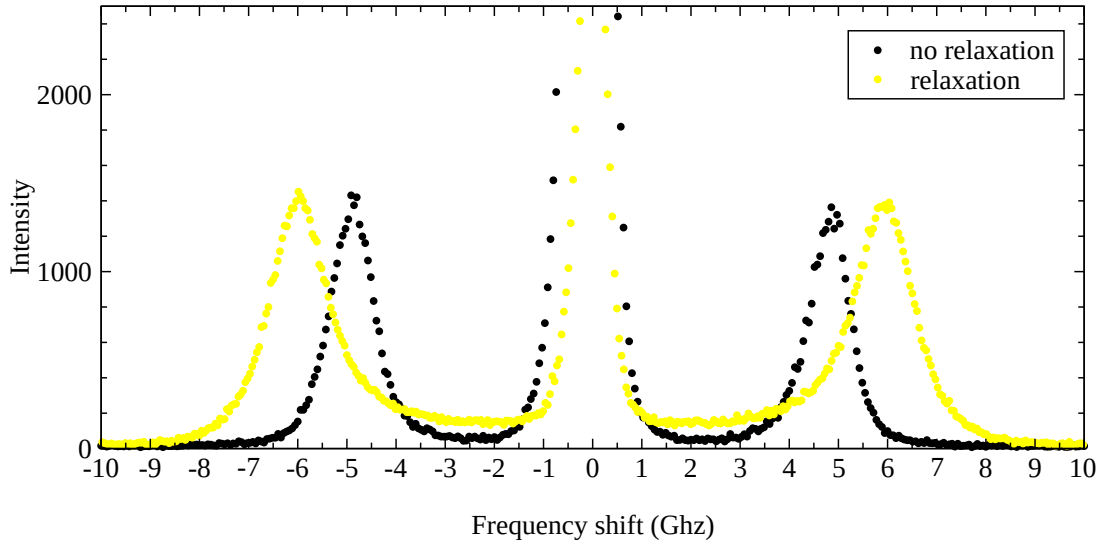

Figure 2.6: Two experimentally measured spectra; one with a very noticeable relaxation mode, the other without. Note the increased background level between Rayleigh and Brillouin peaks and asymmetry of the Brillouin peaks caused by the presence of the broad low-intensity central Mountain mode.

If the Mountain mode is present and of sufficiently high intensity (it is, unfortunately, often extremely weak), the four-Lorentzian expression for the spectrum may be fitted to experimental data in order to extract the relaxation time τ_r. The technique is however unable to provide any information on the physical origin of the relaxation mode(s), for which one must resort to other techniques.

2.3 Summary and discussion

This chapter has attempted to provide some useful background information on the origins and properties of the Rayleigh-Brillouin spectrum of light scattered from a fluid. We began by considering in a qualitative manner the mechanisms of light scattering and thermal fluctuations in liquids, and were able with a minimum of mathematics to deduce the existence and form of the Brillouin spectrum, the most important feature of which is a pair of shifted peaks allowing the velocity and absorption of high-frequency thermally generated sound waves in a liquid to be measured directly.

A summary of a theoretical derivation of the dynamic structure factor $S(\boldsymbol{q},\omega)$ which describes the Brillouin spectrum of a pure monatomic hard-sphere fluid was then presented. Conservation laws were written down for the local densities of the particle number, momentum and energy, which were used to establish a set of hydrodynamic equations. Solving these yielded the density-density correlation function probed in a light scattering experiment, which was then Fourier transformed to obtain an expression for $S(\boldsymbol{q},\omega)$. This confirmed the conclusions of our qualitative discussion, and in addition showed that several thermodynamic and transport properties of the fluid may in principle be extracted from the Brillouin spectrum by numerically fitting $S(\boldsymbol{q},\omega)$ to experimental data. The effect of relaxation processes on the Brillouin spectrum was discussed, highlighting the additional central mode which arises in the presence of thermal, structural or shear relaxation in a molecular liquid.

Brillouin spectroscopy in soft condensed matter research

To date, Brillouin spectroscopy has been applied in the study of several types of soft condensed matter systems. Early experiments followed soon after the invention of the laser in the early 1960's and focused on simple monatomic fluids such as liquid argon (see e.g. Fig. 2.4), quickly moving on to look at more complicated relaxing fluids such as carbon tetrachloride [20, 21]. All of these early experiments are summarised in the review article by Fleury [17]. The specific case of structural relaxation resulting from the approach to the glass transition was studied using Brillouin spectroscopy in the early 1990's following the development of the mode-coupling theory (see e.g. Ref. [22], discussed in Chapter 4). It was found that the technique could be used to accurately measure both the glass transition temperature [22, 24] and under certain conditions the non-ergodicity (Debye-Waller) parameter $f_q(T)$ and MCT crossover temperature T_c [24, 25, 26, 27].

The sensitivity of the Brillouin spectrum to hydrodynamic fluctuations means that it is suitable for the study of critical phenomena in fluids, the theory and applications of which are discussed in Stanley's authoritative text [10] and Refs. [13, 28].

The development of a model for sound propagation in polymer gels by Marqusee and Deutch [29] prompted several Brillouin scattering experiments on a range of gels [30, 31]

which confirmed the predictions of the theory, but these results appear not to have been investigated further. This is surprising, as the materials are of great interest and the success of the model suggests that a great deal of information on the structure of gels and properties of the interstitial liquid should be obtainable from Brillouin spectroscopy.

In fact several other studies of various complex fluids have shown Brillouin scattering to be a novel, non-invasive method of investigating structure and dynamics. Hard-sphere colloidal suspensions (see Chapter 5), emulsions [32], soft colloids [33], liquid crystals [34,35] and other systems have all been shown to exhibit interesting behaviour using Brillouin spectroscopy, but despite this the technique remains under-exploited.

This contributed to the motivation for adding a Brillouin spectrometer to the facilities available for the study of soft condensed matter at Edinburgh. The development and operation of the instrument will be discussed in the next chapter, before the results of its application to two very different areas of current interest are presented in the subsequent Chapters 4 and 5.

Chapter 3

Developing a Brillouin spectrometer: principles, design and operation

The initial aim of this research project was to design, assemble and test a Brillouin spectrometer suitable for the study of soft condensed matter at variable temperature, pressure and scattering vector. Once this had been achieved, the apparatus was successfully used to investigate hypersound propagation in aqueous alcohol solutions at low temperatures (Chapter 4) and colloidal dispersions (Chapter 5). This chapter will first consider from a theoretical perspective the principles of operation of the device which lies at the heart of a Brillouin spectrometer – a multi-pass Fabry-Perot interferometer. The rest of the chapter will discuss the design and operation of all aspects of the spectrometer; illumination of the sample, control of its temperature and pressure, electronic scanning and stabilisation of the interferometer, detection, and data analysis. It should be emphasised that this was *all* original work – the spectrometer and analytical techniques were developed from scratch without any external help. Excluding Sec. 3.1, this chapter should therefore be considered to be part of my original contribution, as opposed to background material.

Much of the practical work presented in this chapter was undertaken in collaboration with Mr. Hugh Vass, who provided invaluable technical support and advice throughout

the development of the spectrometer. He was responsible for the initial set-up of the interferometer and photon-counting detection system, and devised most of the optical alignment techniques which then evolved towards the procedures described here as we both became more familiar with the rather complicated and difficult to use apparatus. Hugh also designed and manufactured all in-house mechanical and electronic components which were required during the project.

3.1 The Fabry-Perot interferometer

Although the Fabry-Perot interferometer is mentioned in almost every undergraduate textbook on optics (see e.g. Ref. [36] for one of the best such treatments), it is seldom described in the correct context or level of detail to highlight the features which make it the cornerstone of most Brillouin spectrometers. Addressing this problem are two extremely detailed and lengthy monographs by Hernandez [37] and Vaughan [38] which discuss every imaginable aspect of the Fabry-Perot interferometer, its history and applications.

The aim of this section is to equip the reader with a sufficient grounding in the principles of operation of a Fabry-Perot in order to allow the following discussion of experimental techniques (the development and application of which were a major part of my research) to be understood. Most of the information given here is drawn from Hernandez [37], Vaughan [38] and the authoritative *Principles of Optics* by Born and Wolf [39], selected and presented in a way which emphasises the features most relevant for the application of the interferometer to Brillouin spectroscopy.

3.1.1 Principles of operation of a Fabry-Perot interferometer

A Fabry-Perot interferometer consists of two highly reflective mirrors fixed parallel relative to one another, a distance d apart. This forms a resonant cavity, only transmitting light of wavelengths which satisfy the condition for constructive interference. Fig. 3.1 is a schematic diagram of multiple reflections within such a plane-parallel cavity.

In Fig. 3.1 an incoming plane wave of monochromatic light with wavelength λ_0 and

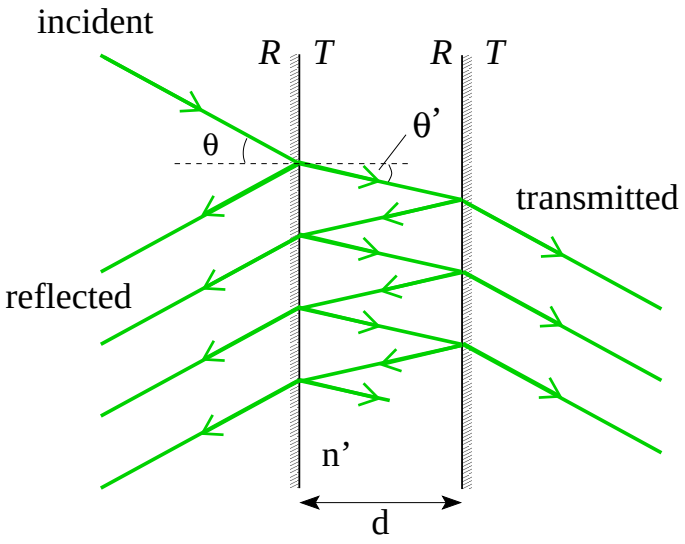

Figure 3.1: Multiple interference between two mirrors.

intensity I_i is incident on the first mirror. It is partially reflected and partially transmitted depending on the reflectivity $\mathcal{R}$ and transmissivity $\mathcal{T}$ of the mirror. If the two mirrors are identical they will have the same values of $\mathcal{R}$ and $\mathcal{T}$, and assuming no absorption takes place* $\mathcal{R}+\mathcal{T}=1$ by conservation of energy. The transmitted part then crosses the gap d between the mirrors and is again partly reflected and transmitted at the second mirror. This time the transmitted beam leaves the cavity, while the reflected light crosses back to the first mirror, and the process occurs again. Repeated reflection back and forth between the mirrors thus results in a series of waves transmitted by the cavity. There will be a phase difference δ between successive transmitted waves proportional to the optical path length of a double pass between the plates. Simple geometry shows this to be

$$\delta = \frac{4\pi}{\lambda_0}\, n' d\, cos\, \theta \tag{3.1}$$

where n' is the refractive index of the material in the cavity. Illuminating the cavity with plane waves over a range of angles will thus result in a varying phase difference, and fringes of constructive interference will occur for $\delta = 2m\pi$ where m is an integer, called the *order* of the fringe. Substituting $\delta = 2m\pi$ in Eq. 3.1 gives the condition for a maximum in the transmitted intensity;

$$m\lambda_0 = 2n'd\cos\theta \tag{3.2}$$

The bright fringes corresponding to satisfaction of this criterion can be seen in the interference pattern shown in Fig. 3.2. We will now consider briefly the functional

*Usually a reasonable assumption for dielectric films, but not true for metallic mirrors – see Ref. [39].

form of the light intensity profile transmitted by a Fabry-Perot interferometer, before introducing the physical parameters which describe the operation of the instrument.

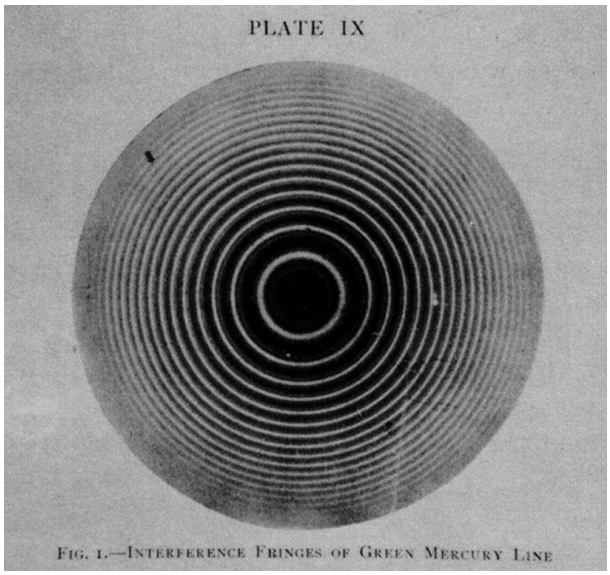

Figure 3.2: Photograph of the circular interference fringes transmitted by a Fabry-Perot interferometer. This is the earliest known picture of the pattern, published in 1901 by Charles Fabry and Alfred Perot (reproduced from Ref. [38]).

3.1.1.1 Transmitted intensity profile: the Airy function

By evaluating the amplitude and phase of each transmitted wave and forming a superposition, the total transmitted intensity may be calculated. Assuming that the plates are large, then as the number of reflected waves in the cavity tends to infinity the intensity of light transmitted by the cavity as a function of the phase difference δ is given by the Airy function [39]

$$I_t = I_i \frac{\mathcal{T}^2}{(1-\mathcal{R})^2 + 4\mathcal{R}\sin^2\frac{\delta}{2}} \tag{3.3}$$

or, since $\mathcal{R} + \mathcal{T} = 1$

$$\frac{I_t}{I_i} = \frac{1}{1 + F\sin^2\frac{\delta}{2}} \tag{3.4}$$

where

$$F = \frac{4\mathcal{R}}{(1-\mathcal{R})^2} \tag{3.5}$$

This function (Eq. 3.4) is plotted as a function of δ in Fig. 3.3 for a range of reflectivities. To measure this experimentally, one would change δ (see Eq. 3.1) by either varying θ (using an uncollimated incident beam or tilting the interferometer) or changing the plate separation d. As expected, maxima occur for $\delta = 2m\pi$, so a series of bright fringes will be observed if the transmitted light is imaged onto a screen. The symmetry of the system about the optic axis results in circular symmetry of the interference pattern, so if the screen is normal to the transmitted wave, the fringes will appear as bright concentric circles on a dark background. Fig. 3.2 is a reproduction of an early photograph of this pattern.

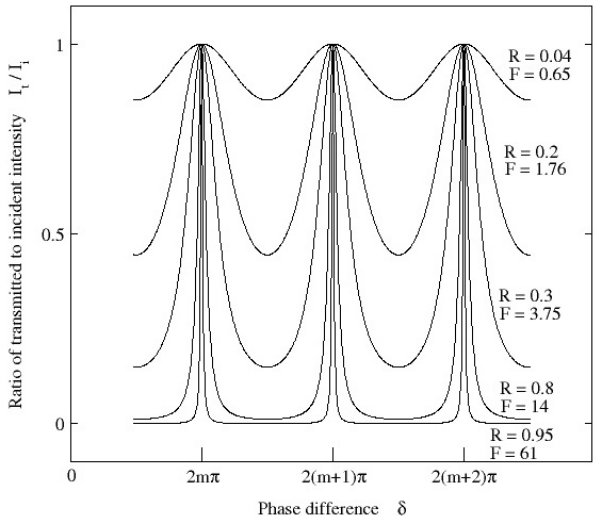

Figure 3.3: Intensity of light transmitted by a Fabry-Perot interferometer as a function of phase difference – the Airy function (Eq. 3.4). Note sharpening of the peaks with increasing reflectivity $\mathcal{R}$ and hence finesse $\mathcal{F}$ (denoted by a non-calligraphic F *in the Figure).*

3.1.1.2 Sharpness of interference fringes: the finesse

The Airy function (Eq. 3.4) plotted in Fig. 3.3 is the intensity profile of a slice through the circular fringe interference pattern (Fig. 3.2). The widths of the peaks in transmitted intensity can clearly be seen to depend on the reflectivity $\mathcal{R}$ in a very sensitive way: they are very broad for low reflectivities, and become sharper with increasing $\mathcal{R}$. For the purposes of frequency-measuring interferometry sharper peaks are of course preferable, allowing smaller frequency differences to be resolved. The *finesse* $\mathcal{F}$ of the

Fabry-Perot interferometer is defined to be the ratio of the separation between fringes of adjacent orders and the half width (full width at half height) of the fringes. The finesse is one of the main parameters used to characterise the performance of a Fabry-Perot , and we will see now that it depends *only* on the reflectivity of the mirrors.

Denoting the FWHH by ϵ, the phase differences where the intensity is half its maximum will be

$$\delta = 2m\pi \pm \frac{\epsilon}{2} \tag{3.6}$$

where m is the order of the transmitted fringe. By definition, at half height $I_t/I_i = \frac{1}{2}$ and substituting for this and δ in Eq. 3.4 gives

$$\frac{1}{2} = \frac{1}{1 + F\sin^2\frac{\epsilon}{4}} \tag{3.7}$$

When the reflectivity and hence F is high enough, ϵ is small so that we can approximate $\sin\epsilon/4 \approx \epsilon/4$, and Eq. 3.7 simplifies to give the half width $\epsilon = 4/\sqrt{F}$. As stated above, the finesse $\mathcal{F}$ is the separation of adjacent fringes (equal to a change in δ of 2π) divided by the FWHH; i.e. $\mathcal{F} = 2\pi/\epsilon$. Substituting for ϵ gives us an expression for the finesse in terms of the reflectivity (recall F depends only on $\mathcal{R}$ according to Eq. 3.5):

$$\boxed{\mathcal{F} = \frac{\pi\sqrt{F}}{2} = \frac{\pi\sqrt{\mathcal{R}}}{1-\mathcal{R}}} \tag{3.8}$$

Note that this is the *ideal reflectivity finesse* determined only by $\mathcal{R}$ and assuming perfectly flat and parallel mirrors; we will see later that practical considerations limit the experimentally achievable finesse to be less than the ideal value. Fig. 3.3 shows the intensity transmitted by a Fabry-Perot cavity as a function of phase difference for various values of $\mathcal{R}$ and hence $\mathcal{F}$. The sharpness of the maxima and the contrast between peak intensity and background level can clearly be seen to increase rapidly with the finesse.

3.1.1.3 Contrast ratio

The finesse is the sole determinant of another important parameter – the *contrast ratio* or *extinction coefficient* $\mathcal{C}$, which is defined to be the ratio of maximum to minimum in the transmitted intensity. In the notation employed above, this is written $(I_t/I_i)_{max}$ / $(I_t/I_i)min$. Assuming no losses due to absorption at the mirrors,

$(I_t/I_i)_{max} = 1$ and, from Eq. 3.4, $(I_t/I_i)_{min} = 1/(1+F)$ hence

$$\boxed{\mathcal{C} \;=\; 1+F \;=\; 1+\frac{4\mathcal{F}^2}{\pi^2} \;\simeq\; \left(\frac{2\mathcal{F}}{\pi}\right)^2} \tag{3.9}$$

The contrast determines the minimum intensity which can be observed using the interferometer. A relatively high finesse of 50 (corresponding to $\mathcal{R} = 0.94$) gives a contrast of approximately 1000, which does not meet the requirements of many applications (such as Brillouin spectroscopy) where weak signals are of interest. Several techniques have therefore been developed to increase the contrast ratio, one of which is to use two or more interferometers in series, or equivalently to divide the mirrors of one interferometer into discrete regions through which the light is routed in turn. This is called *multi-passing* and was found to be necessary for the purposes of this thesis. It is discussed in some detail in Sec. 3.1.3 below.

3.1.2 More than one incident wavelength: the free spectral range

Looking again at Fig. 3.3, we see that the separation between adjacent maxima in transmission corresponds to a phase difference δ of 2π. When the incident light is not monochromatic, this separation limits the wavelength or frequency differences which can be measured unambiguously using the interferometer, is called the *free spectral range* (FSR), and is another very important parameter which characterises the operation of a Fabry-Perot interferometer. If two different wavelengths of light are present in the source, each will generate its own circular fringe system as described above, and the observed pattern will be a superposition of the two. The free spectral range determines how far apart the two wavelengths can be before the fringes of one start to overlap with those belonging to the other, making interpretation difficult.

When the instrument is used to measure the spectrum of wavelengths or frequencies present in the incident light, the smallest resolvable wavelength difference (or minimum *bandwidth*) $(\Delta\lambda)_{BW}$ acts as a lower bound on the frequency difference which can be detected. This is often expressed using the *chromatic resolving power* $R \equiv \lambda/(\Delta\lambda)_{BW}$ where λ is the mean wavelength of the incident light. Alternatively, the resolving power may be expressed in terms of frequencies: $R \equiv \nu/(\Delta\nu)_{BW}$ where ν is the mean frequency of light and $(\Delta\nu)_{BW}$ is the minimum resolvable frequency bandwidth. There

are a choice of resolution limits, the most commonly used of which is the Rayleigh criterion which states that two peaks are resolved if the intensity of the dip between them is less than 0.81 times the peak intensity. Applying this criterion for resolution, the resolving power of a Fabry-Perot interferometer is given by [39]

$$R = \frac{\lambda}{\Delta\lambda_{BW}} = \frac{2\mathcal{F}n'd}{\lambda} \tag{3.10}$$

The resolving power is therefore proportional to the finesse and the optical path length between the mirrors.

The free spectral range limits the wavelength difference which can be measured because a difference greater than the FSR between the transmitted waves of two incident wavelengths λ_1 and λ_2 means that the peak corresponding to the mth order of λ_1 will overlap into the $(m+1)$th order of λ_2. There is no way to tell which order a peak belongs to just by looking at the transmitted intensity pattern, so the situation becomes confusing. To avoid this, the FSR must be chosen large enough such that adjacent orders are well separated. We will now show that the free spectral range of a Fabry-Perot interferometer depends *only* on d, the separation of the mirrors.

The difference in phase $\Delta\delta$ between transmitted waves of different wavelength can be written (c.f. Eq. 3.1)

$$|\Delta\delta| = \frac{4\pi}{\lambda^2}\, n'd\cos\theta\, \Delta\lambda \tag{3.11}$$

In a typical frequency-measuring Fabry-Perot experiment, δ is altered by changing the mirror separation d at constant θ. The material in the gap between the mirrors is air, so the refractive index n' is taken to be precisely 1. The $\cos\theta$ term can also be set equal to 1 by ensuring that the incident beam is normal to the mirror surface. A simplified equation for the phase difference between transmitted waves with wavelengths separated by $\Delta\lambda$ and mean wavelength λ is then

$$|\Delta\delta| = \frac{4\pi d}{\lambda^2}\, \Delta\lambda \tag{3.12}$$

When the spread in incident wavelengths $\Delta\lambda$ is equal to the free spectral range, the transmitted peak corresponding to the mth order of the λ_1 pattern will occur in precisely the same place as the $(m+1)$th order corresponding to λ_2 (for $\lambda_1 > \lambda_2$). So to calculate this limiting value of $\Delta\lambda$, we need to set $|\Delta\delta| = 2\pi$ – the phase separation of

two adjacent peaks in the transmitted intensity – into Eq. 3.12:

$$(\Delta\lambda)_{FSR} = \frac{\lambda^2}{2d} \tag{3.13}$$

or expressed as a frequency (using Eq. 3.2)

$$\boxed{(\Delta\nu)_{FSR} = \frac{c}{2d}} \tag{3.14}$$

for $\theta = 0$ and $n' = 1$. A typical value of $d = 1\,\text{cm}$ therefore gives a free spectral range of 15 GHz. This means that frequency differences greater than 15 GHz will cause the two patterns due to λ_1 and λ_2 to be further apart than the distance between the adjacent maxima of either – the orders therefore 'overlap' and it becomes difficult to assign a given peak to a definite frequency component. Frequency differences greater than the free spectral range cannot therefore be measured unambiguously.

Reducing the mirror separation d will increase the FSR allowing larger frequency shifts to be measured, but Eq. 3.10 shows that this is accompanied by a reduction in resolving power. This compromise can be avoided to some extent using a second Fabry-Perot interferometer in series. The resulting apparatus is referred to as a *tandem* interferometer, but is beyond the scope of this thesis. For details see Ref. [38].

Substituting the resolving power $R \equiv \nu/(\Delta\nu)_{BW}$ into Eq. 3.14, we see that the free spectral range and the finesse determine the minimum resolvable bandwidth:

$$(\Delta\nu)_{BW} = \frac{(\Delta\nu)_{FSR}}{\mathcal{F}} \tag{3.15}$$

Note that this is simply a restatement of the definition of finesse which led to Eq. 3.8 above. As we would expect, a higher finesse allows smaller frequency shifts to be measured. As with improving the contrast ratio, increasing the free spectral range has a detrimental effect on the performance of the interferometer – the minimum resolvable bandwidth also increases.

The finesse and free spectral range together provide all of the information necessary to characterise the performance of a Fabry-Perot interferometer. The finesse depends only on the reflectivity and quality of the mirrors, and the free spectral range is determined solely by the mirror separation. For typical values $\mathcal{F} = 50$ ($\mathcal{R} = 0.94$) and $(\Delta\nu)_{FSR} = 20\,\text{GHz}$ ($d = 7.5\,\text{mm}$) in an air-filled interferometer, the resolving power for $\lambda = 514.5\,\text{nm}$ is 1.5×10^6, allowing frequency shifts as small as 400 MHz to be resolved.

The instrument is therefore capable of measuring frequency differences only in the window between 400 MHz and 20 GHz. The contrast ratio calculated using Eq. 3.9 is 1000, which as mentioned above is not sufficient for our purposes but can be improved by multi-passing as will be shown in Sec. 3.1.3 below.

Note that when using a Fabry-Perot in Brillouin spectroscopy, Brillouin peak shifts ν_B may only be measured for $\nu_B < (\Delta\nu)_{FSR}$ / 2, due to the fact that each unshifted Rayleigh peak is flanked by both up-shifted and down-shifted Brillouin peaks.

3.1.2.1 Using a Fabry-Perot to scan a range of frequencies

If the Fabry-Perot interferometer is to be used as the frequency analyser in a spectroscopic experiment, we need to be able to change the frequencies which are transmitted by the cavity in order to scan across the spectrum which is to be measured. Referring back to Eq. 3.2 we see that the transmitted wavelengths can be altered by changing either the angle of incidence θ or the optical thickness $n'd$ of the gap between the mirrors.

Scanning the spectrum by changing θ (tilting the body of the interferometer or the collecting optics) is not suitable for our purposes because it is accompanied by a large drop in the detected intensity [40]. We want the intensity to be as high as possible when attempting to measure the inherently weak Brillouin doublet.

Changing the optical distance between the mirrors is the alternative approach; it does not affect the intensity collected at the detector. One way of changing $n'd$ is called *pressure scanning*. The refractive index of a gas increases with pressure, so by enclosing the interferometer cavity within a sealed chamber and regulating the pressure of the gas between the mirrors (which are held stationary), $n'd$ and hence the frequencies transmitted by the system can be controlled. For an ideal gas, a linear increase in pressure results in a linear frequency scan. This technique is discussed in some detail in Ref. [38]. The pressure scanning approach was not adopted here because of the availability of a mechanically scanned interferometer.

The most common method of scanning $n'd$ exploits the piezoelectric effect in order to alter the mirror separation electronically. Piezoelectric materials change their length

when an electric field is applied across two opposite faces. If one of the mirrors is somehow mounted on stacks of such a material, changing the voltage of the applied electric field will change d. The interferometer employed in this research has a mirror mounted on three piezolectric stacks equidistant around the circumference of the mirror holder. In addition to applying the same voltage increase to all three stacks in order to change d without altering the orientation of the mirror, such an arrangement allows the implementation of dynamic servo stabilisation of the Fabry-Perot cavity. This enables parallelism of the mirrors to be maintained indefinitely; actively monitoring and optimising the profile of transmitted intensity by applying suitable voltages independently to two of the piezoelectric stacks. This is far superior to purely mechanical methods of stabilisation, enabling spectra to be collected over much longer times. This is important when the signal to noise ratio is low as is often the case in Brillouin spectroscopy. Servo stabilisation will be discussed further in Sec. 3.2.2.3 below.

As shown in Sec. 3.1.1.1 above, maxima in the transmitted intensity will occur when $\delta = 2m\pi$, and from Eq. 3.2 we see that changing d by half of one wavelength is sufficient to move from one order to the next. Scanning d over several times $\lambda/2$ while holding the other variables constant will therefore produce a pattern like Fig. 3.3. In fact in order to observe the three peaks shown in the figure, d would have to be varied by a little more than λ to produce the three maxima shown. When more than one wavelength of light is present as is the case in the spectrum of light scattered from a liquid, changing d in this way allows the intensity of each spectral component to be recorded as a plot of intensity vs. frequency – the light scattering spectrum of the material being studied. Note that, as discussed at the start of this section, only frequency shifts smaller than the free spectral range can be measured satisfactorily using a single Fabry-Perot interferometer.

It should also be noted that this change in d required to scan across a few orders of the interference pattern is negligibly small compared to d itself, which is usually at least a few millimetres. Hence the free spectral range – which depends only on the plate separation – can be assumed to be constant and unaffected by the scanning motion and $(\Delta\nu)_{FSR} = c\,/\,2d$ still holds (Eq. 3.14).

3.1.2.2 Imperfect mirrors: the effective finesse

As was stated in Sec. 3.1.1.2, the finesse $\mathcal{F}$ considered so far is an ideal value which depends only on the mirror reflectivity. It implicitly assumes that the mirrors are perfectly flat and precisely parallel to one another. Real Fabry-Perot interferometers can of course not be manufactured with such complete accuracy. These imperfections act to reduce the actual (or *working*) finesse to some value less than the ideal $\mathcal{F} = \pi\sqrt{\mathcal{R}}/(1-\mathcal{R})$.

Usually the most important reduction in finesse is due to the mirrors not being perfectly parallel. Even with very careful application of the most advanced techniques, it is not possible to produce a mirror surface completely free of defects. A typical high quality mirror is flat to within $\lambda/200$, but even this reduces the finesse and hence resolving power of the instrument; this irregularity means that the mirror separation d varies as a function of position on the mirror surface. Any departure from relative parallelism of the plates across their separation will have the same effect. The r.m.s. value of this variation in d can be used to calculate the reduction in working finesse caused by mirror defects and misalignment [36].

A further reduction in working finesse is due to the finite size of the pinhole used to image the interference pattern onto the detector. The reduction in resolution caused by this effect is due to diffraction, and the corresponding reduction in effective finesse is again calculated in Ref. [36] and is discussed further in Ref. [40].

The typical magnitude of the reduction in finesse from the ideal reflectivity value $\mathcal{F}$ due to the factors discussed above is 15%, so that the effective finesse $\mathcal{F}_E$ observed in an experiment is approximately $0.85\mathcal{F}$ [38]. In the forthcoming discussions of experimental work it will be assumed that the finesse is the effective working finesse of the interferometer, as calculated from measured minimum bandwidths and free spectral ranges. For simplicity, the subscript E will be dropped, using just $\mathcal{F}$ to denote the effective finesse observed in experiments.

3.1.2.3 The instrumental response function

The finite width of the peaks transmitted by a Fabry-Perot interferometer means that any spectral features will be broadened by an amount inversely proportional to the finesse. An infinitely sharp feature will therefore acquire a width equal to the FWHH of the fringes discussed above. In mathematical terms, the true spectrum $S(\boldsymbol{q},\omega)$ of a source is *convolved* with the function which describes the response of the interferometer to a delta function source. This characteristic of the instrument is called the *instrumental response function* (IRF) and is essentially the same as the Airy function discussed above. The IRF of any interferometer may be measured by recording the spectrum of light scattered from a static source – a dilute aqueous suspension of nanometre-sized latex spheres is often used. Once this is known, the true spectrum $S(\boldsymbol{q},\omega)$ may be recovered by *deconvolution* of the IRF from the dataset. This is not a straightforward operation, and is discussed in depth by Ref. [38].

The IRF is a symmetrical function (a Lorentzian), so does not change the position of peaks in $S(\boldsymbol{q},\omega)$ which may therefore be measured without performing a deconvolution. Determination of the real widths of these peaks does however require a correction to be made for instrumental broadening, either by deconvolution of the IRF or by simply subtracting the instrumental width, which can give a fairly good approximation to the true spectral width.

No attempt has been made to correct for instrumental broadening in the results presented later in this thesis, because the nature of the research did not make it necessary to measure true spectral widths. Where widths *are* measured, this is done in order to identify qualitative trends with changing temperature or pressure, which are unaffected by instrumental broadening.

The IRF will not be discussed further in this thesis, but it should be remembered that all of the spectral lineshapes presented in later chapters are broadened to some extent due to the finite finesse of the Fabry-Perot interferometer.

3.1.3 Increasing the contrast: multi-pass interferometers

As calculated in Sec. 3.1.1.3 above, the maximum contrast ratio between peak intensity and background signal obtainable with a single Fabry-Perot interferometer is about 10^3, which is many orders of magnitude short of being sufficient for Brillouin spectroscopic studies of soft condensed matter. The contrast can be increased dramatically by using more than one Fabry-Perot cavity in series. This can be achieved without requiring multiple interferometers by using just one pair of mirrors together with external optics and masking screens to divide the plates into separate regions, through which light travels in sequence. This technique is called *multi-passing* and its implementation was a vital stage in the development of the Edinburgh spectrometer. Fig. 3.4 is a schematic diagram of a commonly employed five pass configuration; masked retroreflectors (sometimes called *corner cubes*) route light through five separate sections of the mirrors so that the transmitted beam has effectively passed through five interferometers in series.

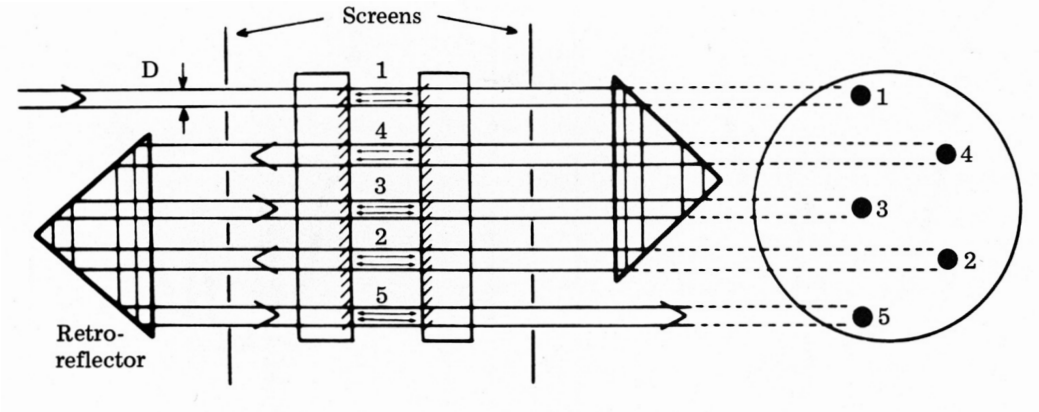

Figure 3.4: Schematic diagram of a five pass Fabry-Perot interferometer designed by Sandercock and reproduced from his paper [41].

The effect of N multiple passes between a single pair of mirrors on the Fabry-Perot parameters discussed above is to raise the single-pass values to the Nth power[†]. The ideal single-pass contrast $\mathcal{C}$ defined by Eq. 3.9 will be reduced to an observed value $\mathcal{C}_1$ by mirror imperfections; the contrast observed after N passes is then given by

$$\mathcal{C}_N = (\mathcal{C}_1)^N \simeq \left(\frac{2\mathcal{F}_1}{\pi}\right)^{2N} \tag{3.16}$$

[†]See Ref. [38], which treats multi-pass interferometers in some detail. Only the most important results will be stated here.

where $\mathcal{F}_1$ is the effective finesse observed for a single pass. Recall that this will be approximately 85% of the ideal reflectivity finesse $\mathcal{F}$, mainly due to mirror defects. The finesse observed for an N-pass interferometer is [38]

$$\mathcal{F}_N = \frac{\mathcal{F}_1}{\sqrt{2^{1/N} - 1}} \tag{3.17}$$

derived in the same way as led to Eq. 3.8 for the single-pass ideal reflectivity finesse.

A parameter which we did not discuss for single-pass interferometers is the *transmission factor* $\tau_{\mathcal{A}}$. We assumed that losses due to absorption of light by dielectric films (which form the mirrors used in this research) are negligible. However for multiple passes the small fraction $\mathcal{A}$ of light absorbed must be taken into consideration. A typical value of $\mathcal{A}$ is 0.005, meaning that half a percent of incident light is absorbed rather than being transmitted or reflected each time it meets a mirror. The transmitted intensity is therefore reduced, and this reduction becomes more pronounced as the number of passes N is increased. Where τ_1 is the transmission factor for a single pass, the value for N passes is [38]

$$\tau_N = (\tau_1)^N = \left(1 - \frac{\mathcal{A}}{1 - \mathcal{R}}\right)^{2N} \tag{3.18}$$

The free spectral range will of course be unaffected by the number of passes, as it is determined solely by the mirror separation d. We therefore have expressions for all of the parameters which describe the operation of a multi-pass Fabry-Perot interferometer. Table 3.1 shows the effect on these quantities of increasing the number of passes from one to six for mirrors of reflectivity $\mathcal{R} = 0.93$ – the value used in my experiments.

Number of passes N	1	2	3	4	5	6
$\mathcal{F}_N$	37	57	72	85	95	105
$\mathcal{C}_N$	549	3×10^5	2×10^8	9×10^{10}	5×10^{13}	3×10^{16}
τ_N	0.86	0.74	0.64	0.55	0.48	0.41

Table 3.1: Multi-pass Fabry-Perot operational parameters for a cavity with single pass ideal reflectivity finesse $\mathcal{F} = 43$ (corresponding to mirror reflectivity $\mathcal{R} = 0.93$). The working finesse was taken to be 85% of the ideal value, and the transmission factor τ_N was calculated assuming a typical absorption coefficient of 0.005.

It can be seen from Table 3.1 that a six-pass interferometer provides a threefold increase

in working finesse while reducing the transmitted intensity by a half with respect to a single-pass interferometer using the same mirrors. The most dramatic effect of multiple passes – the reason why multi-pass interferometers are so widely used – is the increase in contrast of *thirteen* orders of magnitude achieved in moving from single-pass to six-pass configuration. In practice, six-pass operation is usually not implemented because the contrast of a five-pass interferometer is sufficient for the study of most systems, making the additional reduction in transmission associated with the extra pass unnecessary. For the purposes of my work on soft condensed matter, the contrast attainable with five passes was judged to be ideal based on the above calculations and the results of earlier work by other groups on similar systems. Due to the considerable technical difficulties involved in the successful operation of a five-pass interferometer, single-pass then three-pass configurations were developed and refined before moving to the five-pass system (see Sec. 3.2). It should be noted that changing the number of passes between the mirrors of an interferometer is not a simple operation. Major adaptations must be made to the external corner cubes and masks (see Fig. 3.4 above) and a complete realignment of the optical system is required. Thus it is not practical to change back and forth between, say, three-pass and five-pass operation on a regular basis.

One of the advantages of multi-passing is that only one pair of plates has to be kept parallel in order to ensure that each individual pass (essentially a single Fabry-Perot confined to a discrete subsection of the mirrors) is between a parallel set of plates. Unfortunately even this requirement is difficult to satisfy for more than one pass. Mechanical vibrations and thermal gradients both cause parallelism to be lost over time. If a certain degree of departure from parallelism (sometimes called a *wedge* across the plates) is tolerable in single-pass operation, the problem is multiplied for more than one pass, resulting in an unacceptable loss of transmitted intensity. Some method of actively maintaining the parallelism and hence finesse of a multi-pass interferometer for the duration of the experiment is therefore required. The most common procedure – and the one employed here – is to monitor electronically the transmitted lineshape and apply corrective voltages to the piezoelectric stacks on which one of the mirrors is mounted. Parallelism may be maintained for as long as is required using this technique, which is discussed in more detail below (Sec. 3.2.2.3).

3.2 Recording a spectrum: Fabry-Perot operation and data collection

Now that we have established a basic understanding regarding the principles of operation of a Fabry-Perot interferometer, we will move on to consider its implementation in the development of a Brillouin spectrometer. In order to measure the spectrum of frequencies present in the light scattered from a sample one of course requires a frequency-scanning device, and for the relatively small GHz-scale shifts associated with the Brillouin spectrum, its high resolving power makes the Fabry-Perot a natural choice.

3.2.1 Design and construction of the interferometer

The interferometer on which the spectrometer developed during my work is based had been lying unused in our laboratory for some time, and is fortunately ideal for the measurement of Brillouin spectra. It is a Burleigh Instruments RC-110 Fabry-Perot interferometer constructed almost entirely of Super-Invar (an alloy with an extremely low coefficient of thermal expansion) in order to minimise the detrimental effects of thermal gradients on the alignment of the mirrors. A photograph of an identical instrument is shown in Fig. 3.5.

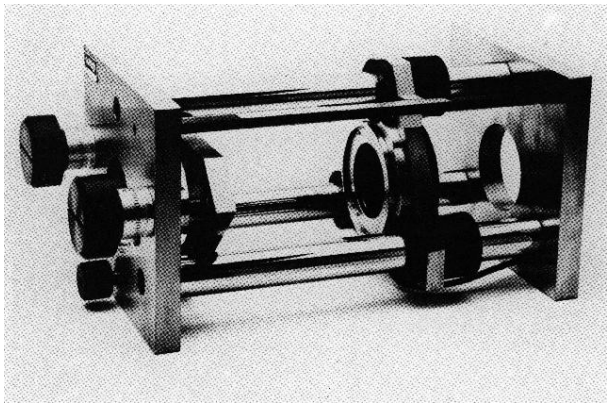

Figure 3.5: Burleigh Instruments RC-110 Fabry-Perot interferometer as used throughout this thesis (reproduced from Ref. [37]).

The importance of the interferometer to the quality and accuracy of all spectra recorded during this research warrants a short discussion of those design features which combine

to make the Burleigh RC-110 suitable for Brillouin spectroscopy of soft condensed matter. Many of the samples studied pose severe difficulties, requiring both high contrast and long collection times (partly due to the reduction in transmitted intensity imposed by five-pass operation) in order to produce a satisfactory spectrum. Detailed information on the design of the apparatus was provided by Burleigh Instruments, Inc. [42].

As mentioned above, the interferometer is made of Super-Invar in order to minimise the destabilising effects of thermal expansion. All connections and joints are rigid – no fixtures are made of soft plastics or other pliable materials which could adversely affect the alignment of the mirrors by creeping or moving. All screws are also made of Super-Invar, and those which require to be adjusted during the alignment process are fitted with large knobs marked accurate to $\pm 0.1\,\mu$m. The piezoelectric material used to make the three stacks which allow the mirrors to be servo-stabilised and their spacing d to be scanned electronically is carefully chosen such that its length increases linearly with the applied voltage to within 1%. Mirror holders are of a design peculiar to Burleigh instruments, intended to ensure that the mirrors are free of mechanical and thermal stresses which could result in distortion of their flat surfaces.

Two choices had to be made when considering which mirrors were to be used in the interferometer; the value of the reflectivity $\mathcal{R}$, and the type of mirror – dielectric film or metallic (silvered) surfaces? All of the mirror sets available were flat to approximately $\lambda/200$, more than adequate for our requirements. The main difference between mirror types is that silvered surfaces maintain their reflectivity across a wide range of wavelengths, while dielectric films are only suitable for use in a narrow band around a specified wavelength. Metallic mirrors, however, have a higher absorption coefficient and hence are not able to provide very high reflectivities. For this reason we decided to use dielectric mirrors designed to operate at the 514.5 nm wavelength produced by an Argon ion laser. Mirrors with a stated reflectivity of 93% (confirmed using a laser power meter) were chosen upon consideration of the working finesse, contrast and throughput which could be achieved (see Table 3.1) using them in single-, three- and five-pass configurations. These mirrors were used with a laser wavelength of 514.5 nm in all of the experiments performed throughout the whole of this research project.

The first step towards incorporating the interferometer into a Brillouin spectrometer

was to assemble and test a system using the Fabry-Perot in the single-pass mode of operation, and this will be discussed in the next section. Multi-pass operation was not attempted at this stage due to the greatly increased requirements of stability and accuracy of alignment that this would create. Subsequent implementation of three-pass and then five-pass configurations will be described in Sec. 3.2.2.5.

3.2.2 Building a Brillouin spectrometer

Although a well-maintained Fabry-Perot interferometer is the most important element in a Brillouin spectrometer, careful design and alignment of the optics before and after the interferometer is also critical. This section will discuss the design and operation of the spectrometer at Edinburgh, from the illumination of the sample through to the computerised collection of the spectrum of frequencies transmitted by the interferometer. The apparatus and procedures presented here evolved towards the final state described below as a result of at least two years working with the spectrometer, the ongoing refinement and development of which was a major part of my research. As stated at the start of this chapter, development of the apparatus was conducted in collaboration with Hugh Vass, and many of the advances discussed in this section would not have been possible without the aid of his technical expertise and ingenuity.

The Fabry-Perot interferometer, laser, illuminating optics, collecting optics and photomultiplier tube were all placed on a heavy steel vibration-free table to minimise disturbances in alignment due to mechanical shocks from the ground. The interferometer was mounted on optical rails fixed semi-permanently to the table with Araldite adhesive, the orientation of the rails thus defining the optic axis of the interferometer. To minimise the disturbing effect of changes in air temperature on the optical stability of the interferometer, an 'igloo' made of polystyrene was constructed and placed over the top of the instrument. Leakage of room lighting and stray reflections of the laser beam from the sample cell were prevented by enclosing the Fabry-Perot , detection optics and photomultiplier tubes within a lightproof environment using high density black cardboard and cloth.

The assembly of the spectrometer splits neatly into three stages: (1) illumination and imaging of the sample onto the interferometer; (2) alignment, stabilisation and scan-

ning operation of the Fabry-Perot and (3) collection and logging of the frequencies transmitted by the interferometer. Development of each of these three stages will now be discussed in turn.

3.2.2.1 Illumination of the sample

The light source used to illuminate the sample being studied is a Spectra-Physics Argon ion laser (with a very stable model 165 resonator and model 265 exciter) producing up to 500 mW at a wavelength of 514.5 nm (a deep green colour). Due to the relatively small frequency shifts observed in Brillouin scattering, it is essential to ensure that the laser produces a well-defined single frequency of light. This *single mode* operation is achieved by placing a suitably spaced low reflectivity (i.e. low finesse) etalon inside the laser cavity, thus ensuring that any wavelengths oscillating in the laser cavity meet resonance criteria both of the etalon and of the laser cavity as a whole [43]. If the free spectral range of the etalon is set larger than the gain profile of the laser, it therefore selects just one of the many modes which exist in the cavity. Most of the gain then occurs in this mode, dramatically reducing the spread of frequencies produced by the laser. Without the etalon the bandwidth of the laser line is of the order of GHz; using the etalon to ensure single mode operation reduces this linewidth to tens of MHz – easily sharp enough to be used as the exciting line in a Brillouin scattering experiment where shifts of a few GHz are measured with a Fabry-Perot interferometer capable of resolving frequency differences no smaller than a few hundred MHz.

One potential problem with using a single mode Ar^+ laser as the light source for Brillouin spectroscopy is the possible occurrence of *mode hopping*. This happens when the single mode supported by the cavity changes to a different mode, caused by mechanical or thermal changes in the etalon or cavity itself. In fact mode hopping is very rarely observed in our experiments. This is likely to be due to the excellent stability of the materials used to construct the laser cavity. The only time when mode hopping was observed in the spectrum was just after a significant change in laser power had been made, which presumably affected the spacing of the intra-cavity etalon due to thermal expansion or contraction. For this reason the laser power was not changed less than ten minutes before the start of data collection, thus avoiding the possibility of corruption

due to the effect.

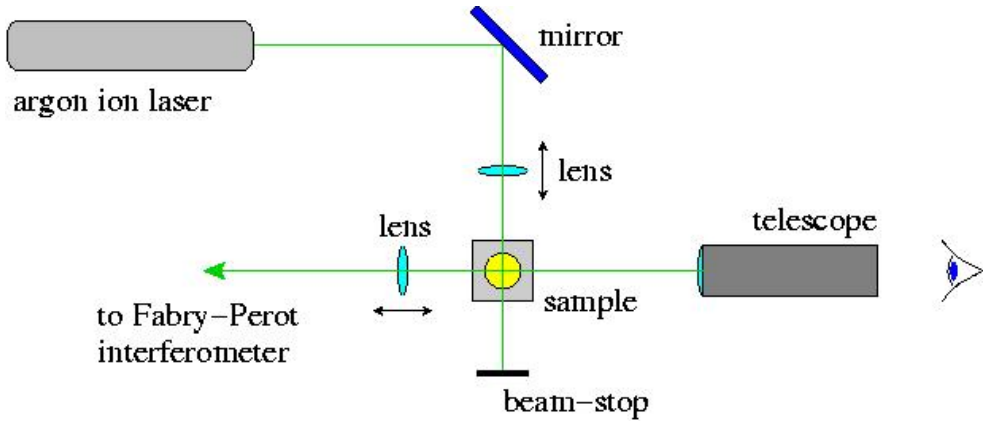

Figure 3.6: Sample illumination and viewing optics for a scattering angle of 90°, upstream from the Fabry-Perot interferometer.

A schematic diagram of the optics before and after the sample is shown in Fig. 3.6. The laser beam is directed towards the sample using a mirror, and focused onto it with a small f=10 cm lens. The sample is attached with a soft wax to the surface of an (x, y, z) translation stage allowing its position to be adjusted in three dimensions with very sensitive vernier-scaled screws. Light scattered from the sample at 90° is then collected by another lens and directed towards the Fabry-Perot interferometer. The key factor in the correct alignment of this arrangement is therefore to ensure that the scattering angle is as close to the desired 90° as possible. This alignment was performed by replacing the sample with a right-angled beamsplitting cube and viewing the reflected and transmitted beams while running the laser at very low power (for safety reasons). A right angle between the light illuminating the sample and the direction in which scattered light is collected can then be set by changing the position of the sample table with the adjusters until the relevant reflected and transmitted beams overlap. Thus when the beamsplitter is removed and the sample placed in the path of the incident light beam, light scattered from it at very close to 90° will be collected and be directed towards the Fabry-Perot interferometer downstream. This alignment procedure must be repeated at regular intervals in case the scattering angle has been changed by disturbances to the optics before and after the sample.

As evidenced by the results presented later in Chapter 4 many interesting experiments

can be performed at a fixed scattering angle by changing other variables (e.g. temperature, pressure, concentration etc.), but the intention to use our Brillouin spectrometer to study the propagation of hypersound in colloidal dispersions (Chapter 5) required some method of varying the magnitude of the scattering vector q to be implemented. Recalling Eq. 2.3 we see that $q = 4\pi n/\lambda \sin\theta/2$ may be changed for a given sample by altering either the laser wavelength λ or the scattering angle θ between incident and scattered light. The Ar^+ and Kr^+ lasers available as light sources in the laboratory are capable of operation at a few discrete wavelengths within the visible spectrum, but in order to vary q continuously over as wide a range as possible a way of changing θ had to be devised. One technique for varying the scattering vector which is widely used in light scattering measurements in our research group and elsewhere is to mount all collection and detection optics downstream from the sample on an arm attached to a turntable with the sample holder positioned at the centre of rotation. This approach was not adopted due to the additional requirements of stability and accuracy of alignment imposed by the presence of the Fabry-Perot interferometer, which would have to be mounted on the rotating part of the apparatus in this arrangement. An alternative method of varying the scattering angle without requiring any sensitive pieces of equipment to be moved was therefore developed, following to a large extent the design employed by the group of Cataliotti at the University of Perugia and reported in Ref. [44]. Rather than rotating the detection optics, the scattering angle is varied by changing the direction from which the incident light reaches the sample. This is done in a very straightforward manner by mounting a rotatable mirror on an arm attached to a small turntable upon which the sample is placed above the axis of rotation. Another rotating mirror is then used to send the laser beam towards the mirror on the arm, which may then be adjusted so that the light is directed towards the sample. This technique is illustrated by the schematic diagram shown in Fig. 3.7. It has many advantages over the more conventional approach of mounting the collection and detection optics on a turntable: the Fabry-Perot interferometer and photomultiplier tube remain stationary and are therefore more mechanically stable; the scattering angle can be varied over a wider range; only two very small pieces of optics require to be rotated, so that the turntable and arm do not require to be constructed of large or heavy materials; and all optical and mechanical realignment associated with a change in scattering angle is performed upstream from the sample, thus not interfering with the sensitive alignment

of the interferometer.

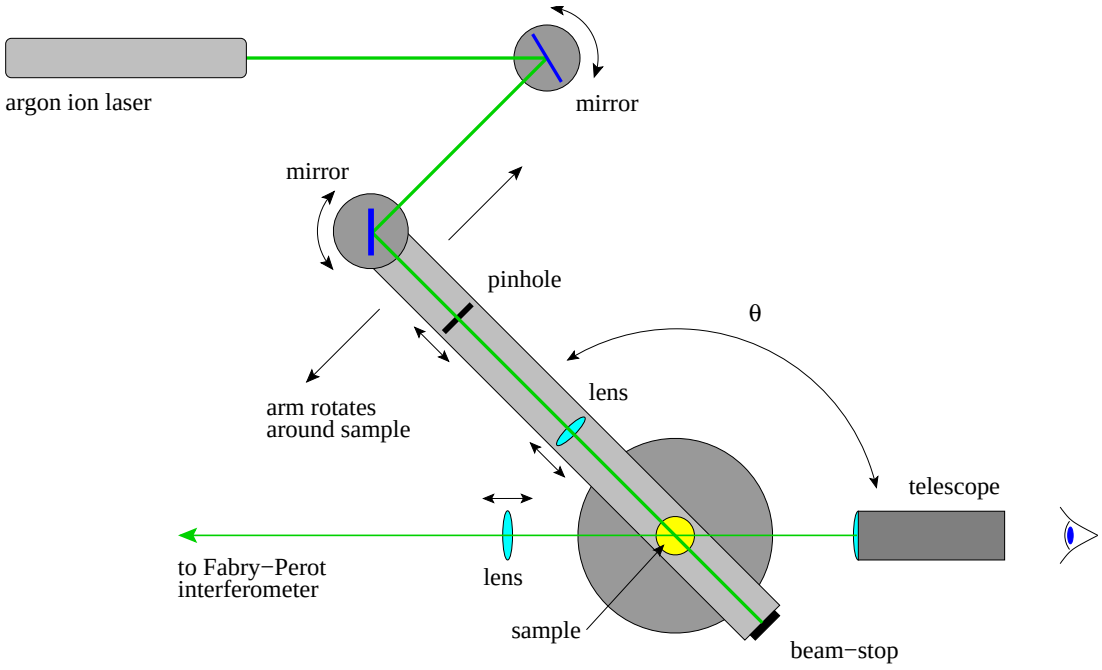

Figure 3.7: System of mirrors enabling the scattering angle to be varied from 10° to 165° as discussed in the text.

The turntable is marked with a vernier scale enabling its angular position to be determined to the nearest tenth of a degree. The angle can be chosen very accurately using an adjuster screw while viewing the vernier scale with a magnifying glass. The alignment technique described above using a beamsplitting cube to define the 90° scattering geometry is again employed to ensure that the rotation axis of the turntable is centred correctly, and to calibrate the vernier scale by finding which angle on the scale corresponds to a scattering angle of 90°. Any scattering angle selected by fixing the arm in a certain position can then be measured very easily using the scale on the turntable.

Mounted on the rotating arm so as to be in alignment between the mirror and sample are a small lens and a pinhole aperture, both of which may be translated back and forth along the arm on rails. The lens is adjusted so that the laser beam is well focused in the sample when viewed using a telescope, while the pinhole allows the straightness of the beam's path along the arm to be checked in order to ensure that the scattering angle does not deviate from the desired value.

A new scattering angle is set as follows. The required value of θ is fixed using the vernier scale on the turntable. The lens immediately downstream from the laser is then rotated until the beam strikes the centre of the mirror on the end of the arm. The pinhole aperture is placed as close to the second mirror as possible which is then rotated so that the beam strikes the centre of the hole (which has previously been set to lie on the optic axis of the turntable arm). If necessary, the pitch of the mirror may also be adjusted until the beam is at the same height as the pinhole to ensure that the height at which the beam reaches the sample is correct. The aperture is then moved downstream to be as close to the sample as possible (i.e. immediately upstream from the lens), and the position of the beam readjusted so that it still coincides with the pinhole. The pinhole is then moved back to its original position near the mirror to examine the effect of the readjustment. Moving the pinhole up and down the optic axis and checking the beam position like this results in correct alignment being achieved in an iterative manner. Satisfactory alignment occurs when the laser beam is seen to lie over the pinhole at all positions as it is moved back and forth along the arm. The pinhole aperture (which is smaller than the beam diameter) is then removed to avoid unnecessary attenuation of the light incident on the sample.

This alignment procedure is very straightforward and reasonably quick – a new scattering angle can be set and aligned in approximately three minutes. Although this is perfectly satisfactory when the angle is changed infrequently, experiments in which many different values of θ are required to be studied become very time consuming. For example when measuring the dispersion relation (ν_B vs. q) for a given sample, spectra at as many as 30 different q values may have to be measured in order to build up enough points to provide a satisfactory dataset (see Chap. 5 for examples of such dispersion relations). The ideal solution to this problem would be to automate the changing of the scattering angle by using a stepper motor to turn the arm between the measurement of each spectrum. Unfortunately the implementation of such a system would be extremely difficult due to the extremely high standard of optical alignment required; for this reason the automation of q-variation was not attempted.

This arrangement is very effective, allowing scattering angles from 10° to 165° to be obtained. This range of angles corresponds (via Eq. 2.3) to a range of scattering vectors $0.0032\,\mathrm{nm}^{-1} \leq q \leq 0.0363\,\mathrm{nm}^{-1}$ for a molecular liquid with a typical refractive index

$n = 1.50$ and incident light with $\lambda = 514.5\,\text{nm}$. It is not possible to get nearer to 180° because the mount holding the lens downstream from the sample impedes further rotation of the arm. Accurate focusing of the laser beam in the sample becomes very difficult at such large scattering angles because the intense beam coming out of the sample cell passes very close to the eye of the observer if the telescope is used. A small uncertainty in θ is therefore introduced, which will be discussed below. Angles smaller than 10° are not obtainable due to the danger of the extremely intense straight-through beam reaching and damaging the photomultiplier tube. Viewing the beam in the sample at such small angles is also difficult because the arm obstructs the line of sight of the telescope. One minor drawback of the 'rotating mirrors' arrangement is that it cannot be used to create a right-angled scattering geometry – the mirror on the end of the arm obstructs the path of the laser beam for $\theta = 90 \pm 2°$. Simply removing the mirror from the arm enables the 90° scattering angle to be set, but this does not allow access to the small range of angles either side of the right angle, which unfortunately cannot be reached using the apparatus shown in Fig. 3.7.

The uncertainty in θ for scattering angles less than 150 ° is ±0.5 °, resulting from human error in reading the vernier scale on the turntable, plus an allowance for any small deficiencies in the alignment of the sample with the incident beam and the optical axis of the interferometer. An additional error of ±2 ° is introduced for $\theta > 150\,°$ due to the aforementioned difficulty of viewing the beam in the sample, although fortunately such large angles are rarely required. The uncertainty in q caused by the ±0.5 ° error in θ is proportional to $\cos(\theta/2)$ (differentiating Eq. 2.3), hence will be most significant at small angles. For the smallest obtainable θ of 10 ° this maximum uncertainty in q is $\pm 0.0001\,\text{nm}^{-1}$, or ±3%. Angles this small are not often used in the experiments reported later in this thesis, so it will be assumed that the uncertainty in q is negligible.

Spatial filter

The biggest difficulty in attempting to measure Brillouin scattering from colloidal dispersions is the extremely high intensity of spurious elastic scattering from inhomogeneities in the fluid. The true Rayleigh peak due to scattering from entropy fluctuations (discussed in Chapter 2) is swamped by scattering of light by the change in

refractive index which occurs at the interface between the colloidal particle and the dispersion medium[‡]. This scattering may be minimised using a technique called *index-matching* which is discussed in Sec. 5.1.1.2, but remains problematic in most samples. The inherently weak Brillouin peaks are therefore difficult to resolve – this is why the high contrast provided by a five-pass interferometer is necessary. However the intensity of elastic scattering is not constant throughout the sample cell. Moving the scattering volume around within the sample and changing its size allows regions with lower spurious scattering to be selected in order to increase the likelihood of recording satisfactory Brillouin peaks. A similar problem occurs in molecular liquids near freezing, when small crystallites can form which scatter very brightly at the frequency of the incident light. Another benefit of being able to choose the part of the sample from which scattered light is observed is that high-intensity reflections of the incident laser beam from optical surfaces near the sample which become problematic at either very high or very low scattering angles may be prevented from reaching the photomultiplier tube and causing damage. In order to allow the region of the sample from which scattered light is passed to the Fabry-Perot interferometer to be chosen, I designed a simple *spatial filter* and added it to the spectrometer.

The principle of operation of a spatial filter is straightforward. A movable aperture in the Fourier plane of a lens illuminated by parallel light rays from the sample is used to select (by trial and error) a region which produces a satisfactory spectrum. A schematic diagram of the design adopted is shown in Fig. 3.8. The filter was constructed using Linos Photonics microbench optical components mounted on rails which allow the positions of anti-reflection coated plano-convex lenses to be adjusted and fixed along the axis of the device. Once its lateral position has been fixed at the focal points of lenses 2 and 3 (see Fig. 3.8), the pinhole aperture can be translated in the two transverse dimensions to allow light from only the selected part of the Fourier plane to pass. To locate a region of the sample in which spurious elastic scattering is at a minimum, the aperture is moved incrementally while observing the spectrum (either in real time on an oscilloscope or by recording short test spectra on the computer) until the place which scatters the lowest intensity of unshifted light is found. The spatial filter is mounted in

[‡]Note that the unshifted peak in the spectrum will still be referred to as the *Rayleigh peak* despite the fact that for some samples most of its intensity originates from a process other than Rayleigh scattering as strictly defined in Chapter 2.

place of the lens immediately downstream from the sample as shown in Figs. 3.6 and 3.7. Significant improvement in the quality of Brillouin spectra from colloids and other brightly scattering samples was observed with the filter in place.

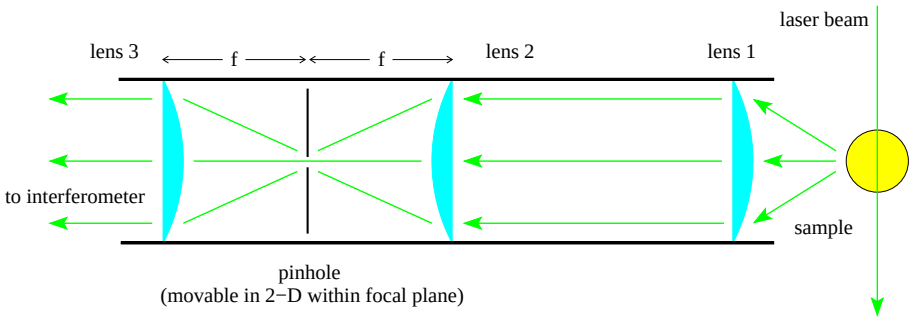

Figure 3.8: Schematic diagram of the spatial filter designed to allow the scattering volume to be translated within the sample in order to avoid regions of intense spurious elastic scattering.

3.2.2.2 Controlling the sample environment: variable temperature and pressure devices

One of the most important aims of developing the Brillouin spectrometer at Edinburgh was to enable the temperature and pressure of the sample to be varied simultaneously in order to observe the effect of changing those variables on the Rayleigh-Brillouin spectrum. The design of various sample cells on the way to achieving this aim was undertaken mostly by Mr. Hugh Vass; my contribution was limited to minor adaptations to the liquid nitrogen cooled temperature cell described below. I was not involved in the design of the pressure cells, which will therefore not be discussed in any detail here. For much more technical information on the development of the sample cells described here the interested reader may wish to consult Hugh's MSc thesis [45].

The most important thermodynamic variable required to be controlled for the purposes of my research is the temperature of the sample. For my studies of supercooled aqueous alcohol solutions it was necessary to heat and cool samples across a wide range of temperatures, whereas only very small deviations of less than 10 K from room temperature were required when looking at colloidal dispersions. The same sample holder was used for both these applications – its versatility allowing it to be very easily adapted to the required specification.

One possible method of temperature control would have been to use a closed cycle cryostat already available in our lab. The main advantage of this device is its ability to cool to extremely low temperatures (approximately 12 K), but several factors resulted in it not being used. The most serious problem with the cryostat is that optical access to the sample is only available through four flat glass windows – continuous variation of the scattering angle is therefore not possible. The cryostat and associated apparatus were also being used for Raman spectroscopy experiments in the lab, so choosing an alternative method of controlling the sample temperature to be used with the Brillouin spectrometer avoided any potential problems associated with sharing the equipment.

The alternative to using this cryostat was to design and build our own system of controlling the sample temperature. In doing this we were able to ensure that our key requirements were satisfied. These were: (1) ability to vary the scattering angle; (2) access to a wide range of temperatures above and below room temperature; (3) accurate control of the chosen temperature; and (4) easy and quick access to facilitate changing and inspection of the sample at any time. A schematic diagram of the final specification of this device is shown in Fig. 3.9.

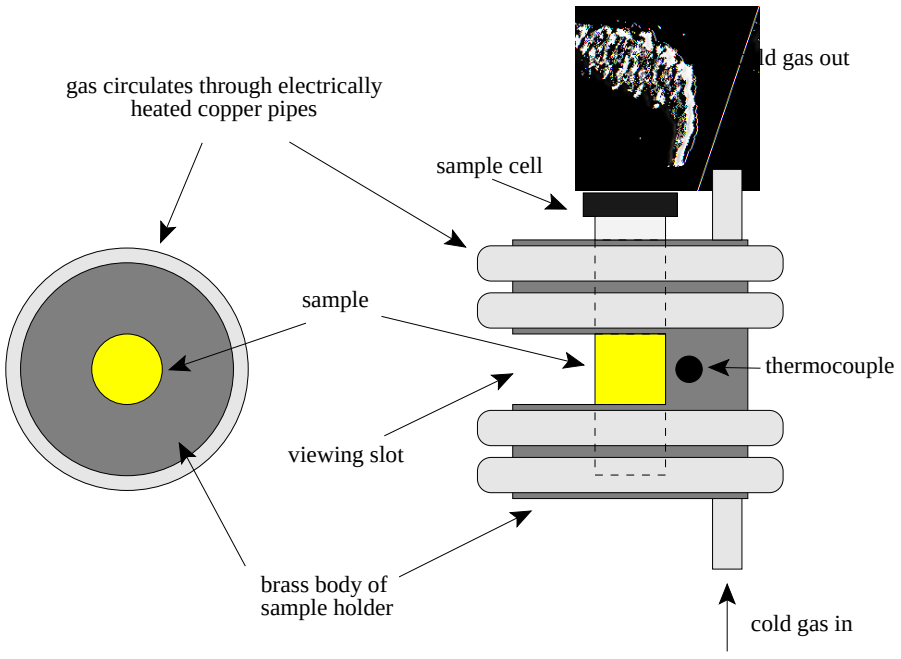

Figure 3.9: Top and side views of the temperature-controlled sample cell employed in most of the experiments performed during my research, capable of cooling to 116 K *and heating to at least 400* K.

The body of the sample holder is made from a 4.5 cm diameter brass cylinder, the material chosen as a compromise between good thermal conductivity and ease of handling (copper is a better conductor of heat, but is more difficult to machine). The sample (contained in a 15 mm diameter, 28 ml cylindrical glass cell) sits in a tightly-fitting hole drilled into the centre of the brass. A slot cut around the sample holder with a height of approximately 1 cm allows optical access to the glass cell holding the sample at a wide range of scattering angles. It was of course not possible to make the viewing slot extend around the entire diameter of the brass cylinder; scattering angles blocked by the remaining part can be accessed by simply rotating the sample holder to allow the incident and scattered light to enter and leave the cell. One of our design criteria is therefore satisfied – the scattering angle can be varied throughout the entire range of useful values. The temperature of the sample is controlled by regulating the temperature of the brass cylinder in which it is housed. This is done by circulating dry nitrogen gas around the outside of the body of the cell. When low temperatures are required, the temperature of this gas is controlled using heating elements on the copper coil through which it flows; at higher temperatures the sample holder is heated directly by elements mounted on the brass cylinder. Varying the voltage supplied to these heaters thus allows the temperature of the brass cylinder – and hence the sample – to be adjusted, with a short delay determined by the thermal conductivity of the brass and the quality of thermal contact between the sample cell and its holder. A variable flow of cold gas is provided by suspending a heater in a large sealed Dewar flask of liquid nitrogen and adjusting the heater voltage to control the rate at which the liquid boils, thus building up pressure which pushes gas out of the flask through a thin copper tube. This tube takes in gas from near the top of the Dewar, then passes below the level of the liquid to cool the gas further, so that the temperature of the gas leaving the flask is just above 77 K (the boiling point of nitrogen). This gas then travels along an insulated rubber tube to the sample holder, where it circulates around a copper tube bonded to the outside of the brass cylinder with a high thermal conductivity adhesive. After passing round the body of the sample holder several times, this tube vents the nitrogen into the air above the sample.

When necessary this exhaust gas can be used to prevent condensation of atmospheric water onto the sample, which would otherwise occur whenever the required temperature

is below the dew point of the air in the laboratory (usually about 7 °C, but varying slightly depending on temperature and relative humidity). Misting on the glass of the sample cell is extremely undesirable, disturbing optical alignments and reducing the intensity of incident and scattered light. The most obvious way to avoid condensation of water from the atmosphere onto a cold surface is to somehow remove the water from the environment. This was very straightforward to implement using the sample holder described above by using the exhaust nitrogen gas to flush the air out of an almost airtight enclosure around the sample. This was fashioned from a cylinder of high density cardboard (a good thermal insulator) with a diameter just large enough to allow it to fit over the brass body of the sample holder. The base of the enclosure was also made of cardboard, fixed semi-permanently to the sample table. The top had to be easy to remove in order to change, move or inspect the sample. A plastic disc with the same diameter as the cardboard cylinder was found to be suitable, with an insulating disc of polystyrene attached to its underside. Thick plastic adhesive tape is used to fix this 'lid' in place and provide extra thermal insulation. As much as possible of the empty space inside the cardboard cylinder is filled with pieces of polystyrene and/or cotton wool in order to help insulate the sample holder. This allows significantly lower temperatures to be reached using the apparatus. Small holes punched in the cylinder and covered with a piece of glass allow the incident and scattered beams to enter and leave the enclosure. If a scattering angle is required which is not provided by an existing window, a new one can be cut and sealed very quickly in the necessary position. At low temperatures (around 210 K and below) cold nitrogen gas leaking from the entry and exit windows was found to cause condensation of atmospheric water onto the lenses close to the sample. This problem was overcome by attaching small heaters to the metal lens mounts, thus gently heating the lens surfaces and preventing condensation from occurring. This allowed spectra to be recorded successfully at temperatures as low as 116 K.

The temperature of the sample is maintained by a Thor Cryogenics model 3010 electronic temperature control unit. This monitors the temperature of the sample holder using a Type T copper-constantan thermocouple fixed to the brass cylinder as near to the sample cell as possible. A calibrated digital meter is also attached to this thermocouple and used to monitor the temperature at the sample throughout an experiment.

The temperature controller regulates the voltage applied to the heaters mounted on the sample holder so that a given temperature can be maintained almost indefinitely. The required temperature is set using a dial on the controller to specify the corresponding thermocouple e.m.f. as found from calibration data in the literature. This active stabilisation allows the temperature to be held accurate to $\pm 0.1\,\mathrm{K}$ for many hours. The duration for which a low temperature may be maintained is of course limited by the supply of liquid nitrogen from which the refrigerating gas is produced, but the large capacity of the Dewar flask used to hold the liquid ensures that this is not a serious problem; refilling the flask prior to an experiment enables even the lowest of attainable temperatures to be held for at least the length of a working day. One problem associated with boiling off nitrogen gas from this container is occasionally encountered when extremely low temperatures or rapid cooling rates demand a high pressure to be built up (by using a large heater voltage) at the top of the Dewar in order to drive the cold gas out quickly. This high pressure, combined with a loss in elasticity due to cooling, can cause the rubber bung sealing the flask to pop out, breaking the seal and thus greatly reducing the flow of nitrogen gas towards the sample holder. This blowout occurs in one of two ways: a dramatic explosion in which the bung is completely expelled from the neck of the flask accompanied by large clouds of gas and ice crystals (and the rapid adoption of evasive procedures by the investigator); or a much less noticeable leakage of nitrogen gas from small gaps in the seal around the edge of the bung. Both of these situations result in a reduction in the pressure of gas inside the flask and thus decrease the flow of refrigerant. This can cause the temperature of the sample to rise uncontrollably, rendering the experiment useless. The most obvious and effective way of avoiding this problem is to push the bung as hard as possible into the neck of the flask when the rubber is at room temperature (and hence forms a better seal). Even when this precaution is taken bung blowouts do occur, but infrequently enough to be acceptable.

In summary, the temperature of the sample is controlled at ambient pressure by placing it inside a brass cylinder around which dry nitrogen gas is circulated. Electronically controlled elements regulate the heating applied to this gas and the cell body in order to maintain the desired temperature for extended periods. When necessary, the atmosphere around the sample is purged of water vapour by placing the sample holder in

an almost airtight enclosure into which exhaust nitrogen from the cooling system is vented. The advantages of this method over the more conventional approach of using a closed cycle cryostat are several: (1) the scattering angle can be varied across a wide range; (2) the sample is easily accessible, allowing adjustments and inspections to be made in a few seconds; (3) the large sample volume allows the evolution of macroscopic temperature-dependent phenomena to be observed by eye. The only significant drawback is the limit imposed by the boiling point of nitrogen on how cold the sample can be made. If temperatures below 116 K are required, a cryostat must be used and the advantages listed here forfeited.

Measuring Brillouin spectra of liquids at high pressures

As stated above, the measurement of Brillouin spectra at high pressure was not a large part of my research, therefore only a very brief description of the variable temperature *and* pressure cell used to obtain the high pressure Brillouin spectra presented in Chapter 4 will be given here.

The construction of a large volume pressure cell capable of reaching at least 15 kbar was undertaken by Hugh Vass, who has a great deal of experience in the design of high pressure cells for scattering experiments. Development of the cell was time consuming and went through many stages before arriving at the specification described below. For a much more detailed account of the design, construction and materials used see Hugh's MSc thesis [45].

The body of the cell is made from a single piece of high-strength heat-treated steel, machined to form a vertical bore which is crossed at the centre of the block by two horizontal bores at right angles to one another. The liquid to be studied is held in the vertical cavity by two tightly fitting pistons, which are provided with a sealing device in order to prevent leakage. One of the horizontal bores allows a laser beam to pass through the sample, while the other enables light scattered at 90° to be observed by the spectrometer and (using a telescope – see Fig. 3.6) the investigator. Light enters and leaves the cell through small windows made from a piece of diamond (chosen for its strength) held and reinforced in a cleverly designed steel mounting which minimises the strain transmitted to the window thus allowing high pressures to be maintained.

Pressure is applied to the pistons via a pressure intensifier using a manually driven hydraulic ram. The pressure experienced by the sample is monitored using a pressure gauge on the ram. Using this apparatus, pressures as high as 15 kbar have been achieved without damaging the cell. Lack of sensitivity in controlling lower pressures means that the cell is not usually used below 1 kbar; the sapphire cell described below is more suited to low pressure work. The temperature of the sample in the pressure cell can also be controlled in a similar manner to the approach described above for the ambient pressure sample holder. Dry gas boiled off from a Dewar flask of liquid nitrogen is circulated around the outside of the cell body through a copper coil fitted with heaters. An electronic temperature control unit is used to monitor and control the temperature of the sample by regulating the voltage applied to the heaters. Using this technique temperatures in the range $170\,\mathrm{K} \leq T \leq 570\,\mathrm{K}$ can be accessed and maintained for several hours. As before, for temperatures below the dew point of air in the lab the sample cell must be enclosed in a nitrogen environment provided by exhaust gas from the cooling system in order to prevent condensation of atmospheric water onto the optical surfaces.

This pressure cell represents a significant improvement over conventional methods of exerting hydrostatic pressure on a liquid sample for the purposes of optical spectroscopy. The alternative approach would be to use a Merril-Basset diamond anvil cell (DAC), which is capable of achieving much higher pressures (hundreds of kbar) but is unsuitable for Brillouin spectroscopy of liquids for several reasons. Perhaps the most important of these is that the DAC is only really suitable for use in two scattering geometries; forward ($\theta = 0°$) and backscattering ($\theta = 180°$), despite attempts by several groups to devise a method for varying the scattering angle. The design of the DAC ensures that it creates a lot of unwanted stray elastic scattering, which is extremely undesirable when attempting to measure the weak Brillouin peaks. The sample volume is also extremely small, with a viewable area of at most 0.5 mm. One other drawback of the DAC is that the pressure can only be found using Raman spectroscopy to measure the frequency of fluorescence of a small piece of ruby placed inside the cell. The large volume pressure cell described above is therefore preferable to a DAC for many reasons, especially for the relatively low pressures ($\leq 15\,\mathrm{kbar}$) at which most interesting phenomena occur in liquid samples.

In its current state of development, the Edinburgh pressure cell does however have some disadvantages. It is relatively difficult to use; preparing and loading the cell with a clean sample and maintaining high pressure are all quite time-consuming, and the investigator must monitor and top up the pressure using the hydraulic ram throughout an experiment. The materials used in the construction of the cell mean that samples can easily become contaminated, requiring the cell to be disassembled and cleaned. It is also not possible to use the pressure cell to study certain chemicals which might react with its steel body at high pressure.

Another important drawback with this design of pressure cell is that the scattering angle is fixed at 90°. For pressures up to a maximum of about 2.5 kbar, another type of cell developed at Edinburgh *can* be used at variable scattering angle. This alternative design consists of a transparent sapphire cylinder with a diameter of about 2 cm, along the length of which (about 3 cm) a small hole is bored in the centre. The sample is held in this cylindrical cavity between two pistons which incorporate a sealing device, and transmit pressure applied by a hydraulic ram. The sapphire is braced using steel bands to increase the pressure which can be maintained in the bore without cracking. The cylindrical symmetry and almost unrestricted optical axis around the sapphire cell allows the scattering angle to be varied. The temperature of the sample may also be controlled to some extent using a method similar to that described for the steel-bodied pressure cell described above.

3.2.2.3 Alignment, stabilisation and operation of a scanning Fabry-Perot

The previous section looked in some detail at the illumination of a sample at variable scattering angle and the control of its temperature and pressure. The next stage of the Brillouin spectrometer is the Fabry-Perot interferometer, the principles of operation of which were the subject of Sec. 3.1. Finding and maintaining accurate alignment of the interferometer is the most important and difficult part of recording a good Brillouin spectrum; this section aims to describe the steps which must be followed to do so. These procedures were developed in collaboration with Mr. Hugh Vass over the considerable period of time which was required to familiarise ourselves with the peculiarities of what is an extremely sensitive and difficult experiment to perform. Even with the

benefit of the following 'instructions', the complexity of the apparatus means that a novice should expect to spend a great deal of time (at least two months) working with the spectrometer before being able to obtain high quality Brillouin spectra on a regular basis. This section will consider only single-pass operation – discussion of the additional requirements posed by a multi-pass interferometer is postponed until later (Sec. 3.2.2.5).

The first task is to align the Fabry-Perot so that the mirrors are parallel and the intensity of light leaving the interferometer is maximal. To do this, the required free spectral range is set by choosing the corresponding mirror separation $d = c \,/\, 2(\Delta\nu)_{FSR}$ (Eq. 3.14) using a travelling microscope to examine a vernier scale on the interferometer while adjusting d by manually sliding one of the mirrors along the three rails on which it is supported. Tightening the screws which hold d constant can cause it to change slightly, so the measurement is repeated after the plate position has been fixed. The resulting uncertainty in d is ± 0.04 mm, which creates an error of less than $\pm 0.5\%$ in the FSR for a typical mirror separation. This uncertainty is small enough to be neglected, hence for the purposes of measuring peak frequencies and widths (see Sec. 3.3.2 below), the frequency scale calculated using the FSR may be considered to be exact. The plates are then aligned using two of the three large adjuster screws to change the orientation of the other mirror – one adjuster is left untouched to avoid altering d.

A bright scatterer such as a piece of white paper or a cloudy sample is placed on the sample table and illuminated at a 90° scattering angle. Ensuring that the intensity of light is as low as possible to avoid injuring the eye, the position of the scatterer is altered while viewing through the telescope (see Fig. 3.6) until the reflection from the front mirror of the interferometer coincides with the position of the incident beam on the scatterer. The laser power is then increased, and a small white screen is used to monitor the pattern of light intensity between the mirrors of the interferometer. The mirrors are set to scan slowly (see the following section) back and forth at a rate of around 1 Hz, causing the pattern of fringes on the screen to change with time. The two adjusters discussed above are moved very slowly in turn until many sharp fringes come into focus[§]. Minute adjustments to the mirror orientation are then made in order to

[§]A detailed description of these fringes is beyond the scope of this thesis, but can be found in Ref. [38].

cause the fringe separation to increase, with the aim of filling the screen with a spot of light from just one fringe. When this is achieved, the alignment of the interferometer is almost complete, and may be fine-tuned electronically using the 'Align' potentiometers on the DAS-10 controller (see below for how this refinement is performed) and a much faster scan rate. When switching on the photomultiplier tube in order to use the DAS-10, care must be taken to reduce the light intensity to avoid damaging the PMT.

Scanning: the ramp generator and DAS-10

In order to build up a composite spectrum with a satisfactory signal-to-noise ratio, the mirror spacing of the interferometer must be scanned repeatedly across a small range in order to accumulate many individual spectra. This is achieved using a specially designed *ramp generator* to apply a sawtooth voltage to the piezoelectric stacks upon which one of the mirrors is mounted. Unfortunately the ramp generator intended for use with our interferometer and stabilisation electronics is no longer available from Burleigh Instruments, but they kindly provided the necessary components and circuit diagrams to allow the instrument to be built to the required specification in the Department's electronics workshop. The amplitude of the ramp is proportional to the distance through which the mirror is translated, and the period of the waveform determines the time taken to make this change – i.e. the frequency at which the interferometer is scanned. For the spectra presented in the following chapters, these parameters were chosen to suit the requirements of the multichannel analyser used to collect data, and will be discussed in Sec. 3.2.2.4 below. Three trim controls on the instrument must be adjusted such that parallelism of the mirrors is maintained as the separation is changed. Detailed instructions of the difficult alignment technique required to do this are provided in the instruction manual of the ramp generator and will not be discussed here. Note that for some reason the ramp generator requires a warmup period of approximately 30 minutes during which the ramp is slightly non-linear, resulting in corrupted Brillouin spectra.

Fine adjustments to the alignment of the Fabry-Perot are made using the set of three 'Align' potentiometers on a Burleigh DAS-10 electronic stabilisation and control unit. These control a bias voltage applied to each of the three piezoelectric stacks on which

the moving mirror is mounted, thereby allowing its orientation to be fine-tuned until it is parallel with the other plate. The alignment is performed by using a brightly scattering sample (such as a cloudy gel) and observing the signal produced by the detection system (Sec. 3.2.2.4) on an oscilloscope screen while making very small adjustments to the bias voltages. A typical ramp amplitude should result in several (usually three) orders of the interference pattern transmitted by the interferometer being shown on the screen – the interferometer is considered to be properly aligned when the unshifted peaks in the spectrum are at their sharpest and most intense.

If it proves impossible to obtain a satisfactory alignment using the DAS-10, one usually has to resort to the much more time-consuming mechanical method discussed in the previous section. Providing the interferometer is not subjected to any major disturbances, this eventuality should arise only once every few weeks; day-to-day thermal and mechanical perturbations are not normally sufficient to create misalignments outside the range of the piezoelectric stacks.

The DAS-10 is also used to re-align the interferometer between spectra collected during a sequence of experiments on a certain sample (e.g. changing the temperature or scattering vector). Before collecting each spectrum, the intensity and symmetrical shape of the unshifted peaks displayed on the oscilloscope screen are optimised by adjusting the bias voltages applied to the piezoelectric stacks as described above.

When the sample being studied is a particularly weak scatterer (a good example of this is water near 4 °C – see Ref. [3]) it was found that alignment of the interferometer using this technique could not be performed due to the low intensity of the unshifted peaks in the spectrum displayed on the oscilloscope. A solution to this problem was found to be to allow some unshifted laser light to reach the Fabry-Perot , either by replacing the sample with a cloudy gel or redirecting the laser beam away from the sample to fall on a piece of tissue paper situated such that some of the light scattered from it falls on the interferometer. One has to be very careful to limit the intensity of this light in order to prevent damage to the photomultiplier tube. This latter approach is preferable when the sample is far from ambient temperature or pressure, as it does not require the sample to be removed.

Active stabilisation of the interferometer

As stated above, the interferometer sits on a heavy vibration-damping table and is shielded from thermal disturbances, but unfortunately this is not sufficient to prevent the gradual loss of alignment over the period of a few tens of minutes. Left unattended, a well-aligned instrument will typically be unable to produce an acceptable Brillouin spectrum after 30 minutes, and the rate at which alignment is lost increases greatly in multi-pass operation. Collection times of several hours are commonly required in Brillouin scattering studies of soft condensed matter, hence some method of preventing this loss of alignment must be adopted.

Fortunately, the Burleigh DAS-10 electronic stabilisation unit is specifically designed to maintain the alignment of a Fabry-Perot interferometer almost indefinitely. This is achieved using a feedback mechanism, whereby the instrument monitors the finesse of the signal detected by the PMT and applies compensatory voltages to the piezoelectric stacks in order to recover any loss of alignment detected between scans. The technical details of how this is implemented will not be discussed here, but may be found in Refs. [37] and [38]. The applied test voltages are small, so the DAS-10 takes a few minutes to recover the optimum finesse after some disturbance causes the alignment to be lost. The signal reaching the computer may be blocked during this period to prevent corruption of the recorded spectrum.

For some samples (e.g. water near 4 °C – see Ref. [3]) the Rayleigh peak is less intense than the Brillouin peaks, and therefore too weak for the DAS-10 to monitor. In this unusual situation it was found to be possible to trigger instead on one of the Brillouin peaks, although the inherent weakness and greater width of these peaks increases the likelihood of stabilisation failing over extended periods of time.

Failure of stabilisation can occur due to flashes of intense scattering from dust particles in the sample, mechanical or thermal shock to the interferometer, or electrical interference from nearby apparatus. These may all cause the peak monitored by the DAS-10 to weaken or move so that it can no longer control the finesse. If this happens, collection must be halted immediately to avoid corruption of the data already accumulated. The alignment techniques described above (electronic or mechanical depending on the

extent of the disturbance) must then be repeated before starting a new experiment.

Alignment will also be lost if the automatic adjustments required to stabilise the interferometer are outside the range of one of the piezoelectric stacks which control the mirror orientation. This situation is indicated by a warning light on the DAS-10. If noticed immediately, manual adjustments may be made to all three 'Align' potentiometers in an attempt to 'walk' the mirror back into the controllable range. This requires a lot of skill, and is not always successful.

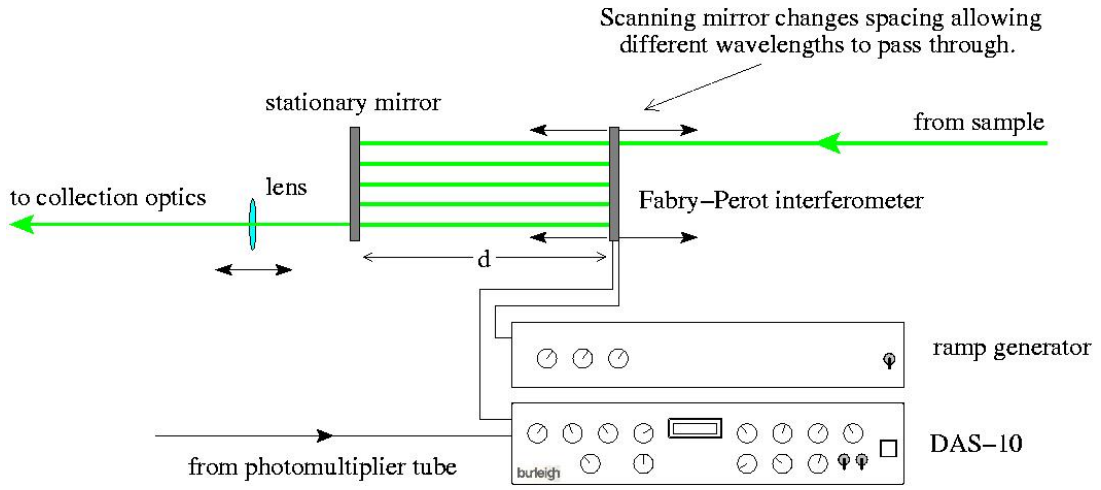

Figure 3.10: Schematic diagram of an electronically scanned and stabilised Fabry-Perot interferometer.

3.2.2.4 Detection of the transmitted intensity profile

The last part of the Brillouin spectrometer is required to take the light transmitted by the Fabry-Perot interferometer and use it to produce a spectrum which can be recorded as a dataset on a personal computer. There are two key pieces of apparatus which enable this function to be performed: a photomultiplier tube turns light of varying intensity into an electrical signal, which is then fed to a multichannel analyser connected to the PC, enabling many sequentially recorded spectra to be accumulated in order to produce a composite spectrum with a satisfactory signal-to-noise ratio.

Before reaching the photomultiplier tube (PMT), light from the interferometer must be focused onto its pinhole aperture using a lens mounted on a precision (x, y, z) translation

stage. This alignment is done by trial and error. The position of the lens is adjusted while observing the spectrum displayed on the oscilloscope. The best focus corresponds to the position which results in the sharpest and most intense Rayleigh peaks. This alignment is checked regularly as poorly focused light at the PMT has an extremely detrimental effect on the resolution of the recorded spectrum.

As a precaution against stray light (in addition to the lightproof environment created with the screens described above) a *spike filter* is fitted to the aperture of the photomultiplier tube. This prevents light with frequencies outside a very narrow interval centred on the laser line ($\lambda = 514.5\,\mathrm{nm}$) from reaching the PMT, thereby reducing background noise and improving the quality of the spectrum.

When light falls on a photomultiplier tube each photon creates a cascade of electrons, thereby converting an optical signal (the light transmitted by the interferometer) into an electrical current. The output of the PMT is used in three ways: (*i*) displayed on an oscilloscope to allow the finesse of the interferometer to be assessed visually, (*ii*) passed to the DAS-10 to be monitored in order to stabilise the cavity against misalignment, and (*iii*) fed to a multichannel analyser which enables the spectrum to be accumulated as a data file on the computer. A PMT can be irreparably damaged if exposed to a very high-intensity light source, so great care must be taken – especially during alignment of the interferometer – to ensure that reflections of the laser beam cannot reach the detector.

The multichannel analyser (MCA) is in the form of an expansion card installed on the PC which is used to collect data. It converts the time-varying output of the PMT into a dataset consisting of a fixed number of channels. The input to the MCA is periodic in frequency because of the sawtooth voltage applied to the scanning interferometer by the ramp generator (Sec. 3.2.2.3), so correct choice of the MCA operating parameters results in each channel corresponding to a fixed frequency. Repeated scanning of the Fabry-Perot then allows a given channel to record and accumulate the intensity of light transmitted at its allotted frequency, so that the data collected across all the channels represents the frequency spectrum transmitted by the interferometer.

The most important of these MCA parameters are the dwell time (the time for which each channel is open to collect data in every scan), the number of channels (up to

a maximum of 1,024) and the recycle number (how many times the interferometer is scanned to build up the spectrum over time). Typical choices were a dwell time of 1600 μs, 1,000 active channels and 3,000 recycles. The so-called true time (the amount of time for which the MCA records data) would then be the product of these three values; 4,800 s or 80 minutes in this case. The actual time taken to record this compound spectrum would be slightly longer, due to the finite flyback time taken for the mirrors to return to their starting position at the end of each scan (about a tenth of a second). The Burleigh DAS-10 unit interfaces with the MCA to ensure that data-logging is suspended during flyback, and re-commences at the start of the next scan.

The operation of the MCA is controlled entirely by software provided by Aptec, the manufacturers of the card. One program allows all of the parameters to be set and controls the accumulation of data, while another displays the spectrum during and after collection. Simple analysis routines are available, the most important of which allow peaks in the spectrum to be located for the purposes of frequency calibration as discussed in Sec. 3.3.1 below. The spectrum may be saved and exported in a variety of formats, ready for subsequent analysis using more advanced software.

3.2.2.5 Increasing the contrast: moving to five pass operation

Single-pass operation of the Fabry-Perot interferometer does not give good enough finesse or contrast ratio to be used for Brillouin spectroscopy of liquids and complex fluids. The instrument was upgraded to triple-pass operation as soon as practical, and further improved to five-pass once the necessary expertise in alignment and stabilisation had been established.

The main complication introduced by multi-pass operation is that correct alignment is both more critical and harder to maintain than for single-pass. A small misalignment which has a negligible effect on the finesse in single-pass configuration is magnified in multi-pass, causing unacceptable degradation of the transmitted spectrum. The techniques discussed above remain effective in establishing and stabilising the alignment of a multi-pass interferometer, but each stage is more demanding, time-consuming and sensitive to error. The DAS-10 finds it much more difficult to maintain the finesse in five-pass operation, meaning that even small disturbances can result in corrupted

datasets. Some additional issues regarding the alignment of a multi-pass interferometer are mentioned in Ref. [46], but the above discussion will suffice for the purposes of this thesis.

An example of the improvements which accompany the change from triple-pass to five-pass operation can be seen in the spectra from colloidal suspensions displayed in Fig. 5.11. The increased contrast and finesse allow spectral features which are hidden in three-pass to be clearly resolved by the five-pass interferometer.

3.3 Data analysis

The previous section outlined the design, set-up and operation of the apparatus required to record the raw data of a Rayleigh-Brillouin spectrum. The next stage in the evolution of the Brillouin spectroscopy facility at Edinburgh was to devise a method of calibrating and analysing such a spectrum. In contrast to the practical work discussed in the previous section which was carried out in close collaboration with Hugh Vass, the development of the analysis techniques and computer programs described below was all my own work.

A spectrum recorded by the multichannel analyser as described above is by default stored in a proprietary Aptec data file (with filename extension `.s0`) which is not suitable for subsequent analysis outside of the Aptec software suite. The best alternative was found to be to convert this to a simple 'comma-separated values' (`.csv`) file which can be read by all data-handling software and used without modification as the input to analysis routines written in any programming language. The `.csv` file exported by the Aptec software consists of three columns: channel number, calibration data and intensity. For the purposes of this thesis the calibration data is not required – it is produced by a feature of the Aptec software intended to be of use in nuclear physics and was not found to be useful in the production of Brillouin spectra. This column is therefore ignored in subsequent analysis of the data file – either by deleting it or simply by reading only from the other two columns at the first stage of the routine. The remaining two columns can be plotted to give a graph of intensity vs. channel number, but what we really require is a plot of intensity vs. frequency shift if the spectrum is

to be presented in the most meaningful and accessible way.

3.3.1 Obtaining a frequency spectrum from experimental data

In order to convert MCA channel data to frequency data the results of Sec. 3.1.2 regarding the free spectral range must be recalled. The FSR is the difference in frequency between adjacent orders in the interference pattern transmitted by the Fabry-Perot interferometer. If the height of the ramp voltage is set so that several orders are scanned, then the frequency difference between successive orders will be equal to the free spectral range. Thus the separation in channel numbers between adjacent Rayleigh peaks can be used together with the FSR to calculate the frequency interval corresponding to a single channel, and hence convert the channel number data to frequency shifts, arbitrarily choosing one of the Rayleigh peaks to be the zero-shift origin. This method is perhaps best explained with the aid of a diagram – see Fig. 3.11.

This procedure was implemented in two different ways during the course of my research. The first approach was to write a short program in c to perform the calculation, which requires the channel number of two adjacent Rayleigh peaks to be measured from the spectra. Later on, a more advanced routine was developed using the Origin graphing and analysis package which obviates the need for separate measurement of Rayleigh peak positions, thereby reducing the process to just one step.

The c program was named `jig`, and is run from the command line on a Unix system with the names of input and output data files as arguments. The input must be a three column `.csv` file exported from the Aptec software with no descriptive header text. The program requests values for the position (in channel numbers) of two adjacent Rayleigh peaks and the free spectral range of the interferometer. The latter can be calculated easily from the mirror spacing d using Eq. 3.14 as described above. Rayleigh peak positions can be read from a graph of the raw data file by eye, but a much quicker and more accurate technique is to use the 'Peak Search' tool in the 'Analysis' menu of the Aptec software immediately after data collection. This finds the position of sufficiently intense peaks in the spectrum using an iterative process, and was able to determine accurately the positions of all Rayleigh peaks in every useful spectrum collected during my work. Given the position of two adjacent Rayleigh peaks, `jig`

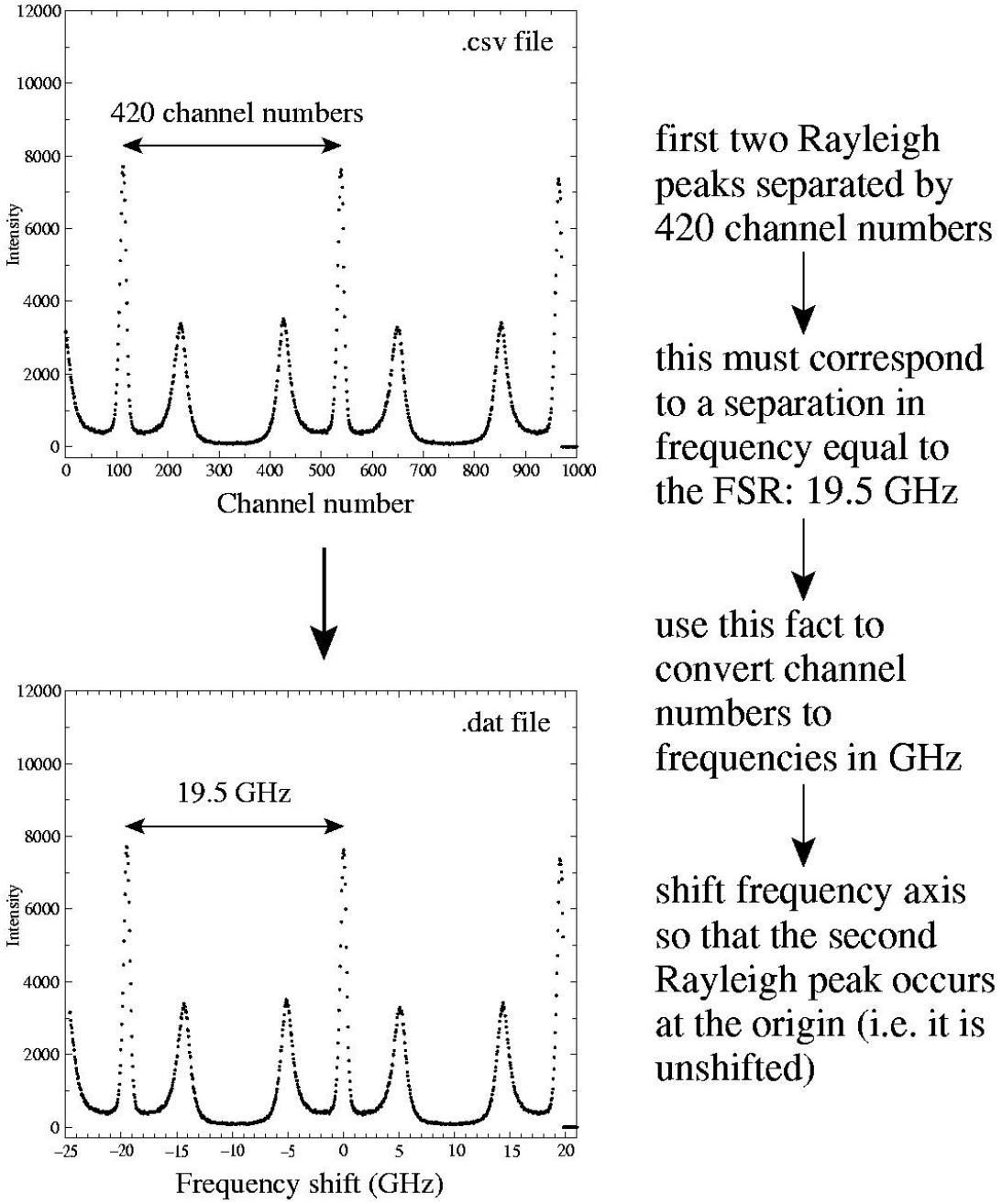

Figure 3.11: Method of converting MCA channel numbers to frequency shifts for a spectrum recorded using a free spectral range of 19.5 GHz.

simply subtracts one from the other and sets the difference in channel number equal to the free spectral range in order to calculate the frequency interval corresponding to one channel number. The user is asked to specify which of the two Rayleigh peaks is to be used as the central unshifted line of the spectrum and its channel number subtracted from all channel data, thus setting the channel number of the chosen peak to zero. The channel numbers are then multiplied by the frequency interval corresponding to one channel to produce a spectrum of intensity vs. frequency (measured in GHz). The two Rayleigh peaks adjacent to the central one will then have frequencies equal to $\pm(\Delta\nu)_{FSR}$ and other spectral features (i.e. the Brillouin peaks) will be at intermediate frequencies. The output file can be named with any extension, but the convention adopted in my research was to use the extension `.dat` for all spectra which have been processed to give a frequency spectrum. The `.dat` file output by `jig` consists of just two columns – frequency and intensity – ideal for subsequent analysis in order to determine Brillouin peak positions and widths (see Sec. 3.3.2 below).

This combination of using Aptec software on Windows to find Rayleigh peak positions followed by a c program on a Unix machine to produce a frequency spectrum from raw data works well, but a much faster and more powerful approach was found to be possible using Origin v6.1 – a commercial graphing and analysis software package for Windows. Its key advantage is that all data handling and analysis routines are able to be invoked and modified using an inbuilt object oriented scripting language called LabTalk. Writing a suitable LabTalk script allowed all analysis to be automated and carried out on the same Windows PC as used for data collection, avoiding the cumbersome transfer of files back and forth between Windows and Unix systems required in order to use the method described above, and speeding up the analysis of a spectrum by at least an order of magnitude.

This script was written with definite aims in mind: (1) to reduce to just one step the task of converting a raw data file to a frequency spectrum; (2) to allow many spectra measured using the same experimental parameters to be processed simultaneously; and (3) to allow future users perhaps not familiar with certain aspects of the procedure described above to produce spectra as quickly and easily as possible.

On running the script (named `brillouin.ogs`, although the user should not need to

know this as it is called from a button on the Origin toolbar – see below) a window appears asking the user to choose data files to be processed. These can be either 3 column `.csv` files exported from Aptec with no header text (the default type) or a two column (channel number, intensity) text file. An unlimited number of files can be selected at this stage for analysis. Clicking 'OK' loads the chosen files into individual automatically named worksheets[¶]. For each dataset a dialogue box appears requesting the free spectral range to be entered and (by means of a drop-down menu) which Rayleigh peak should be used as the unshifted zero frequency line. At this stage the user is also asked to tick a box if any of the Rayleigh peaks are of lower intensity than any of the Brillouin peaks (a graph of intensity vs. channel number is visible). This situation is unusual so by default the box is unchecked. The reason for asking this question will become clear when the method of finding Rayleigh peak positions is discussed below.

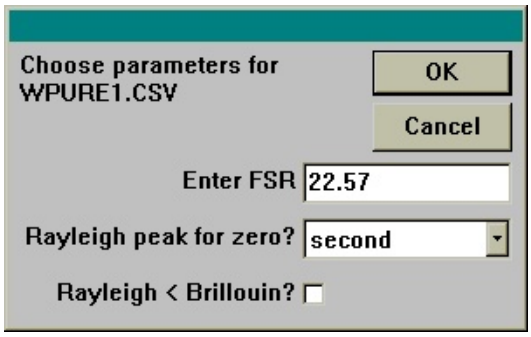

Figure 3.12: Dialogue box generated for each data file to be loaded by the LabTalk script `brillouin.ogs`*, requesting the user to enter information necessary to process the dataset.*

In order to avoid having to first find and note Rayleigh peak positions using the Aptec software, it is necessary to call an Origin peak finding routine from within `brillouin.ogs`. Several are provided with the software; these were all tested and the most suitable was found to be the 'pickPeaks' tool. This method was by far the most successful at finding peaks of low intensity compared to background noise, and did not wrongly identify spurious noise pulses as spectral features. This is mainly because the search parameters can be specified when calling the routine; the best choice for finding Rayleigh peaks was found to be a minimum peak height of 0.01, and a

[¶] *Worksheet* is the name given to the spreadsheet-like system of storing and manipulating datasets in Origin.

search rectangle of width 0.02 and height 0.05[‖]. These parameters are specified by the programmer within the script – the general user is not made aware of them.

Raw data files from Brillouin scattering experiments performed using our equipment usually consist of three orders of the transmitted intensity pattern. In other words there will be three Rayleigh peaks plus several Brillouin peaks present in the spectrum. The script must be able to identify the Rayleigh peaks correctly. This is achieved by simply assuming them to be the three most intense peaks in the spectrum using information provided by the peak fitting routine. The only situation in which this method fails to distinguish the Rayleigh peaks correctly is when they are not the highest peaks in the spectrum – in other words when one or more Brillouin peaks are more intense than one of the Rayleighs. This is very unusual but can occur, notably in the spectrum of water near 4 °C at atmospheric pressure (as can be seen in Fig. 3.13). When this occurs the user must tick the relevant box at the bottom of the dialogue window which appears when each dataset is loaded (Fig. 3.12). The script then no longer assumes the Rayleigh peaks to be the three most intense features. Instead the user is shown a plot of intensity vs. channel number in which all of the peaks found by the routine are labelled with large star symbols. A dialogue box appears which asks for two of these to be specified as Rayleigh peaks. Fig. 3.13 shows this method of picking the Rayleigh peaks in progress.

Once the Rayleigh peak positions have been found (either automatically or by the user) they are passed to a subroutine which performs exactly the same function as the c program `jig` described above. The separation in channel numbers of two adjacent Rayleighs is used to convert the channel number axis to frequency data (in GHz) centred on the peak chosen earlier to be the zero-frequency unshifted line. The spectrum is then displayed as a graph ready for subsequent analysis using Origin's curve fitting routines. Frequency data and peak positions are stored in the worksheet, and a two column (frequency, intensity) `.dat` file can be exported for use with other software by calling a script from a button placed on the worksheet by `brillouin.ogs`.

An added benefit of using this peak finding routine is that all but the weakest Brillouin peaks are usually successfully identified along with the Rayleighs and stored in

[‖] These numbers are expressed as percentages of the total amplitude of data in the range being searched.

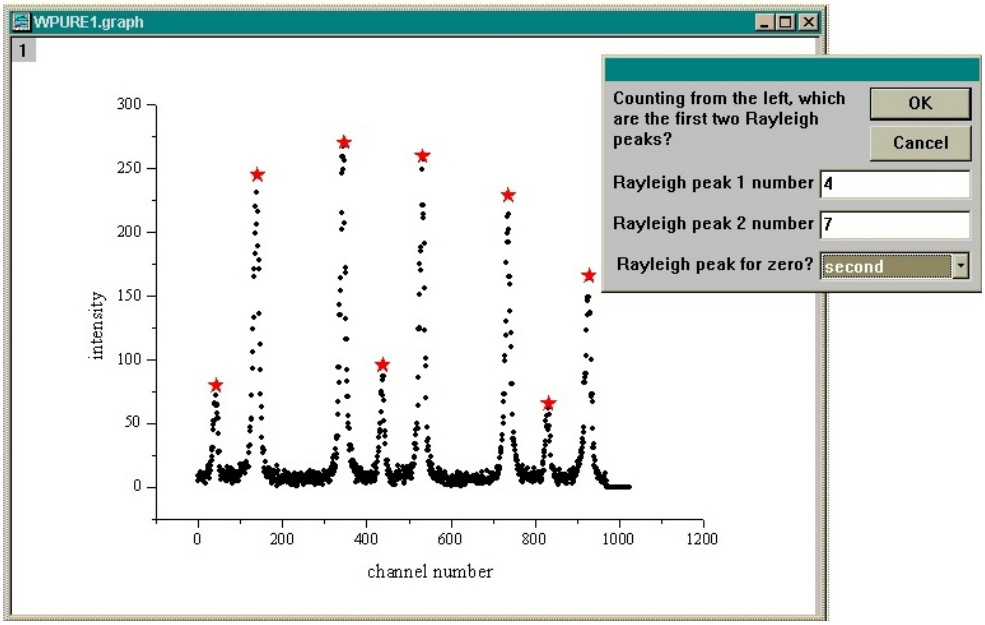

Figure 3.13: Method of identifying Rayleigh peaks manually in `brillouin.ogs` *to be used when one or more Brillouin peaks are more intense than one of the Rayleighs.*

the worksheet containing the spectrum data. A fairly reliable value for the Brillouin frequency shift is therefore obtained with no extra effort, although it is definitely preferable to use a Lorentzian fit to the peak (see Sec. 3.3.2 below) to make the most accurate measurement of ν_B.

For ease of use, `brillouin.ogs` is assigned to a custom button on the Origin toolbar so that simply loading Origin and clicking this button is enough to run the program and produce frequency spectra from `.csv` files. The user therefore does not even need to spend time learning the peculiarities of the Origin software – all that one is required to do is follow on-screen prompts generated by the script.

In summary, writing the LabTalk script `brillouin.ogs` improved the process of producing Brillouin spectra from MCA channel data in several ways: (1) simply clicking one button on the Origin toolbar and entering the free spectral range is enough to convert a `.csv` file into a frequency spectrum; (2) the time taken to process one file is reduced from about 1 minute to less than 5 seconds; (3) an unlimited number of data files can be processed simultaneously; (4) the analysis can be done entirely on the same Windows PC as used to collect the data; and (5) the position of Brillouin peaks is usually found and stored by the routine.

Once a Brillouin spectrum of intensity vs. frequency has been obtained, the next step in a typical analysis is to measure somehow the positions and widths of the Brillouin peaks. Methods of doing this are discussed in the next section.

3.3.2 Measuring Brillouin peak positions and widths

As with the processing of raw `.csv` data files discussed in the previous section, several techniques of measuring Brillouin peak positions and widths were employed during the course of my work, the most advanced and accurate of which again uses the Origin graphing and analysis software, which was only acquired towards the end of the three year research project. The approach I adopted before this was the most straightforward method – using a graphing program to display the spectrum and locating Brillouin peaks manually.

This simple technique was implemented using the `grace` graphing software for Unix. A `.dat` file prepared using either the c program `jig` or the LabTalk script `brillouin.ogs` described above is displayed as a graph of intensity vs. frequency with the unshifted peak in the centre of the screen. Suitable scales for the axes are chosen to display a single order of the spectrum and make the red- and blue-shifted Brillouin peaks large enough to see clearly. A crosshair cursor is then positioned at the maximum of each Brillouin peak and the frequency ν_B at which this occurs noted from an on-screen display of its (x, y) coordinates. The left and right (down- and up-shifted) peak positions can be averaged to reduce uncertainties, which are always less than $\pm 0.15\,\mathrm{GHz}$ and may be reduced to $\pm 0.05\,\mathrm{GHz}$ if the peak is very strong. This method of measuring peak positions yields perfectly acceptable, reproducible results, but has the drawback of being rather time consuming. Measuring peak *widths* using this approach is much less satisfactory (especially for weak Brillouin peaks) due to human error in determining background levels, heights and widths.

To obtain a width at half height (FWHH or HWHH as required) from a graph displayed in `grace` three measurements must be made using the crosshair cursor. These are the background signal level, the peak intensity and the width. The background level is found by assuming the spectrum to be superimposed on a flat background which can be measured with the crosshair cursor using a flat part of the spectrum either between

Brillouin peaks of adjacent orders or between Rayleigh and Brillouin peaks. The latter becomes difficult or even impossible when an intense Mountain peak is present (see Sec. 2.2.3 for a discussion of when this occurs). The maximum intensity of a Brillouin peak is simply read from the graph using the crosshair. The background level and peak height are then used to calculate the half height of the peak, and the crosshair used again to finally obtain the width of the peak at this point. An uncertainty of approximately $\pm 10\%$ (although this can be considerably lower if the peak is very well-defined) and the length of time required to measure one half-width using this method mean that it is definitely not a viable option when many spectra require to be analysed, as was often the case during the course of my research.

An alternative – much preferable – approach to measuring ν_B and $\Delta\nu_B$ is to fit the Brillouin peak numerically using a curve fitting algorithm. The possibility of doing this using `grace` on Unix was investigated, but its limited fitting abilities were not sufficient or robust enough to be relied upon[**]. This was one of the main reasons for acquiring Origin for Windows. Its wide range of fitting routines are much more suitable for the fast and accurate measurement of Brillouin peak widths. A method was quickly developed of finding peak positions and widths by fitting with Lorentzians, which is a big improvement on measuring them by hand as described above.

As discussed in Sec. 2.2.2 the functional form of all the features in a Rayleigh-Brillouin spectrum is a Lorentzian curve. A Lorentzian is fully specified by its position, width and height, so that these parameters obtained from a numerical fit of a Lorentzian to a Brillouin peak should be an excellent way of determining the frequency ν_B and half-width at half height $\Delta\nu_B$. Origin v6.1 has an extremely powerful curve fitting tool which is ideally suited to this task.

An intensity vs. frequency `.dat` file containing a Brillouin spectrum must first be loaded into a graph in Origin before the fitting process can be begun (for this reason, running the LabTalk script `brillouin.ogs` on one or more `.csv` files conveniently loads each spectrum into an individual graph). Firstly, the range over which the data will be fitted must be specified using the 'Data Selector' tool on the toolbar. When fitting an isolated (i.e. not overlapping with either the Rayleigh or another Brillouin) peak it was

[**]The curve fitting tool in `grace` is still under development and as such is not yet fully functional.

found to be best to include as much flat background as possible on either side in order to achieve a good fit. The selected range can be seen in Fig. 3.14 denoted by vertical pairs of arrows at roughly 2 GHz and 10 GHz. Once the range has been set, one simply selects 'Fit Lorentzian' from the 'Analysis' menu and a fit to the peak will be calculated and displayed on the graph of the spectrum, allowing the quality of the fit to be checked by eye. The smooth line through the data points of the right hand Brillouin peak in Fig. 3.14 is a Lorentzian fit produced using this method. A quantitative measure of the goodness of fit is displayed in the 'Results Log' window which can be seen in the figure. The peak position and full width at half height of the fitted Lorentzian are also shown in the Results Log, so for a good fit to the Brillouin peak this method is a fast and straightforward way to measure the frequency shift and half-width. The fit data (i.e. the data points which describe the Lorentzian fit to experimental data) is stored in a hidden worksheet enabling the dataset to be exported for analysis or display using programs other than Origin.

Uncertainties in peak frequencies measured using this method are always less than ± 0.1 GHz, with ± 0.05 GHz being a typical error margin for all but the weakest peaks. The uncertainty in width arising from a Lorentzian fit is normally less than ± 0.15 GHz, but this may increase to ± 0.3 GHz for very low-intensity peaks, as will be discussed when measurements from such spectra are presented in later chapters.

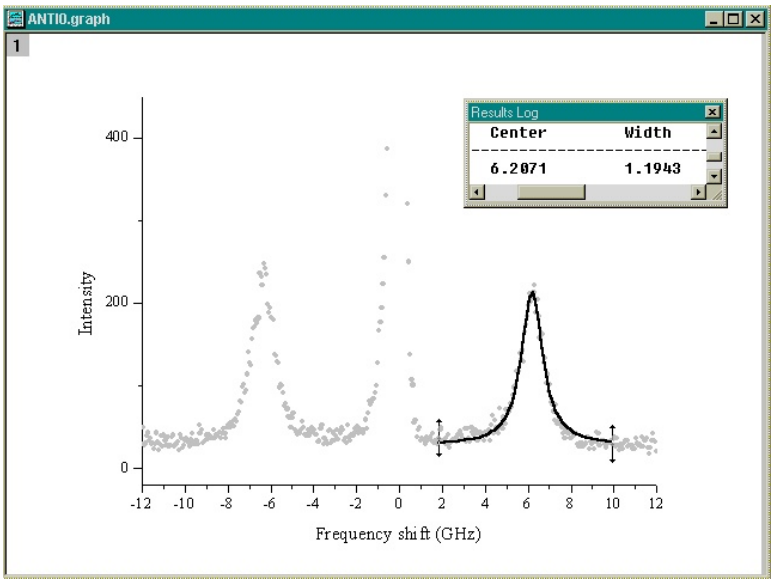

Figure 3.14: Measuring Brillouin peak position and width by fitting a Lorentzian curve to the lineshape using Origin.

Dealing with overlapping orders: multi-peak fitting

Fitting a Lorentzian curve to the Brillouin peak shape becomes difficult when the peak is not isolated from neighbouring spectral features. In this situation an alternative method of fitting to the one discussed above had to be developed. Fortunately, in a Rayleigh-Brillouin spectrum any overlapping features will also have a Lorentzian form, allowing the menu-driven 'fit multiple Lorentzians' feature of Origin v6.1 to be used over a selected data range containing both the Brillouin peak and the peak with which it overlaps.

A multi-peak fit is very simple to implement. As in the single Lorentzian fit described above, the first step is to use the Data Selector to define a range over which peaks are to be fitted. 'Fit Multi-peaks:Lorentzian' is then chosen from the 'Analysis' drop-down menu, opening a dialogue box in the Origin window which asks the user how many peaks are to be fitted. A further dialogue box asks for an initial estimate of the FWHH of the individual peaks – this choice was found to be non-critical with even the roughest estimate producing a rapidly converging fit. The final step in the process asks the user to estimate the position of each peak to be fitted. This is achieved by simply double-clicking as near as possible to the mid-point of the peaks. When the number of peaks specified in the first dialogue box have been chosen, the fit proceeds automatically, displaying the individual fitted Lorentzians and a composite curve which should be a good fit to the experimental data. As before, information such as peak positions, widths and goodness of fit are displayed in the Results Log. An example of a 2-peak fit to overlapping Brillouin peaks belonging to adjacent orders is shown in Fig. 3.15. The smooth curves produced by the fit are again stored in a worksheet and can be exported for use outside Origin.

A multi-peak fit to two overlapping Brillouin peaks is considered to be unsatisfactory if the widths and heights of the two fits produced by the routine differ significantly from each other. The spectrum is then disregarded as unable to be analysed. If Brillouin data for the system and conditions which produced the overlapping spectrum is required, the free spectral range of the Fabry-Perot interferometer must be increased (by reducing the mirror spacing) and the experiment repeated in order to separate the peaks belonging to adjacent orders. The one situation in which such extremely overlapped Brillouin

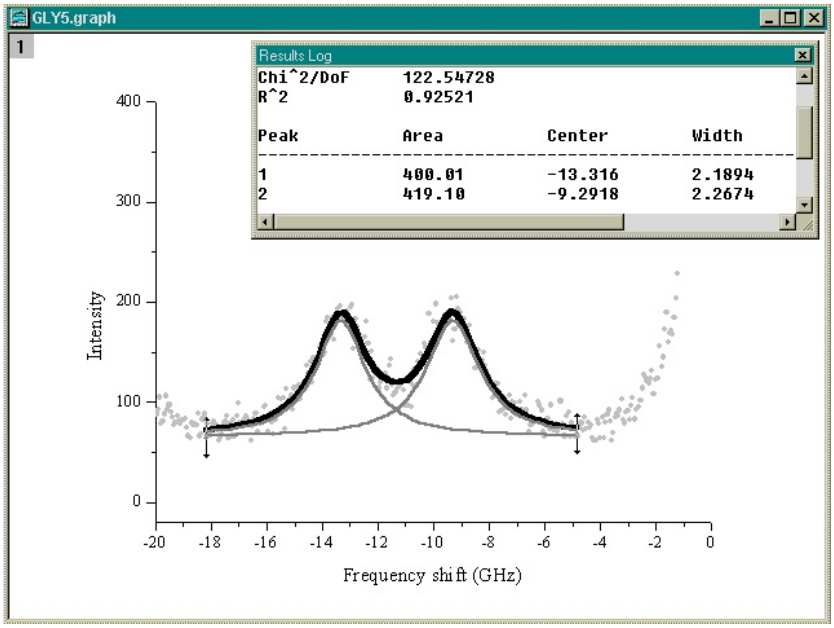

Figure 3.15: Measuring peak positions and widths of overlapping Brillouin peaks using the multi-peak fitting tool in Origin.

peaks may be analysed successfully is when they fall precisely on top of one another[††], in which case the resultant lineshape will be a single Lorentzian which can be fitted in a straightforward manner as described above.

3.3.3 Summary of data analysis techniques

This section has discussed the methods which were developed to deal with two tasks essential to the analysis of any Brillouin spectrum: conversion of raw channel data to a calibrated frequency spectrum, and measurement of Brillouin peak frequencies and widths. In both cases, Unix-based procedures involving a fair amount of manual input were superseded by much more automated routines developed using the Origin software for Windows. Both approaches are capable of producing very accurate results, with the main advantages of the newer methods being greatly increased processing speed and reduced uncertainties in peak frequencies and widths.

One limitation of the methods discussed above is their inability to deal satisfactorily with the measurement of widths when the Brillouin peak is asymmetric, as is the case for colloidal suspensions under certain conditions (see e.g. Fig. 5.7). Fitting a

[††]This will occur if the Brillouin shift ν_B is exactly half the free spectral range.

Lorentzian to such an obviously non-Lorentzian shape is meaningless, rendering this technique useless. Finding the frequency at maximum intensity of such a peak is not problematic using the `grace` method, but the FWHH may no longer be representative of the true width of the peak when asymmetry is present. The only solution to this problem would be to fit the peak with some expression which describes its shape, but this is not always possible due to lack of a suitable theoretical model. In the case of the colloids studied in Chapter 5, for example, no theory exists which predicts the unusual shape of the spectra, so no accurate measurement of peak widths can be achieved.

Chapter 4

Anomalous effects in the low temperature Brillouin spectra of aqueous solutions

Study of the molecular structure and dynamics of water both in the pure liquid state and in solution has been a major focus of experimental, theoretical and computational efforts for many years. Ongoing experimental work on aqueous methanol solutions in the Applied Optics group at the University of Edinburgh using Raman spectroscopy and neutron diffraction is helping to establish a picture of the hydration of amphiphilic solutes – a fundamental problem which underlies many important but poorly understood biological processes. The background, motivation and results of this work will be discussed in Secs. 4.1 and 4.2 below. These techniques provide static structural information on molecular lengthscales, but are not best suited to probing the bulk dynamical properties exhibited by a macroscopic sample of the liquid. This presented an ideal opportunity to apply the newly available (in our lab) technique of Brillouin spectroscopy developed as described in Chapter 3 in order to investigate hypersonic sound propagation (i.e. bulk properties) in these methanol–water mixtures.

Motivation for commencing a program of research using Brillouin spectroscopy to study aqueous alcohol solutions was therefore twofold. Firstly, fundamental physical questions about the molecular and bulk properties of the system – especially in the low

temperature and supercooled régime – remain to be answered, and Brillouin scattering provides potentially very enlightening information complementary to our current Raman and neutron experiments. In addition to this, the relative ease of preparation, handling and obtaining a satisfactory spectrum of these optically transparent binary mixtures suggested that alcohol–water solutions would be an ideal system on which to base the first major investigation using the recently developed Brillouin spectrometer. The temperatures and pressures accessible with the apparatus also cover the range within which any interesting effects might be observed in such mixtures of molecular liquids.

This chapter will detail the results of investigations into the propagation of hypersound in a range of aqueous solutions. The background and motivation for studying these mixtures will be discussed, and the anomalous behaviour of supercooled water introduced, before presenting variable concentration and temperature results from Brillouin spectroscopy at ambient pressure. The most thorough investigations were performed on aqueous solutions of methanol (Sec. 4.2) due to its simplicity and the availability of complementary information from neutron diffraction and Raman spectroscopy. Preliminary results from x-ray diffraction (Sec. 4.2.5) and further neutron studies of aqueous methanol (Sec. 4.2.6) will also be shown. Interesting and novel results from the methanol–water system led to the Brillouin experiments being repeated for aqueous solutions of tertiary butanol (Sec. 4.3), for which neutron scattering data is also available. The anomalous behaviour apparent in methanol and tertiary butanol aqueous solutions was then compared with several other aqueous solutions in order to test the generality of these novel effects (Sec. 4.4). Some findings from high pressure studies of pure water and methanol–water mixtures will be shown (Sec. 4.5), before a summary of results and an attempt to identify some general trends and relate these to the unusual properties of supercooled pure water are given in the concluding section.

4.1 Why study aqueous alcohol solutions using Brillouin spectroscopy?

The physical properties of aqueous solutions are studied intensively by chemists and physicists due to their wide-ranging and fundamental importance, with alcohol–water solutions being of particular interest because of the prototypical amphiphilic properties exhibited by alcohol molecules. An *amphiphile* is a molecule which has a love/hate relationship with water molecules: it contains both *hydrophilic* (water-loving – able to form hydrogen bonds with nearby water molecules) and *hydrophobic* (water-hating – not able to form H-bonds with water) chemical groups. This behaviour is illustrated for the methanol molecule shown in Fig. 4.3 later in this chapter. The properties of aqueous solutions are to a large extent determined by whether the solute is hydrophilic (e.g. sugars) or hydrophobic (e.g. oils), hence it is not surprising that aqueous solutions of amphiphiles display some very interesting effects.

The most dramatic and biologically important of these is the creation of extended macromolecular superstructures, which assemble due to the preference of hydrophobic parts of the solute molecules to arrange themselves in a formation which minimises their contact with water molecules. One example of such a structure is the membrane which forms the walls of cells in biological systems [47]. This is made up of tadpole-shaped (a hydrophilic head attached to a hydrophobic tail) amphiphilic molecules called phospholipids, which form sheets where the headgroups pack together with the tails arranged parallel and adjacent to one another. The 'tails side' of two such layers then mesh together to form a bilayer in which the hydrophobic tails are shielded from water by the hydrophilic heads on the outer sides of the membrane. This structure is therefore held together not by chemical bonds, but by the *hydrophobic interaction*. This is defined to be the net attraction between nonpolar (hydrophobic) groups due to the free energy cost associated with their hydration by water; this attraction is manifested in the tendency of these nonpolar groups to aggregate when in aqueous solution in order to minimise their contact with water [47]. The hydrophobic interaction remains poorly understood, but has recently become a focus of attention due to its importance in determining the shape – and hence biological function – of proteins, which are also amphiphiles. A single protein molecule possesses many different hydrophilic and

hydrophobic groups and therefore in aqueous solution folds itself into a shape which collects the hydrophobic parts together and screens them from contact with water using the hydrophilic parts [48].

An alcohol molecule is amphiphilic because it consists of a polar (hydrophilic) hydroxyl ($-$OH) group bonded to a nonpolar (hydrophobic) alkyl group. The size and branching of the alkyl group determines the degree to which the alcohol is soluble in water [47]. If it is too big, the alcohol will be insoluble due to the inability of the surrounding water to accommodate such a large nonpolar group. This will be discussed further when considering the water-solubility of the methanol molecule in Sec. 4.2 below. The alcohols which *are* soluble in water are therefore very small compared with biologically and industrially important amphiphiles such as the phospholipid molecules discussed above – too small to form macromolecular superstructures. The relative simplicity of an alcohol molecule in solution does however make it much more amenable to study using experiments and computer simulation than these larger systems. Improving our understanding of hydration and hydrophobicity in aqueous alcohol solutions thus becomes an important stage in attempts to describe and model, for example, the folding of proteins in water. Methanol is the smallest and simplest alcohol, hence aqueous methanol solutions are a natural choice of system in which to study these effects at a fundamental level.

Recent experimental work has indeed been focused on developing a molecular-level description of hydration and the hydrophobic interaction in aqueous methanol. Perhaps the most valuable technique in these studies is neutron scattering, the results of which can be used as the input to simulations which provide a wealth of information on the configuration of solvent and solute molecules in the mixture. This technique will be discussed briefly in Sec. 4.2.6. These simulations can be used to produce a three-dimensional image showing the actual positions and orientations of the hundreds of molecules contained in the simulation box; an invaluable insight into what is going on in the solution at this most fundamental level. The results of room-temperature neutron experiments on aqueous methanol performed by members of my research group will be summarised in Sec. 4.2.1 below. Preliminary findings from a subsequent neutron scattering study of the effect of cooling on the configuration of molecules in a 50% methanol–water solution will also be reported in Sec. 4.2.6. This experiment was

motivated by the results of my Brillouin scattering studies, and was performed by a team of which I was a member.

Optical spectroscopy has also made important contributions to the understanding of solvation in aqueous alcohols at the molecular level. The information which these techniques provide is limited in comparison to the findings of a neutron scattering experiment, but important inferences may still be made concerning the surroundings of a typical methanol molecule using, for example, Raman or infrared spectroscopy to look at changes in the vibrational frequencies of the alcohol as a function of concentration. This is typified by the work of Sanhita Dixit at Edinburgh, who used Raman spectroscopy to establish a picture of the progressive hydration of methanol molecules in aqueous solution as the alcohol content is increased [49]. The findings of this study will be summarised in Sec. 4.2.1 below. The advantage of optical spectroscopy over neutron diffraction is that both performing and analysing a neutron experiment on even a single sample at a fixed temperature is *extremely* expensive and time-consuming, whereas the entire concentration range may be surveyed at variable temperature using optical spectroscopies in a few days. They are thus very high throughput techniques which have an important rôle to play in investigating the molecular-level details of solvation and hydrophobicity.

Brillouin spectroscopy is complementary to Raman and neutron experiments in that it probes macroscopic bulk properties rather than the behaviour of single molecules (Raman) or small groups of molecules (neutron scattering). As discussed in Chapter 2, Brillouin spectroscopy provides information on the propagation of hypersound (sound waves with a frequency of $\sim 10^9$ Hz) in liquids. Two properties which are immediately obtainable from a Brillouin spectrum are the hypersonic sound speed v_s and absorption α. The sound speed is proportional to the Brillouin shift ν_B and is determined by the density and adiabatic compressibility, whereas the absorption is proportional to the width of the Brillouin peak $\Delta\nu_B$ and depends on viscosity and thermal conduction according to Eq. 2.38. The technique is therefore a useful method of monitoring trends in the high-frequency dynamics of a liquid mixture as parameters such as concentration, temperature and pressure are varied. Similar studies at lower frequencies (typically $\sim 10^6$ Hz) may be performed by measuring directly the speed and absorption of ultrasound which has propagated through the liquid. This approach has been used to

measure the adiabatic compressibility of several aqueous alcohol solutions as a function of concentration and temperature [50,51,52] from which inferences about the molecular structure of the mixtures were made, although these conclusions require some modification in the light of much more recent Raman, neutron and x-ray experiments (see Sec. 4.2.1 below). This ultrasonic work however, like almost all of the literature on aqueous alcohol solutions, for some reason avoids looking at temperatures below 10 °C. This is rather surprising given the extent to which the addition of a small amount of alcohol depresses the freezing point of the mixture (see e.g. the phase diagram of aqueous methanol in Fig. 4.5) and the degree of interest in the properties of liquid water below 0 °C (see Sec. 4.1.1 below). Perhaps the most likely explanation for this is that our understanding of how and why aqueous solutions behave as they do at room temperature has until recently been rather poor. Complicating the matter by changing the temperature has therefore been avoided, despite the sensitivity of protein folding to temperature and the widespread use of methanol–water solutions as cryogens for the storage of biological matter.

Two pieces of work which did look at the dynamics of alcohol–water solutions at subzero temperatures produced interesting results. Conde, Teixeira and Papon [53] used low concentrations of ethanol in water to suppress freezing in order to further their Brillouin scattering studies of pure supercooled water. Their discussion focuses not on the observed unusual behaviour of the sound speed in ethanol–water solutions but instead on the properties of water; they also limit their investigation to temperatures above -20 °C. These results will be discussed in more detail in Sec. 4.4.3.1. Bermejo *et al* [54] added a small amount of water to methanol in their studies of hypersonic relaxation in the alcohol, and again saw interesting behaviour of the sound speed and absorption, but concentrated instead on the properties of pure liquid methanol.

The interesting results from Raman and neutron studies performed by members of my research group, lack of investigation at low temperatures, and anomalous but seemingly unpursued Brillouin scattering results in the literature all combine to create a strong motivation for a program of research using Brillouin spectroscopy to probe the high-frequency dynamics of aqueous alcohol solutions, particularly at low temperatures. Although this original motivation was aimed at attempting to contribute to the understanding of hydration and hydrophobicity in these systems, the results which were

obtained and will be presented later in this chapter proved to be suggestive of a link with the behaviour of *pure* water at low temperatures. The following section will therefore summarise briefly the unusual and as yet largely unexplained behaviour of supercooled water, highlighting those features which – as will be proposed later (Sec. 4.6) – may be present not only in the pure material but also in certain aqueous solutions, even at fairly high solute concentrations.

4.1.1 Hidden depths: unexplained effects in supercooled water

Perhaps unsurprisingly given its natural abundance and biological importance, water (H_2O) has without doubt been the most widely and intensely studied liquid throughout the history of the sciences. One might therefore expect a comprehensive understanding of its physical properties and behaviour to have emerged by now, but this is far from being the case. Water exhibits many features which are the opposite of the behaviour seen in almost all other liquids, for reasons which are only just beginning to be understood. Several of these oddities turn out to have been instrumental in shaping our world; for example the fact that water has maximum density at 4 °C has been known for at least 300 years to be the reason why ice is less dense than water. For a solid substance to be less dense than its liquid phase is extremely unusual, but if this were not so in water then icebergs would not float, pipes would not burst in winter and ponds would freeze from the bottom up making life rather difficult for freshwater fish. This catalogue of curious behaviour and obvious relevance to everyday life have resulted in the distinction of water being one of the few chemicals to become the subject of a popular science book aimed at the general public, Philip Ball's "H_2O: a biography of water" [48].

One particularly active and hotly debated area of current research focuses on the dynamic and thermodynamic properties of liquid water when cooled to temperatures below its melting point T_m – the metastable so-called *supercooled* region of the phase diagram [55, 56, 57]. Using carefully designed and applied experimental techniques, liquid water has been cooled to lower than -30 °C without freezing, although avoiding crystallisation at such low temperatures requires a great deal of effort, with -20 °C being a more typical lower bound on the temperatures studied in work on bulk macroscopic

samples*. There is in fact an insurpassable limit on how cold liquid water can be without freezing; this is determined by the existence of a line of spontaneous homogeneous nucleation $T_H(P)$ in the phase diagram [57]. At atmospheric pressure $T_H = -38\,^\circ\mathrm{C}$: below this temperature nucleation cannot be avoided using even the cleanest samples and most ingenious methods of preventing crystallisation.

Several of water's anomalous features are particularly striking in the supercooled liquid. Most noteworthy is the apparently singular behaviour of several thermodynamic response functions discovered by Austen Angell and coworkers more than twenty years ago [59,60], the explanation for which is still the subject of heated debate. The isothermal compressibility, constant-pressure heat capacity, coefficient of thermal expansion and other quantities related to the microscopic dynamics (such as viscosity and relaxation times) all increase dramatically as water is cooled below its melting point. These increases were shown to follow power laws as the temperature was reduced towards the limiting temperature T_H, which if continued to lower – experimentally inaccessible – temperatures would diverge at a singular temperature $T_s = -45\,^\circ\mathrm{C}$. This singular behaviour was extremely unexpected and unable to be explained at the time. Spontaneous freezing at T_H renders further experimental investigation of this apparent divergence impossible, while computer models of a molecular liquid like water are still hindered by the lack of a sufficiently accurate intermolecular potential with which to simulate the system. However the fundamental importance of the question has ensured that the question remains the subject of intense study, resulting in the emergence of several competing theories, each of which attempt to explain the diverging response functions first seen by Angell.

Three main hypotheses have been proposed in order to explain this mysterious behaviour of water in the supercooled régime. The phase behaviour predicted by each of these scenarios is illustrated in Fig. 4.1. The so-called "stability limit conjecture" suggested by Speedy [61] assumes that the apparently singular behaviour of thermodynamic response functions results from the existence of a spinodal temperature line $T_s(P)$ which re-enters the $(P-T)$ phase diagram from negative pressure, where it connects to an extension of the liquid-gas spinodal for superheated water. Recent experiments

*Lower temperatures have often been achieved using unusual samples such as microscopic droplets or water confined to nanometre-scale pores or layers – see e.g. Ref. [58].

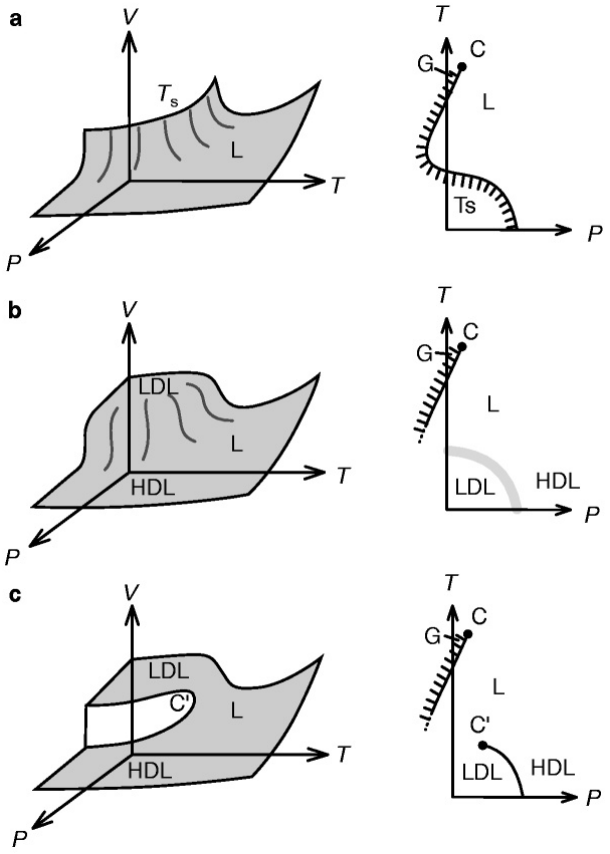

Figure 4.1: Thermodynamic behaviour corresponding to the three competing scenarios described in the text: (a) the stability limit conjecture, (b) the singularity-free hypothesis, and (c) the liquid-liquid phase transition hypothesis. The left-hand diagrams represent the $V(P,T)$ equilibrium equation of state surface; the right-hand diagrams are a projection onto the (P,T) plane. C and C' respectively denote the known and postulated second critical points, and $T_s(P)$ in (a) is the hypothesised re-entrant spinodal line. G and L are the gas and liquid phases which exist below C, with LDL and HDL being the proposed low-density and high-density liquid phases existing below C'. Reproduced from Ref. [57].

seem to indicate that this picture is unlikely to be correct [62].

Another scenario is that, since the data showing singular behaviour exists only above $T_H = -38\,^{\circ}\mathrm{C}$, it is possible that their rapid increase ceases below this temperature; the "singularity-free hypothesis". In this picture, the dramatic increases in thermodynamic properties result from relaxation phenomena of the hydrogen-bonded water network (see Sec. 4.1.1.1 below); there is no requirement for the existence of a singularity below T_H [63]. Evidence for this idea comes mainly from computer simulations [64], and suggests a link to the predictions of the mode-coupling theory of supercooled and glassy dynamics [65].

A glass is a metastable amorphous solid formed when the shear viscosity η_s of a supercooled liquid becomes so large that the molecules are no longer able to move appreciably on the timescale of an experiment; the liquid no longer flows. The shear viscosity of a typical glass-forming liquid varies over more than 15 orders of magnitude, increasing from $\sim 0.1\,\mathrm{Pa.s}$ in the normal liquid above T_m to $\sim 10^{14}\,\mathrm{Pa.s}$ at the calorimetric glass transition T_g. According to the Maxwell theory of viscoelasticity, the shear viscosity can be thought of as a product of a shear modulus G_∞ and a structural relaxation time τ_s; $\eta_s = G_\infty \tau_s$ [66]. Mode-coupling theory (MCT) is the first and most successful microscopic theory which attempts to explain the glass transition, doing so in terms of the trapping of a reference molecule by a cage of its neighbours [67]. The structural relaxation time may then be identified with the time taken by a given particle to diffuse one inter-particle distance [66], hindered by the caging effect which becomes more extreme as the temperature is lowered. The passing of this so-called α relaxation time with cooling through the timescale probed by a given experimental technique has been identified in several glass-forming liquids as the cause of effects very similar to the anomalies seen in the Brillouin spectra of aqueous alcohol solutions presented in this thesis. The implications of this similarity will be discussed in Secs. 4.4.3.2 and 4.6 later in this chapter.

Water does indeed form a glass at $T_g = 136\,\mathrm{K}$, well below the homogeneous nucleation temperature T_H [57]. Advocates of the singularity-free hypothesis (see Ref. [64] and references therein) suggest, based on successful MCT analyses of light scattering [68] and neutron scattering [69] experiments and computer simulations [65], that the apparently singular behaviour of the thermodynamic response functions which appear to diverge at $T_s = -45\,^\circ\mathrm{C}$ are nothing other than precursors of the glass transition which are predicted by MCT and observed in a wide range of glass-forming liquids. T_s is then identified with a crossover temperature between two distinct dynamical régimes, again predicted by MCT and experimentally verified in other liquids [64].

A third proposed explanation for the anomalous properties of supercooled water is that the singular behaviour results from the presence of a metastable second critical point (in addition to the familiar liquid–gas critical point at $T_c = 647\,\mathrm{K}$ and $P_c = 0.22\,\mathrm{kbar}$) which terminates a phase boundary between two liquids with different densities at a critical temperature $T_c' \approx -50\,^\circ\mathrm{C}$ and pressure $P_c' \approx 1\,\mathrm{kbar}$ in the 'forbidden' region

of the phase diagram made inaccessible by the homogeneous nucleation curve $T_H(P)$. This rather unlikely-sounding phenomenon was first discovered in computer simulations performed by Poole *et al* [70], in which at temperatures below the new critical point the liquid was found to separate into two distinct liquid phases – a low-density liquid (LDL) at low pressures and a high-density liquid (HDL) at high pressure [71]. Water near this hypothetical second critical point would therefore be a fluctuating mixture of patches of molecules whose local structure is close to that of either LDL or HDL, resulting in anomalous behaviour. In recent years, this hypothesis has been actively pursued and promoted by the group led by Prof. H. Eugene Stanley of Boston University (see e.g. [57]). Several pieces of experimental and theoretical support for this scenario have been accumulated over the last few years, and can be divided into three categories: plausible theories of first-order liquid-liquid phase transitions in general[†] [73,74], evidence for the existence of the two forms (LDL and HDL) of liquid water which does not necessarily imply the existence of a critical point [75,76,77,58], and evidence for the existence of the second critical point itself (listed in a recent review article by Stanley [71]).

There is currently no general agreement on which, if any, of these three scenarios is most likely to be correct. The two main candidates are the singularity-free (glassy dynamics) picture and the liquid–liquid phase transition hypothesis, the key difference between these being the prediction of a second critical point by the latter. Efforts to ascertain whether either of these ideas describes the behaviour of real water are therefore focused on proving or disproving the existence of this critical point, a task made extremely difficult by its proposed location in an inaccessible region of the phase diagram.

Despite the fundamental differences between these theories, they both agree that the underlying origin of the anomalous properties of water – both in the metastable supercooled régime and in the more familiar stable part of the phase diagram above T_m – is the existence and behaviour of the hydrogen-bonded network formed by water molecules in the liquid. The following section aims to provide a very brief description of this network formation in pure water, before moving on to look at hydrogen bonding and hydrophobicity in methanol–water mixtures.

[†]This is a novel idea – very few examples of such a transition in a pure material have been observed to date (see e.g. Ref. [72]).

4.1.1.1 The hydrogen-bonded network in liquid water

The network structure of liquid water occurs due to the ability of each water molecule to form hydrogen bonds with four of its neighbours. The presence of these hydrogen bonds accounts for the extremely high (in comparison to most other molecular liquids) melting and boiling points of water. They form because the hydrogen atoms are partially positively charged due to the large electronegativity of the oxygen atom, which also results in the placing of two lone pairs of electrons at two corners of the tetrahedron shown in Fig. 4.2. The familiar 'bent' shape formed by the atoms in the water molecule is therefore a manifestation of this approximately tetrahedral arrangement. Hydrogen bonds between water molecules form due to the electrostatic attraction between a positively charged hydrogen atom and a lone pair of electrons, hence a hydrogen atom in one molecule points towards the oxygen atom of another. The tetrahedral symmetry of the molecule therefore results in a tetrahedral network; each molecule can form four hydrogen bonds. An attractive visualisation of this network formation (Fig. 4.2) is given by Ball in his "biography" of water [48]. If one imagines a water molecule to be a person with hands representing hydrogen atoms and feet representing lone pairs of electrons, then the hydrogen bond can be thought of as a preference for one person's hands to hold onto someone else's ankles. As shown in Fig. 4.2, this results in a tetrahedral arrangement of neighbours around each molecule.

It must be stressed that this hydrogen-bonded network is not permanent; after all, water is a liquid which implies that its molecules are free to move around. The tetrahedral structure of liquid water is an *average* arrangement. In the liquid state molecules have sufficient thermal energy to break a hydrogen bond – they can then diffuse for some distance before forming a new bond with another molecule. Alternatively one can think of the tetrahedral network as being a snapshot of the positions of the molecules at one instant in time. Despite the transient nature of the network (a given configuration persists only for a few picoseconds [78]), the self-attraction of water molecules results in a fluid which is very cohesive and structured compared to non-hydrogen-bonded liquids. All of the anomalous properties of water can be traced back to this fact.

Surprisingly, Brillouin scattering data which will be presented later in this Chapter exhibits behaviour reminiscent of the anomalous, apparently singular, properties of su-

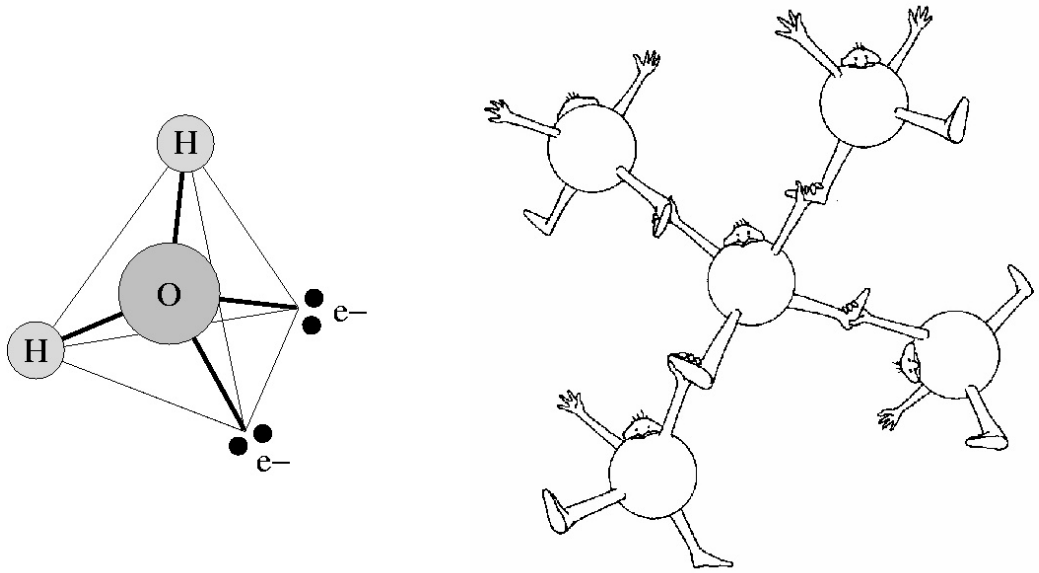

Figure 4.2: Tetrahedral configuration of the water molecule, resulting in a hydrogen-bonded liquid network in which each molecule bonds to four neighbours. In this cartoon (reproduced from Ref. [48]) each water molecule is represented as having hands for hydrogen atoms and feet for lone pairs of electrons. The hydrogen bond then results in a tetrahedral network due to the preference of hands (positively charged) to grab onto a foot (negatively charged) from a neighbouring molecule.

percooled water as discussed above; not in pure water but in aqueous solutions. This represents a possible link between the properties of pure water and of water when mixed with other liquids. The origin of such a similarity may be related to the microscopic molecular details of these solutions determined by hydrogen-bonding interactions between water molecules and solute molecules as discussed in general above (Sec. 4.1) and for the specific case of methanol in the following section. It will be proposed in Sec. 4.6 that the water-like effects seen at low temperatures in these aqueous solutions are due to the presence of a relatively unperturbed H-bonded water network described above – in other words the solutions are not homogeneously mixed on small enough length-scales, resulting in a patchwork of interconnected water-rich and solute-rich regions. This is a suggestion which sounds unlikely but is supported by results from the recent Raman spectroscopy, x-ray diffraction and neutron scattering experiments discussed in Sec. 4.2.1 below. Preliminary results from even more recent neutron scattering experiments performed as part of my research (see Sec. 4.2.6) also strongly indicate the presence of an extended tetrahedral water network in methanol–water solutions con-

taining as much as 50% methanol by mass.

4.2 Methanol–water mixtures

The methanol molecule (CH_3OH, MeOH) consists of a hydrophilic polar hydroxyl (OH) group connected directly to a hydrophobic nonpolar methyl (CH_3) group. The hydroxyl group is capable of forming three hydrogen bonds with water molecules (accepting two and donating one as shown in Fig. 4.3), while the nonpolar methyl group does not form any. Methanol is therefore a prototypical amphiphile, although its small size prevents it from forming the extended self-assembled structures adopted by larger amphiphilic molecules such as the phospholipids or proteins discussed briefly in Sec. 4.1. Methanol is the simplest alcohol and is soluble in water at all concentrations and all practical temperatures and pressures [79]. The next smallest alcohol is ethanol (C_2H_5OH) which is also fully soluble in water, but as the size of the alkyl residue increases further in the higher alcohols it becomes more difficult for this nonpolar group to be accommodated by the surrounding water, resulting in them being insoluble under most conditions. The largest alcohol to be fully miscible with water at all concentrations is tertiary butanol [80], aqueous solutions of which will be studied in Sec. 4.3 below.

Before presenting the results of Brillouin scattering studies on methanol–water solutions at low temperatures, the next section will summarise some very recent experimental results on the system in order to put my work into the wider context of current research. Some of these findings have yet to be published, thus the following discussion is the first attempt to present a an up-to-date synthesis of the new insights gained from these most recent results.

4.2.1 Current opinions on hydration and hydrophobicity in methanol–water solutions

We have seen that an understanding of the solvation of methanol molecules in water is an important starting point in uncovering the molecular details of hydration in much larger and more complex systems such as self-assembling macromolecules and proteins,

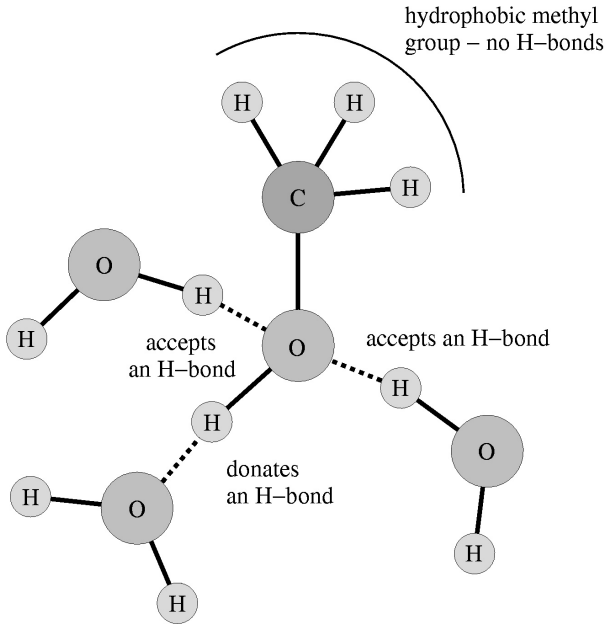

Figure 4.3: Hydrogen bonds formed by a methanol molecule in aqueous solution.

which are of great scientific and technological importance. For this reason, methanol–water solutions were studied using Raman spectroscopy and later neutron diffraction by my fellow PhD student at Edinburgh, Sanhita Dixit [81]. Measurements of the Raman band corresponding to the $C-O$ stretch frequency ν_{CO} showed a strong non-linear dependence on concentration at room temperature and atmospheric pressure [49] which was used to deduce a picture of the hydration of methanol in the solution as the mole fraction (a measure of concentration defined on p.111) x_m increases from 0 to 1[‡]. Three régimes of hydration were identified: (1) below $x_m \approx 0.25$ the methanol hydroxyl groups are completely surrounded by water, and the nonpolar methyl groups are progressively hydrated as a function of increasing water content – by $x_m \approx 0.05$ they are completely hydrated; (2) in the intermediate range $0.25 \lesssim x_m \lesssim 0.70$ the hydrogen-bonded chains of methanol molecules which exist in the pure alcohol are broken due to individual molecules being hydrated; and (3) at high methanol concentrations $0.70 \lesssim x_m \lesssim 1$ this chain structure remains intact despite the presence of water molecules, which only hydrate the ends of the chains.

This demarcation of three distinct régimes of hydration is remarkably similar to the findings of a contemporary study using x-ray diffraction and mass spectrometry to study

[‡]See Table 4.1 and the accompanying discussion of the relationship between mole fraction, mass fraction and volume fraction representations of sample composition.

clustering and structure in aqueous methanol solutions as a function of concentration at room temperature [82]. Mass spectra show that the average hydration number of methanol decreases with increasing methanol concentration with inflection points at $x_m \approx 0.3$ and $x_m \approx 0.7$, while radial distribution functions (RDFs) derived from x-ray diffraction show a similar trend in the number of hydrogen bonds per water oxygen atom. Analysis of these results led to the conclusion that these inflection points mark transitions between different types of hydration in the solutions. For $x_m < 0.3$ the tetrahedral water structure is not disturbed, for $0.3 < x_m < 0.7$ chain clusters of methanol molecules gradually evolve without significantly changing the structure of the water, and at $x_m > 0.7$ chain clusters of methanol are predominant – little of the hydrogen-bonded structure remains in the water which is still present. This picture is entirely consistent with the scenario derived from Raman results, discussed above. This work is currently being extended to look at the effect of cooling on the RDF. I was involved in these new experiments, preliminary results of which will be presented in Sec. 4.2.5 below. A third study (again published within months of the Raman and x-ray work) also found similar behaviour in the methanol–water system at room temperature using a dielectric relaxation technique [83].

These findings from Raman spectroscopy motivated the study of two extreme concentrations ($x_m = 0.05$ and $x_m = 0.70$) using neutron scattering (see Sec. 4.2.6 below for a brief introduction to the technique), which as stated in Sec 4.1 enables direct visual representation of the configurations of solute and solvent molecules in the solution, as well as more quantitative measurements of their separations and orientations. A short summary will now be provided here, but the interested reader should refer to Sanhita Dixit's PhD thesis, a Nature letter discussing the $x_m = 0.70$ results [84] or her forthcoming publications for a full discussion [81].

The first detailed neutron diffraction study of the hydration of methanol in aqueous solution was published in 1993 by Soper and Finney [85] who found that, contrary to the conclusions of earlier work, methanol molecules in an $x_m = 0.10$ at 20 °C do not modify significantly the orientational order of the water molecules. They are incorporated into the hydrogen-bonded water network (see Sec. 4.1.1.1 above) by the formation of a loose cage or shell of water molecules, in a manner which allows the roughly tetrahedral structure of pure water to be maintained.

The experiments performed by Sanhita were in collaboration with Soper and Finney, and extended their work to look at a much more concentrated solution ($x_m = 0.70$) and a more dilute one ($x_m = 0.05$). They found that, again contrary to the accepted view, water molecules in the $x_m = 0.70$ solution cluster together and attach strongly to the hydroxyl group of the methanol molecules. Previously it had been thought that the water structure was completely destroyed by such a high alcohol content, resulting in single water molecules being dispersed randomly. This clustering is allowed due to the amphiphilic nature of methanol and the tendency of water molecules to bond to one another: clusters of water hydrogen-bond to the hydroxyl groups in order to keep away from the hydrophobic methyl groups, which bunch together in order to minimise their contact with water. In the dilute $x_m = 0.05$ solution, methanol molecules still tend to associate, with 80% of them existing in clusters of 3 to 8 molecules. This association is mediated not by hydrogen-bonding (as is the case in pure methanol) but by the hydrophobic interaction. The water structure in the $x_m = 0.05$ solution *is* affected by the presence of methanol; the tetrahedral configuration of the pure water is preserved, but the second coordination shell of water molecules in the mixture closes in more tightly around a reference molecule. Interestingly, a very similar effect was seen in neutron diffraction experiments on pure water at high pressure [77].

Neutron diffraction, Raman spectroscopy and x-ray diffraction have therefore led to a fairly complete description of the hydration of methanol by water molecules at room temperature, resulting in a particularly detailed knowledge of the behaviour in extremely dilute ($x_m = 0.05$) and concentrated ($x_m = 0.70$) solutions. These techniques do not however provide information on bulk properties of the mixtures. How do the details of molecular segregation, the existence of hydration shells and the effect of alcohol molecules on the hydrogen-bonded water network determine the macroscopic behaviour of the liquids? Brillouin spectroscopy is one technique which has the potential to answer these questions.

4.2.1.1 Raman spectroscopy: evidence for inhomogeneous mixing

Another intriguing feature of the Raman spectra observed for certain concentrations of these methanol–water mixtures – which to our knowledge had never been seen pre-

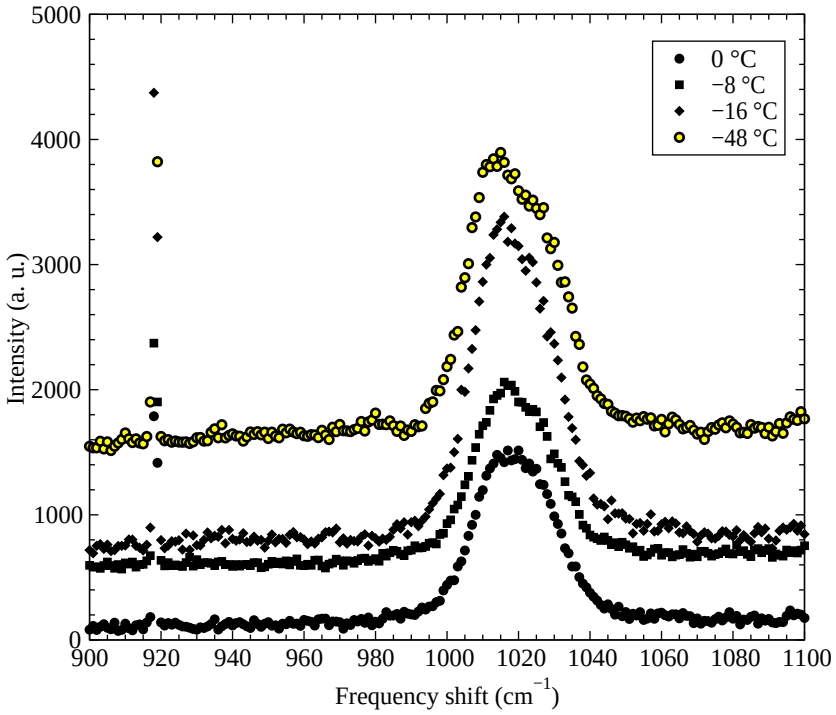

Figure 4.4: Raman spectra of $x_m = 0.27$ (40% by mass) methanol–water solution, showing splitting of the totally symmetric $C-O$ stretch mode upon cooling. The narrow peak at 916 cm^{-1} is a neon emission line of known frequency, introduced for the purposes of calibration.

viously – was a splitting of the $C-O$ mode upon cooling below room temperature. The $C-O$ stretch is a totally symmetric mode, hence the only possible explanation for splitting of the peak into a doublet is that methanol molecules in the solution exist in two distinct environments. In other words, the methanol and water molecules are not homogeneously mixed in the solution on the molecular lengthscales probed by Raman spectroscopy, despite the fact that the two substances are completely miscible across the entire concentration range [79]. Fig. 4.4 shows the evolution on cooling of the lineshape of the Raman band corresponding to the $C-O$ stretch in a 40% by mass ($x_m = 0.27$, roughly 50/50 by volume at room temperature) mixture of methanol and water. These particular spectra were measured by Sanhita Dixit in our laboratory using a triple grating Coderg T-800 spectrometer. One can see that at 0 °C the band is a broad single peak, but upon cooling two separate components emerge. In the spectrum at −48 °C the two peaks can be easily distinguished; the less intense peak appears as a prominent shoulder on the right hand side of the stronger one. This splitting was seen at similar temperatures and for several methanol concentrations with $0.15 < x_m < 0.60$. These findings remain unpublished, but were reported in the MPhys thesis of Neal Cramp-

ton [86], an undergraduate student who worked with me, repeating and extending these methanol–water measurements to cover a wider range of temperatures and concentrations. He also studied the effect in aqueous solutions of tertiary butanol, results from which will be discussed briefly in Sec. 4.3.

The implication that the molecules are not homogeneously mixed was – at the time of these experiments (1999) – extremely surprising, but this conclusion has since been corroborated by the results of the neutron diffraction experiments [84] discussed above and in Sec. 4.2.6 below, as well as the recent x-ray diffraction [82] and dielectric relaxation [83] experiments discussed in the preceding paragraphs.

Raman spectroscopy probes the average behaviour and environment of a single molecule, hence the complementary information on bulk properties (such as hypersonic sound velocity and absorption) obtainable from Brillouin spectroscopy was thought likely to provide further insight into the complex and incompletely understood solvation phenomena in aqueous methanol described above. For this reason, a preliminary experiment measuring Brillouin scattering from an arbitrarily chosen 40% methanol by volume ($x_m = 0.27$) aqueous solution at variable temperature was undertaken, which produced sufficiently novel and interesting results to prompt further study of a range of compositions.

The results of this work will be presented and discussed below, but first let us look briefly at some of the background to these experiments; the methanol–water temperature-concentration phase diagram, the relationship between mole fraction (defined on p.111) and volume percent measures of composition in aqueous methanol, and details of the method of sample preparation.

4.2.2 Background information: phase diagrams and sample preparation

A survey of the literature revealed two independent measurements of the phase diagram of aqueous methanol at atmospheric pressure. The most recent of these is from a program of work by Murthy [87] in which the phase diagrams of several alcohol–water systems were measured using both Differential Scanning Calorimetry (DSC) and

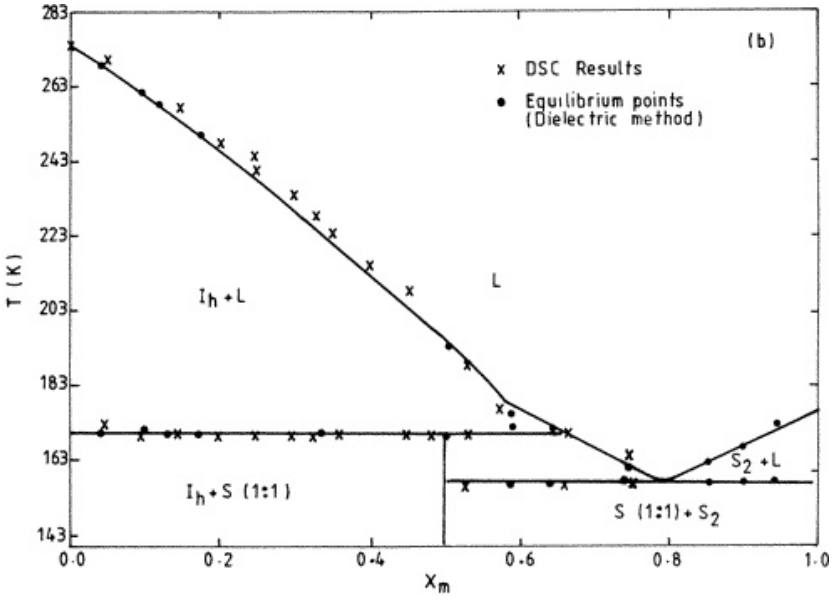

Figure 4.5: Phase diagram of methanol–water mixtures reproduced from the paper by Murthy [87]. Note that his measurements were made by heating the sample from the lowest-temperature solid phase, in contrast to my experiments which cooled from room temperature. Identification of the various phases is discussed in the text.

dielectric spectroscopy (the phase diagram for aqueous tertiary butanol reproduced later in this chapter [Fig. 4.17] is also from this paper). A reproduction of Murthy's MeOH–water phase diagram is shown in Fig. 4.5. His measurements were performed by cooling samples to form the lowest-temperature solid phase, then warming in order to locate the various melting transitions which exist at different concentrations. My Brillouin scattering experiments were however performed by cooling, the observed freezing points being lower than the melting points shown in the phase diagram by as much as 50 K. All melting transitions observed during my work on aqueous methanol solutions agreed with Murthy's phase diagram to better than ±0.5 °C. The various solid phases below the liquid region L correspond to different combinations of hexagonal ice (I_h) and solid methanol (S_2). X-ray diffraction experiments (see Sec. 4.2.5) confirmed that the methanol–water solutions were in the liquid state at all temperatures for which the Brillouin spectra presented below were collected.

Another measurement of the low temperature phase diagram of aqueous methanol was performed by a Japanese group [88], again using DSC. Their determination of melting points is almost identical to the diagram shown in Fig. 4.5, but in addition to heating they also performed some measurements on cooled solutions in order to obtain several

metastable hydrates in addition to the equilibrium phases investigated by Murthy.

A large proportion of the work which has been done on the properties of aqueous solutions has been by chemists, and as such there are some terms in the literature which may be unfamiliar to the physicist. The most important of these, and the only one which merits discussion here, is the *mole fraction*, used to measure the composition of multi-component systems. We have already met this quantity when discussing results from neutron scattering above, and Murthy's phase diagram (Fig. 4.5) also uses it.

The mole fraction x is the number ratio of particles present in a mixture. The mole fraction x_a of compound a in a binary solution with another substance b is thus simply $N_a/(N_a + N_b)$ where the N's are the number of moles of each. The dilute $x_m = 0.05$ aqueous solution of methanol discussed above therefore has 19 water molecules for every one methanol molecule present. From the physicist's point of view, the mole fraction is perhaps less physically intuitive than the volume fraction ϕ or mass fraction. Volume fraction is not a useful measure for the solutions studied here due to its dependence on density and therefore temperature. Their change in density with temperature is not known, hence volume fractions cannot be calculated other than at 20 °C, at which temperature density values are available in the literature. Mole fraction and percentage by mass depend only on the relative numbers of particles present, and are thus independent of temperature and pressure. Lookup tables for converting between these quantities will be provided for each composition of the different mixtures discussed in the following sections.

4.2.2.1 Sample preparation

Spectrophotometric grade methanol with a purity of at least 99% was purchased in 500 ml bottles from Sigma. No further purification was deemed necessary, but the possibility of contamination by dust particles (flashes of intense elastic scattering from which seriously impair the quality of Brillouin spectra) was minimised by pouring directly from freshly opened supplies and filtering the samples before and after mixing (see below). HPLC grade (maximum residue on evaporation 0.0003%) water from Sigma was used as it was consistently found to be of higher purity than water distilled, de-ionised and filtered using the apparatus in our preparation laboratory.

Samples were prepared by weight using a precision electronic balance, accurate to ±0.0005 g. Sample cells were flushed with acetone and dried in an oven at 50 °C before being filled with the desired weights of methanol and water using separate syringes fitted with 0.22 um Millipore filters. These filters have to be pre-wetted with alcohol before they will allow water to pass, hence the first few millilitres of each component were disposed of as per the manufacturer's instructions in order to avoid contamination of the water in the sample. Sample bottles were kept tightly closed and sealed by wrapping PTFE tape around the area between cap and glass. In order to minimise evaporation, all samples were stored in a freezer at approximately -10 °C. Even with these precautions in place, solutions were disposed of after two weeks in case significant changes in the concentration had somehow occurred. Uncertainties in the composition of the samples studied in the following sections are therefore negligible; weighing a selection of them every few days showed no appreciable change in their mass over the two week period.

This reliable and straightforward method of sample preparation was used for all of the samples in the Brillouin scattering experiments reported in this chapter. Any additional requirements or changes in the method necessitated by the properties of the solute (e.g. the high freezing point of tertiary butanol – see Sec. 4.3) will be discussed at the start of the section in which the results from that system are presented.

The results of Brillouin scattering from several concentrations of methanol–water mixtures will be shown and discussed in the following pages. The concentration of a sample will often be given as both mole fraction and percentage mass of solute, but in order to allow easy reference to the densities, refractive indices etc. published in the CRC Handbook of Physics and Chemistry [89], and to facilitate the conversion between the two measures of composition, Table 4.1, a lookup table, is provided. These calculations were performed using the molecular weights of methanol and water to convert from molar to mass fractions. The corresponding percentage methanol by volume at 20 °C is also given in Table 4.1.

Methanol mole fraction x_m	0	0.05	0.15	0.20	0.27	0.30	0.40	0.70	1
Methanol mass %	0	9	23	31	40	43	54	81	100
MeOH volume % at 20 °C	0	11	28	36	46	49	60	84	100

Table 4.1: Lookup table relating methanol mole fraction to volume percent and mass percent for methanol–water compositions studied in this section.

4.2.3 Preliminary measurements: 40% by mass aqueous methanol

The sample was prepared as described in Sec. 4.2.2.1 above. Brillouin spectra were recorded with the Fabry-Perot interferometer in the five-pass configuration with a free spectral range of 22.37 GHz, using the nitrogen-cooled temperature cell described in Sec. 3.3.2 to cool from room temperature. The scattering angle was set at $90 \pm 0.5°$. No values for the refractive index of the solution as a function of temperature could be found in the literature, so the magnitude q of the scattering vector could not be calculated other than at 20 °C, for which temperature a table of concentrative properties[§] of aqueous solutions is available in the CRC Handbook of Chemistry and Physics [89]. The value given for a 40% by mass aqueous methanol solution is $n = 1.3428$, which gives $q = 0.0232 \pm 0.0001\,\mathrm{nm}^{-1}$ at 20 °C, calculated using Eq. 2.3. The value of q is likely to remain within a few percent of this over the entire range of temperatures studied, due to the usually extremely weak dependence on temperature of the refractive index.

The evolution of the methanol–water spectrum as the temperature is reduced can be seen in Fig. 4.6. Several trends are immediately apparent:

1. below -20 °C, the Brillouin peak frequency ν_B begins to increase very rapidly with cooling and reaches the extremely high value (for a liquid) of 10 GHz by the lowest temperatures measured;

2. the width of the Brillouin peak $\Delta\nu_B$ increases dramatically starting at -20 °C and appears to reach a maximum around -40 °C before sharpening again upon further cooling;

[§]Molarity, density, refractive index, freezing point depression and viscosity are all listed for a wide range of methanol–water concentrations.

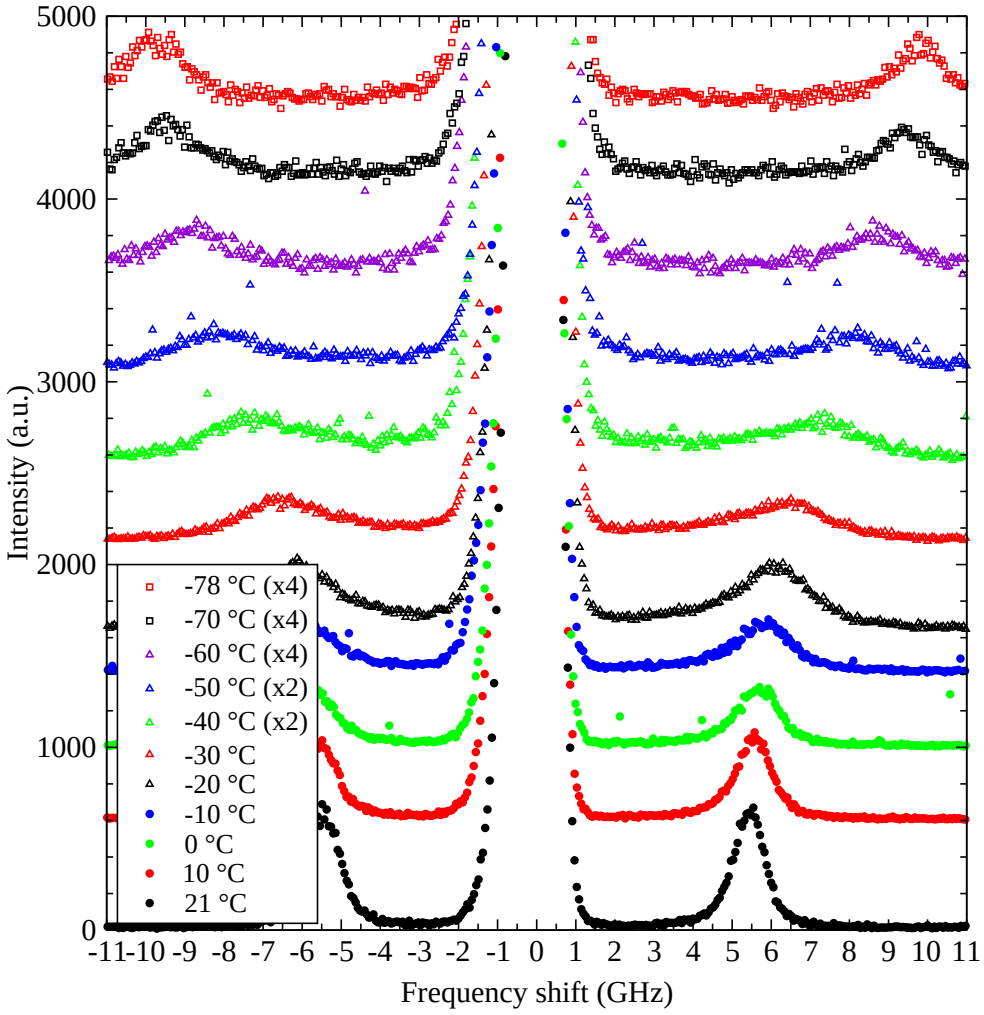

Figure 4.6: Brillouin spectra of a 40% methanol by mass ($x_m = 0.27$) methanol–water mixture upon cooling from room temperature. The noise pulses visible in some of these datasets are due to electrical interference caused by power tools being operated in an adjacent lab.

3. the intensity of the Brillouin peak decreases markedly as the temperature is lowered;

4. a weak second central mode (the Mountain peak discussed in Sec. 2.2.3) indicative of structural or thermal relaxation on timescales comparable to the inverse of its width (i.e. $\sim 10^{-9}$ s) is just visible in the spectra between -30 °C and -60 °C.

In order to explore quantitatively the effect of cooling on the Brillouin peak frequency and width, the Lorentzian curve-fitting methods described in Sec. 3.3.2 were used to measure these variables from the spectra shown in Fig. 4.6. The Brillouin shift and peak widths for this $x_m = 0.27$ (40% methanol by mass) solution are plotted in Figs. 4.7 and 4.8 respectively. The trends noted above are even more clearly displayed. Fig. 4.7 shows the large increase in ν_B which occurs on cooling, with a change of slope to a more rapid increase between -20 °C and -30 °C. The maximum in peak width $\Delta\nu_B$ is shown in Fig. 4.8 and can now be seen to be quite sharp, centred at around -45 °C.

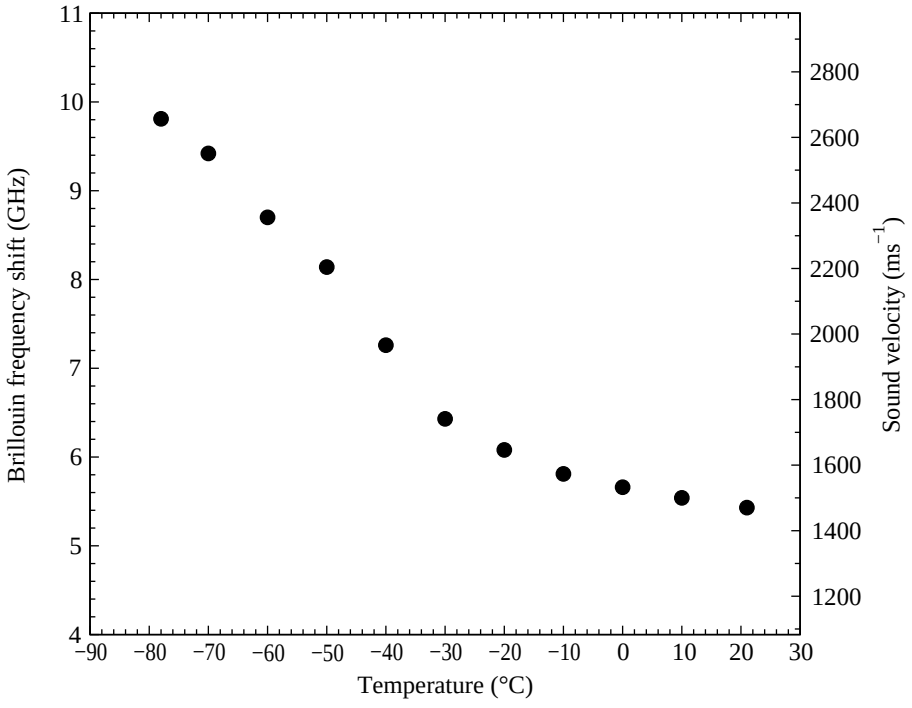

Figure 4.7: Brillouin peak shifts and corresponding approximate sound velocities (see text) in a cooled $x_m = 0.27$ methanol–water mixture.

Sound velocities v_s were calculated from the peak frequencies ν_B according to the equation $v_s = 2\pi\nu_B/q$ using the scattering vector ($q = 0.0232\,\mathrm{nm}^{-1}$) derived from a

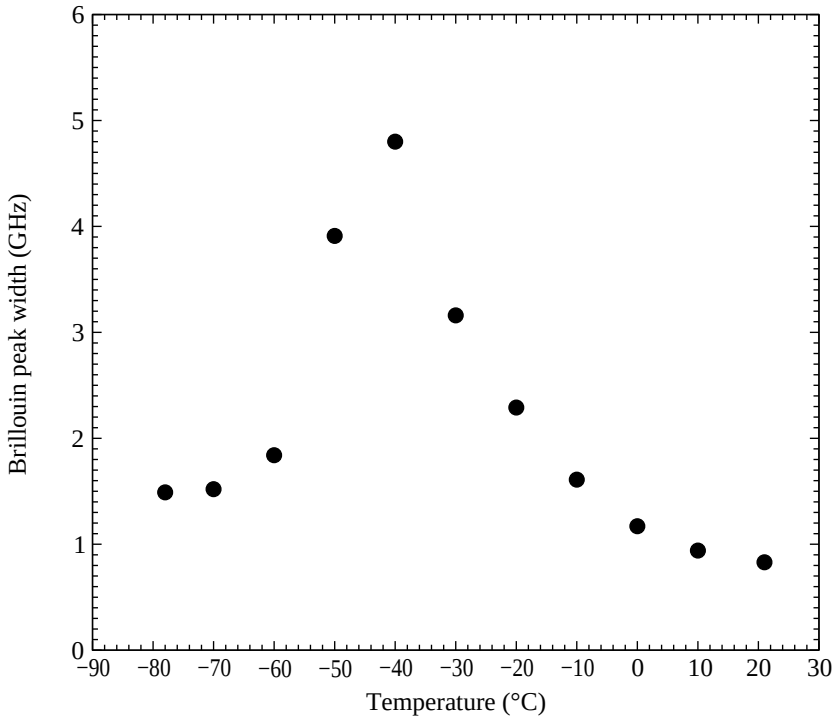

Figure 4.8: Brillouin peak widths in a cooled $x_m = 0.27$ methanol–water mixture.

literature value for the refractive index at 20 °C (see above). The variation of the refractive index with temperature is unknown, so the sound velocities which are displayed to the right of Fig. 4.7 are not exact. It is however likely that the refractive index remains within a few percent of its room temperature value, so the corresponding uncertainty in v_s will be of similarly small magnitude. The values for v_s at 10 °C and 20 °C agree with ultrasonic (2 MHz) measurements by Onori [50] to within 4%, which is reasonable given the possibility of dispersion of the sound velocity with frequency.

4.2.4 Brillouin spectra at variable concentration and temperature

These unexpected features in the Brillouin spectra of an $x_m = 0.27$ methanol–water solution were deemed sufficiently interesting to merit further investigation. Samples of several other concentrations were therefore prepared following the method described in Sec. 4.2.2.1 and studied at low temperatures using the ambient pressure nitrogen-cooled and electically heated cell. Table 4.1 shows the percentage of methanol by mass which corresponds to the methanol mole fraction of each composition studied. The Fabry-Perot interferometer was again operated in the five-pass configuration with a

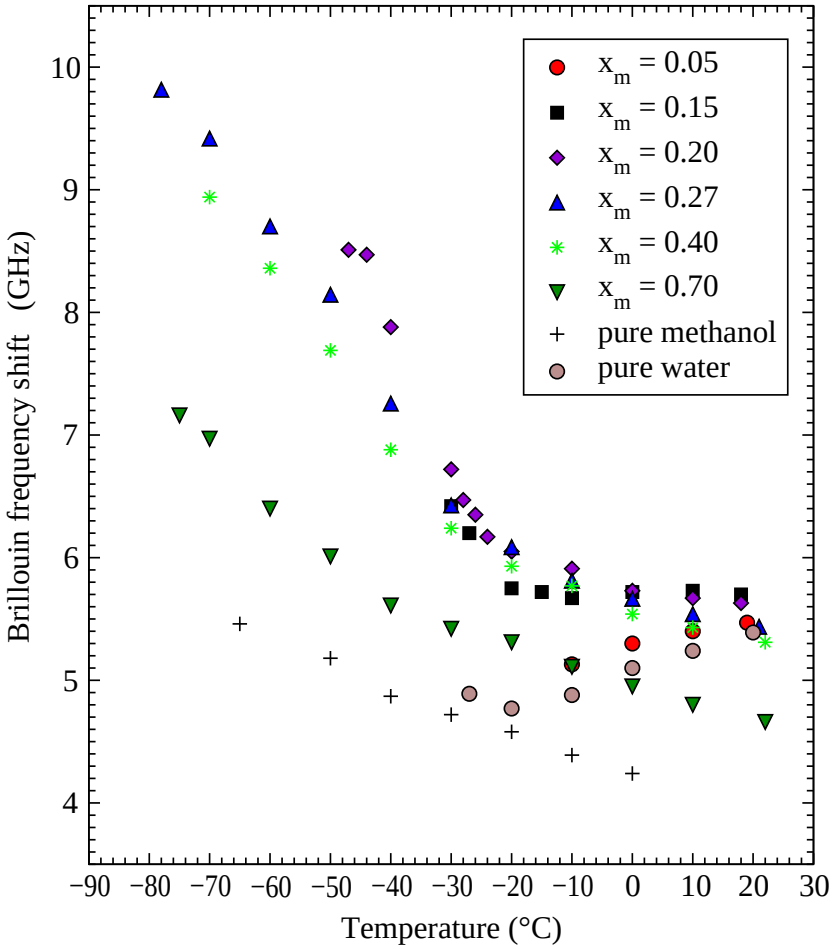

Figure 4.9: Brillouin peak shifts for a range of compositions of methanol–water mixtures cooled from room temperature. A detailed discussion of the behaviour of each concentration can be found in the text (Sec. 4.2.4.1), but the most important feature is the beginning of an increase in peak frequency (and hence sound velocity) at -20°C in solutions with $0.15 \leq x_m \leq 0.40$. Note also the minimum in the sound velocity of supercooled pure water at approximately the same temperature.

free spectral range of 22.37 GHz and the scattering angle fixed at $90 \pm 0.5°$. Spectra for the pure alcohol were collected in the same way. Data for pure water was also obtained, with temperatures in the supercooled régime (below 0 °C) being taken from the literature (for the frequency shifts) or created in our lab (peak widths) as will be discussed below. Brillouin frequency shifts (Fig. 4.9) and peak widths (Fig. 4.10) were measured by fitting Lorentzian curves to the spectra as described in Sec. 3.3.2, resulting in uncertainties of ±0.1 GHz in both quantities.

We will now discuss the behaviour of the frequency shifts (directly proportional to the hypersonic sound velocity $v_s = \omega_B/q$) as a function of concentration and temperature

(Fig. 4.9). The data for the 40% methanol–water solution ($x_m = 0.27$) first shown in Fig. 4.7 is included in Fig. 4.9, and the most striking feature of the new data is that the Brillouin shifts at several other concentrations ($x_m = 0.15$, $x_m = 0.20$ and $x_m = 0.40$) follow a very similar trend on cooling. The large amount of data presented in Fig. 4.9 to some extent masks the variation of the trend with sample composition, hence a careful discussion of the behaviour at each concentration in this important figure is merited.

4.2.4.1 Discussion of changes in the Brillouin frequency shift on cooling

In pure water, the Brillouin peak frequency ν_B, and hence adiabatic hypersound velocity v_s, *decreases with temperature* as it is cooled from 20 °C. This unusual behaviour is well documented, and is due to the properties of the hydrogen-bonded water network [90]. The data for pure water shown in Fig. 4.9 is taken from Ref. [91] (reproduced in Fig. 4.15) and was measured at exactly the same wavevector (determined by scattering angle and laser wavelength) at which the methanol–water experiments were performed. This literature data (and also a similar, more recent piece of work – Ref. [92]) shows that the decrease in sound velocity on supercooling pure water does not continue indefinitely – v_s begins to *increase* with cooling below -22 °C. There is therefore a well-defined minimum at -22 °C in the hypersound velocity of pure supercooled water. Adding a very small amount of methanol to water ($x_m = 0.05$) does not change appreciably the behaviour of the Brillouin shift with cooling; it still decreases. The $x_m = 0.05$ solution was unable to be supercooled to any significant extent, so it cannot be said whether or not the dilute solution also possesses a minimum in the sound velocity. Moving up in methanol concentration to $x_m = 0.15$ has a much more significant effect – the Brillouin shift no longer decreases with temperature on cooling from room temperature. Instead, ν_B is almost constant down to -20 °C, in agreement with the findings of Ref. [93]. Below this temperature, the $x_m = 0.15$ solution exhibits an *increase* in sound velocity, continuing until the sample froze at just below -30 °C. The next most concentrated methanol–water solution, $x_m = 0.20$, behaves similarly, but has a much lower freezing point, hence we are able to see a continuation of the increase in ν_B down to -47 °C. Note that this increase is more rapid than at any other concentration. The sound velocity in the $x_m = 0.20$ solution is again fairly constant above -20 °C. The behaviour of the Brillouin frequency shift in the $x_m = 0.27$ (40% by mass) methanol–water mixture

has already been discussed in some detail in Sec. 4.2.3 above; the trend is again the same. Note that this solution and all the more concentrated samples had not frozen at the lowest temperature measured, so in principle one could extend these measurements to lower temperatures. This was not possible at the time due to limitations of the temperature control unit, which was improved later. The $x_m = 0.40$ solution is again very similar to the $x_m = 0.20$ and $x_m = 0.27$ mixtures, although the transition between the two régimes at -20 °C is less distinct; there is a slight increase in ν_B with cooling above this point, in contrast to the independence of temperature in the $x_m = 0.15$, $x_m = 0.20$ and $x_m = 0.27$ solutions. In this sense, the $x_m = 0.40$ solution is becoming more like pure methanol, a trend which is even more evident in the $x_m = 0.70$ data. In this more concentrated solution, there is no transition at -20 °C, and the Brillouin frequency shift does not reach values as high as in the intermediate concentrations. This behaviour is qualitatively the same as in pure methanol, with the water content seeming only to increase ν_B by approximately 1 GHz.

The transition between 'normal' behaviour above -20 °C and a rapid increase to extremely large (for a liquid) ν_B at lower temperatures is what will be referred to in this thesis as the 'anomalous' behaviour of the Brillouin frequency shift. As we have just seen, this occurs in aqueous methanol solutions with $0.15 \leq x_m \leq 0.40$, although this range may be extended by performing further experiments at other concentrations. The effect is not observed for $x_m = 0.05$ (although no concerted effort was made to supercool the solution) and has certainly disappeared by $x_m = 0.70$. Perhaps the most obvious question posed by these findings is whether or not the anomalous behaviour of the aqueous methanol solutions is related to the behaviour of pure supercooled water? Is it a coincidence that the upturn in the sound velocity happens at the same temperature in pure water as in the solutions, and that the effect disappears when too much methanol is added? This will be discussed further in Sec. 4.2.7 below; let us now look in some detail at the behaviour of the Brillouin peak *widths* as a function of concentration and temperature.

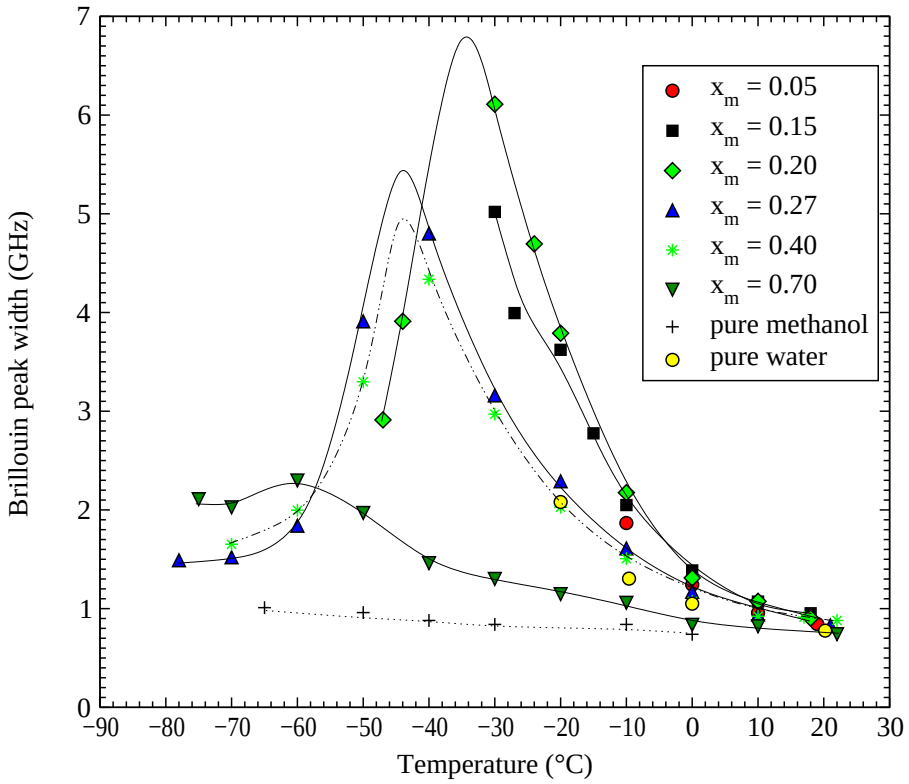

Figure 4.10: Brillouin peak widths (FWHH) for a range of compositions of methanol–water mixtures cooled from room temperature. Curves drawn through the data points for each concentration are a visual aid only – they do not represent fits to the data. A detailed discussion of this figure is given in Sec. 4.2.4.2.

4.2.4.2 Discussion of changes in the Brillouin peak width on cooling

Fig. 4.10 shows the full widths at half height of the Brillouin peaks whose positions were plotted in Fig. 4.9 and discussed in the preceding section above. The necessity of displaying so many data sets in one graph unfortunately results in a somewhat cluttered figure, hence we will now comment on the behaviour of each sample, again starting with pure water and moving up in concentration towards pure methanol.

Although data for pure supercooled water derived from Brillouin peak widths is available in the literature (Ref. [91, 92], reproduced in Fig. 4.15), it is expressed as the classical sound absorption α/f^2, for which one needs knowledge of the refractive index to extract the peak width[¶]. This information was not readily available for temperatures other than 20 °C, so a method of cooling pure water to as low as -20 °C was

[¶]From Ref. [94], $\alpha/f^2 = 2\pi\Gamma/(v_s\omega_B)^2$ where Γ and ω_B are as defined in Eq. 2.36. The refractive index is required in order to calculate q and hence v_s.

implemented in our laboratory in order to measure $\Delta\nu_B$ directly. The technique was developed by Hugh Vass [45] using very clean water in thin sample tubes, the insides of which were flamed to improve their smoothness, thus minimising the likelihood of crystal nucleation. Although this approach was able to achieve significant supercooling of the water, the quality of Brillouin spectra was not very good, so where possible data from the literature was used instead (e.g. the water data in Fig. 4.9). The margin of uncertainty in the Brillouin peak widths for pure water shown in Fig. 4.10 is greater than that discussed in Sec. 3.3.2 due to the poor signal to noise ratio of these spectra; they are accurate to better than ± 0.3 GHz below 0 °C.

From Fig. 4.10, one can see that the Brillouin peak width in pure water is almost identical to that found in all the methanol–water mixtures at 20 °C, and increases with growing rapidity as the temperature is lowered. By -20 °C (the lowest temperature achieved before crystallisation occurred) the FWHH has grown from 0.8 GHz to 2.1 GHz. Refs. [91, 94] show that this increase in absorption (directly proportional to $\Delta\nu_B$) is continued down to -27.4 °C, the lowest temperature studied, by which time the sound absorption is roughly 11 times greater than at 20 °C. Looking again at Fig. 4.10 we see that the most dilute aqueous methanol solution, $x_m = 0.05$, behaves very similarly, although the width at the lowest-temperature data point at -10 °C is significantly (0.6 GHz) higher than the corresponding point for pure water. The $x_m = 0.15$ solution is almost identical to $x_m = 0.05$ for $T \geq -10$ °C, but its lower freezing point enables us to follow the increase in FWHH down to almost -30 °C, by which it has risen from 0.9 GHz to 5.0 GHz. This behaviour is very striking: the FWHH of the Brillouin peak (which is directly proportional to the absorption of hypersound and depends on viscosity and thermal conduction according to Eq. 2.38) appears to be diverging as the temperature is reduced. The data from the next most concentrated solution, $x_m = 0.20$, matches this trend very closely above -30 °C, but at lower temperatures (down to -48 °C) the width *begins to decrease*. In other words, there is a distinct maximum in the temperature-dependence of the FWHH of the Brillouin peak in an $x_m = 0.20$ aqueous methanol solution. This behaviour is even more apparent and fully-developed in the $x_m = 0.27$ (40% methanol by mass) mixture which has already been noted in Sec. 4.2.3 and shown in Fig. 4.8. For this solution, data is available down to almost -80 °C, and by -60 °C the decrease in width on the low-temperature side of the maximum seems to

have levelled off at a FWHH of 1.5±0.1 GHz. The $x_m = 0.40$ solution behaves almost identically. The $x_m = 0.70$ solution, however, does not seem to follow this trend. The Brillouin peak width in this most concentrated solution increases very gradually from 0.8 GHz at 20 °C (the same value as all of the other solutions at this temperature) to 2.1 GHz at -75 °C, with a slight 'hump' in the data between -40 °C and -70 °C. This may or may not be related to the much larger and wider maximum seen at intermediate concentrations; if it is then the effect is vestigial at $x_m = 0.70$. The Brillouin peak width in pure methanol is even less affected by cooling, increasing monotonically from 0.7 GHz at 0 °C to 1 GHz at -65 °C with no evidence of an intervening maximum.

The key finding of this study of changes in the width of the Brillouin peak in aqueous methanol solutions as a function of temperature is therefore that a well-defined maximum in the peak width (and hence absorption of hypersound) exists in solutions of intermediate concentration at a temperature between -35 °C and -45 °C.

4.2.5 X-ray diffraction

The Brillouin scattering experiments on methanol–water mixtures reported above show surprising and anomalous behaviour of bulk dynamical properties (peak frequency and width) on cooling below -20 °C. The technique is however unable to probe directly the static structure of the solutions, and no such information at these low temperatures is available in the literature. An opportunity to use x-ray diffraction to investigate structural changes in the aqueous methanol solutions as a function of temperature and concentration was therefore extremely welcome. Perhaps most importantly, this allowed us to confirm that the samples are indeed in the liquid state (as opposed to crystalline or amorphous solids) at all the temperatures for which Brillouin spectra were measured and anomalous hydrodynamic behaviour observed.

After discussing my spectroscopic results on low-temperature aqueous methanol solutions with Prof. John Finney of University College London, he kindly offered to use two days of his allocated beam time at the UK Synchrotron Radiation Source at the Daresbury laboratory of the Council for the Central Laboratory of the Research Councils to look at changes in the structure of the solutions as they are cooled. We chose to study three concentrations: $x_m = 0.3$, $x_m = 0.4$ and $x_m = 0.7$ (see Table 4.1 for

the equivalent mass percentages). These experiments were performed by myself, Prof. Finney and Prof. Toshio Yamaguchi of Fukuoka University, Japan. Yamaguchi's recent research has focused on the use of x-ray diffraction to study molecular clusters in aqueous alcohol solutions (see e.g. Refs. [95, 82]) and he is currently extending his existing studies at room temperature to investigate the effect of cooling on the phenomena in which he is interested. The concentrations and temperatures chosen were therefore a compromise, intended to be as useful as possible to both of us.

Experiments were performed on Station 9.1 at the Daresbury Synchrotron with a curved image-plate (CIP) camera which uses a photostimulable phosphor film to record two-dimensional diffraction patterns at high spatial resolution over a large solid angle. This film is then scanned into a computer to produce an image like the one shown in Fig. 4.11. Custom-made software is used to integrate numerically around the rings in the two-dimensional pattern to produce a conventional one-dimensional plot of intensity vs. 2θ, d or q. These patterns can then be analysed following the method reported in Ref. [82] to produce structure functions and radial distribution functions which provide valuable information on intramolecular and intermolecular structure in liquids [95].

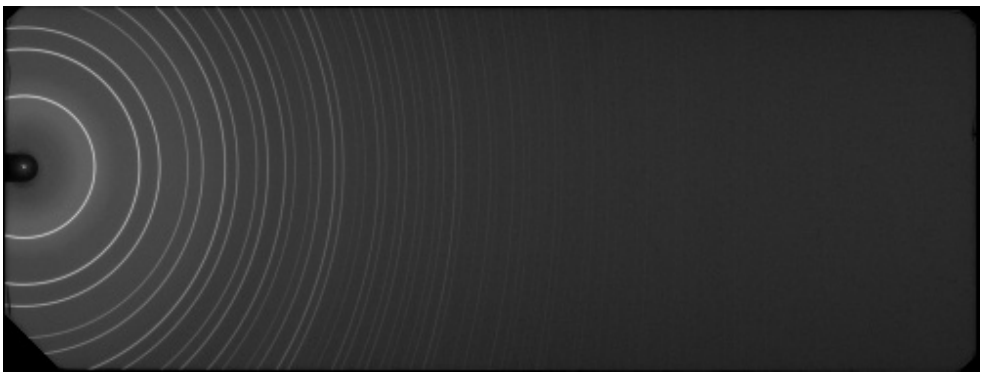

Figure 4.11: Example of a curved image-plate x-ray diffraction pattern.

The temperature of the sample was controlled using an Oxford Cryostream system. This produces a temperature-controlled jet of nitrogen gas, which is passed over the sample cell. The nitrogen is surrounded by an accompanying stream of very dry air in order to avoid condensation of ice from water in the atmosphere around the sample. Sample temperatures were estimated to be accurate to $\pm 5\,\mathrm{K}$ [96]. Freezing points for the $x_m = 0.3$, $x_m = 0.4$ and $x_m = 0.7$ solutions studied agreed (within this error bound)

with those observed during my spectroscopic measurements in much larger cells.

Samples were prepared by weight as described in Sec. 4.2.2.1 above, and loaded into 0.5 mm diameter borosilicate capillary cells. These were sealed by dipping the open ends of the capillary into melted beeswax, which then solidified to provide an airtight closure. This wax had previously been found not to cause contamination by reacting with methanol–water solutions [97].

X-ray diffraction patterns were recorded for methanol–water mixtures with $x_m = 0.3$, $x_m = 0.4$ and $x_m = 0.7$, cooling from room temperature until freezing. For each composition, at least one pattern in the solid phase was measured in order to allow the composite solids to be compared with pure ice and crystalline methanol structures. The wavelength of radiation used was $\lambda = 0.4868$ Å at a current decreasing from 220 mA to 100 mA with time after each injection of electrons into the storage ring. The beam had a cross-sectional area of 0.5 mm^2 at the sample. Liquid-state diffraction patterns were collected for approximately one hour, while runs in the solid phase required only 10 minutes to achieve an acceptable signal-to-noise ratio.

X-ray diffraction patterns (corrected to account for various experimental artefacts) for the three methanol–water mixtures are shown in the form of intensity vs. distance in Fig. 4.12. The most noticeable trend in the $x_m = 0.3$ and $x_m = 0.4$ solutions is the sharpening of the small peak at 2.2 Å as the temperature is lowered. This feature corresponds to the second coordination shell in the tetrahedral structure of pure water, showing that this structure is present despite such high alcohol content, and is enhanced by cooling [97]. Limited beam time and a problem with the sample meant that only three temperatures were able to be investigated in the $x_m = 0.7$ solution. The water structure peak at 2.2 Å seems still to be present even at this concentration, but not enough data is available to be able to say much more than that.

The low-temperature patterns in Fig. 4.12(a) and (b) clearly show that a solid phase has formed in the $x_m = 0.3$ and $x_m = 0.4$ solutions. It should be possible to identify the peaks in these patterns by referring to literature data for the various ices (crystalline and amorphous) and two solid methanol structures (referred to as α and β), but this analysis has not yet been performed. However we can make some statements about what these diffraction patterns show. Firstly, it is clear that the solid phase formed

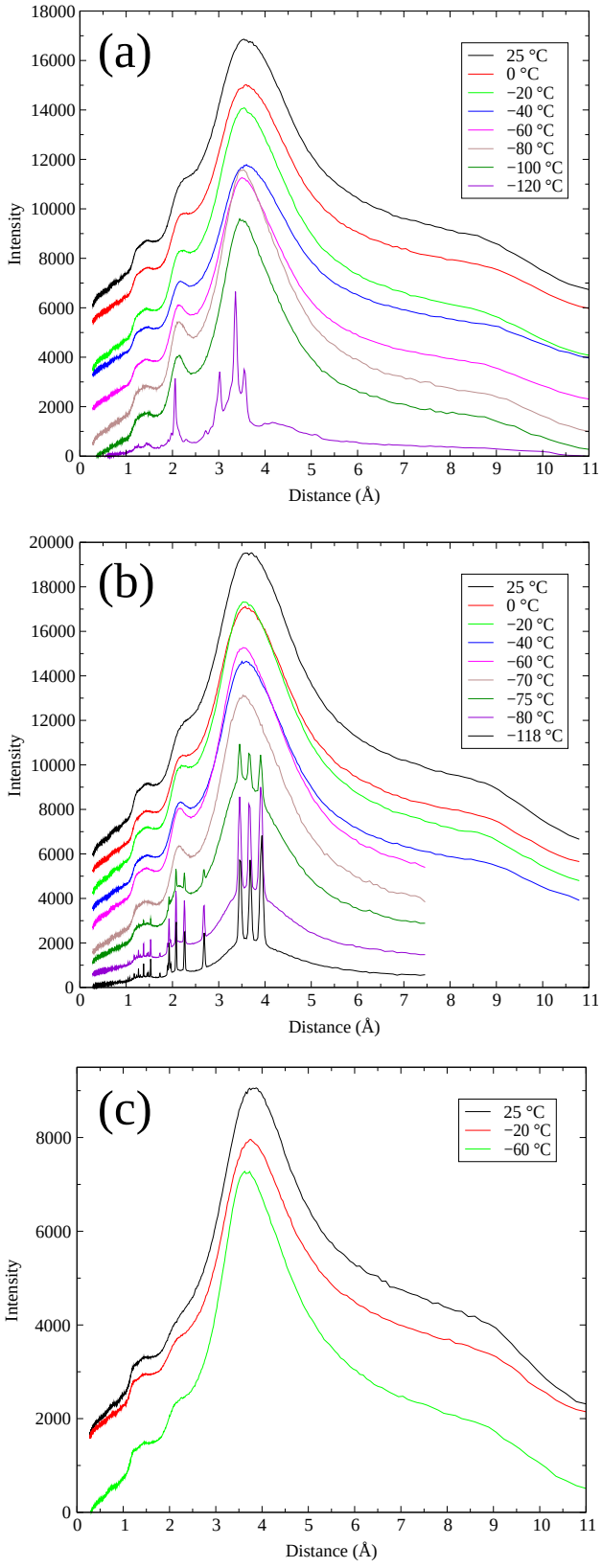

Figure 4.12: X-ray diffraction patterns (Intensity vs. d-spacing) for ***(a)*** $x_m = 0.3$, ***(b)*** $x_m = 0.4$ *and* ***(c)*** $x_m = 0.7$ *methanol–water mixtures. Spectra have been scaled and displaced so that moving from top to bottom corresponds to reducing temperatures.*

by the $x_m = 0.3$ mixture is different to that formed by the $x_m = 0.4$ solution; the lowest temperature datasets in each case have peaks in different places. The triplet structure of the most intense group of peaks in the $x_m = 0.4$ mixture suggests that hexagonal ice (Ih) is present [98]. Note also that the sharp peaks due to the solid in the $x_m = 0.4$ mixture are superimposed on an amorphous background which reduces in intensity with cooling. This does not appear to be the case for the $x_m = 0.3$ solution.

Radial distribution functions have been calculated from the diffraction patterns shown in Fig. 4.12 by Prof. Yamaguchi using the method reported in Ref. [82]. Interpretation of these complicated functions is beyond the scope of this thesis, hence these results will not be presented here. A detailed publication based on this work is currently in preparation, but the key finding of analysis performed so far is that the hydrogen-bonded structure of the solutions is enhanced with cooling in the liquid phase, with significant preservation of the tetrahedral water network [97]. This is consistent with the findings of neutron diffraction experiments at room temperature (Sec. 4.2.1) and at -35 °C as will be discussed in the following section.

4.2.6 Neutron diffraction

As discussed in Sec. 4.2.1 above, neutron diffraction experiments have recently been used to probe solution structure on molecular lengthscales in $x_m = 0.05$ and $x_m = 0.70$ methanol–water mixtures at room temperature. The wealth of information provided by the technique suggested that a neutron study of the effect of cooling on the system would be likely to help explain the anomalous behaviour of the hypersonic sound speed and absorption discovered using Brillouin spectroscopy.

Such an experiment was performed using the ISIS pulsed neutron source at the Rutherford Appleton Laboratory, in collaboration with Prof. Alan Soper and Sanhita Dixit, a fellow PhD student at Edinburgh. My supervisor Dr. Jason Crain and an undergraduate student, Jason Blackstock, were also on the team. A methanol–water mixture with $x_m = 0.27$ was studied at two temperatures, 20 °C and -35 °C, chosen in order to compare with the normal and anomalous régimes of hydrodynamic behaviour identified in Sec. 4.2.3 above. The analysis and modelling of results from this work is extremely time-consuming and beyond the scope of this thesis. Only preliminary results are

available at the time of writing, and are presented here only as corroborative evidence for the hypothesis that extended regions of relatively unperturbed tetrahedral water structure are present in a solution as concentrated as $x_m = 0.27$ (40% methanol by mass, 46% methanol by volume at room temperature). The following discussion will therefore be extremely brief; an in-depth explanation of the technique may be found in Sanhita's thesis [81] and a comprehensive treatment of the results will be given in a future publication.

Neutron scattering is a very valuable technique in the study of the molecular structure of matter. Neutron wavelengths of a few Ångströms (and hence energies of a few MeV) are comparable to the separation of atoms and molecules in a liquid, hence the scattered neutrons contain information on the positions of these fundamental constituents. Specifically, the scattered intensity is proportional to the static structure factor $S(\boldsymbol{q})$, from which the radial distribution function (or pair correlation function) $g(r)$ may be extracted under favourable conditions [99]. This gives the probability of finding another atom a distance r from an arbitrary reference atom. If the reference atom is surrounded by a shell of nearest neighbours at a radius r, there will be a corresponding peak in $g(r)$, the integral of which gives the number of atoms in this shell (called a *coordination number*. In a molecular liquid (or indeed a mixture of such liquids) there are of course several different species of atoms present, each of which has a certain scattering length. Hence it is in principle possible to extract *partial* structure factors $S_{xy}(\boldsymbol{q})$ and pair correlation functions $g_{xy}(r)$ which relate to the relative separations of species x and y.

When the system being studied contains hydrogen atoms, an ingenious technique called *isotope substitution* may be used to label these hydrogens according to which molecule (in our case methanol or water) they belong to, and even where in the molecule they are situated (i.e. in the case of methanol, either the hydroxyl group or the methyl group). This labelling exploits the difference in scattering lengths between hydrogen (H) and its isotope deuterium (D), and is now widely used in studies of liquid structure [100]. Scattering experiments on several carefully chosen isotope substitutions may then be combined in order to measure partial structure factors between various combinations of atoms in different molecules.

The degree of complexity of the information resulting from such an experiment (e.g.

nine different composite partial structure factors may be obtained from a methanol–water mixture [81]) renders it extremely difficult to extract useful information from raw data. This problem is overcome by using experimental results as the input to sophisticated data-modelling algorithms, which we will now discuss very briefly.

The technique used to model the data from the earlier neutron diffraction experiments summarised in Sec. 4.2.1, and which is currently being applied to the variable temperature experiments described here is the Empirical Potential Structure Refinement (EPSR) method developed by Prof. Alan Soper at ISIS [100, 101]. Standard literature intermolecular potentials are used to calculate an initial configuration of molecular coordinates, from which composite partial structure factors are calculated. The difference between these and the experimental results is then used to update the intermolecular potentials, and a new simulation is performed. This process is iterated until the simulation agrees with experimental structure factors. The resulting model contains all the information required to calculate the full set of interatomic partial pair distribution functions.

Neutron diffraction data from a sequence of 7 isotope-substituted $x_m = 0.27$ methanol–water mixtures was collected at 20 °C and -35 °C on the SANDALS diffractometer at ISIS. Normal and deuterated water and methanol of the highest purity available were obtained from Sigma and samples were prepared by weight with an accuracy in composition of better than 0.5 %. The temperature was regulated to within ±1 K using a computer-controlled cryostat. Satisfactory diffraction data was obtained for all the samples studied. Note that direct comparison with the results of experiments on normal (i.e. not deuterated) methanol–water solutions may be complicated by perturbation of the phase diagram due to the presence of deuterated species. No investigation into this problem was attempted, as no quantitative comparisons with my Brillouin scattering results were deemed necessary at this stage in the research.

The necessary corrections were applied to the data before commencing the lengthy EPSR routine. This modelling is not yet complete, but is in its final stages meaning that reliable preliminary results are available. This analysis is being performed by Alan Soper and Sanhita Dixit, and has of course not yet been published. Figs. 4.13 and 4.14 are snapshots of the simulation box calculated using intermolecular potentials produced

by EPSR, at 20 °C and -35 °C respectively. The black spheres represent carbon atoms in methanol molecules, and the light grey spheres represent water oxygens. These pictures are extremely unlikely to change appreciably with further iterations of the EPSR; partial structure factors calculated from the configurations are very similar to the experimental results.

From the snapshot at 20 °C (Fig. 4.13) we can see that large interconnected patches of water exist alongside clusters of methanol molecules. A very significant amount of segregation into water-rich and alcohol-rich regions therefore takes place on a lengthscale of a few molecular sizes. A cluster analysis shows that the size of these water 'clusters' is larger than the simulation box (a cube of side 20 Å containing approximately 400 molecules). The snapshot at -35 °C (Fig. 4.14) seems to show that the methanol and water are better mixed, but segregation still occurs and the maintenance of the water structure is just as apparent.

The more quantitative information provided by partial structure factors and pair distribution functions will not be presented here – a full analysis will be undertaken only when the final results of the data modelling process become available. Some important features have however been noted from preliminary results. At 20 °C water–water (oxygen atoms) partial pair distribution functions show that the water network is present and almost unchanged with respect to pure water. Integration of the peak due to the first coordination shell shows that the first coordination number only decreases from 4 – 4.5 in pure water to 3.5 in the mixture. The only effect of cooling on the water structure seems to be sharpening of the peaks, indicating that the structure is slightly enhanced. This agrees with the behaviour of the radial distribution functions calculated from the x-ray diffraction experiments discussed in Sec. 4.2.5. More hydration of the methanol molecules is observed at the lower temperature, and methanol molecules are closer together in the solution than in the pure alcohol. These findings are all consistent with the earlier neutron diffraction experiments performed on $x_m = 0.05$ and $x_m = 0.70$ solutions as discussed in Sec. 4.2.1 above.

A final – potentially very important – outcome of this first look at quantitative output from the EPSR simulation is that the structure of water in the solutions (as measured by the water–water oxygen partial pair correlation function) tends towards that of low-

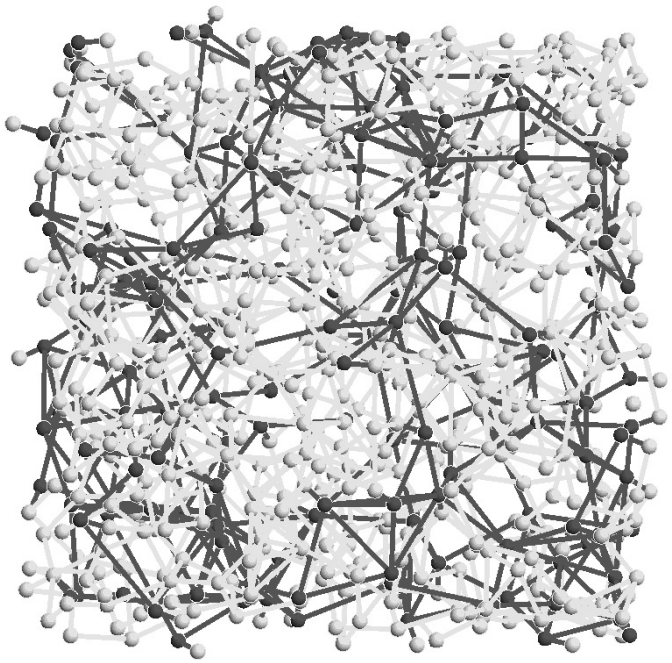

*Figure 4.13: Snapshot of the EPSR simulation box (2*nm *on each side) for* $x_m = 0.27$ *aqueous methanol at 20*°C*, very near the end of the refinement process. Note the existence of extended water-rich (grey dots) and methanol-rich (black dots) regions.*

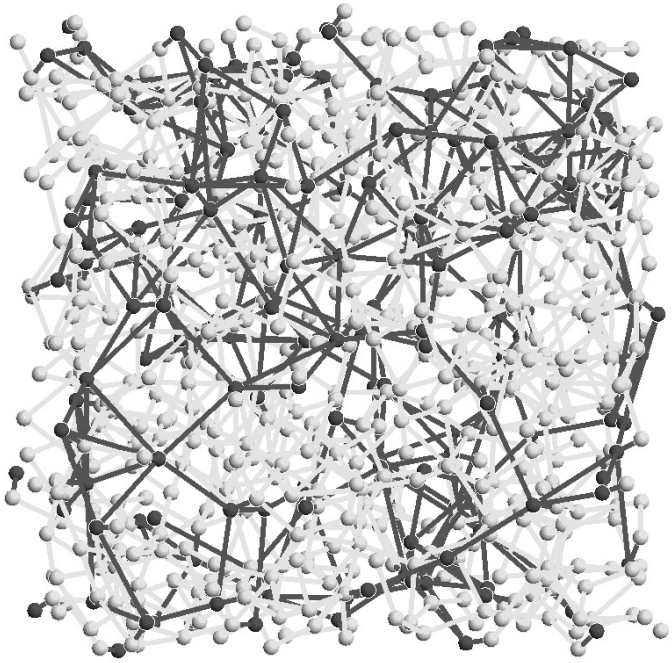

Figure 4.14: Snapshot of the EPSR simulation box for the $x_m = 0.27$ *methanol–water mixture at -35*°C*. The solution appears to be better mixed than at 20*°C*, but significant clusters of water remain present.*

density amorphous (LDA) ice rather than a crystalline phase. This was discovered by comparing newly measured (unpublished) data on LDA with the methanol–water results at both temperatures. It is extremely surprising that the water structure in the $x_m = 0.27$ solution at a temperature as high as 20 °C exhibits this likeness with supercooled pure water. The similarity with this glassy water phase is more marked at the lower temperature, as might be expected.

Might the presence of this pre-glassy water in the solution be the underlying cause of the anomalous high-frequency dynamics observed in the Brillouin spectra presented in Sec. 4.2.4 above?

4.2.7 Summary of all results on methanol–water mixtures

We are now in a position to compare results on cooled methanol–water solutions from Brillouin spectroscopy, Raman spectroscopy, x-ray diffraction and neutron scattering. This section will summarise my findings using these techniques, highlighting any similarities and differences. A tentative hypothesis attempting to explain the anomalous behaviour in the Brillouin spectra will then be proposed, motivating further study of other aqueous solutions which will be presented in the remainder of this chapter.

Two unexpected effects were observed in the Brillouin spectra of low temperature aqueous methanol solutions presented in Sec. 4.2.4. Firstly, the Brillouin peak frequency ν_B and hence adiabatic hypersonic sound velocity $v_s = \omega_B/q$ begin to increase very rapidly at -20 °C, reaching solid-like values at the lowest temperatures probed (Sec. 4.2.4.1). X-ray diffraction experiments (Sec. 4.2.5) confirm that the samples are however still liquid despite such high sound speeds. This behaviour was seen for solutions with $0.15 \leq x_m \leq 0.40$, although the observation of an increase in Brillouin shift at -22 °C in deeply supercooled pure water suggests that a similar effect may be masked by the higher freezing points of solutions with $x_m < 0.15$.

Surprising behaviour was also found in measurements of the Brillouin peak width $\Delta\nu_B$, which is proportional to the absorption of hypersound in a liquid. These results were discussed in detail in Sec. 4.2.4.2. A well-defined maximum in the peak width was seen between -35 °C and -45 °C in solutions with $0.20 \leq x_m \leq 0.40$. No such maximum

was seen at higher methanol concentrations, but all of the solutions with $x_m < 0.20$ (including pure water) exhibit a similar rate of increase on the high-temperature side of the maximum. The reason for the maximum not being observed in these high water-content solutions may therefore simply be because they freeze above -35 °C.

Both of these anomalous hydrodynamic effects are therefore present in methanol–water solutions with $0.20 \leq x_m \leq 0.40$, with similar behaviour observed at lower methanol concentration although not fully expressed due to the intervention of freezing.

As mentioned above, x-ray diffraction patterns (Sec. 4.2.5) show that the methanol–water solutions are indeed in the liquid phase at all temperatures and concentrations in which the anomalous effects are observed. Earlier x-ray work [82] showed that the water structure remains present for methanol concentrations up to $x_m = 0.70$ at room temperature, and radial distribution functions calculated by Toshio Yamaguchi from my data (not presented in this thesis) shows that this is also the case at lower temperatures [97]. The solid phases formed by $x_m = 0.30$ and $x_m = 0.40$ mixtures are different, but have not yet been identified from their diffraction patterns.

Neutron diffraction experiments modelled using the EPSR technique also showed the existence of an extended water network almost unchanged from the pure liquid in an $x_m = 0.27$ aqueous methanol solution at 20 °C and -35 °C (Sec. 4.2.6). This is in agreement with earlier neutron experiments performed by colleagues at room temperature, which found significant preservation of the water structure even at $x_m = 0.70$ [84] (discussed in Sec. 4.2.1). On nanometre lengthscales, the solution is significantly demixed into methanol-rich and water-rich regions. The structure of the water in these solutions was found to become more like LDA ice (glassy water) than a crystalline phase as the temperature is lowered.

The splitting of the C − O stretch mode in the Raman spectra of methanol–water mixtures discussed briefly in Sec. 4.2.1 provides further evidence for this heterogeneity on short lengthscales. It implies that methanol molecules inhabit two different environments in the mixture, consistent with the existence of methanol–rich and water–rich regions persisting for longer than the timescale of a light scattering experiment. The effect is most obvious at low temperatures, but at 20 °C the C − O peak is very broad, suggesting that two components are present but are too broad and close together to be

resolved separately [86].

A common conclusion of all of these techniques other than Brillouin spectroscopy is therefore that methanol and water do not mix homogeneously on lengthscales of a few nanometres. Moreover, structural information from x-ray and neutron diffraction experiments show that the water-rich regions which result from this demixing possess a structure extremely similar to that of pure water, even at $x_m = 0.7$. This is consistent with the earlier work at room temperature discussed in Sec. 4.2.1, which also shows that the extent of this tetrahedral water network decreases as methanol clusters grow on increasing x_m from 0.3 to 0.7.

4.2.7.1 Are the anomalies related to the behaviour of pure water?

Are these findings able to explain the anomalous behaviour of the Brillouin peak frequency and width (i.e. sound velocity and absorption) in cooled methanol–water mixtures? The presence of an essentially unperturbed water structure in the concentration range where these effects are present may indeed be related to these unexpected hydrodynamic effects in aqueous solution. In considering this possibility, let us first appeal to the work of Maisano *et al* on hypersound propagation in deeply supercooled water [91].

We have already referred to this important study – the Brillouin peak frequencies for pure water plotted in Fig. 4.9 were taken directly from the paper. In order to emphasise the similarity between effects seen in supercooled pure water and those observed in methanol–water solutions at low temperatures, the key figures from Ref. [91] are reproduced in Fig. 4.15 below. Note that identical results from Brillouin scattering in supercooled water were later obtained by other groups – see Refs. [94] and [92].

Several datasets are shown in Fig. 4.15, with the Maisano *et al* Brillouin scattering results which are directly comparable to the methanol–water experiments denoted by squares. Signatures of the anomalous hydrodynamics seen in aqueous methanol solutions are clearly present in pure water; the sound velocity begins to increase sharply at around -22 °C and the sound absorption (proportional to the Brillouin peak width) shows a similar rapid increase with cooling below 0 °C. Interestingly, both Refs. [94] and [92] extrapolate from this increase in widths to suggest a maximum broadening

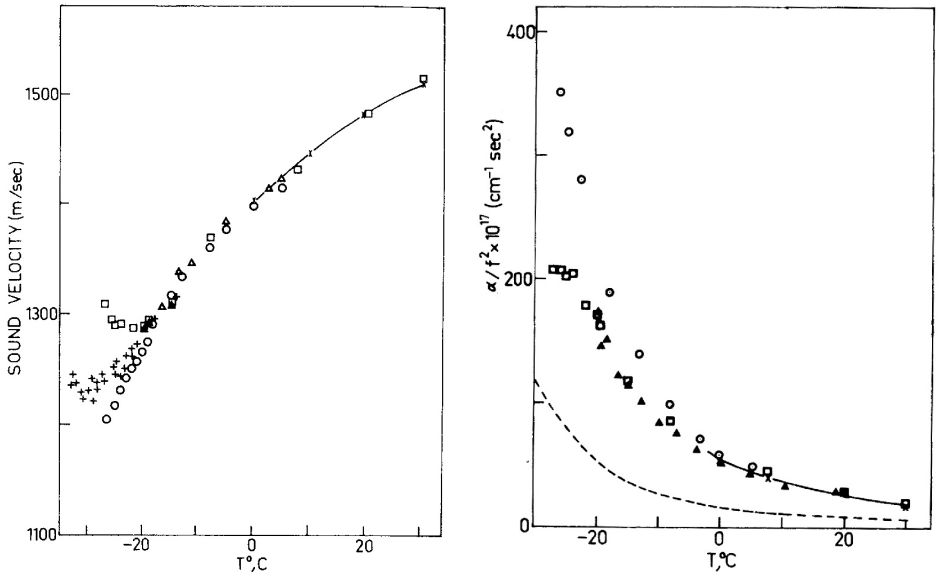

(a) Sound velocity.

(b) Sound absorption α/f^2.

Figure 4.15: (a) *Sound velocities and* (b) *sound absorption (proportional to Brillouin peak frequencies and widths respectively) in deeply supercooled pure water, reproduced from Ref. [91]. Hypersonic data measured using Brillouin spectroscopy is shown by squares, other datasets are earlier results from ultrasonics and other low-frequency techniques.*

in pure water at -45 °C, the same temperature as the maximum in aqueous methanol. As this behaviour is preserved despite the addition of fairly high concentrations of methanol, it is tempting to suggest that the effects seen in methanol–water solutions have their origins in this pure water behaviour. This hypothesis seems reasonable given the wealth of evidence discussed above for the existence of an essentially unperturbed water structure in the solutions in which the anomalies are apparent.

If the effects *are* due to the properties of supercooled water, the rôle of methanol in producing the anomalous behaviour would therefore be to suppress freezing, thereby removing the need for ingenious supercooling techniques and allowing the trends shown in Fig. 4.15 to be extended to lower temperatures than possible in pure water.

Evidence for this conjecture is of course circumstantial. The effects in solution appear very similar to those in pure water, and are not present in solutions with methanol content higher than $x_m = 0.7$, the composition at which x-ray and neutron diffraction show that the extended water network is destroyed at room temperature. The increase in Brillouin peak frequency below -20 °C in aqueous methanol (see Fig. 4.9) is also

most extreme in the solutions with highest water content, and gradually becomes less prominent with the addition of methanol. The temperature at which the increase begins in the solutions is independent of concentration, and very similar to the corresponding temperature in pure water.

Are the hydrodynamic anomalies related to the properties of water, or just a peculiarity of the methanol–water system? Further investigation of Brillouin scattering from aqueous solutions might be key in attempting to answer this question, and the remainder of this chapter will present the results of experiments on several such systems.

4.3 A second system: Brillouin scattering from aqueous tertiary butanol

The results described above from Brillouin and Raman scattering studies of cooled aqueous methanol solutions were presented at the January 2001 meeting of the EPSRC UK Liquids Network in Bath. After discussing my work with Profs. John Finney and Alan Soper of University College London and the Rutherford Appleton Laboratory, they suggested that it would be valuable to extend the scope of the research to look at cooled aqueous solutions of tertiary butanol (also called tertiary butyl alcohol, or TBA) in order to compare the results of optical spectroscopy with their existing measurements from neutron scattering experiments [80, 102, 103, 104, 105].

Tertiary butanol (C_2H_9OH) is the largest alcohol to be fully miscible with water at all concentrations [80]. If the hydrophobic part of the TBA molecule (the nonpolar methyl groups – see Fig. 4.16) were any bigger, the hydrophilic $-$OH group would be unable to compensate and the alcohol would not be soluble in water. For the same reason, TBA can be thought of as the most hydrophobic of the water-soluble alcohols, and aqueous tertiary butanol solutions are thus a natural system in which to study the hydrophobic effect (see Sec. 4.1 above for a discussion of the motivation for such a study). Neutron scattering experiments and EPSR simulations (introduced in Sec. 4.2.6) performed by Bowron, Finney and Soper have recently revealed the molecular details of hydrophobic interactions in several concentrations of aqueous TBA [80, 102]. They looked at three TBA mole fractions; $x_b = 0.06$, $x_b = 0.107$ and $x_b = 0.167$. The most dilute

composition is close to a region of the phase diagram which has interesting thermodynamic properties, while the most concentrated sample shows thermodynamic behaviour similar to the pure alcohol [80].

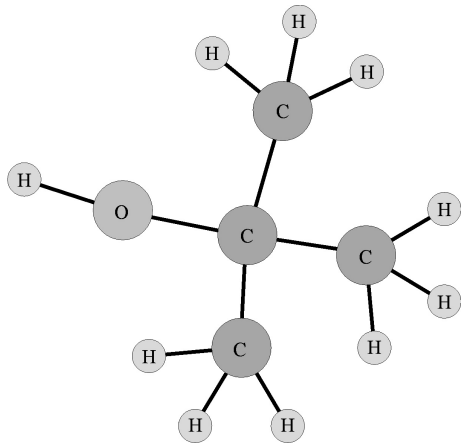

Figure 4.16: The tertiary butanol molecule. The neutron scattering experiments discussed in the text show that, at room temperature, TBA molecules in even the most dilute aqueous solutions tend to form clusters driven by the hydrophobic effect, i.e. the nonpolar methyl groups of neighbouring molecules prefer to bunch together. TBA molecules also prefer to hydrogen-bond to water rather than to each other.

This neutron scattering work focused on the behaviour of the alcohol molecules; the effect of TBA on the water structure was not discussed in detail, although the data which would enable this to be extracted does exist. The findings of these experiments can be summarised quite succinctly. Tertiary butanol molecules exist in clusters even in the most dilute solution studied. These clusters grow with increasing TBA mole fraction, and the origin of the clustering is hydrophobic – the methyl groups prefer to be together in order to minimise contact with water. No hydrogen-bonding is present between alcohol molecules, implying that a TBA molecule always prefers to H-bond to water rather than another TBA molecule. There is also evidence of polar-nonpolar contact between alcohol molecules, which was unexpected [102]. Unpublished small-angle neutron scattering data from experiments performed by the same researchers also shows unequivocal evidence of extremely long-range (tens of nm) structural correlations in dilute ($x_b < 0.06$) aqueous solutions of tertiary butanol [103, 104, 105]. It is unclear how such long-range effects can be produced by the hydrophobic hydration mechanism, and further studies are required to explain this extremely surprising phenomenon.

As was the case for the methanol–water mixtures discussed above, all of this existing data on aqueous tertiary butanol solutions is at the molecular level of detail, and no reports of Brillouin spectroscopy on the system have been published. Given the anomalous behaviour of the Brillouin shift and widths observed on varying the concentration and temperature in the methanol solutions, it was clear that a similar study of Brillouin scattering from aqueous TBA might both yield further novel results, and provide some information on bulk properties of the mixtures not probed by the neutron experiments.

Tertiary butanol with a stated purity of greater than 99% was obtained from Sigma and used without further purification. Aqueous tertiary butanol samples were prepared by weight using HPLC grade water, following the method described in Sec. 4.2.2.1 above. An additional complication was introduced due to the relatively high melting point of tertiary butanol (26 °C). The supply of pure TBA had first to be melted by placing the bottle in a shallow bath of warm water, then all glassware through which the alcohol passes during sample preparation had to be preheated in order to prevent solidification. Particular care was required to ensure that none of the water used for heating could contaminate the sample. Stages of preparation involving the pure alcohol had to be performed quickly, else cooling of glassware towards room temperature could cause the TBA to solidify.

Table 4.2 relates the tertiary butanol mole fractions x_b studied here to mass percentages and volume percentages at 20 °C in order to aid understanding of the results shown below. The phase diagram of aqueous tertiary butanol published by Murthy [87] using DSC and dielectric spectroscopy is shown in Fig. 4.17. All melting points measured during my experiments were consistent with this diagram. Significant hysteresis between melting and freezing points was observed, although the maximum difference of 12 °C is much less than the hysteresis observed in aqueous methanol (Sec. 4.2). For the purposes of this thesis, a discussion of the details of what solid phases lie below the liquid line is not necessary; the interested reader is referred to Murthy's paper [87].

TBA mole fraction x_b	0	0.061	0.107	0.167	1
TBA mass %	0	21	33	45	100
TBA volume % at 20 °C	0	25	38	51	100

Table 4.2: Lookup table for aqueous tertiary butanol compositions studied in this section, relating mole fraction, percentage TBA by mass and percentage TBA by volume at 20°C.

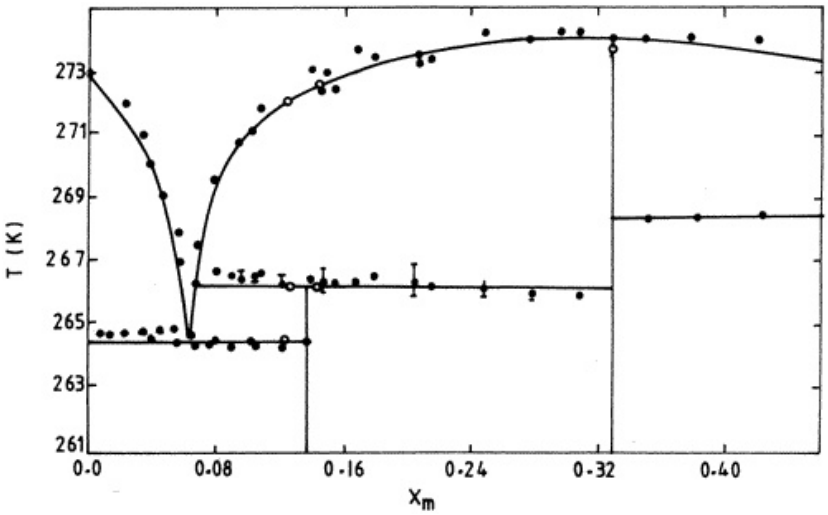

Figure 4.17: Phase diagram of aqueous tertiary-butanol reproduced from the paper by Murthy [87]. Note again that his measurements were made by heating the sample from the lowest temperature solid phase, in contrast to my experiments which cooled from room temperature.

Brillouin scattering from aqueous tertiary butanol solutions with TBA mole fractions $x_b = 0.06$, $x_b = 0.107$ and $x_b = 0.167$ were collected using the Brillouin spectrometer at Edinburgh. The Fabry-Perot interferometer was operating in the five-pass configuration with a free spectral range of 22.57 GHz and scattering angle of $90 \pm 0.5°$. The temperature of the samples was controlled at ambient pressure using the nitrogen-cooled and electrically heated sample holder described in Sec. 3.2.2.2. Spectra for the pure alcohol were collected in the same way. Data for pure water was also measured, with temperatures in the supercooled régime (below 0 °C) being taken either from the literature (for the frequency shifts) or achieved in our lab (peak widths) as discussed in Sec. 4.2.4 above. The results of these experiments are shown in Figs. 4.18 and 4.19, showing the Brillouin peak positions and full widths at half height respectively. These were measured from the spectra using Origin to perform Lorentzian fits to the data as

described in Sec. 3.3.2, incurring uncertainties of less than ±0.1 GHz in both quantities.

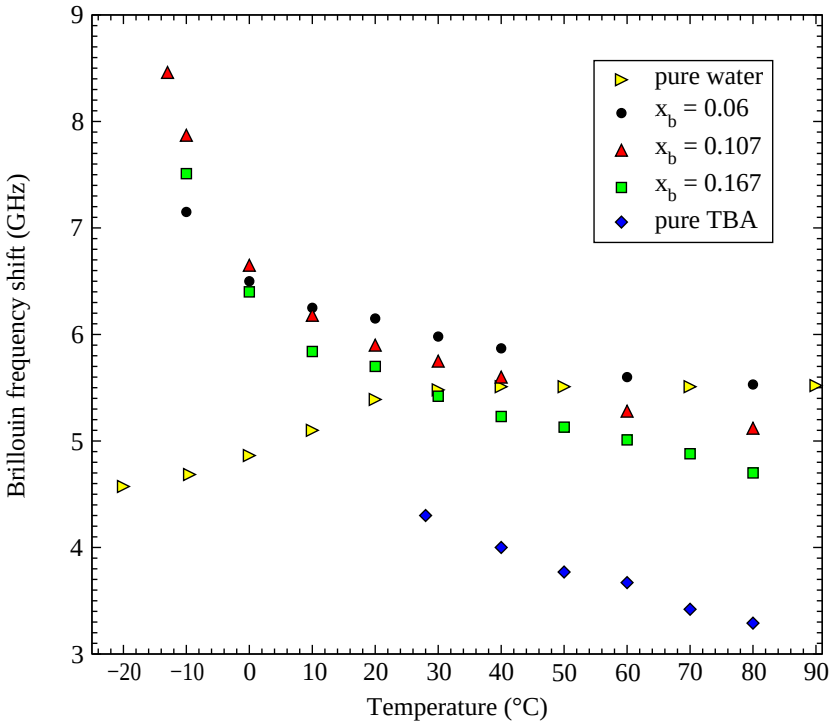

Figure 4.18: Temperature dependence of Brillouin peak frequencies for aqueous tertiary butanol. Data for pure water below 0°C is reproduced from Ref. [91], also shown in Fig. 4.15.

Several features in the behaviour of the Brillouin frequency shift ν_B may be noted from Fig. 4.18. Firstly, below 20 °C, the addition of even the smallest amount of tertiary butanol reverses the trend seen in pure water, in which the sound velocity (directly proportional to the Brillouin shift) *decreases* with temperature. Instead, the aqueous TBA solutions show a marked transition from a gradual increase above roughly 10 °C to a much more rapid increase below this temperature. This behaviour is qualitatively similar to the dramatic increase in sound velocity observed in the aqueous methanol spectra shown earlier (Fig. 4.9), with similarly high (∼ 9 GHz) frequency shifts occurring at the lowest temperatures, just above freezing. The higher freezing points of the TBA solutions mean that the region of anomalously high Brillouin shift is restricted to a 15 °C interval, whereas the increase could be traced across a range of at least 60 °C in intermediate concentrations of aqueous methanol. Note that the largest increase in Brillouin shift is seen in the $x_b = 0.107$ solution, which also has the lowest freezing point.

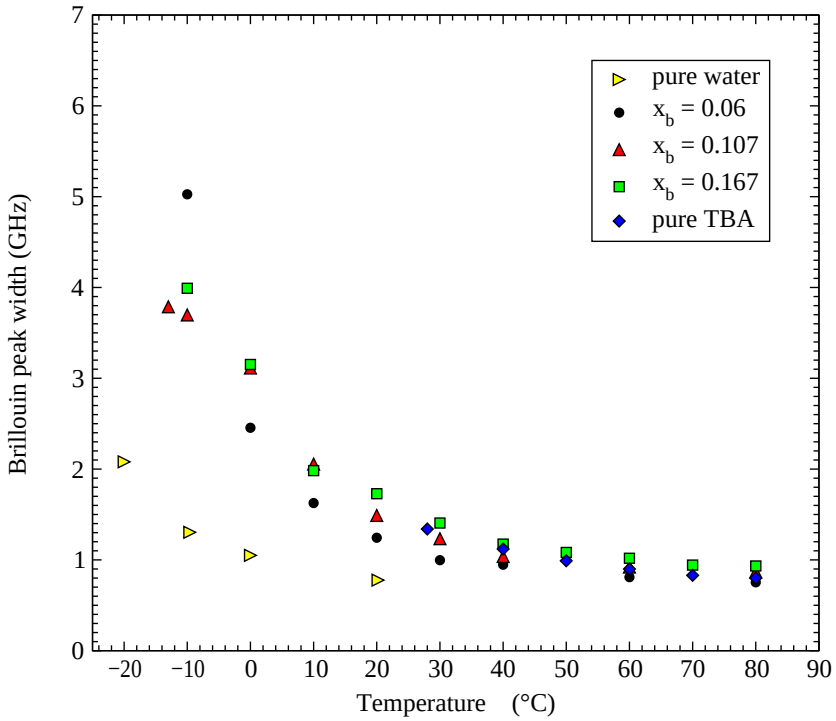

Figure 4.19: Temperature dependence of Brillouin peak widths for aqueous tertiary butanol. Data for pure water below 0 °C was obtained by supercooling water to −20 °C in our lab (see Sec. 4.2.4.2).

Looking at the behaviour of the Brillouin peak FWHH as shown in Fig. 4.19, one can see that, above 40 °C, there is very little difference in the widths of the three solutions and the pure alcohol. Below this temperature, the peak widths for all of the solutions increase rapidly, seemingly displaying a divergent behaviour which is not fully manifested due to the onset of freezing at ≈ −10 °C. Pure water behaves similarly, but the increase is not as dramatic at the temperatures probed here. As discussed in Sec. 4.2.4 above, Brillouin peak widths for pure supercooled water were not able to be extracted from the data for the classical absorption coefficient in Ref. [91] (reproduced in Fig. 4.15), so a method of supercooling water to −20 °C was devised in our lab (discussed in Sec. 4.2.4.2 above). The resulting spectra were of relatively poor quality, hence the uncertainty in the water data below 0 °C in Fig. 4.19 is greater than usual, being ±0.3 GHz.

As was the case in methanol–water mixtures (see Sec. 4.2.3), a weak additional central mode (the Mountain mode – due to structural or thermal relaxation) begins to appear in TBA–water spectra at all three concentrations at temperatures where the Brillouin

frequency and width are increasing rapidly. The mode is very weak and appears only in spectra just above freezing, making any quantitative analysis impossible.

The qualitative similarities (which will be discussed more fully in Sec. 4.3.1 below) between the effects seen in the Brillouin spectra of aqueous TBA and those found first in aqueous methanol suggested that it would be interesting to look at Raman scattering from the tertiary butanol solutions. Recall that the totally symmetric $C-O$ stretch mode in the Raman spectra of methanol–water mixtures splits into two peaks on cooling (Fig. 4.4) indicating that the methanol molecules must exist in two distinct environments (discussed in Sec. 4.2.1). Would a similar effect be seen in TBA–water mixtures, and if so, does this fit in with either the anomalous behaviour of the Brillouin shift and width shown in Figs. 4.18 and 4.19 or the results of neutron scattering summarised above?

Neal Crampton, an MPhys project student working with me during his undergraduate research project, agreed to perform these Raman experiments on aqueous tertiary butanol solutions. The results have not yet been published, but are reported in his Masters thesis [86] and are worth mentioning here. The tertiary butanol $C-O$ peak in TBA–water is indeed split, not into a doublet as for methanol–water, but into a *triplet*. This triplet was observed at all concentrations and temperatures studied (a similar range of x_b and T to the Brillouin experiments presented above was used). Note that the $C-O$ peak in *pure* TBA is also a triplet. These results suggest that TBA and water do not mix homogeneously in solution, for the same reasons as were discussed for the case of methanol–water in Sec. 4.2.1. This is consistent with the findings of the neutron diffraction experiments discussed above.

4.3.1 Discussion of results from TBA–water

Now that we have seen the results from Brillouin spectroscopy of aqueous tertiary butanol solutions, let us summarise briefly the most important findings, compare them to earlier findings on the methanol–water system, and discuss the resulting motivation for the less comprehensive Brillouin scattering experiments which will be presented in the remainder of this chapter.

The most important finding of these experiments on TBA–water is that behaviour qualitatively very similar to the anomalous effects first seen in methanol–water solutions is again exhibited. To recap, the Brillouin peak frequency ν_B (and hence the hypersonic sound velocity) undergoes a transition from a régime in which it varies little with cooling to a dramatic increase in ν_B which persists at temperatures below a point which is almost independent of sample composition. The Brillouin peak widths begin to increase rapidly with cooling below a certain temperature.

Although these effects are qualitatively the same as those observed in aqueous methanol and pure water, the temperatures at which the increases in peak frequency and width are approximately 20 °C higher in TBA–water. No maximum in peak width is observed in aqueous TBA, perhaps simply due to the higher freezing points which prevent sufficient cooling. If the maximum width occurs 20 °C higher than in methanol–water, this would put it between -15 °C and -25 °C, temperatures which were not obtainable in the liquid state in my experiments.

Without a clear idea of the origin of this anomalous hydrodynamic behaviour, this shift of the effects to higher temperature is difficult to explain. The direct quantitative comparison with the properties of pure supercooled water which was made in Sec. 4.2.7 for methanol–water is clearly not applicable in TBA, despite the similarity of the observed trends. Unlike that of methanol, the melting point of tertiary butanol is higher than that of water. Might this be relevant?

Unfortunately, no information on the effect of TBA on the structure of water in the solutions is available from the literature as was the case for methanol–water. The relevant radial distribution functions were not presented in the papers discussed above. This again makes a link between the properties of the solution and those of pure water very difficult to establish.

In summary, all we can say from these Brillouin scattering experiments is that very similar anomalous effects to those seen in methanol–water mixtures and pure water are present, but occur at roughly 20 °C higher in the aqueous tertiary butanol solutions. The next section will present the findings of a search for similar effects in other mixtures, both by performing further experiments and resorting to the literature. Time constraints meant that this survey had to be very cursory in comparison to the ex-

tensive work on methanol–water and TBA–water which form the main focus of this chapter.

4.4 Are the anomalous effects general? Extending the survey to other solutions

Having ascertained that aqueous solutions of tertiary butanol exhibit anomalous hydrodynamic behaviour very similar to that first observed in methanol–water mixtures, it was decided to look for similar effects in a range of other solutions. Brief Brillouin scattering studies of TBA–methanol mixtures and aqueous solutions of ammonia, ethylene glycol, sulfuric acid and other liquids were undertaken, the results of which are presented in the following sections. An extensive survey of the literature revealed hints that the anomalous behaviour is present in ethanol–water mixtures (Sec. 4.4.3.1) and is certainly found in aqueous lithium chloride solutions (Sec. 4.4.3.2) and several non-aqueous glass-formers.

4.4.1 TBA–methanol mixtures

As the interesting behaviour of the Brillouin frequencies and widths described above were observed in aqueous solutions of methanol and tertiary-butanol, a natural next step was to determine whether similar effects could be seen in a mixture of methanol and TBA. As discussed earlier, similarities between trends occurring in the mixtures and the behaviour of the corresponding quantities in supercooled pure water suggest that the effects seen in the solutions may be due to the presence of a relatively unperturbed water structure. The occurrence of these effects in a mixture not containing water would be a strong piece of evidence to counteract this idea.

A 50% by mass mixture of tertiary-butanol and methanol was prepared according to the method described in Sec. 4.2.2.1. This corresponds to a methanol mole fraction of $x_m = 0.70$ and a volume fraction of 50% at 20 °C. Brillouin spectra were recorded at ambient pressure using the nitrogen-cooled cell to access temperatures from 80 °C down to -90 °C, by which point the sample had not yet frozen. At the time when these

experiments were performed the cell was not able to cool any further; later developments enabled temperatures as low as -157 °C to be achieved, but given the results presented below it was not deemed necessary to extend the study of TBA–methanol solutions to lower temperature. The Fabry-Perot interferometer was again operated in the five-pass geometry with a scattering angle of 90 ± 0.5 °. Brillouin peak frequencies and widths (FWHH) measured using Lorentzian fits for the 50% by mass mixture of tertiary-butanol and methanol are presented in Figs. 4.20 and 4.21 respectively, along with several other datasets shown in order to allow comparisons to be made with the pure materials and aqueous solutions.

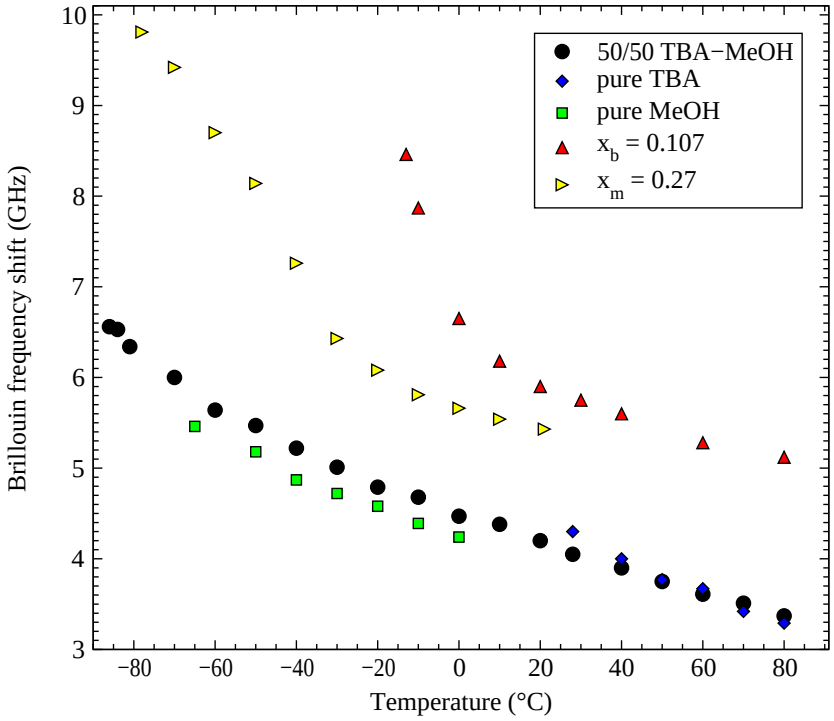

Figure 4.20: Brillouin peak frequencies for a 50% by mass TBA–methanol mixture. Data for the pure materials and aqueous solutions of both alcohols are also presented.

It can be seen from Fig. 4.20 that the Brillouin peak frequency ν_B and hence hypersonic sound velocity $v_s \sim \nu_B/q$ in a 50% TBA–methanol solution increases relatively slowly and almost linearly with cooling across the temperature range studied. This behaviour is very typical of molecular liquids. There is no sign of the anomalously large change in slope of this increase which occurs at around -20 °C in methanol–water solutions (the $x_m = 0.27$ data is shown in the Figure – see Fig. 4.9 for other concentrations) and at

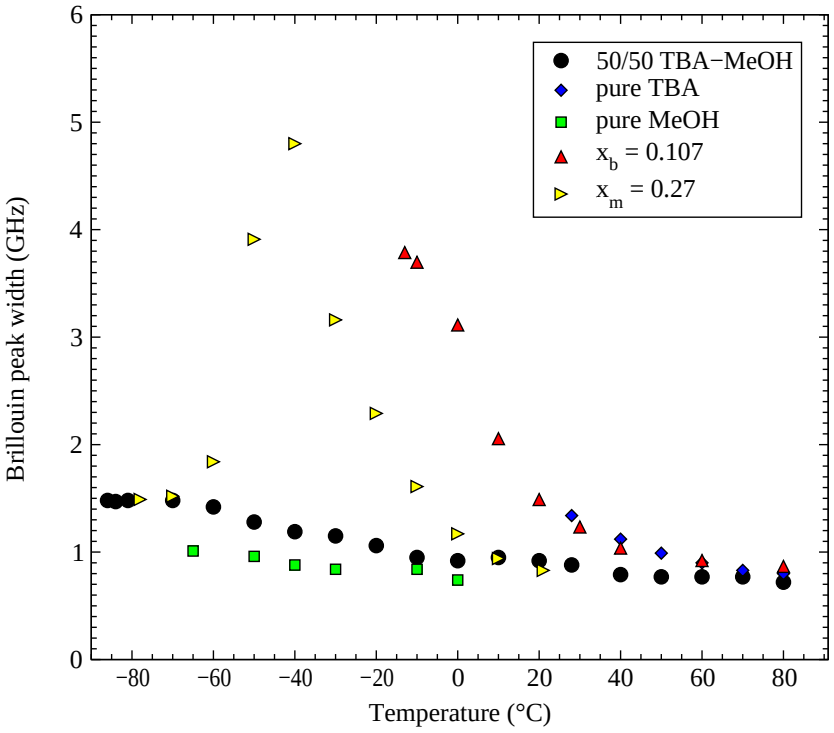

Figure 4.21: Brillouin peak widths (FWHH) for a 50% by mass TBA–methanol mixture. Data for the pure materials and aqueous solutions of both alcohols are also presented.

0 °C in the TBA–water solutions (see Fig. 4.18).

At temperatures above the melting point of tertiary-butanol (26 °C) Fig. 4.20 shows that ν_B has very nearly the same value in the pure material as in the 50% by mass solution. At temperatures where data for pure methanol is available, the Brillouin frequencies are only slightly higher in the TBA–methanol solution. Mixing equal masses of the alcohols together therefore has very little effect on the speed of hypersound in the liquid. Brillouin frequencies in the aqueous solutions are larger than in TBA–methanol and both pure materials at all temperatures shown, even before the approach to extremely high values seen at lower temperatures in the mixtures containing water.

The effect of reducing temperature on the Brillouin peak width in the TBA–methanol mixture (Fig. 4.21) is again typical of a non-relaxing molecular liquid. It gradually increases by only a very small amount across the entire temperature range studied, differing just slightly from the data for pure methanol. The rapid increase of peak width in both aqueous solutions (and subsequent narrowing in $x_m = 0.27$ methanol–water) is in stark contrast to this. Note however the slight increase seen in pure tertiary butanol before it freezes.

No Mountain mode (the additional central mode due to thermal or structural relaxation) was present in the TBA–methanol spectra at any temperature. Recall that such a mode was found to be present in methanol–water mixtures in the anomalous temperature régime (see Sec. 4.2.3), and seemed to appear at temperatures where the width is large just before freezing in the TBA–water mixtures (Sec. 4.3).

In summary, the results of Brillouin scattering from a 50% by mass mixture of tertiary-butanol and methanol across a wide range of temperatures do not show any of the anomalous behaviour present in the aqueous solutions of methanol and TBA studied in Secs. 4.2 and 4.3 above. This supports, but does not prove, the hypothesis that these anomalies are related to very similar behaviour in pure water, as proposed in Sec. 4.2.7 above. This motivated us to look for the effects in several other aqueous solutions, as will be discussed in the following section.

4.4.2 Survey of Brillouin spectra of several other aqueous solutions

Brillouin spectra were collected for several different aqueous solutions as a function of temperature using precisely the same apparatus and techniques as described for the methanol–water experiments in Sec. 4.2 above. Binary mixtures of water with ammonia (NH_3), ethylene glycol (antifreeze) ($C_2H_4(OH)_2$), sulfuric acid (H_2SO_4), glycerol ($C_3H_5(OH)_3$) and salt (brine) (NaCl) were studied in order to ascertain whether or not the anomalous effects observed in methanol–water and TBA–water are present in other aqueous solutions. Only one arbitrarily chosen concentration of each mixture was used in order to survey as many solutes as possible in the limited time available. All chemicals were obtained at the highest purity available from Sigma. These experiments were performed in collaboration with Mr. Hugh Vass.

Figs. 4.22 and 4.23 show the Brillouin peak frequencies and widths respectively of a 30% by mass ammonia–water mixture, a 53% by mass solution of ethylene glycol in water and a 35% by mass aqueous solution of sulfuric acid. These were measured using Lorentzian fits as described in Sec. 3.3.2 and are subject to the minimal uncertainties discussed therein. Trends very similar to the anomalous behaviour first observed in methanol–water mixtures are clearly present in these solutions, as will be discussed below.

Data from brine and glycerol–water are not shown because the brine could not be cooled sufficiently in the liquid phase to reach the anomalous temperature range, and aqueous glycerol displayed similar anomalous behaviour of peak shift and width, but at much higher temperatures. This was suspected to be due to the glass-forming properties of glycerol itself, which is approximately 200 times more viscous than water at room temperature [9] and has a glass transition at -93 °C [55]. Measurements on pure glycerol supported this hypothesis – the anomalous effects were observed at similar temperatures.

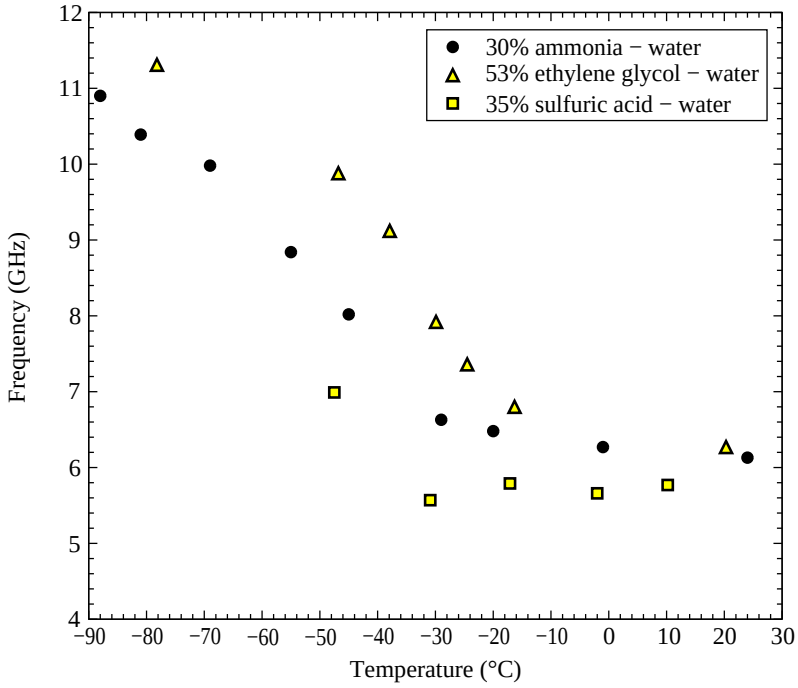

Figure 4.22: Brillouin peak frequencies for a 30% by mass ammonia–water mixture, a 53% by mass solution of ethylene glycol in water and a 35% by mass aqueous solution of sulfuric acid as a function of temperature.

The Brillouin peak frequencies in all three aqueous solutions shown in Fig. 4.22 display the anomalous increase observed in methanol–water and TBA–water mixtures. In the ammonia solution this occurs near -30 °C, in aqueous ethylene glycol -20 °C and in aqueous sulfuric acid -30 °C again. Recall that the increase occurred at -20 °C in methanol–water and 0 °C in TBA–water regardless of sample concentration.

The Brillouin peak widths (FWHH) shown in Fig. 4.23 also all display anomalous behaviour similar to that observed in the alcohol–water solutions earlier in this chapter.

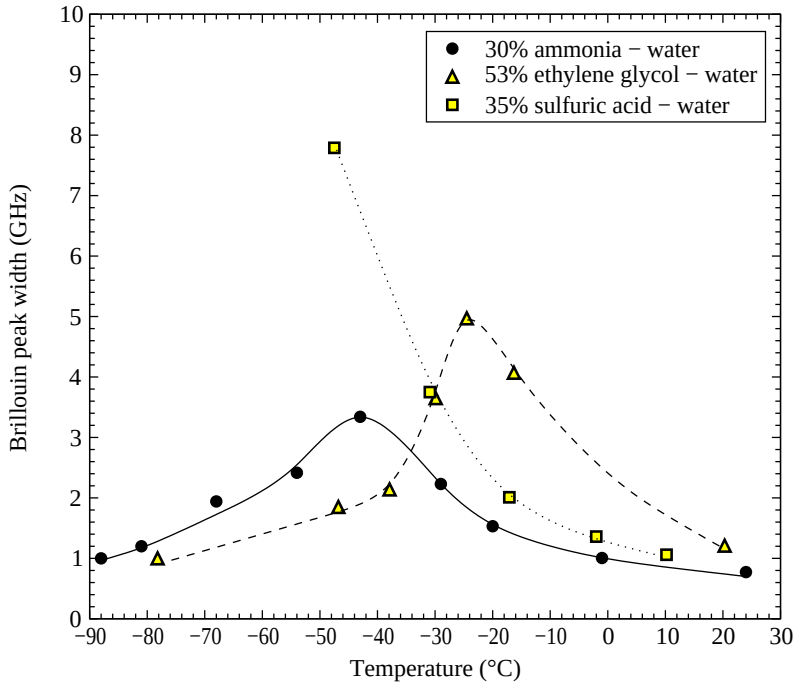

Figure 4.23: Brillouin peak widths for a 30% by mass ammonia–water mixture, a 53% by mass solution of ethylene glycol in water and a 35% by mass aqueous solution of sulfuric acid as a function of temperature. Lines through the data points are included merely as a guide to the eye – they are not numerical fits.

Aqueous ammonia has a distinct maximum broadening at -45 °C, the same temperature at which the maximum width in methanol–water occurs. Aqueous ethylene glycol has a sharper maximum at -24 °C. The Brillouin peak width in aqueous sulfuric acid increases even more dramatically with cooling, but the sample froze before any temperature of maximum broadening was observed. Based on the behaviour of all the other aqueous solutions studied in this chapter, it seems likely that narrowing will occur at some temperature resulting in a maximum below -48 °C, or if the lineshape is extremely sharp, perhaps between -48 °C and -31 °C. Further measurements between these temperatures would test this possibility.

4.4.2.1 Summary of results from aqueous solutions

In summary, effects qualitatively the same as observed in methanol–water and TBA–water mixtures have been found to be present in four further aqueous solutions. The only aqueous solution studied which did not display the anomalous behaviour was brine, which froze at such a high temperature that any effects which may be present

in the supercooled liquid were hidden. Results from the glycerol–water mixture were complicated by the glass-forming nature of the solute; the increase in sound speed and maximum absorption were observed at much higher temperatures than in the other aqueous solutions. In aqueous ammonia, ethylene glycol and sulfuric acid the same anomalous increase in sound speed as was observed at -20 °C in methanol–water and 0 °C in TBA–water occurred between -20 °C and -30 °C. The maximum in sound absorption which was observed around -40 °C in methanol–water was seen at -45 °C in ammonia–water and -24 °C in aqueous ethylene glycol. A maximum below -31 °C seems likely, but was not observed, in aqueous sulfuric acid.

4.4.3 Brillouin studies of other mixtures in the literature

In addition to the experiments reported above which showed that anomalous hydrodynamic behaviour occurs in a range of aqueous solutions, a survey of the literature revealed that similar effects have been observed in a few other systems. The most important of these – aqueous solutions of ethanol and lithium chloride – will now be discussed in some detail.

4.4.3.1 Ethanol–water and D_2O–water mixtures

One of the first studies of sound propagation in supercooled water was published in 1982 by Conde, Teixeira and Papon [53] who used Brillouin spectroscopy to measure sound velocities at temperatures as low as -20 °C. Due to the difficulties involved in preventing crystallisation in pure water, they added small amounts of an impurity in order to suppress freezing, making it much easier to access the lowest temperatures. Two such mixtures were studied as a function of temperature and concentration: aqueous solutions of heavy water (D_2O) and ethanol (C_2H_5OH).

The D_2O–water solutions do not exhibit any of the anomalous effects noted above. The sound velocity follows the same trend as seen in pure water above -20 °C; it decreases monotonically with cooling. It is of course possible that the small upturn in the hypersound velocity in pure water seen by Maisano *et al* [91, 94] and Cunsolo and Nardone [92] at -22 °C (see Fig. 4.15) might occur in the mixture at lower temperatures,

but no measurements below -20 °C are reported in Ref. [53].

Much more interesting is the behaviour seen in the ethanol–water solutions. For ethanol mole fractions from $x_e = 0.032$ up to $x_e = 0.0825$ (the highest concentration studied) the sound velocity shows a distinct upturn at around -15 °C. The trend is very similar to that seen in the methanol–water mixtures looked at in Sec. 4.2 above. At lower ethanol concentrations the velocity decreases as the temperature is reduced, before passing through a minimum and then increasing rapidly with further cooling. At higher concentrations the velocity does not change with cooling until about -15 °C, then again begins to increase.

Evidence of a new trend?

Thus the anomalous increase in sound velocity is not present in D_2O–water solutions above -20 °C, but does occur in ethanol–water mixtures, beginning at around -15 °C – between the temperatures at which the effect is manifested in methanol–water (-20 °C) and TBA–water solutions (0 °C). This is suggestive of a trend: the temperature at which the sound velocity begins to increase in aqueous alcohol solutions seems to rise with the size of the alcohol. Extension to lower temperatures of the work on ethanol–water presented in Ref. [53], together with a search for the effect in aqueous propanol (C_3H_7OH) solutions would therefore be extremely interesting.

Unfortunately the Conde *et al* paper [53] does not present any information on widths of the Brillouin peak in either solution. Hence it is not possible to determine whether or not the maximum in peak widths observed upon cooling several aqueous solutions as discussed above is present in D_2O–water or ethanol–water mixtures.

4.4.3.2 Glass-forming liquids – aqueous and non-aqueous

Behaviour very similar to the anomalous hydrodynamic effects observed in aqueous solutions of methanol, tertiary butanol and the other solutes discussed in Sec. 4.4.2 was found in an extremely detailed Brillouin scattering study of glass formation in aqueous lithium chloride (LiCl) [22]. This paper by Tao, Li and Cummins used both conventional generalised hydrodynamics and (for the first time) the mode-coupling theory introduced in Sec. 4.1.1 to analyse the results of Brillouin spectroscopy, and

were able to identify a glass transition temperature T_g in agreement with the results of other techniques. The results of this work on aqueous LiCl are so similar to my findings in aqueous alcohols, and the treatment of the hydrodynamic effects with reference to the glass transition so complete, that the findings of Tao *et al* will now be discussed in some detail.

The glass-forming ability of aqueous LiCl solutions is composition dependent; a glass only forms between mole fractions $x_l = 0.11$ and $x_l = 0.30$ with both weaker and stronger concentrations crystallising easily on cooling. The glass transition in an $x_l = 0.15$ solution is stated to be at $-128\,^{\circ}\mathrm{C}$ based on earlier heat capacity measurements, and other glass-forming samples vitrified within a few degrees of this temperature.

The behaviour of the Brillouin peak shift with cooling (Fig. 4.24 (a)) is extremely like that observed in aqueous methanol, as described in Sec. 4.2.4.1 above. Solutions with $x_l \leq 0.15$ show a decrease in sound speed[‖] down to -20 °C, below which a rapid increase begins. The two higher concentrations show a similar transition between a normal rate of increase with cooling and a much more rapid growth at a higher temperature, approximately 20 °C. Solutions which do not crystallise exhibit a second change in slope at around 145 K or $-128\,^{\circ}\mathrm{C}$, the glass transition temperature T_g. This 'levelling off' was not seen in any of my experiments and since the work of Tao *et al* has come to be identified as a signature of the glass transition.

The Brillouin peak width (proportional to sound attenuation) also behaves very similarly in aqueous LiCl (Fig. 4.24 (b)) and aqueous methanol (Fig. 4.10). A pronounced maximum is apparent, with increasing concentration of solute allowing the low-temperature side of the maximum to be more fully revealed. A difference between the two systems is that the position of the maximum seems to be much more dependent on concentration in aqueous LiCl. The three lowest concentrations have a maximum at -40 °C (the same as in aqueous methanol) whereas the two higher concentrations have the maximum near 0 °C. If anything the trend in methanol–water solutions is the opposite – lower concentrations may have the maximum a few degrees higher than stronger solutions (see Fig. 4.10).

[‖] Taken by the authors to be evidence that "part of the water in the solution retains the structure of pure water" as was proposed for the methanol–water mixtures in Sec. 4.2.7 above.

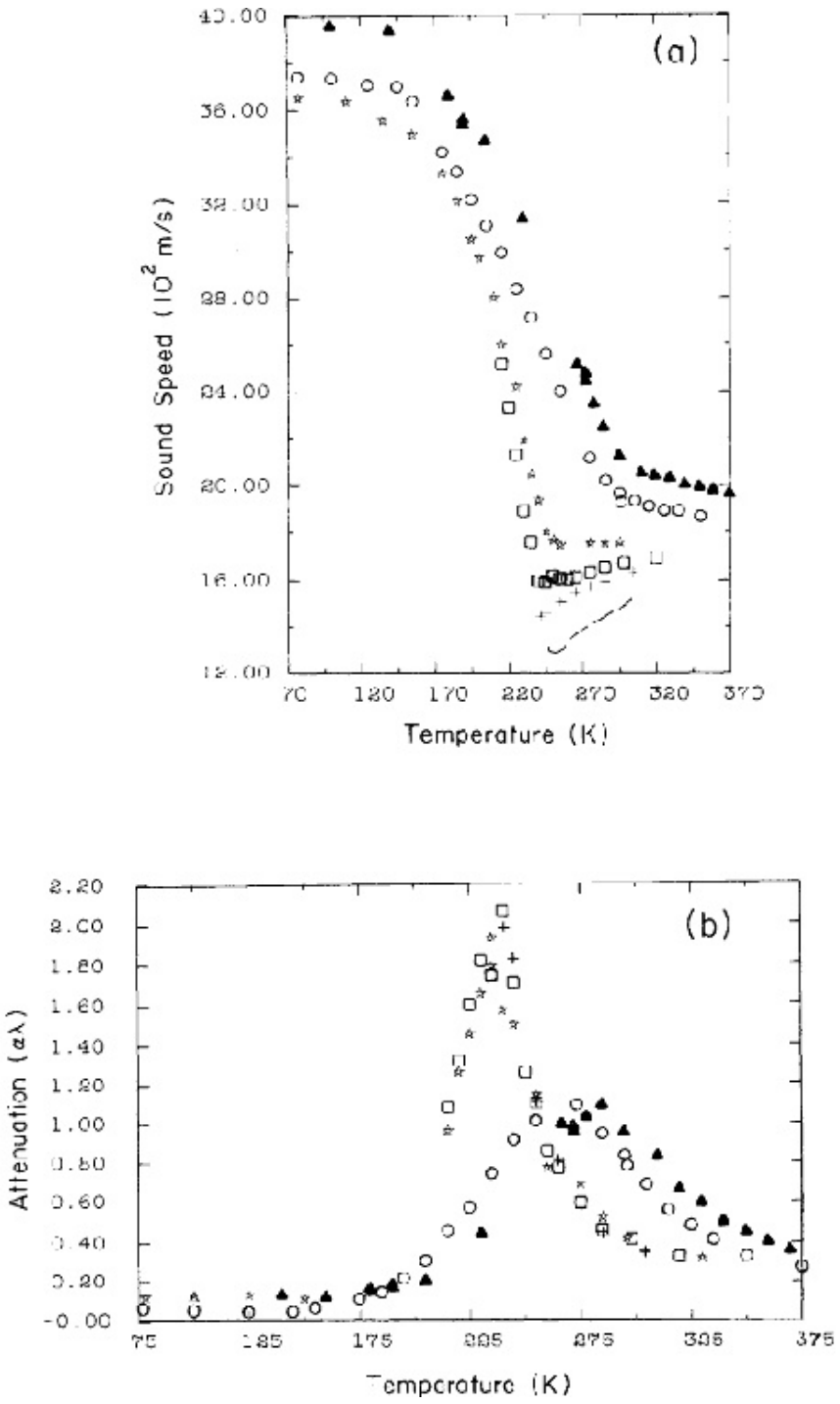

Figure 4.24: (a) *Sound speed and* (b) *attenuation in cooled aqueous* LiCl, *reproduced from Ref. [22]. Note the similarities with the anomalous Brillouin shifts and widths found in aqueous methanol solutions earlier in this chapter. Triangles, circles, stars, squares and crosses represent* x_l = 0.36, *0.30, 0.15, 0.10 and 0.05 respectively. The dashed line in* (a) *is the data for pure water from Ref. [91].*

An additional central (Mountain) mode is seen to arise and narrow with cooling in the aqueous LiCl solutions, disappearing into the wings of the Rayleigh peak at very low temperatures. This same mode was seen in aqueous methanol (Sec. 4.2.3) and the other mixtures in which the anomalous Brillouin shifts and widths were observed.

All this behaviour is explained in two different but complementary ways. The most straightforward interpretation of the data is that the sound speed increases from liquid-like to solid-like behaviour with cooling towards and through the glass transition, in agreement with the old model of a glass-forming system as an evolving composite of liquid-like and solid-like cells. The alternative approach postulates a single structural relaxation, the timescale of which moves through the frequency window probed by Brillouin spectroscopy as the sample is cooled. Ref. [22] successfully uses the generalised hydrodynamics framework (i.e. the Mountain mode introduced in Sec. 2.2.3) to fit the spectra at all temperatures, confirming the ability of a structural relaxation to produce the anomalous Brillouin peak shifts and widths in aqueous LiCl. The relaxation time in generalised hydrodynamics is introduced *ad hoc* without relation to any physical model of what it means, hence Tao *et al* appealed to an idealised version of the then very new mode-coupling theory in order to attempt to identify this relaxation with the slow MCT α relaxation (see Sec. 4.1.1). They found that the theory produced Brillouin spectra showing the same qualitative trends as experiments, but perhaps due to the simplicity of the model were unable to obtain good quantitative agreement.

One feature of the results of Ref. [22] which is not discussed in the paper is that the compositions which do not form a glass appear to behave very similarly to those which do. Although not fully expressed, both the increase in sound speed and maximum absorption are both clearly present in the $x_l = 0.05$ and $x_l = 0.10$ solutions. It seems that 'pre-glassy' behaviour is exhibited but prevented from developing further by the intervention of the crystalline phase. Is this concept relevant in interpreting the results from alcohol–water mixtures? Glasses were not formed during any of my experiments, but the anomalous hydrodynamics seem to be very similar to these pre-glassy dynamics in aqueous LiCl.

It is possible that my Brillouin scattering studies of methanol–water mixtures did not reach low enough temperatures for any glass transition to be observed, but x-ray diffrac-

tion patterns suggest that crystallisation occurs in $x_m = 0.3$ and $x_m = 0.4$ not far below the low-temperature limit of the optical experiments. It would however be very interesting to extend the Brillouin studies down to the lower temperatures which became achievable later in the development of the temperature cell in order to search for the levelling off of the sound speed indicative of the glass transition. Tao *et al* also observed the emergence of transverse acoustic (TA) modes at temperatures above T_g, indicating the ability of the supercooled liquid to support shear waves (see e.g. Ref. [106]). These were never seen in methanol–water solutions – might they appear at lower temperatures than studied in Sec. 4.2?

Another point which is not discussed in Ref. [22] is that the glass transition in aqueous LiCl ($T_g = -128\,^\circ$C) is very close to the glass transition in pure water, which occurs at -137 °C [57]. This may be purely coincidental, but could it suggest that the properties of pure water (the structure of which is well maintained in the solution) are important in determining the behaviour of the solution? Note that T_g is unchanged by the concentration of LiCl in the glass-forming range. All but the two highest concentrations of aqueous LiCl exhibit the anomalous increases in peak frequency and width at the same temperature as pure water.

Unfortunately, no other Brillouin scattering studies of aqueous glass-formers could be found in the literature. The qualitative agreement with the predictions of mode-coupling theory did however prompt several applications of the technique to various non-aqueous glass-forming liquids. Experiments on salol [24, 27], propylene carbonate [25, 26], *m*-fluoroaniline [107], meta-toluidine [108] and several other systems all show a levelling off of the sound speed at T_g and a maximum in attenuation at a higher temperature, identified in all cases with the MCT α relaxation. Transverse acoustic modes are also observed above T_g. The temperature at which the effects occur vary greatly in these non-aqueous liquids depending on the location of the glass transition and the type of glass-former (the classification of glass-formers is beyond the scope of this thesis).

4.4.4 Summary of findings from a range of liquids

This section has discussed the results of Brillouin scattering on a wide range of liquids in an attempt to identify the common features shared by those systems which exhibit the anomalous trends in Brillouin peak shifts and widths observed in my experiments on methanol–water mixtures. Aqueous solutions of ammonia, sulfuric acid and lithium chloride all display an increase in sound speed and a maximum in sound absorption very near to the temperature at which these effects occur in aqueous methanol and – perhaps most importantly – pure water. No maximum broadening has been observed in pure water at ambient pressure due to the intervention of freezing, but both groups who have studied deeply supercooled water extrapolated from the increase in width with cooling to propose that a maximum should occur at -45 °C, the same temperature at which it is seen in methanol–water (see Sec. 4.2.7.1 above). Similar effects occur at different temperatures in TBA–water, glycerol–water and several non-aqueous glass-formers. Precursors to the anomalies are present in aqueous ethanol above -20 °C.

Two important conclusions may be drawn from the contents of this section. Firstly, the increase in sound speed and maximum in sound absorption appear to be present in all aqueous solutions which can be cooled to a low enough temperature, and most of these exhibit this behaviour very near to the temperature at which it occurs in pure water. Secondly, a link has been established with the behaviour of glass-forming liquids in general, suggesting that the effects seen in aqueous solutions may be successfully modelled using the mode-coupling theory which describes structural relaxation in supercooled liquids approaching the glass transition. This will be discussed further in Sec. 4.6 below.

4.5 Brillouin spectroscopy of compressed water and aqueous solutions

As stated at the outset and discussed in Chapter 3, one of the initial aims of this research project was to develop a pressure cell enabling the measurement of Brillouin scattering from liquids from atmospheric pressure up to at least 15 kbar. The design and

construction of this device was undertaken by Mr. Hugh Vass as part of his MSc research [45], and was summarised in Sec. 3.2.2.2. The development of the pressure cell was completed at a time when the all of the results presented so far in this chapter had been collected and analysed, and they suggested that an exploratory program of Brillouin spectroscopy on compressed water and aqueous solutions might be an enlightening first application of the new apparatus. All of the experiments reported here using the pressure cell were performed by Hugh Vass due to the difficulty of loading and pressurising the system without damaging it and/or the operator.

There are two main reasons for suspecting that high pressure studies should shed some light on the anomalous hydrodynamic effects observed in aqueous solutions at ambient pressure. Firstly, the application of high pressure inhibits the formation of solid phases with cooling in water; the lowest temperature at which stable liquid water exists is near the ice-I/ice-III triple point at $T = -22\,^{\circ}\mathrm{C}$, $P = 2.09\,\mathrm{kbar}$ [55]. Several pieces of evidence have been presented in the preceding sections which show that the bulk water structure persists in aqueous solutions even at quite high solute concentrations, hence this suppression of freezing may occur in mixtures as well as pure water. Recall also that the debate over the reason for the anomalous behaviour of deeply supercooled pure water (discussed in Sec. 4.1.1) hinges on the existence or otherwise of a second critical point in a region of the phase diagram not accessible to experiments. This point terminates a phase boundary between two liquid phases of different density, suggesting that variable pressure work may provide valuable new information.

Few such studies have been reported, probably due to the difficulties inherent in performing experiments at high pressures and low temperatures on large enough volumes of liquid. Soper and Ricci [77] used the advanced neutron diffraction techniques discussed in Sec. 4.2.6 to reveal for the first time a continuous transformation from a low- to high-density water structure as the pressure is increased from 0 kbar to 5 kbar at -5 °C. Mishima and Stanley [75] reported volumetric measurements showing a line of first order transitions between low- and high-density amorphous ices which they take to be supporting evidence for the existence of the second critical point. No work on Brillouin scattering from water or aqueous solutions at variable temperature and pressure has been reported.

Brillouin scattering from pure water and a 50% by mass methanol–water solution was measured at pressures up to 5 kbar in the large-volume pressure cell described in Sec. 3.2.2.2, with the temperature controlled to better than ±0.2 °C using the nitrogen gas system detailed in the same section together with electrical heaters mounted in the cell body. HPLC grade water from Sigma was used and the cell was thoroughly cleaned before and after each run to avoid contamination of the sample. No systematic attempt to supercool the water was made, hence the low-temperature limit of the data is set by the equilibrium freezing point of water at the pressures studied. Brillouin frequency shifts as a function of temperature and pressure – measured from the experimental spectra using Lorentzian fits (see Sec. 3.3.2) – are shown in Fig. 4.25. The four lowest-temperature data points for pure water at ambient pressure are reproduced from Ref. [91] because of the difficulty of supercooling to such an extent in our laboratory. The ambient pressure data for the $x_m = 0.27$ (roughly 50% by mass) methanol–water mixture studied in Sec. 4.2.3 is included in the figure for comparison. Full widths at half height of the Brillouin peak measured from Lorentzian fits are displayed for pure water and a 50% by mass methanol–water mixture at variable temperature and pressure in Fig. 4.26.

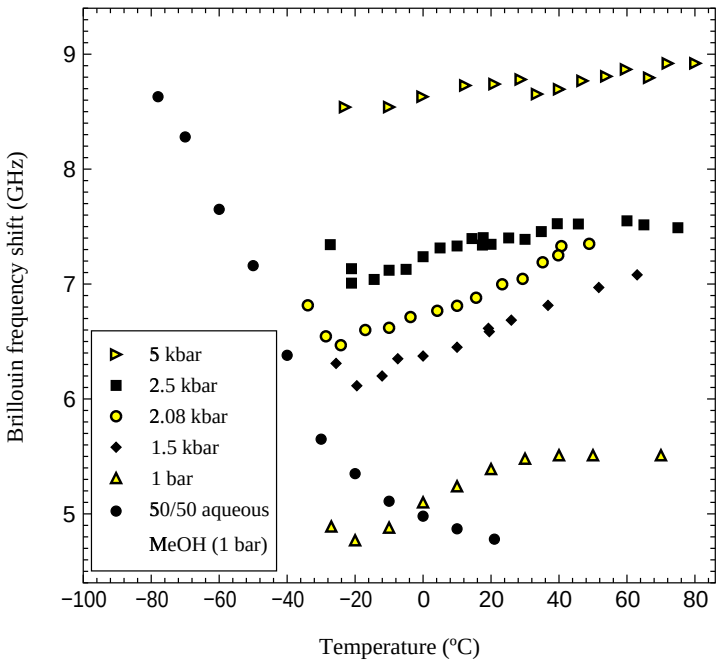

Figure 4.25: Brillouin shifts of pure water as a function of temperature at several pressures up to 5 kbar. *Ambient pressure data for an* $x_m = 0.27$ *methanol–water mixture is included for comparison. Low-temperature ambient pressure data for pure water is taken from Ref. [91].*

The Brillouin frequency shifts (and hence hypersound speeds) for pure water shown in Fig. 4.25 display the typical decrease with temperature associated with its hydrogen-bonded structure [90] at all pressures. The key finding however is that at all pressures other than 5 kbar this trend is reversed near -20 °C, below which the sound speed *increases* sharply with further cooling. This is precisely the same behaviour, at the same temperature, as was observed at ambient pressure in methanol–water (Sec. 4.2.4) mixtures, aqueous solutions of ammonia and ethylene glycol (Sec. 4.4.2) and aqueous lithium chloride (Sec. 4.4.3.2). This is illustrated by comparison with the ambient pressure $x_m = 0.27$ methanol–water solution in Fig. 4.25; the sharp increase in Brillouin peak frequency occurs at the same temperature as in compressed water.

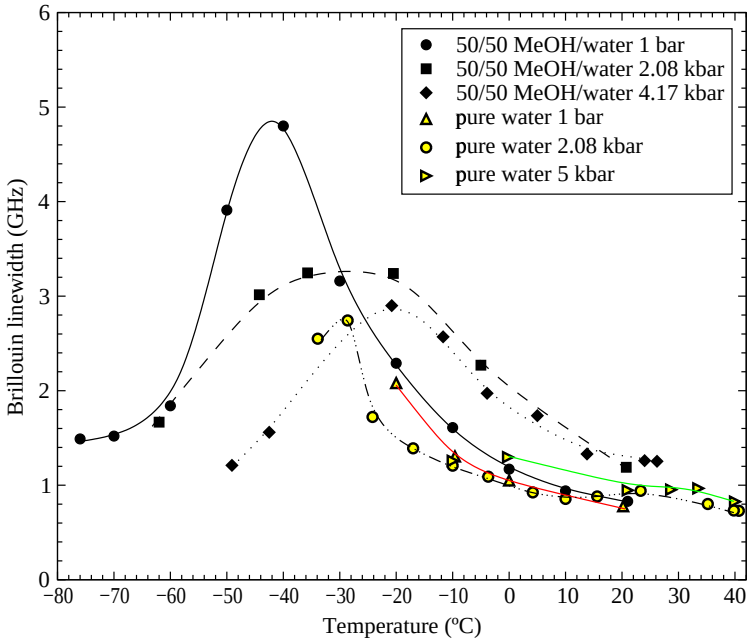

Figure 4.26: Brillouin peak widths (FWHH) of water and 50/50 methanol–water as a function of temperature at several pressures up to 5 kbar. *Lines joining the points are included merely as visual aids – they are not numerical fits to the data.*

The Brillouin peak widths (and hence hypersound absorption) in compressed pure water and 50% by mass methanol–water solution shown in Fig. 4.26 also display behaviour very similar to that seen at ambient pressure in the aqueous solutions studied at ambient pressure earlier in this chapter. Looking firstly at the effect of compression on the methanol–water mixture, we see that the position of the maximum in peak width moves to higher temperatures with increasing pressure. At ambient pressure the max-

imum occurs between -40 °C and -45 °C as was discussed in Sec. 4.2.3, at 2.08 kbar the maximum is at -30 °C and is broader, whilst at 4.17 kbar the maximum narrows slightly and is centred on -20 °C. There is therefore a roughly linear increase of the temperature of maximum broadening as the methanol–water solution is compressed.

Less may be said about the behaviour of the Brillouin peak width in pure water under pressure because the intervention of freezing limits the temperatures to which the liquid can be cooled in the pressure cell, which is not suited to any attempt at supercooling. At ambient pressure, the widths in water increase in a very similar manner to the mixture at the same pressure, as has been commented on in Sec. 4.2.4.2 above. At 2.08 kbar (the pressure at which the melting point of water is at a minimum [55]), there appears to be a sharp maximum in the peak width at -30 °C, although only one data point showing subsequent narrowing of the peak could be obtained due to the sample freezing close to -35 °C. This maximum occurs at the same temperature as the maximum broadening in the methanol–water mixture at the same pressure. Pure water at 5 kbar froze at too high a temperature for any significant broadening to be observed.

4.5.1 Summary of results on compressed water and aqueous methanol

This first ever study of Brillouin scattering as a function of temperature in compressed water and a 50% by mass methanol–water mixture has identified at least two very interesting trends:

- the Brillouin peak frequency (and hence speed of hypersound) changes from decreasing (normal behaviour) to increasing with cooling below -20 °C at all pressures below 5 kbar, the same temperature at which the sound speed begins to increase in aqueous solutions of methanol at ambient pressure;

- a maximum in Brillouin peak width (and therefore sound absorption) is observed at -30 °C and 2.08 kbar, and aqueous methanol has a maximum at the same P, T. At ambient pressure, the maximum occurs at -45 °C in methanol–water, the temperature at which a maximum in pure water is suggested, but not observed, by Refs. [92] and [94].

The shape of the maximum absorption in aqueous methanol under pressure is also worthy of comment; it is very broad, most noticeably at 2.08 kbar. At this pressure, the broadening of the Brillouin peak begins roughly 40 °C higher than in pure water, despite the fact that the centre of the maximum occurs at the same temperature for both liquids.

4.6 Discussion: anomalous hydrodynamics in aqueous solutions at low temperatures

This chapter set out to apply the newly available technique of Brillouin spectroscopy to the study of aqueous alcohol solutions, in an attempt to provide information complementary to the results of recent neutron diffraction [81,84] and Raman spectroscopy work [49]. Surprising hydrodynamic behaviour – a sudden increase in the high-frequency sound velocity and a maximum in its absorption – was discovered on cooling a range of methanol–water mixtures and subsequently found to occur at low temperatures in all other aqueous solutions tested.

No direct link to the findings of the neutron diffraction research was apparent until it was noticed that the same anomalous hydrodynamic behaviour had earlier been observed in supercooled pure water [91, 94, 92]. Could the effect in solution be due to the presence of a relatively unperturbed hydrogen-bonded water network? This seems consistent with the findings of the latest neutron [84], Raman [49] and x-ray [82] experiments performed by my colleagues at Edinburgh and our collaborators. All of these techniques have produced unequivocal evidence for the existence of a water structure almost identical to the bulk liquid up to concentrations as high as $x_m = 0.7$ methanol–water at room temperature. If the water network is present, it is reasonable to assume that the peculiar sound propagation characteristics of supercooled pure water might be evident in the Brillouin spectrum of the solution at the same temperature.

What is the origin of this strange increase in Brillouin peak frequency and width in supercooled pure water? The most plausible answer to this question is suggested by a detailed Brillouin scattering study of the glass transition in aqueous lithium chloride [22] (discussed in Sec. 4.4.3.2), which again provides evidence for the existence of bulk water

in aqueous solution. The same anomalous hydrodynamic behaviour was observed in this system at very similar temperatures, and is explained in terms of a structural relaxation passing through the window of frequencies probed by Brillouin spectroscopy as it slows down due to increasing viscosity with cooling towards the glass transition. These pre-glassy dynamics can be described in terms of an additional Mountain mode as described in Sec. 2.2.3, but more interestingly may also be identified with the α relaxation of the mode-coupling theory.

It has recently been proposed that the anomalous apparently singular properties of supercooled pure water (see Sec. 4.1.1) are also hallmarks of the approach to a glass transition [64], consistent more with the singularity-free hypothesis than the proposed second critical point scenario. We would then expect the Brillouin peak frequencies and widths to follow the same trends as those in the glass-forming aqueous LiCl and the other aqueous solutions studied here. This does indeed appear to be the case, although the behaviour is not fully expressed (no maximum width is observed) because the line of homogeneous nucleation ensures that sufficiently low temperatures cannot be reached in the laboratory.

A hypothesis explaining the anomalous hydrodynamic behaviour seen on cooling aqueous methanol solutions may therefore be formulated as follows. Segregation on molecular lengthscales allows an extended water network very similar to that of bulk water at the same temperature to exist even at methanol concentrations as high as $x_m = 0.7$. The increase in hypersound velocity and absorption associated with this bulk water is observed in the Brillouin spectrum, and may be traced to lower temperatures in the solution due to suppression of freezing by the dissolved species. This enables the structural relaxation behaviour predicted by MCT and observed in aqueous LiCl to be fully manifested by the water in the solution as it supercools towards water's glass transition – the absorption of sound goes through a maximum and the sound velocity increases towards a solid-like value.

Preliminary results from the neutron diffraction experiments presented in Sec. 4.2.6 support this idea – the structure of the water-rich areas in a 50/50 methanol–water solution tends with cooling towards that of low-density amorphous ice rather than the crystalline solid.

Further pieces of evidence for this hypothesis are the existence of glassy signatures in the low-frequency Raman spectrum of aqueous methanol solutions, a transitory Mountain mode indicative of structural relaxation in the Brillouin spectrum at low temperatures, and the fact (perhaps a coincidence) that aqueous LiCl has a glass transition at a temperature very close to that of pure water. The fact that pre-glassy dynamics are observed in a wide range of non-glass-forming aqueous solutions is also consistent with the idea that it is the water, not the solution as a whole, which is approaching a glass transition.

The most important question which is not answered by this proposed explanation is that although the anomalous effects occur at the same temperature as in pure water for most of the aqueous solutions studied here, some of them exhibit the behaviour at higher temperatures (notably TBA–water and glycerol–water). These solutions differ from the others in that glycerol itself is a glass-former with a much higher T_g than water, and TBA freezes at a higher temperature than water. Might these differences be responsible for the effect shifting to higher temperatures than in pure water?

It is clear that this picture of pre-glassy dynamics exhibited by regions of bulk water in aqueous solutions requires further investigation, but the suggestion does appear to be consistent with most of the available data from other sources, and as such deserves attention. Hopefully the final results of the variable temperature neutron diffraction experiments discussed in Sec. 4.2.6 will provide some additional insight, but it may be some time before a full understanding of the molecular-level hydration of alcohols at low temperatures is achieved.

Chapter 5

A new sound: Brillouin scattering in colloidal suspensions

A colloidal suspension (or *colloid* for short) is a complex fluid in which discrete units of mesoscopic (nm to μm) size are dispersed throughout a continuous medium. Both dispersed and dispersion phases may be solid, liquid or gas. Everyday examples of colloidal suspensions are mist (liquid droplets suspended in a gas), milk (liquid droplets dispersed throughout another liquid – an emulsion) and foams (bubbles of gas suspended in a liquid). The intermediate size of the dispersed particles ensures that they are large enough to be treated classically, but small enough such that Brownian motion dominates over settling due to gravity on the timescale of a typical experiment. The mesoscopic lengthscale also ensures that structural relaxation times are orders of magnitude longer than in molecular systems: $\sim 10^{-2}$ s in a colloidal fluid compared to $\sim 10^{-12}$ s in liquid water.

Colloids are industrially important, present in many biological systems and at the forefront of several recent technological developments (e.g. photonics). A large proportion of research on colloidal systems is therefore applications-driven, although their rich structural and dynamical behaviour also stimulates much curiosity-led investigation. Colloidal suspensions are also of interest on a more fundamental level, since the mesoscopic lengthscales and timescales – combined with easily tunable interactions between particles – allow them to be used as scaled-up models of atomic and molecular systems.

Light scattering and optical microscopy may then be used to study colloidal dynamics, phase-separation and crystallisation in detail, from which an insight may be gained into the behaviour of atomic systems with the same interaction potential.

The Condensed Matter research group in the Department of Physics at Edinburgh have employed a wide range of experimental, theoretical and simulation methods in the study of many aspects of colloidal systems (and complex fluids in general) over the last decade or so. The addition of Brillouin spectroscopy to the portfolio of techniques available for these investigations was one of the primary aims of this research. Brillouin scattering provides information on the propagation of sound with wavelengths which can be tuned (by selection of the scattering angle) to be greater than, smaller than or equal to the structural lengthscale in the colloidal system, hence it might be expected that interesting phenomena should be observed. Existing research using Brillouin spectroscopy to study colloidal suspensions and other complex fluids is however rather scarce.

Discovery of a new sound mode in colloidal suspensions

Perhaps the most interesting study of Brillouin scattering in colloids was undertaken about ten years ago by a group led by David Weitz and Ping Sheng, both then at Exxon Research and Engineering in New Jersey (see e.g. Ref. [109]). Their study of hypersound propagation in hard spheres suspended in a solvent showed that under certain conditions the colloid supported *two* longitudinal acoustic sound modes, manifested as an additional doublet in the Brillouin spectrum. Distinct gaps in the dispersion relation of one of these modes were also observed. These results were extremely surprising – the existence of a second sound mode in a suspension of unconnected particles had not been predicted or observed before. In a short series of papers (which will be discussed in Sec. 5.1 below) they established a theoretical framework which reproduced the experimental results, showing that the new mode could be explained in terms of an interfacial wave at the surface of a sphere, which can propagate throughout the suspension if the spheres are close enough together. Unfortunately these findings were not further investigated due to the break-up of the Exxon research group. In fact their observations have never been extended or reproduced in published work on any colloidal system.

Predicted acoustic bandgaps in colloidal suspensions

Another interesting phenomenon which should be detectable using Brillouin spectroscopy – but which has not so far been experimentally investigated – is the postulated existence of acoustic (or *phononic*) bandgaps in colloidal crystals. Following a similar argument to that which leads to the establishment of band structure for electrons in crystals (semiconductors) and electromagnetic waves in photonic crystals, it has been shown that a suitable periodic structure should theoretically produce bandgaps in the propagation of acoustic (elastic) waves through the material [110]. Sound with a frequency in the bandgap may not propagate in the material, and will be perfectly reflected by it. Acoustic bandgaps have recently been observed for low frequencies in a periodic structure of macroscopic absorbing spheres [111] but have not yet been found in the hypersonic régime where band structure is predicted to emerge in colloidal systems.

Motivation for a new Brillouin scattering study of hard-sphere colloids

These two novel phenomena (the second sound mode and acoustic bandgaps) were considered to be ideal for investigation using the apparatus for Brillouin spectroscopy developed during this research project. Confirmation of the existence of the new sound mode would be a valuable result, as would any extension of the limited work carried out by the group who discovered the effect.

The experimental challenges posed by colloidal systems ensure that these measurements are much more demanding of both the equipment and the investigator than the work on aqueous solutions reported in Chapter 4. Whereas mixtures of molecular liquids are completely transparent and very straightforward to make, colloids require involved and time-consuming preparation and steps must be taken to suppress multiple scattering of light in order to detect the weak Brillouin peaks. Even with a well-prepared colloid sample, collecting a single spectrum may take several hours, and as many as thirty such individual spectra are needed to construct the dispersion relations which are the goal of the research (see e.g. Fig. 5.10 below).

This chapter will present the results of Brillouin scattering measurements on hard-sphere colloidal suspensions, in which the second sound mode is indeed observed in

agreement with the results of Weitz, Sheng *et al*. The work is then extended to look at much smaller particle sizes, and a new effect in the variation of the second mode with wavevector is found. A preliminary study of *binary* colloidal suspensions is then reported. Limited time and problems with the binary samples meant that this topic was not able to be investigated properly, and the search for acoustic bandgaps in colloidal crystals was not implemented for the same reasons. However these intriguing subjects will be discussed briefly at the end of the chapter, with suggestions made for future reference on how best to approach the experiments.

5.1 Sound propagation in hard-sphere colloids

Before going on to discuss the methods and results of these experiments on hypersound propagation in colloidal suspensions, some background information is required. The first part of this section aims to introduce the simple type of colloidal suspension in which Weitz, Sheng *et al* discovered the new sound mode. The same colloid was used in the new studies presented later in the chapter. A summary of their findings will then be given in order to facilitate comparison with the results obtained during this research project.

5.1.1 Hard-sphere colloidal suspensions

A suspension of identical hard-sphere particles is one of the simplest colloidal systems and has been intensively studied using computer simulation, theory and experiment. Perfect hard spheres interact only by touching; the interaction is zero for separations greater than $2R$, where R is the radius of each sphere. The rigidity of the particles ensures that any overlap or deformation is forbidden, hence they experience an infinite repulsive force upon contact with one another. This absence of long-range interactions means that the hard-sphere system is often used as a model for atomic fluids, treating any finite interactions as perturbations when required.

The interaction between hard spheres is therefore either zero or infinite. This lack of energy scale means that changing the temperature does not affect the behaviour of the system. The only thermodynamic variable which is required to describe an ideal

hard-sphere suspension of N particles confined to a volume V is the number density N/V of particles, or alternatively the *volume fraction*

$$\phi = \frac{4}{3}\pi R^3 \frac{N}{V} \tag{5.1}$$

Computer simulations [112, 113] have been used to establish the phase behaviour of a suspension of monodisperse (i.e. all particles the same size) hard spheres. A complete schematic 'phase diagram' is shown in Fig. 5.1. Note that this is not really a two-dimensional phase diagram as the y-axis represents the percentage χ of crystal phase present in the sample, which is not a true thermodynamic variable.

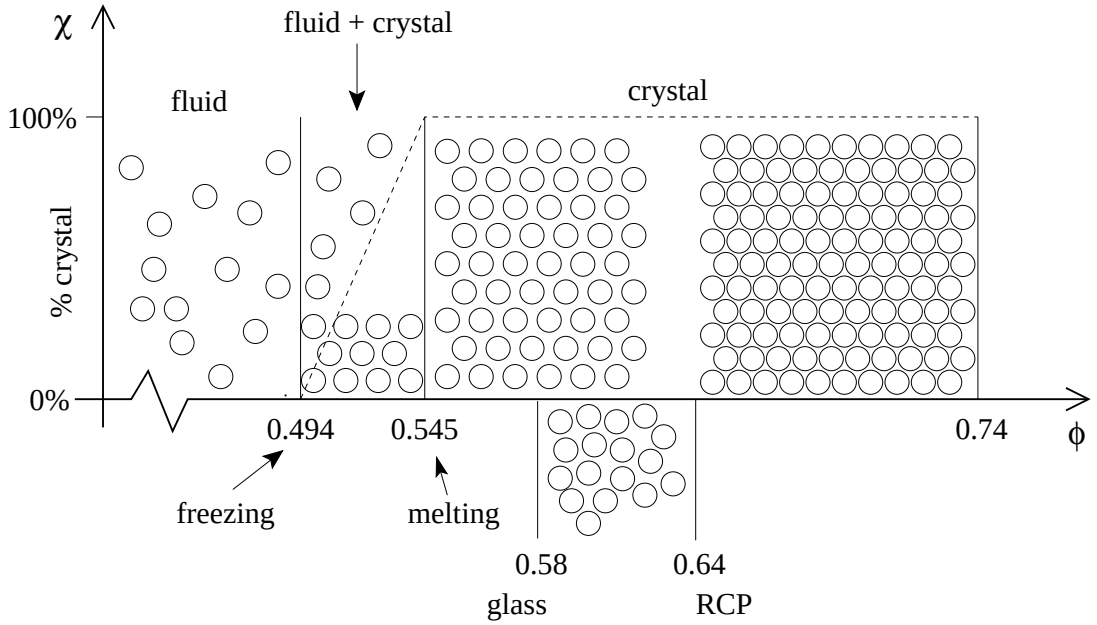

Figure 5.1: Schematic phase diagram for a suspension of hard spheres.

At volume fractions below 0.494 the particles exhibit no long-range order and are free to diffuse throughout the volume of the sample; this phase is called a *colloidal fluid*. For higher volume fractions $0.494 < \phi < 0.545$ there is a region of the phase diagram in which the lowest free energy state is a coexistence of colloidal fluid at the freezing volume fraction $\phi_f = 0.494$ and *colloidal crystal* at the melting fraction $\phi_m = 0.545$. In a colloidal crystal the spheres are arranged periodically on a three-dimensional lattice, like the placement of atoms or molecules in a conventional crystal. In this coexistence region, the overall volume fraction ϕ increases by forming crystals with ϕ_m at the expense of fluid at the lower ϕ_f. As this increase in the volume of crystalline phase

is linear (indicated by the dashed line in Fig. 5.1), measurement of the fraction χ of crystal in the sample allows the overall volume fraction of a suspension with ϕ in the coexistence region to be determined. This measurement is made straightforward by the sedimentation due to gravity of the crystallites (which are denser than the fluid since $\phi_m > \phi_f$) to form a polycrystalline layer at the bottom of the sample. The equilibrium state of the suspension for volume fractions above the melting point is fully crystalline up to the maximum possible ϕ, determined by the theoretical closest packing for spheres in three dimensions, $\phi_{cp} = \pi\sqrt{2}/6 \approx 0.74$. As ϕ increases towards this limiting value, the particles in the colloidal crystal become progressively more tightly packed.

Suspensions of hard spheres also exhibit non-equilibrium behaviour. There is a glass transition at $\phi = 0.58$ where homogeneous nucleation of crystals is avoided due to the arrest of long-time diffusion. Amorphous states cannot exist above the maximum packing fraction $\phi_{rcp} \approx 0.64$ for randomly arranged (*random close-packed*) spheres.

How can there be a freezing transition in a hard-sphere system in which there is no long-range attraction between particles? The answer – as shown thirty years ago using computer simulations [113] – is that entropy considerations alone are sufficient to cause crystallisation. This can be understood by identifying the two contributions to the entropy in a hard-sphere system: configurational entropy of the whole sample (S_{conf}) and vibrational (or *free volume*) entropy (S_{fv}) associated with the local volume which an individual particle is free to explore. When arranged with crystalline order, each sphere has more room to move about in (although its time-averaged position remains on the lattice point), corresponding to an increase in S_{fv} which compensates for the reduction in S_{conf} associated with the formation of a crystal from a fluid at the same volume fraction. Crystallisation will therefore be entropically favourable when the decrease in S_{conf} is more than compensated for by the increase in S_{fv}.

Although established using theory and simulation without recourse to experiments, this phase behaviour has been found to be in excellent agreement with the results of measurements on real colloidal dispersions (see e.g. Ref. [114]). However the case of perfect hard spheres with no interactions other than infinite repulsion upon contact is not realisable in practice, hence such experiments rely on the use of ingenious techniques which are in fact capable of providing an excellent approximation to the ideal system.

This will be discussed in the next section, focusing on the particular system on which the experiments described later in this chapter were performed.

5.1.1.1 The real thing: model hard-sphere suspensions

The most important obstacle to the preparation of colloids with purely hard-sphere interactions is the existence of the attractive van der Waals force between particles. This is an electromagnetic force which acts between fluctuating dipoles; it exists in systems of neutral particles because dipoles are induced in a body due to fluctuations in the charge distributions of its neighbours. A detailed treatment of the van der Waals force is beyond the scope of this thesis – the interested reader is referred to the book by Israelachvili [115]. Its key features are that it is short-range, sufficiently attractive to outweigh the thermal energy k_BT in a colloidal dispersion and depends inversely on the separation of the particles. A real suspension of spherical particles will therefore cluster and aggregate irreversibly due to van der Waals attraction unless steps are taken to prevent this.

The solution to this problem is to stabilise the suspension by choosing particles in which surface effects prevent them from coming close enough together for the (very short-ranged) van der Waals force to act. *Charge-stabilised* colloidal spheres are surrounded by a polarised electrical double-layer induced by the presence of ionised groups on their surfaces. Each sphere is then surrounded by a cloud of ions, and behaves as a charged macroion. This introduces a short-ranged repulsive interaction between spheres due to the overlap of like-charged double-layers when they approach one another. In a range of systems, this effectively screens out the van der Waals attraction resulting in a very good approximation to the behaviour of an ideal hard-sphere suspension. For a more detailed discussion of theoretical and experimental aspects of charge-stabilised colloids, see Ref. [116] and references therein.

The alternative method of screening the van der Waals attraction in spherical colloids is *steric stabilisation*, in which a thin (relative to the particle radius) layer of polymer is chemically grafted to the surface of the sphere. This arrangement is shown in Fig. 5.2 below. The grafted layer can be thought of as polymer 'hairs' with one end fixed to the particle surface. If the dispersion medium of the colloid is a good solvent for the

polymer hairs, each will adopt an extended configuration – in other words the hairs will stick out into the solvent as shown in the figure. When the colloidal spheres approach one another, the layers of hairs on the surfaces of different particles will begin to interpenetrate. This interaction leads to a repulsive force which prevents the particles from coming close enough together for the van der Waals attraction to come into play. The origin of the repulsion caused by the overlap of two polymer layers can be thought of in two complementary ways, by considering either the osmotic pressure or the entropy. An increase in osmotic pressure which pushes the particles apart is due to the increased concentration of polymer in the regions where the coatings of adjacent spheres overlap. In entropic terms, interpenetration of the polymer layers results in reduced freedom for each hair. The entropy cost of this restricted configuration contributes to a rise in the free energy, hence the particles prefer not to approach one another closely enough for the overlap to occur.

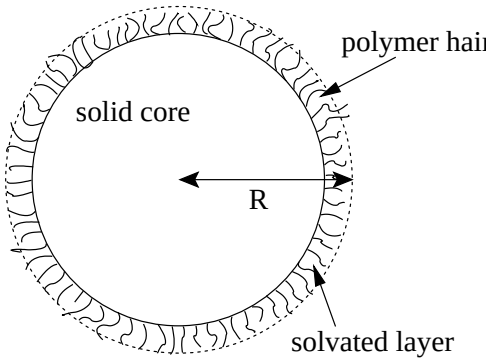

Figure 5.2: A colloidal sphere sterically stabilised by a thin coating of polymer 'hairs' grafted onto its surface. If two such particles approach one another closely enough, their hairs will interpenetrate resulting in a loss of entropy which causes them to repel. This is sufficient to avoid aggregation due to van der Waals attraction, and the particles behave like perfect hard spheres.

The interaction between sterically stabilised hard spheres has been shown to be a very good approximation to that in the ideal system (see e.g. Refs. [117,114]). Any deviation from ideality is likely to be due either to polydispersity – it is very difficult to synthesise particles with sizes which have a standard deviation of less than a few percent about the mean* – or a slight softness of the interaction potential due to compressibility of

*Although Nature seems to be rather good at this – proteins and viruses can be extremely monodisperse.

the polymer coating. These corrections are however small enough to be neglected for the purposes of the work presented here.

Steric stabilisation is preferable to charge stabilisation for several reasons, and is the method used to stabilise the colloidal suspensions studied in this chapter. The solid particles are made from polymethylmethacrylate (PMMA), with a layer of poly-12-hydroxystearic acid (PHSA) grafted onto the surface to provide the stabilising layer of polymer hairs. PMMA spheres with radii from around 100 nm to 500 nm may be synthesised with a PHSA layer thickness of approximately 15 nm using the methods reported in Refs. [118] and [119]. This is the same colloid as used in the experiments which discovered the second sound mode in the Brillouin spectrum (see Sec. 5.1.2 below), and has also been widely studied and established as exhibiting very nearly hard-sphere behaviour [117, 114] in several suitably chosen solvents.

Although the temperature of an ideal hard-sphere colloidal suspension does not influence its behaviour (as discussed in Sec. 5.1.1 above), it is important in determining the properties of these sterically stabilised particles. This is due to the temperature-dependence of the solvent's affinity for both the polymer hairs (in our case PHSA) and the material from which the particle cores are made (PMMA). For the hard-sphere interaction to be approximated as closely as possible we require the dispersion medium to be a good solvent for the polymers in order to ensure that they adopt extended configurations (i.e. 'stand up') with maximal solvent contact rather than the preferred self-interaction and resultant aggregation of colloidal particles which would occur should the medium be a poor solvent for the polymers. It must however be a poor solvent for the core of the colloidal spheres in order to minimise swelling caused by penetration of the dispersion medium into the particles. These affinities change with temperature, hence care must be taken to ensure that the colloid is not taken outwith the range in which steric stabilisation remains effective. For PHSA-coated PMMA spheres in the solvents used in this research, steric stabilisation ensures a nearly hard-sphere interaction from below 4 °C up to about 120 °C [120].

5.1.1.2 The invisible colloid: index-matching

One feature of colloidal suspensions of PHSA-coated PMMA spheres which makes them particularly suited to study using light scattering techniques such as Brillouin spectroscopy is that multiple scattering (which has a deleterious effect on the outcome of such experiments) may be suppressed by careful choice of the dispersion medium.

Light is scattered by changes in the refractive index n (this was discussed at the start of Chapter 2). If the refractive index of the solvent n_s is exactly the same as that of the colloidal particles n_p then no light will be scattered at the solvent–particle interface. This is referred to as *index-matching*. A perfect index match is possible only at a single temperature and wavelength of incident light, due to the dependence of the refractive indices on these quantities. In practice the perfect index match is not achievable, but it is possible to make the match close enough to ensure that the probability of multiple scattering is negligible.

For PHSA-coated PMMA spheres, there are a number of solvents which can provide a satisfactory index match. An additional requirement specific to this system is that the dispersion medium must be a good solvent for PHSA and a poor solvent for PMMA at the temperature where the refractive index matches that of the particles (see above). No single solvent is able to satisfy all of these requirements, but several binary mixtures are suitable. If one component of such a mixture has $n < n_p$ and the other has $n > n_p$, choosing a suitable volume ratio of the two allows the refractive index to be matched to that of the colloidal particle. For typical PHSA-coated PMMA spheres, this is $n_p = 1.495$ [121]. For the colloids studied in this chapter, a mixture of *cis*-decalin ($n = 1.48$) and tetralin ($n = 1.54$) was used as the dispersion medium, as will be discussed in Sec. 5.2.1 below.

Note that a similar approach may be adopted in order to match the *density* of the solvent to that of the colloidal particles, rendering them neutrally buoyant in order to study their behaviour in near-zero gravity. A suitably chosen mixture of *cis*-decalin and bromocycloheptane provides a good density match *and* a near index match for PMMA spheres, allowing light scattering techniques to be used to study colloidal suspensions in the absence of gravitational effects (see e.g. Ref. [122]).

5.1.2 A new sound mode in hard-sphere colloids

As stated in the introduction to this chapter, the main motivation for initiating a program of research using Brillouin spectroscopy to study the propagation of sound in hard-sphere colloidal dispersions was the detection of a new longitudinal sound mode in such systems by David Weitz, Ping Sheng *et al* at Exxon in the early nineties. Despite the novelty and potential importance of this discovery, no further experiments have been published which confirm or extend the original work. This section aims to summarise the experiments (reported in Refs. [109,123,32][†]) and theoretical treatment (Refs. [124,125,126]) which revealed the existence and explained the origin of the second sound mode, in order to provide a basis for comparison with the new results which will be presented later in this chapter.

The propagation of sound waves in random fluid–solid composites is of significant practical interest largely due to the importance of such materials to the oil industry. The widespread use of acoustic probes during exploration and testing means that detailed knowledge of the mechanisms by which sound propagates through random media is required if data from the field is to be interpreted correctly. Useful information may be extracted from acoustic measurements because the structure of – and correlations between – the grains can strongly influence the propagation of sound in a granular material [32]. A disordered suspension of monodisperse solid spheres in a liquid is one of the simplest examples of a random composite, with the lengthscale of the particle sizes determining at what frequency any interesting acoustic effects occur. This model system has been studied since the days of Lord Rayleigh, with more recent theoretical and experimental work showing that only one longitudinal sound mode can propagate for wavelengths $\lambda \gg d$ where d is the diameter of the spheres [127,128]. This is in contrast to the case of composites in which both the solid and fluid phases form connected networks with finite elasticities, predicted by Biot to support two longitudinal modes: a fast mode propagating mainly in the solid network and a slower mode predominantly in the fluid continuum. The prediction has been confirmed in these so-called *porous media* by experiment – for a detailed discussion of this scenario the reader is referred to a review article by Attenborough [129]. The absence of connectivity between the solid

[†]Note that these papers all present the same results. Ref. [123] is the most complete report, Ref. [32] provides the most detailed commentary, and Ref. [109] is a short letter.

particles in a suspension of solid spheres ensures that the only sound which can propagate in the limit $\lambda \gg d$ is a single longitudinal mode due to the inability of the fluid phase to support shear [130]. This was long expected to remain valid at shorter wavelengths, comparable to the particle diameter, until Brillouin scattering experiments performed by the Exxon group (Weitz, Sheng *et al*) showed that a second longitudinal sound mode appears when $\lambda \sim d$.

The colloidal system studied in these experiments consisted of PMMA spheres coated with a 15 nm layer of grafted polymer to provide steric stabilisation as discussed in Sec. 5.1.1.1 above. Two particle sizes were studied, with diameters of 370 nm and 680 nm including the polymer layer. The corresponding diameters of the PMMA core of the spheres, not including the polymer layer, are then $d_c = 340$ nm and 650 nm respectively. Multiple scattering was eliminated by using an index-matched mixture of dodecane ($n = 1.42$) and carbon disulfide ($n = 1.62$) as the dispersion medium. Despite this precaution, the Rayleigh peak was still four orders of magnitude more intense than the Brillouin peak due to residual scattering from the spheres, requiring the Fabry-Perot interferometer to be used in the five-pass configuration (see Sec. 3.1.3) in order to achieve high enough contrast and resolution to observe the Brillouin spectrum. Changing the scattering angle between limits of 7 ° and 170 ° and using laser wavelengths of 514.5 nm and 647.1 nm enabled scattering vectors in the range $0.002\,\mathrm{nm}^{-1} \leq q \leq 0.04\,\mathrm{nm}^{-1}$ to be selected according to the relation $q = (4\pi n/\lambda) sin\theta/2$ (Eq. 2.3). This, together with the use of both sizes of colloidal spheres, allowed values of the dimensionless quantity qd_c ranging from 1 to 25 to be obtained. This parameter qd_c is the ratio of the acoustic wavelength to the diameter of the spheres (excluding the stabilising polymer layer, since the polymers were found to behave more like the fluid surrounding the spheres than the solid PMMA core), which as will be seen below is extremely important in determining the nature of sound propagation in the colloid. The following discussion summarises the results from both sizes of colloids; the same quantitative behaviour was observed for both sets of particles when q is rescaled to qd_c.

At small scattering angles (i.e. $\lambda \gg d_c$) a single longitudinal mode was observed at core volume fractions $\phi_c = 0.16$, 0.38 and 0.51. Note the preferred use of the *core* volume fraction, which is that of the PMMA sphere not including the volume of the stabilising polymer layer. The corresponding hard-sphere volume fractions (which determine phase

behaviour as discussed in Sec. 5.1.1) are $\phi = 0.21$, 0.49 and 0.64. The motivation for choosing to work with the core volume fraction ϕ_c is the same as the reason for talking in terms of the core diameter d_c, and will be discussed below. The existence of this single mode at small angles (such that $\lambda \gg d_c$) is in agreement with the earlier work referred to above, and the dependence of the sound velocity on the core volume fraction of solid particles is accurately reproduced by a simple effective-medium theory. Note that much better agreement between experiment and the effective-medium theory was found by using ϕ_c rather than ϕ, suggesting that the polymer layer behaves more like the fluid than the solid. This is one of the reasons for choosing to work with the core volume fraction ϕ_c and the core diameter d_c in describing later experiments – propagating sound waves do not 'see' the polymer coating as part of the solid sphere (see Ref. [123] for further discussion of this point). Thus even though the highest volume fraction ($\phi_c = 0.51$, $\phi = 0.64$) corresponds to the maximum random close packing ϕ_{rcp} discussed in Sec. 5.1.1 above, the solid cores never touch due to the presence of the (acoustically) fluid-like polymer layers. The frequency, shape and intensity of the Brillouin doublet in the $\phi_c = 0.16$ sample is virtually unchanged in comparison to that in the pure solvent at these long wavelengths. With increasing volume fraction, the Brillouin peak moves out to higher frequencies as expected due to the greater proportion of solid (in which the sound velocity is higher than in the solvent) in the suspension.

This 'normal' single-mode behaviour (normal in the sense that it is what we would expect for a suspension of solid spheres in a fluid based on theory and experiment – see Refs. [127, 128, 130]) continues with increasing scattering angle up to $qd_c \approx \pi$ corresponding to an acoustic wavelength of about twice the diameter of the spheres: $\lambda \approx 2d_c$. Beyond this value of qd_c, the behaviour departs from this expected trend in an extremely surprising way: *a second sound mode appears* at higher frequency for all but the lowest volume fraction. On increasing the scattering vector still further, the two modes become more sharply resolved, and are of approximately equal intensity by $qd_c \approx 2\pi$. This is illustrated by the spectra shown in Fig. 5.3, which is reproduced from Ref. [123]. Both modes were confirmed as being longitudinal in polarisation due to the absence of any depolarised (VH geometry) scattering. Note the rather poor signal-to-noise ratio of the spectra, due to weakness of the Brillouin peaks relative to the high intensity of spurious elastic scattering from the solvent–particle interface in

colloidal suspensions.

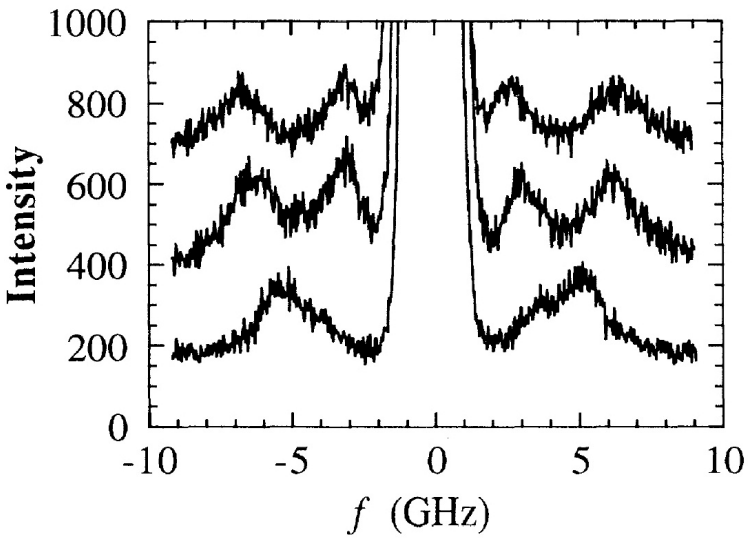

Figure 5.3: Brillouin spectra at $qd_c = 2.8\pi$ for a $d_c = 340\,\mathrm{nm}$ PMMA colloid at three different core volume fractions; $\phi_c = 0.16$, 0.38 and 0.54 from bottom to top. Two sound modes are clearly distinguishable at the two higher volume fractions, while the asymmetry of the peak at $\phi_c = 0.16$ suggests that two modes may be present but are not able to be resolved. Reproduced from Ref. [123]. Compare with the new results for a very similar system shown in Fig. 5.7 below.

The evolution of the Brillouin spectrum in these colloidal suspensions upon increasing from $qd_c \approx 1$ to $qd_c \approx 14$ for the smaller ($d_c = 340\,\mathrm{nm}$) spheres is concisely illustrated by the plot of the two Brillouin peak positions as a function of q shown in Fig. 5.4, which is reproduced from Ref. [123]. This is a dispersion relation – a graph of frequency vs. wavevector. This range of qd_c corresponds to increasing the acoustic wavelength probed from much greater than d_c, through $\lambda \approx d_c$, continuing to high qd_c where $\lambda \ll d_c$. For the purposes of comparison, Fig. 5.4 also shows the linear dispersion relations observed in the pure solvent (dashed line) and pure PMMA (solid line).

The dispersion relation for the suspension of larger ($d_c = 650\,\mathrm{nm}$) particles is qualitatively and quantitatively very similar, with the range of qd_c covered in this case extending from roughly 2 to 25 [123, 32]. For comparison with the new results for different particle diameters presented later in this chapter, the dispersion relations for both sizes of spheres studied by the Exxon group are plotted together in Fig. 5.5, which is reproduced from Ref. [123]. Both axes in this figure have been scaled by d_c, so that

the x-axis measures the dimensionless parameter qd_c (the ratio of acoustic wavelength to particle diameter) and the y-axis becomes ωd_c, which has units of velocity.

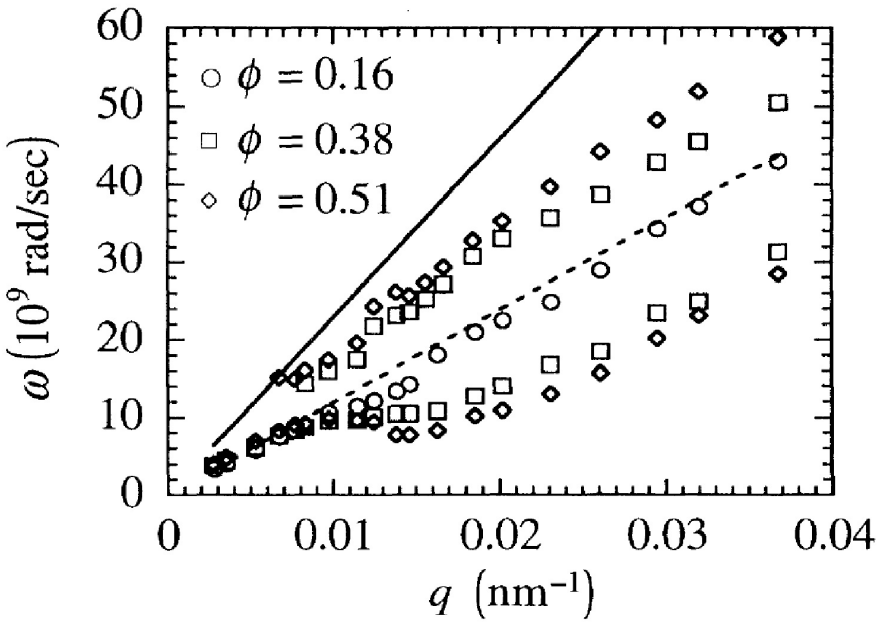

Figure 5.4: Dispersion relation for a colloidal suspension of $d_c = 340\,\mathrm{nm}$ PMMA spheres, showing the emergence and evolution of the two-mode Brillouin spectrum with increasing scattering vector q. Reproduced from Ref. [123]. Compare with the results presented for a $d_c = 319\,\mathrm{nm}$, $\phi_c = 0.38$ colloid in Sec. 5.3 below (Fig. 5.10).

These dispersion relations (Figs. 5.4 and 5.5) display the trends in the Brillouin peak frequency which were summarised above. Below $qd_c \approx \pi$ there is only one peak at all volume fractions, which has a linear dispersion relation very close to that of the pure index-matched dispersion medium. Above $qd_c \approx \pi$ ($q \approx 0.008\,\mathrm{nm}^{-1}$ for the colloid of Fig. 5.4) a second mode appears at higher frequency in all but the samples with the smallest ϕ_c. At the lowest volume fraction for each size of colloid studied, the single mode at $qd_c < \pi$ persists to higher wavevectors, closely following the dispersion relation of the pure solvent. For the higher volume fractions, the second mode persists with increasing qd_c, and the splitting between the two modes is larger for higher ϕ_c. The lower frequency (or 'slow', since $v_s = \omega_B/q$) mode flattens significantly just above the qd_c at which the second mode arises (this is best illustrated by Fig. 5.4).

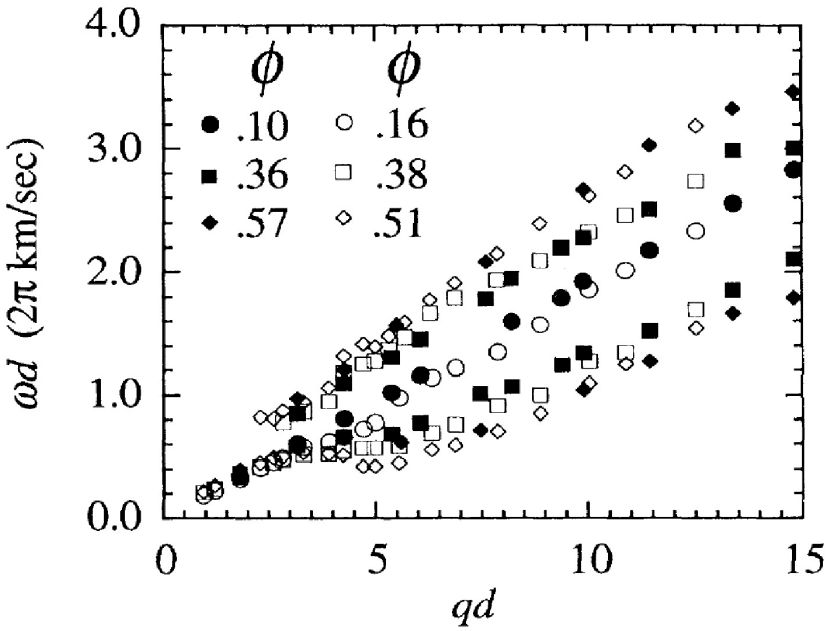

Figure 5.5: Dispersion relations for both sizes of colloid at several volume fractions ϕ_c, scaled by multiplying each axis by d_c. Solid symbols refer to the large ($d_c = 650\,\mathrm{nm}$) spheres and open symbols refer to the smaller ($d_c = 340\,\mathrm{nm}$) ones. Reproduced from Ref. [123]. Compare with the results presented in Sec. 5.3 below (Fig. 5.14).

5.1.2.1 Origin of the two modes

Some conclusions may be drawn from the dispersion relations shown above without recourse to the detailed analysis based on comparison with theory which will be discussed in the next section. The higher frequency ('fast') mode always lies between the frequencies of sound propagation in the pure liquid and pure solid phases, as seen for the small spheres in Fig. 5.4 (the same is true for the larger spheres). Its frequency also increases with increasing volume fraction. This behaviour is what would be expected for a sound wave propagating in a binary composite material in which the constituents have different sound velocities. The single mode which exists at $qd_c < \pi$ (equivalent to $\lambda \gg d_c$) shares these characteristics, hence the authors suggest that the fast mode is a continuation of the low-q single mode and that this excitation propagates in an effective medium consisting of both the fluid and the solid phases.

The behaviour of the slow mode at scattering vectors $qd_c > \pi$ is much more surprising. As shown by Fig. 5.4, it propagates at a velocity less than the velocity of sound in either of the two pure phases. According to Weitz, Sheng *et al* [123] the *only* mode

which can propagate in a fluid–solid composite slower than the longitudinal velocity in either material is a so-called *Stoneley wave*, which is an interfacial wave propagating at the boundary between fluid and solid [131, 132], often observed travelling along the walls of a fluid-filled borehole in oil exploration. This excitation is analogous to the surface plasmon – light waves which are confined to the interface between materials with different refractive indices – which results in the electromagnetic surface modes observed for small metallic spheres [133]. The magnitude of the Stoneley oscillation decays exponentially away from the interface in both solid and fluid phases, so that if the spheres are close enough together (i.e. the volume fraction is high enough) it can hop between neighbours and "propagate coherently from sphere to sphere" in the words of Ye *et al* [123]. This explains why the slow mode is not observed in the colloids with relatively low volume fractions. They calculated the velocity of a Stoneley wave at a flat interface between PMMA and the index-matching solvent and found excellent agreement with the asymptotic limit to which the phase velocity $v = \omega_B/q$ of the slow mode tends at high qd_c. At such high q, the surface of the spheres may be approximated by a flat interface on the lengthscale of λ, which is now $\ll d_c$. This calculation provides further support for the identification of the low-frequency mode as an interfacial excitation at the surface of the spheres.

5.1.2.2 Theoretical calculation of the two-mode dispersion relation

In addition to the experimental program summarised above, the Exxon group also produced a comprehensive theoretical treatment which underpins a convincing explanation of the origin of the two longitudinal sound modes which were discovered in hard-sphere colloidal suspensions for $qd > \pi$. This theory was published first as a short letter [124] then later as an extremely detailed report [125] in which it was extended to consider the propagation of electromagnetic waves in dispersed metallic random media. The description of wave propagation in a strongly scattering medium[‡] with scatterers of sizes comparable to the wavelength is extremely difficult, and requires methods only just developed at the time of the publication of these original papers (see e.g. Ref. [134]). The theory relies on an involved analysis utilising a Green's functions approach and

[‡]This scattering is due to the different acoustic impedances of the solid and fluid phases. Multiple scattering of *light* at the solvent–sphere interface is suppressed by index-matching, but sound waves are scattered strongly.

numerical simulations, which is beyond the scope of this thesis. The following is a very brief summary of this treatment, focusing on the outcomes which are relevant to the results of the experiments presented later in this chapter.

The aim of these calculations is to find the density of states (DOS) as a function of frequency and wavevector. Peaks in the DOS correspond to the acoustic modes which appear in the Brillouin spectrum. The DOS is calculated by considering the multiple scattering of longitudinal sound waves from each scattering unit in the colloidal suspension. This basic scattering unit is taken to be a solid sphere surrounded by a coating of the dispersion medium, the thickness s of which is is determined by the volume fraction of the colloid according to $\phi = d^3/(d+2s)^3$. Note that the complication of the polymer layer present in real sterically stabilised colloids is ignored – the fluid coating in which the sphere sits is simply composed of an appropriate volume of the index-matched solvent. The bulk properties of a suspension of spheres may then be found by placing the 'coated-sphere' scattering unit in a homogenised background effective medium made up of many other such units, in which sound waves propagate at an effective-medium speed v_m. This v_m must be determined by some self-consistent condition. The approach of the Exxon group was to adopt a common approximation scheme – the *coherent potential approximation* – within which this self-consistent condition is the requirement that the forward-scattering amplitude $f(0)$ vanishes through the adjustment of v_m.

The coherent potential approximation (CPA) allows the exact Green's function G for an acoustic wave in a random medium to be expressed as

$$G = G_0 + G_0 T G_0 \tag{5.2}$$

where G_0 is the Green's function for a homogeneous effective medium and T is the total scattering operator which includes all multiple scattering from the spheres [135]. It can be shown that when $\langle T \rangle = 0$, $\langle G \rangle = G_0$ (angled brackets denote configurational averages) and not only does the total scattering vanish, but scattering from each individual scattering unit vanishes also, since $\langle T \rangle \approx nt$ in the limit of weak scattering, where t is the single-scatterer forward-scattering amplitude and n is the volume concentration of the scatterers [124]. This vanishing of forward-scattering for the whole medium on average is the condition for the existence of a coherent mode, hence finding the q and

v_m for which $\langle T \rangle = t = 0$ is sufficient to allow identification of the modes which are able to propagate with frequency ω in the suspension.

In order to calculate the density of states for suspensions of hard spheres, Sheng and co-workers employed a generalised version of this CPA condition to find the q for which scattering of elastic waves is at a minimum (not necessarily zero) for a given frequency ω. In other words instead of requiring $\langle T \rangle = 0$, they look for values of q at which $\langle T \rangle$ is a local minimum. These minima provide the best conditions for the existence of a mode because reduced scattering allows the wave to propagate over longer distances. The scattering does not vanish on average, so the modes identified in this manner are *quasimodes* – they have a finite lifetime. Minima of $\langle T \rangle$ correspond to maxima of the density of states, which may be obtained by evaluating the imaginary part of the Green's function $\langle G \rangle$ for elastic scattering [125].

The problem is then reduced to calculating the Green's function for a single coated-sphere scattering unit sitting in an effective medium. This rather unpleasant task is treated in detail by Ref. [125], and will not be discussed here. Suffice to say that the approach begins with a statement of the elastic wave equation in each of the three homogeneous regions (solid, fluid coating and effective medium) and produces a Green's function which describes the response of density fluctuations (to which the scattering of light is coupled) to a point scalar source.

Two-dimensional contour plots of the DOS as a function of the dimensionless units $\omega d/v_l$ and qd, where v_l is the wave speed in the fluid, were obtained using this method. An example of such a plot is shown in Fig. 5.6, which is reproduced from Ref. [125]. All material parameters (wave speeds and densities) were chosen to match those of the PMMA colloids studied in the Exxon group experiments discussed in Sec. 5.1.2 above. The volume fraction ϕ of the suspension is altered by choosing the thickness s of the liquid coating layer in the scattering unit. Recall that maxima in the DOS correspond to scattering minima, at which (ω, q) acoustic quasimodes propagate in the suspension. With this in mind, the experimental dispersion relations (suitably rescaled to the dimensionless units and displayed as black dots at the mode frequency, with bars either side indicating the Brillouin peak width) are overlaid on the calculated DOS to allow comparison with the theoretical results. Note that the theory contains

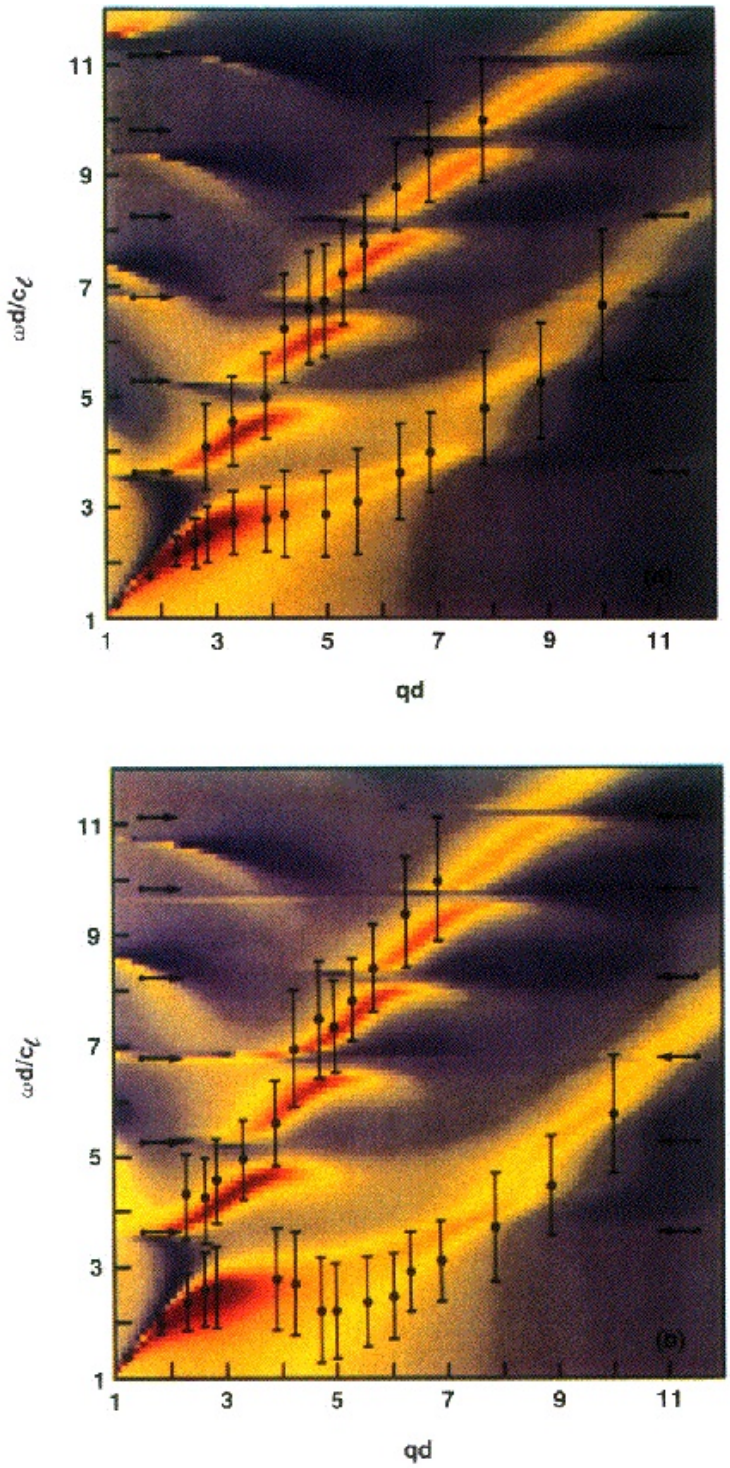

Figure 5.6: Calculated density of states plotted as a function of the dimensionless units $\omega d/v_l$ and qd for suspensions of spheres with volume fractions $\phi_c = 0.38$ (upper graph) and $\phi_c = 0.51$ (lower graph). Experimentally determined dispersion relations are overlayed, with black dots denoting Brillouin peak frequencies and bars on either side representing peak widths. Arrows at the sides of the graphs indicate peaks in the single-sphere scattering amplitude (see Sec. 5.1.2.3) This figure is reproduced from Ref. [125].

no adjustable fit parameters.

Fig. 5.6 clearly shows remarkable agreement between calculated and measured dispersion relations for $\phi = 0.38$ and 0.51 (for the experimental results, this is the core volume fraction ϕ_c). Two branches of maxima ('fast' and 'slow') are present in the DOS, and the measured mode frequencies match these very closely across the entire range of q and ω probed. The peak widths however agree only roughly with the theoretical DOS maxima. Much more realistic widths were obtained by extending the basic scattering unit to consist of multiple spheres within the coating layer of fluid. Good agreement between calculated and measured widths was found for a scattering unit containing four spheres [125]. This increased accuracy has its origin in the inclusion of random scattering between neighbouring spheres.

5.1.2.3 Gaps in the dispersion relation of the fast mode

The contour plots calculated for the density of states (Fig. 5.6) reveal an intriguing feature of the high-frequency mode: well-defined frequency gaps are present where the excitation cannot propagate. The positions of these gaps in the figure match up with the black arrows on either side of the graph. The first two gaps in the fast mode are also clearly discernible in the experimental dispersion relations in Fig. 5.4. The black arrows in Fig. 5.6 in fact correspond to peaks in the calculated scattering amplitude for longitudinal acoustic waves incident on a single solid sphere immersed in a fluid [125]. The fact that gaps in the dispersion relation open up at frequencies where scattering is at a maximum is not surprising, and gives an additional insight into the nature of the high-frequency mode. Recall that the fast mode travels through both solid and fluid, so if scattering of sound from the solid–fluid interface becomes very large at a certain ω (due to the impedance mismatch for acoustic waves to cross from one material to the other) the mode can no longer propagate at this frequency, causing a gap in the dispersion relation. A maximum in scattering from an individual sphere results from the excitation of an internal resonance [124, 125], hence the propagation of the high-frequency mode results from the *antiresonance* condition of a single sphere, at which scattering is minimised. Note that gaps in the calculated dispersion relations at higher frequencies than the first two are not well matched to the experimental data,

postulated by Jing *et al* [124] to be due to the effect of viscosity, which is not included in the simplest version of the theory.

Note that the existence of the slow mode may also be explained in terms of single-sphere resonances, so that all of the novel behaviour observed in the Brillouin spectra of these hard-sphere colloids can be related to the scattering of sound by individual coated-sphere scattering units (indeed the fact that a density of states matching the experimental results may be calculated by minimising the scattering matrix $\langle T \rangle$ is testament to this). The arrows in Fig. 5.6 denoting peaks in the scattering amplitude of a single sphere correspond to peaks in the DOS for the low-frequency mode, so that this mode must be the direct result of these single-sphere resonances. This is the opposite of the origin of the fast mode, which as discussed above cannot propagate at frequencies where resonances are excited and is therefore associated with antiresonances of the individual spheres.

These resonances depend strongly on the shear modulus μ of the solid from which the colloidal spheres are composed. It was found that reducing the shear modulus from that used to produce Fig. 5.6 (the value for solid PMMA) causes the slow mode to weaken, vanishing completely when $\mu = 0$. The only change observed in the fast mode is the disappearance of gaps in its dispersion relation. The effect on both modes on decreasing the shear modulus is therefore as expected from the above explanation of their origin in terms of multiple scattering and single-sphere resonances.

Jing *et al* [124,125] looked only at the consequences of *reducing* the shear modulus from that of PMMA, but what if it takes a much higher value, so that the acoustic impedance mismatch at the fluid–solid interface is greater, resulting in stronger scattering? One assumes that the two modes should persist, with gaps in the dispersion relation of the fast mode and perhaps an even stronger slow mode, but no comment on this possibility is made in these papers. Colloidal silica spheres have a much higher shear modulus than PMMA, so Brillouin scattering investigations of the harder spheres might be able to answer this question experimentally. The only such study in the literature shows just one mode in $d = 118\,\mathrm{nm}$ silica colloids, but the values of qd probed are too small ($qd < 4$) to rule out the emergence of a second mode at slightly higher wavevectors [136] (recall that the crossover to two-mode behaviour occurs at $qd_c \approx \pi$ for the PMMA

colloids). Intriguingly, a pre-publication version of a paper on Brillouin scattering in soft colloids mentioned in passing that the authors (the Fytas/Economou group in Greece) *had* observed two modes in a colloidal suspension of silica spheres, but this was not included in the final published article [137]. If correct, this is a particularly interesting result, because Stoneley's original paper [131] states that the interfacial wave only exists "when the wave-velocities are not too widely different for the two media". Further investigations into the existence or otherwise of the second sound mode in different colloidal suspensions would clearly be very valuable.

5.1.3 Summary of background information

Before moving on to discuss the new experiments which will be presented later in this chapter, let us first summarise the points raised in this background section.

Beginning with a brief discussion of hard-sphere colloids and their phase behaviour, we then noted that although perfect hard spheres are not realisable in practice, a very good approximation to the ideal case may be achieved using sterically stabilised colloidal particles. Real colloids may also be rendered completely transparent (and therefore suitable for study using light scattering techniques such as Brillouin spectroscopy) by matching the refractive index of the dispersion medium to that of the colloidal spheres.

The novel experimental and theoretical results of a study of sound propagation in hard-sphere colloids were then summarised. It was found that a second longitudinal sound mode exists in these systems for $qd_c > \pi$ and $\phi_c > 0.2$, revealed by the emergence of a second doublet in the Brillouin spectrum when these conditions are met. The phenomenon was observed for two different sizes of colloidal spheres, $d_c = 340\,\text{nm}$ and $d_c = 650\,\text{nm}$. Based on these results, it was suggested that the high-frequency mode propagates in both fluid and solid phases, seeing them as an effective medium, whilst the low-frequency mode is due to surface excitations (Stoneley waves) at the interface between the particle and the solvent which hop from one sphere to another at large enough volume fractions, resulting in a second propagating sound mode.

This explanation is supported by a theoretical treatment based on calculating the density of states which results from the multiple scattering of sound waves in a suspension of

hard spheres with the same material properties as those used in the experiments. With no adjustable parameters, these calculations produced results in excellent agreement with the measured dispersion relations. This showed that the origin of the two-mode spectrum can be attributed to the scattering of sound by individual spheres in the colloid. The high-frequency mode cannot propagate (gaps open up in its dispersion relation) when scattering is strong, so is associated with single-sphere antiresonances, whereas the low-frequency mode is the result of single-sphere resonances coupled due to an interaction mediated by the exponentially-decaying part of the surface mode which extends into the solvent.

The aim of the new research presented in this chapter was to reproduce and extend the work discussed above using the new Brillouin spectrometer developed as part of this project (see Chapter 3). Despite being discovered more than ten years ago, no further investigations of the novel phenomena have been published. Given the limited scope of these original experiments and generality of the predictions made by the theory, many interesting avenues for research into the second sound mode in colloidal suspensions remain open. The work described below is a first step in this direction.

5.2 Sample preparation

The accurate preparation and characterisation of a highly monodisperse colloidal suspension of sub-micron polymer-coated PMMA spheres is a difficult and time-consuming business. Time and effort devoted to sample preparation constitutes a major part of the task of measuring the Brillouin spectrum in such a system. This section will discuss the most important aspects of the methods used to produce a transparent suspension of known volume fraction from a stock solution of colloidal spheres.

The process can be broken into two distinct stages; (*i*) the chemical synthesis of spherical PMMA spheres and grafting onto them of a monolayer of PHSA polymer chains to produce a stock solution of a colloidal suspension of known particle size, and (*ii*) the subsequent use of this stock solution in the preparation of an index-matched colloid with the desired volume fraction of hard spheres. Colloidal synthesis was performed in our laboratories by Dr. Andrew Schofield following the methods of Refs. [118] and [119].

The particle size is ascertained using a variety of techniques including light scattering and thermodynamic measurements which combine to give a value for the hard-sphere diameter with an uncertainty of at most 2%. The suspensions used in this thesis have a polydispersity (defined as the standard deviation of the particle size) of less than 5%, which does not perturb the phase behaviour significantly with respect to the idealised monodisperse colloids discussed in Sec. 5.1.1 above [121]. Stock solutions are dispersed in dodecane, which has a refractive index different to that of PMMA, resulting in strong multiple Rayleigh scattering of light; the suspension appears milky as discussed in the introduction to Chapter 2.

As discussed above, the suppression of multiple scattering is vital if the inherently weak Brillouin peaks are to be detected. Even with the extremely high contrast provided by a five-pass Fabry-Perot interferometer (see Sec. 3.1.3), any deviation from transparency of the sample makes the measurement of a Brillouin spectrum extremely difficult, if not impossible. Multiple scattering from the colloids studied in this chapter was minimised by replacing the dodecane in which the stock particles are suspended with an index-matched dispersion medium.

5.2.1 Washing the colloid

The index-matching solvent most frequently used for PMMA colloids by the group at Edinburgh is a mixture of *cis*-decahydronapthalene (abbreviated to *cis*-decalin) and tetrahydronapthalene (tetralin). At 20 °C *cis*-decalin has a refractive index of 1.48 and tetralin 1.54, so that a carefully measured mixture of the two can be made to match the refractive index of PHSA-coated PMMA particles ($n = 1.495$) very closely. The procedure for replacing the dodecane in the stock suspension with the index-matched mixture of *cis*-decalin and tetralin is known as 'washing' the colloid. The required volume of the stock suspension is spun in a centrifuge at roughly 3000 revolutions per minute until all of the colloidal particles have settled to form a random close-packed (RCP) structure at the bottom of the sample cell. The sedimentation velocity of the spheres is proportional to their radius squared, so smaller colloidal particles must be centrifuged for a longer time before this settling is complete [121]. For the sphere diameters used in this study, centrifugation times of about 1 day (for the larger particles)

and 2 days (smaller particles) were required. The solvent above the RCP sediment is devoid of colloidal particles, and may be removed by simply pouring out of the sample cell as the sediment does not flow when the cell is tilted. The solvent which is present between the spheres of the RCP structure however remains present. The amount of this remnant depends on the volume fraction ϕ_{rcp} of the sediment, which for hard spheres is 0.64 [138]. The small compressibility of the PMMA spheres and any polydispersity will increase this to slightly greater than the ideal value. The volume fraction of solvent present in the sediment will then be $1 - \phi_{rcp}$. The sample cell is now filled (over the RCP sediment) with the desired dispersion medium (in our case a mixture of *cis*-decalin and tetralin prepared to match the refractive index of PMMA) and redispersed by tumbling or shaking on a mechanical device for approximately half an hour. This process of centrifugation, replacement of solvent and redispersion constitutes one wash cycle.

After redispersion, the original solvent which was trapped in the RCP sediment will be mixed with the new solvent, thus altering the refractive index and impairing the index match with the colloidal spheres. If a fraction f of the sample cell was occupied by the sediment after centrifugation, the fraction Y_1 of impurity (old solvent) in the total solvent volume after one wash will be

$$Y_1 = \frac{(1 - \phi_{rcp})f}{1 - \phi_{rcp}f} \tag{5.3}$$

Taking $\phi_{rcp} = 0.64$ and assuming a typical value of 0.5 for f, this results in an impurity of $Y_1 \approx 0.25$; one part in four of the dispersion medium is the original solvent (dodecane). Repeated wash cycles reduce this impurity fraction – after w washes the fraction of original solvent will be Y_1^w. For a good index match, we require an impurity of less than approximately one part in ten thousand, which will occur after about $w = 6$ washes. All colloids used in this project were therefore washed at least six times, as the quality of index match is a critical determinant of the quality of Brillouin spectra which may be obtained from the sample. After the last wash, the purity of the dispersion medium extracted from the solvent layer in the centrifuged sample was checked by measuring its refractive index using an Abbe refractometer [139] and comparing with the pure solvent. Agreement to better than 0.1% was found in all cases and taken to be satisfactory. The colloid can be seen to become more and more pellucid with each wash, starting completely opaque and ending up almost totally transparent, although

often with a yellowish tint – this will be discussed in Sec. 5.2.3 below.

5.2.2 Determining the volume fraction

Once the stock colloidal suspension has been through the washing process and an index-matched colloid has been produced, the next task is to measure its volume fraction ϕ. The core-shell structure of each polymer-coated sphere means that simply allowing the solvent to evaporate off, measuring the mass fraction of particles and converting this to a volume fraction using the densities of PMMA and the solvent is not an accurate method of determining ϕ. This would in fact measure only the *core* volume fraction ϕ_c; it does not take account of the fact that the effective *hard-sphere* volume of each particle is increased by the presence of the thin polymer layer grafted onto each sphere. This was discussed in Sec. 5.1.1.1 above, and it is the hard-sphere volume fraction ϕ which determines the most important properties such as phase behaviour in these colloids.

Note that the methods of determining ϕ which will be described below rely on the measurements of the relative *heights* of certain horizontal interfaces which may occur in colloidal suspensions. In a sample cell of constant horizontal cross section, this is equivalent to the measurement of absolute volumes.

5.2.2.1 Estimating the volume fraction: centrifugation

A rough estimate of the hard-sphere volume fraction may be obtained by measuring the height of the RCP sediment which forms after centrifugation. As stated above, the volume fraction of this structure is $\phi_{rcp} \approx 0.64$, with the uncertainty deriving from polydispersity, deformation of the spheres, and possible deviation from true random packing (see Refs. [121] and [122] for further discussion of uncertainties associated with this method). If f is the fraction of the colloid occupied by the sediment (obtained by measuring its height and dividing by the total height of the sample), this method provides an estimate (typically accurate to within 5%) of the hard-sphere volume fraction

$$\phi \approx f\phi_{rcp} \tag{5.4}$$

This estimate is however not sufficiently accurate for our purposes. A more accurate technique is required.

5.2.2.2 A more accurate method: the thermodynamic approach

The most accurate and widely-used method of determining the effective hard-sphere volume fraction in these coated PMMA colloids exploits the phase behaviour of the system, shown in Fig. 5.1 above. There is a window of volume fraction between freezing ($\phi_f = 0.494$) and melting ($\phi_m = 0.545$) within which a hard-sphere system separates into coexisting phases of fluid at ϕ_f and crystal at ϕ_m. The fraction of crystal in the colloid increases linearly from zero to one as the volume fraction increases from ϕ_f to ϕ_m. Since $\phi_m > \phi_f$, the crystallites settle towards the bottom of the sample much faster than the individual particles in the fluid phase, resulting in the formation of a fluid–crystal interface after a few hours. The height of this interface may then be divided by the total height of the sample to give the fraction χ of the colloid which has crystallised, from which the effective hard sphere volume fraction ϕ may be calculated:

$$\phi = (1 - \chi)\phi_f - \chi\phi_m \tag{5.5}$$

Unfortunately, the process of measuring χ is complicated by the effect of gravity, which causes the heights of the fluid–crystal and fluid–solvent[§] interfaces to change with time. Accurate measurement of χ requires the height of the fluid–crystal interface to be monitored over several weeks, as described in Ref. [140]. Extrapolation to zero time of the linear part of the resulting curve allows an accurate value for χ in the absence of gravity to be calculated.

Accurate determination of the volume fraction using this technique therefore requires the colloid to be in the coexistence region of the phase diagram ($\phi_f < \phi < \phi_m$). This may be arranged by adding or removing solvent based on a rough estimate of ϕ from the centrifugation method described in Sec. 5.2.2.1 above. The height of the resulting fluid–crystal interface is then measured over time, from which the effective hard-sphere volume fraction may be calculated. Once ϕ is known, the colloid may be diluted or concentrated as required by the addition or removal of a known volume of solvent.

[§]The fluid phase sediments more slowly than the crystal, forming an interface with the pure solvent much later than the formation of the fluid–crystal interface.

Alternatively, a known mass of solvent may be added or subtracted if one appeals to the densities of effective hard-sphere particles incorporating the solvated polymer layer measured by Eldridge *et al* for a range of radii [141].

The use of values for ϕ_f and ϕ_m from simulations means that this method requires two important assumptions to be made about the colloidal suspension: firstly that the particles behave as ideal hard spheres, and secondly that they are perfectly monodisperse. A realistic minimum polydispersity of a few percent is expected to alter these melting and freezing volume fractions, thus introducing a systematic error into the measurement of effective hard-sphere volume fraction using this technique. This is discussed in the PhD thesis of David Fairhurst [121] of the Edinburgh group, who concluded that these sources of uncertainty were negligible, and calculated a typical error in ϕ of only 0.25% based only on a generous estimate of 5% for the uncertainty in χ due to measurement errors (see Sec. 5.2.2.3 below).

Once a desired volume fraction in a given sample had been obtained, any changes due to evaporation were minimised by closing the sample cell with a tightly fitting lid and wrapping PTFE tape around the seal, as was done for the aqueous solutions in Chapter 4. Colloids were not however kept in the freezer due to the sensitivity of the polymer layer to temperature; changing the temperature alters the interaction between PHSA and the solvent. Monitoring the mass of the samples showed that the change in volume fraction after one month was negligible, and due to the problems associated with yellowing of the solvent (see Sec. 5.2.3) colloids much older than this were usually not sufficiently transparent to be used for Brillouin spectroscopy. The volume fractions of the colloids studied in Secs. 5.3.2 and 5.3.3 were remeasured approximately 5 months after preparation and found to have changed by less than 1%, hence evaporation of the solvent does not have a significant effect on the concentration of these samples.

5.2.2.3 Method of measuring heights

Both the rough (Sec. 5.2.2.1) and accurate (Sec. 5.2.2.2) techniques for the determination of colloid volume fraction – as well as any adjustments to the volume fraction which may be required – depend on precise measurements of the heights of interfaces in the sample. The method used follows the approach adopted in earlier work at Edinburgh

– see for example Refs. [121] and [122].

Height measurements were made using a vertically mounted set of vernier callipers accurate to ±0.05 mm. Samples were viewed using a swan-necked fibre-optic lamp which allowed the interface to be illuminated from the direction best suited to precise determination of its location. This also avoided the problem of heating associated with more conventional light sources. The uncertainty in heights determined using this method of measurement was ±0.5 mm, which for a typical interface height of 3 cm corresponds to an error of less than 2%.

Determination of volume fractions requires the total height of the sample to be measured in addition to the height of the fluid–crystal interface. This is complicated by the presence of a meniscus, which in *cis*-decalin was found by Fairhurst [121] to contribute an additional volume equivalent to an increase in total sample height of 0.6 mm above the bottom of the meniscus. The total height of the sample was therefore determined by measuring the height of the meniscus base, then adding 0.6 mm to take into account the volume of solvent in the meniscus.

As stated above, this method of measurement when used with the thermodynamics-based method described in Sec. 5.2.2.2 allowed the effective hard-sphere volume fraction of a suspension of PHSA-coated PMMA spheres to be calibrated accurate to better than 1%. This is perfectly adequate for the purposes of this thesis.

5.2.3 Limited lifetime of colloids: solvent discolouration

The process of washing and determining the volume fraction of a colloidal suspension as described above is rather time-consuming, typically requiring three or four weeks before the sample is ready for use in a Brillouin scattering experiment. This long preparation time is made more problematic by the unfortunate fact that the colloids studied here have a finite – rather short – lifetime during which Brillouin spectra may be measured.

The problem lies in the dependence of Brillouin spectroscopy on optical transparency of the sample. The inherent weakness of the Brillouin doublet requires suppression of spurious elastic scattering from impurities (and in this case the colloidal particles themselves), despite the high contrast provided by multi-pass Fabry-Perot interferometers

like the one used in this research. As described above, colloidal suspensions may be rendered transparent by matching the refractive index of the solvent to that of the colloidal particles, which in this case was achieved using a carefully chosen binary mixture of solvents as the dispersion medium.

However it was found that within a few weeks of preparation, the transparency of colloids prepared in this way begins to be impaired by a distinct yellowing of the suspension. The effect of this discolouration on the quality of Brillouin spectra is very noticeable. The detection of Brillouin peaks is impaired by the reduction in signal-to-noise ratio resulting from the increase in the intensity of the Rayleigh peak.

This discolouration is due to autoxidation of the tetralin in the dispersion medium of the colloidal suspension, which occurs in the presence of dissolved or atmospheric oxygen to form tetralin hydroperoxide [142]. This process is caused by the presence of radicals which are formed by the action of light on the solvent, and may be prevented by the addition of antioxidants such as vitamin E which remove these radicals. This was not however attempted due to the unknown effects of such an addition on the colloidal particles [120]. A small proportion of PMMA colloids in *cis*-decalin/tetralin do not exhibit this yellowing, but it is not yet known why this might be.

Note that the yellowed solvent seeps into the core of the spheres after a few weeks, so the effect cannot be removed by simply replacing the dispersion medium with freshly prepared solvent.

The length of time which elapsed from completion of preparation before a colloid became too discoloured to allow the Brillouin peaks to be detected ranged from one month to three months for the samples used during this research. When possible they were kept in the dark in order to minimise the number of radicals created by ambient light, but the effectiveness of this precaution seemed to be minimal. Presumably most of the damage is caused by the high intensity of light in the laser beam used to excite the spectra, which is unavoidable. One approach which might prolong the useful lifetime of the colloids would be to bubble nitrogen through the samples immediately after preparation, thus displacing any oxygen from the solution and the atmosphere above it. This would however be rather difficult to implement and was not attempted with the colloids which were studied in the work presented below.

Another possibility would be to use the same dispersion medium as the earlier experiments discussed in Sec. 5.1.2 above – an index-matched mixture of carbon disulfide and dodecane. This avoids yellowing but introduces new problems. Not only does carbon disulfide smell extremely unpleasant, it can be very harmful to health even in small quantities, and is therefore not used as a solvent in the labs at Edinburgh.

5.3 Sound propagation in monodisperse colloids

The simplest example of a hard-sphere colloid contains only one size of particle and is therefore described as *monodisperse*. *Polydisperse* suspensions are comprised of many sphere-sizes, which introduces considerable additional complexity to the behaviour of the system. For this reason, most fundamental investigations into the properties of colloids choose to focus on monodisperse suspensions. This has been the case with all experimental and theoretical studies of high-frequency sound propagation in colloids published to date; the simplifications resulting from the fact that every colloidal particle is identical in a monodisperse suspension being a distinct advantage when so little is known about the subject.

The bulk of the research presented below on Brillouin scattering from colloids therefore focuses also on monodisperse suspensions. A preliminary survey of the Brillouin spectra of several colloids at fixed scattering angle produced encouraging results, which were followed by detailed variable-q measurements of dispersion relations for two samples. The first of these was chosen to be almost identical to one of the colloids studied in the original research discussed in Sec. 5.1.2 above in order to attempt a first confirmation of their results and test the performance of the new spectrometer by comparison with the earlier work. The second sample was a suspension of spheres much smaller than any studied previously, chosen to establish the generality or otherwise of conclusions drawn for the two larger colloids of Ref. [123].

5.3.1 Preliminary results at fixed scattering vector

Before proceeding to a detailed study of sound propagation in colloidal suspensions, some preliminary experiments were performed in order to confirm the ability of our new

Brillouin spectrometer – still in development at the time – to detect the two longitudinal sound modes discussed in Sec. 5.1.2 above.

Fortunately, two polymer-coated PMMA colloids which had already been washed and index-matched by Dr. Andrew Schofield were available for immediate use, with hard-sphere diameters $d_1 = 224\,\text{nm}$ and $d_2 = 650\,\text{nm}$ corresponding to core diameters $d_{c_1} = 194\,\text{nm}$ and $d_{c_2} = 620\,\text{nm}$, since the thickness of the polymer layer is 15 nm. The index-match was confirmed both by eye (the colloids were extremely transparent – small text on white paper could easily be read through the sample) and by measuring the refractive index of the pure solvent using an Abbe refractometer, which in both cases was equal to the refractive index of the coated PMMA particles to within experimental error. Samples were tightly sealed in cells with a 1 cm square cross-section.

At the time these experiments were performed, the Brillouin spectrometer was being operated in the three-pass configuration (see Sec. 3.1.3), as the optical stability of the Fabry-Perot interferometer and performance of the stabilising electronics was not yet considered good enough to move to the much more demanding five-pass specification. The laser wavelength was 514.5 nm operating at a power of about 200 mW, and the scattering angle was set at $90 \pm 0.5°$ giving a scattering vector of magnitude $q = 0.0258 \pm 0.0001\,\text{nm}^{-1}$, calculated using Eq. 2.3 with $n = 1.495$ (the refractive index of the colloidal spheres, to which the index of the solvent is matched). The inherent weakness of the Brillouin peaks compared to the intense elastic scattering present in the colloids (despite ensuring the best possible index-match) meant that extremely long collection times were required to accumulate enough data to give a satisfactory spectrum. The spectra shown below are typically the sum of 3,000 individual spectra, with each composite dataset taking approximately 90 minutes to record.

Tuning the index-match by changing the temperature

The aim of index-matching is to make the refractive index of the solvent equal to that of the colloidal particles in order to render the suspension transparent. Here this is achieved using a binary solution of two liquids with refractive indices higher and lower than the required, with the index of the mixture depending on the concentration of the components. Although a very good index-match can be obtained using the

method described in Sec. 5.2.1, it was found that a further reduction in the intensity of light scattered by the spheres could be achieved by making small adjustments to the temperature of the colloid.

This is because the refractive indices of the three constituents (coated PMMA spheres and the two solvent components) vary weakly with temperature at different rates of change. By altering the temperature until the elastic scattering of laser light in the sample is at a minimum, one can therefore usually achieve a better index-match for light at the laser wavelength than that produced for white light during the washing procedure. The improvement can be quite marked – the best index-matches obtained by tuning the temperature even allow the orange laser-induced fluorescence from tetralin in the dispersion medium to be observed around the focused beam in the sample.

The temperature was controlled using the apparatus described in Sec. 3.2.2.2, which is capable of maintaining the temperature of the sample for much longer than the duration of any Brillouin scattering experiment. The best index-match was always obtained within $\pm 6\,^{\circ}\mathrm{C}$ of the typical room temperature of $20\,^{\circ}\mathrm{C}$. Such a small alteration in temperature is not sufficient to cause any significant changes in the interaction of the stabilising polymer layer with the solvent, so the particle size and volume fraction will not be affected [120].

5.3.1.1 A small colloid: $d_{c_1} = 194\,\mathrm{nm}$

Brillouin spectra were recorded for the small colloid ($d_{c_1} = 194\,\mathrm{nm}$) at core volume fractions $\phi_c = 0.13$, 0.26, 0.32 and 0.42, corresponding to hard-sphere volume fractions $\phi = 0.2$, 0.4, 0.5 and 0.64 ($\phi_c = (d_c/d)^3\,\phi$, which for a polymer layer 15 nm thick simplifies to $\phi_c = (1 - 30/d)^3\,\phi$). The highest volume fraction was obtained by centrifugation of the sample to form a layer of sediment at the random close-packed $\phi_{rcp} = 0.64$. The best index-match was found to be at $15\,^{\circ}\mathrm{C}$, hence all experiments were performed at this temperature. Raw datasets were converted to frequency spectra using the `jig` program described in Sec. 3.3.1, and are shown together in Fig. 5.7 below. No features were present in the depolarised (VH) spectrum, confirming the longitudinal nature of the observed sound modes.

The results of these first attempts at Brillouin spectroscopy on colloidal suspensions were extremely encouraging. The $\phi_c = 0.32$ spectrum in Fig. 5.7 clearly shows two Brillouin peaks on either side of the unshifted Rayleigh peak, corresponding to the two longitudinal sound modes discovered in almost identical colloids by the Exxon group (see Sec. 5.1.2). Though less intense, the slow mode is also present in the $\phi_c = 0.26$ colloid. There is only one peak present for the sample with $\phi_c = 0.13$, although it is very broad and asymmetric, suggesting that an unresolved second mode may exist. All of these findings are in excellent qualitative agreement with the earlier results discussed in Sec. 5.1.2, as may be seen by comparing Fig. 5.7 with the figure (Fig. 5.3) reproduced from the work on a $d_c = 340\,\mathrm{nm}$ colloid at similar q and ϕ_c by Weitz, Sheng *et al* [123].

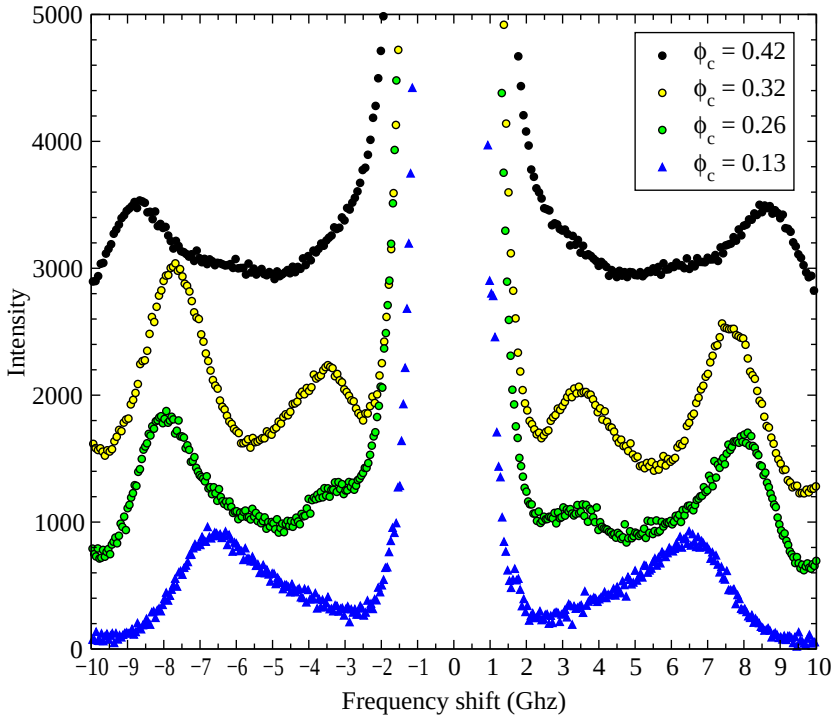

Figure 5.7: Brillouin spectra of the $d_{c_1} = 194\,\mathrm{nm}$ colloidal suspension at several volume fractions and $q = 0.0258\,\mathrm{nm}^{-1}$, so that $qd_{c_1} = 5.0$. The $\phi_c = 0.13$ dataset has been magnified by a factor of two, resulting in a lower SNR than the other spectra, which have all been displaced (but not scaled) for ease of comparison. As discussed in Sec. 3.3.2 the uncertainty in frequency is $\pm 0.1\,\mathrm{GHz}$. Compare with the spectra published by Ye et al [123], reproduced in Fig. 5.3 above.

There are however significant differences between the original work and the new results shown in Fig. 5.7. The most obvious disparity is between the spectra at the highest volume fraction in each study, both of which were obtained by making a ran-

dom close-packed sediment at the hard-sphere $\phi_{rcp} = 0.64$. The $\phi_c = 0.54$ spectrum from Ref. [123] exhibits two modes of equal intensity, but the $\phi_c = 0.42$ spectrum in Fig. 5.7 does not. There does appear to be a hint of the slow mode at about 3.5 GHz (particularly on the right hand side of the central peak – this asymmetry is a feature of multi-pass interferometry [38]) but this is swamped by the wings of the Rayleigh peak. This suggests that the difference may be due to the fact that Ref. [123] used a five-pass Fabry-Perot interferometer which allows smaller frequencies to be detected – the interferometer used in the collection of the spectra in Fig. 5.7 was operating in the triple-pass configuration.

This difference in the specification of the interferometers may also be responsible for the other important difference between the spectra presented here and those of the original publication: the signal-to-noise ratio (SNR) is much better for the spectra shown in Fig. 5.7. As discussed in Sec. 3.1.3, five-pass operation allows less light to be transmitted, resulting in a reduced SNR compared with the three-pass configuration. The new spectra reveal the shape of the peaks with much more detail and accuracy than the noisy five-pass data of Fig. 5.3.

The relative merits of triple-pass and five-pass operation will be discussed further in Sec. 5.3.2.1 below.

Asymmetric peak profiles

We can now see for the first time that there is a great deal of asymmetry in the peak profiles at all volume fractions. It has been postulated that the unusual shape of the $\phi_c = 0.13$ spectrum is due to an unresolved low-intensity slow mode, but why are the peaks so asymmetric for the other volume fractions? At $\phi_c = 0.26$ the fast mode is still highly non-Lorentzian while the slow mode is not sufficiently resolved to comment on its shape. At $\phi_c = 0.32$ the fast mode is almost symmetrical, but the slow mode is definitely not. The shape of the slow mode at this volume fraction is hinted at by the profile of the corresponding peak in the noisy $\phi_c = 0.38$ spectrum of Ref. [123] (see Fig. 5.3), but is much better defined in Fig. 5.7 above. Finally, we note that the $\phi_c = 0.42$ spectrum is also of an extremely unusual appearance. If we assume that the feature at 3.5 GHz is a low-intensity slow mode, then what is the origin of the 'kink'

on the low-frequency shoulder of the fast mode peaks?

It is difficult to speculate on the possible causes of the asymmetry in the spectra shown in Fig. 5.7. The similarity with peak profiles observed in the original work reported in Ref. [123] proves that the effect is not an experimental artefact, but no comment on the unusual shapes was made in the earlier publications. The improved quality of the spectra obtained using the new Edinburgh spectrometer with a triple-pass interferometer raises the possibility of fitting these asymmetric spectra to dynamic structure factors obtained from the density of states calculated by Jing *et al* [124, 125] (see Sec. 5.1.2.2 above). According to Prof. Ping Sheng – who worked on the theory reported in these publications – the peak shapes are indeed possible to calculate, although this would be difficult and time-consuming [143]. This improvement in the new spectra compared with the earlier work is therefore extremely significant.

5.3.1.2 A large colloid: $d_{c_2} = 620\,\text{nm}$

Brillouin spectra were then recorded for the larger colloid ($d_{c_2} = 620\,\text{nm}$) at core volume fractions $\phi_c = 0.17$ and 0.56 corresponding to hard-sphere volume fractions $\phi = 0.2$ and 0.64, with the largest volume fraction again being that of the RCP sediment. Experimental parameters were unchanged from the previous experiments on the smaller colloid, although the best index-match for this sample was obtained by setting the temperature at a slightly higher 18 °C. The resulting spectra produced from raw data using the `jig` program discussed in Sec. 3.3.1 are shown in Fig. 5.8. A spectrum was also obtained for the pure index-matched dispersion medium above the sediment, which is included in Fig. 5.8.

The spectra shown in Fig. 5.8 are again more or less as expected from the original publications on sound propagation in hard-sphere colloids, discussed in Sec. 5.1.2 above. As was the case for the smaller colloid, the new spectra are much less noisy than those of Ref. [123], allowing the peak profiles to be seen more clearly. The $\phi_c = 0.17$ spectrum shows only a hint of the second mode at about 4 GHz in the form of a slight shoulder on the low-frequency side of the main peak. This compares well with the low-ϕ_c spectra of both Ref. [123] and Fig. 5.7 above. Both longitudinal sound modes are apparent in the $\phi_c = 0.56$ spectrum, again comparing favourably with Ref. [123]. However the

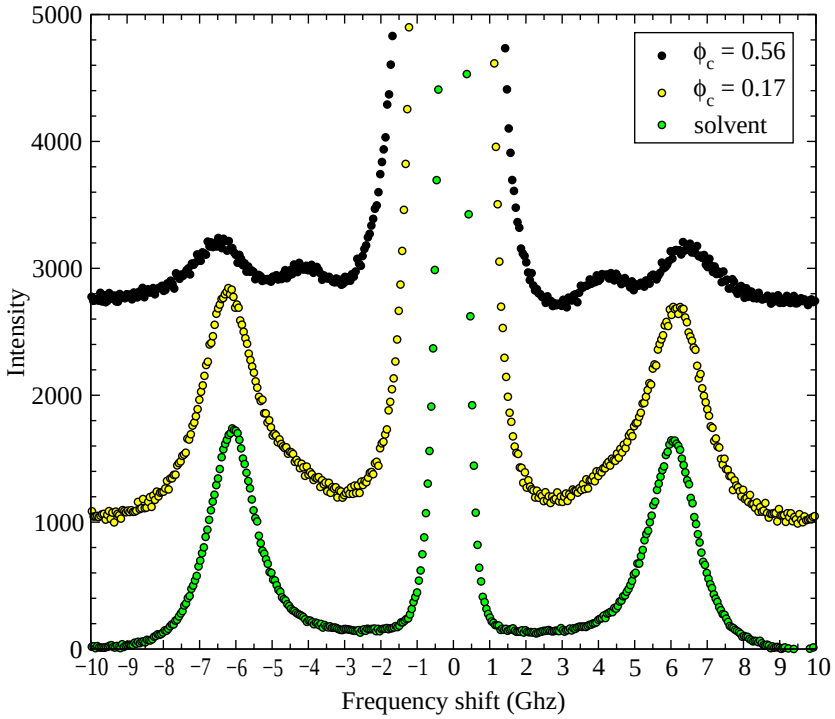

Figure 5.8: Brillouin spectra of a $d_{c_2} = 620\,\mathrm{nm}$ colloidal suspension at several volume fractions and $q = 0.0258\,\mathrm{nm}^{-1}$, together with the spectrum for the pure index-matched dispersion medium. At this scattering vector $qd_{c_2} = 16.0$.

slow mode is significantly less intense than the fast mode in Fig. 5.8, whereas they are of roughly equal intensity in the earlier publication. The spectrum of the pure solvent is just as expected; a single sound mode propagates at a velocity very close to that of the single mode in the $\phi_c = 0.17$ colloid. Note that the background between the Brillouin peaks and the central Rayleigh peak is non-zero for the pure solvent, which is evidence for the existence of thermal or structural relaxation, as discussed in Sec. 2.2.3. This is irrelevant for the purposes of our work on colloids and was therefore not further investigated.

Quantitative comparison with the results of earlier work

While the spectra shown in Fig. 5.8 are in good qualitative agreement with those of Ref. [123], this colloid ($d_{c_2} = 620\,\mathrm{nm}$) is close enough in size to the $d_c = 650\,\mathrm{nm}$ sample studied in the earlier work to allow a quantitative comparison of the peak positions to be made. Peak positions were read from Fig. 5.8 (using the crosshair cursor in `grace` – see Sec. 3.3.2) and extracted from the literature data reproduced in Fig. 5.5, and are

displayed in Table 5.1 below. The uncertainty in the peak frequencies measured for both sets of data is ±0.1 GHz at most.

d_c	qd_c	Volume fraction ϕ_c	Slow mode (GHz)	Fast mode (GHz)
620 nm (new)	16	0.17	—	6.2
		0.56	4.1	6.5
650 nm (Ref. [123])	15	0.10	—	4.3
		0.57	2.8	5.2

Table 5.1: Peak positions of the two longitudinal sound modes in a hard-sphere colloid from the work presented above, compared with measurements on a suspension of almost identical spheres under the same experimental conditions, extracted from the publications of Ye et al [109,123,32].

It is clear from Table 5.1 that there are considerable differences between the frequencies of the modes in the two samples, despite very similar sphere sizes, volume fractions and values of qd_c. The single mode at low volume fraction in the large colloid discussed above ($d_{c_2} = 620\,\text{nm}$) corresponds to a sound velocity 44% higher than that in the suspension studied in the earlier work. The slow mode at higher volume fractions also occurs at a frequency 46% higher in the new colloid. The frequency of the fast mode at the higher volume fraction is also greater in the new colloid, but by the smaller margin of 25%.

The most likely source of these disparities is the fact that a different dispersion medium was used in the earlier work; recall that experiments reported here are performed on spheres suspended in an index-matched solution of *cis*-decalin and tetralin, whereas the solvent used by the authors of Refs. [109,123,32] was a mixture of dodecane and carbon disulfide. From their data, the velocity of sound in this mixture is $v_s' = 1200\,\text{ms}^{-1}$ at ambient temperature (no indication of the uncertainty in this measurement is given), and the frequency of the peak in the pure solvent spectrum of Fig. 5.8 corresponds to a velocity $v_s = 1460 \pm 30\,\text{ms}^{-1}$ at 20 °C in *cis*-decalin/tetralin. This difference of 22% in the sound velocities may have sufficient effect on the propagation velocities of the two sound modes to create the variations noted above, but further investigation of this hypothesis is required.

5.3.1.3 Comparing the two colloids

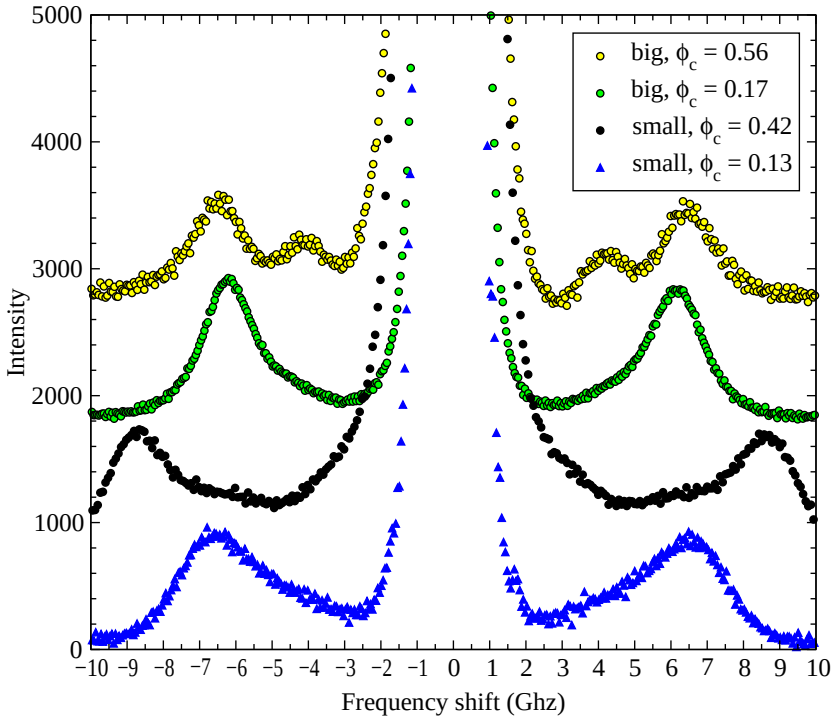

Figure 5.9: Brillouin spectra for the big ($d_{c_2} = 620\,\mathrm{nm}$) and small ($d_{c_1} = 194\,\mathrm{nm}$) colloids at similar core volume fractions and $q = 0.0258\,\mathrm{nm}^{-1}$, giving $qd_{c_1} = 5.0$ and $qd_{c_2} = 16.0$. Spectra have been scaled to similar intensities to make comparisons between the two colloids easier.

Before moving on to a more detailed investigation into sound propagation in hard-sphere colloids, let us take a brief look at the similarities and differences between the new data obtained for the two sizes of colloid discussed above. Fig. 5.9 shows two spectra from each of the colloids, with core volume fractions which are close enough to allow meaningful comparisons to be made. It should be noted that the dimensionless parameter qd_c which determines the acoustic properties of the suspensions (see Sec. 5.1.2) is quite different for these two colloids, equal to 5.0 for the small spheres and 16.0 for the larger ones. Quantitative comparisons between the two should therefore be expected to yield significant differences, although qd_c is above the established threshold ($qd_c \approx \pi$) for the existence of two longitudinal modes in a colloidal suspension.

The lowest volume fraction spectra for each colloid ($\phi_c = 0.13$ for the small spheres and $\phi_c = 0.17$ for the large spheres) are very similar both in peak frequency and lineshape. In both cases, an unresolved slow mode causes the peak to be very broad

and asymmetric. The spectrum from the larger colloid is slightly less asymmetric, narrower, and the kink on the low-frequency side of the peak is more pronounced, likely due to the higher volume fraction of this sample; recall that $\phi_c = 0.20$ was established in Sec. 5.1.2 as the concentration above which the spheres are close enough together for the second mode to propagate.

In contrast to the similarity at low ϕ_c, the spectra for the higher core volume fractions ($\phi_c = 0.56$ for the large spheres and $\phi_c = 0.42$ for the smaller ones[¶]) are very different. The most obvious disparity is the clear resolution of two modes in the larger colloid. The slow mode is not well defined in the smaller colloid, with only a hint of its existence present at approximately 3.5 GHz. The other main difference is the frequency at which the peaks occur. Despite the fact that the smaller colloid is being probed at less than a third of the value of qd_c, the frequency of the fast mode is much larger: 8.5 GHz compared to 6.5 GHz for the larger spheres. In addition, the frequency of the slow mode in the small colloid appears to be at 3.5 GHz, while it occurs at 4.2 GHz in the larger colloid. In other words, the separation of the peaks is much greater for the small colloid ($d_{c_1} = 194\,\text{nm}$) than for the large one ($d_{c_2} = 620\,\text{nm}$). This is consistent with the observations of Ye *et al*, who note that "the splitting between the normalised frequencies of the two modes is consistently less pronounced for the larger spheres than for the smaller spheres" [123].

Following the success of these preliminary measurements at fixed scattering angle, the next task was to attempt to confirm – and then if possible extend – the work of the Exxon group at variable q which revealed the emergence and dispersion of two longitudinal sound modes in hard-sphere colloids.

5.3.2 Reproducing the dispersion relation for a $d_c = 319\,\text{nm}$ colloid

A program of research aiming to repeat the pioneering work which led to the discovery of a second sound mode in colloidal suspensions was considered to be worthwhile for two main reasons. Firstly, the observations of the group led by Weitz and Sheng have never been reproduced – even if no new information is obtained here, confirmation of their

[¶]Note that these are the highest core volume fractions possible for each colloid, corresponding to the hard-sphere $\phi_{rcp} = 0.64$.

findings would be a valuable result. Secondly, the study of one of the few complex fluids for which some earlier Brillouin scattering data is available in the literature seemed to be a wise choice for the first detailed investigation of a colloidal system using the new Brillouin spectrometer at Edinburgh.

The larger of the two colloids studied in the experiments presented in the previous section (Sec. 5.3.1) would have been ideal for use in such an investigation as it was very similar in size to the larger of the colloids used by the authors of Ref. [123]. However after completion of the preliminary work reported above, the sample had become quite yellowed due to the passage of time and exposure to laser light (the reasons for this yellowing were discussed in Sec. 5.2.3) making it very difficult to obtain a satisfactory Brillouin spectrum. A new sample was therefore required, with properties as similar as possible to one of the colloids studied in the original work.

As discussed in Sec. 5.3.1.2, the two peaks are separated by a larger frequency gap for smaller sphere diameters. It was thus decided to use a colloid similar to the smaller of the two studied by Ye *et al* ($d_c = 340\,\mathrm{nm}$), in order to facilitate the observation of each sound mode without the complications of analysis caused by overlapping Brillouin peaks. The closest match to this size available from the stock of colloidal particles synthesised at Edinburgh by Dr. Andrew Schofield had a core diameter $d_c = 319\,\mathrm{nm}$, and was designated 'ASM36'.

Approximately 50 ml of this colloid was washed following the method described in Sec. 5.2.1, resulting in an index-matched suspension suitable for light scattering experiments. The core volume fraction was set to $\phi_c = 0.39$, as close as possible to the intermediate concentration ($\phi_c = 0.38$) in the work of the Exxon group. The two sound modes are well developed and easily resolvable at this volume fraction. Roughly 20 ml of this sample was sealed in a 15 mm diameter cylindrical glass cell using PTFE tape. For the ASM36 spheres, a core volume fraction $\phi_c = 0.39$ corresponds to a hard-sphere volume fraction $\phi = 0.51$ which is in the coexistence region of the hard-sphere phase diagram (see Sec. 5.1.1). The sample therefore crystallised over the period of a few days, so had to be redispersed each morning before beginning experiments. Approximately 30 minutes of vigorous automated shaking was sufficient to achieve this, after which the colloid became cloudy due to the formation of small air bubbles. These required a

further 30 minutes to rise to the top of the sample before it regained transparency and was ready for use.

Brillouin spectra were recorded using the Fabry-Perot interferometer in the triple-pass configuration with the usual laser wavelength ($\lambda = 514.5\,\mathrm{nm}$) and a power of 200 mW at the source. The cell discussed in Sec. 3.2.2.2 was used to hold the temperature at 16 °C, for which the best index-match was found to occur. The scattering angle was varied between 10 ° and 155 ° using the apparatus and techniques described in Sec. 3.2.2.1, corresponding to $0.0032\,\mathrm{nm}^{-1} \leq q \leq 0.0360\,\mathrm{nm}^{-1}$ and $1.0 \leq qd_c \leq 11.5$. Larger scattering angles were not used due to overlapping fast modes from adjacent spectral orders at high q and the marginal increase in q which would be obtained due to the $q \sim \sin\theta/2$ relationship. The free spectral range of the interferometer was kept at around 20 GHz for most of the measurements, but at very high and very low q this was reduced to around 10 GHz in order to allow observation of the slow mode and the single low-ϕ_c mode respectively. The low intensity of the Brillouin peaks meant that rather long collection times were required. Typically, 3,000 individual spectra were accumulated, taking about 90 minutes to produce a composite spectrum with a satisfactory signal-to-noise ratio. Brillouin spectra were also recorded in the pure solvent at various scattering angles after centrifuging the sample until all of the colloidal spheres formed an RCP sediment at the bottom of the cell. The dispersion relations for the two sound modes which were the product of these measurements on the ASM36 colloid are shown in Fig. 5.10. These will be discussed below and compared with the corresponding results from the original work by the Exxon group (reproduced in Fig. 5.4).

Once the interferometer had been upgraded to operate in a five-pass configuration (see Sec. 3.1.3), several spectra were recorded at various scattering angles in order to compare with the triple-pass measurements. This will be discussed below.

Unfortunately, the process of accumulating enough data to produce the dispersion relations plotted in Fig. 5.10 proved to be extremely time-consuming. Each satisfactory spectrum required about 90 minutes of collection, and contributes at most two data points (the frequencies of the two sound modes). In addition to time spent accumulating data, the colloid had to be redispersed and the interferometer realigned at least once

each day; tasks which could be performed concurrently but took between one and two hours. The selection of a new scattering angle and subsequent alignment of the illumination optics (Sec. 3.2.2.1) adds at least 20 minutes to the time taken to obtain each spectrum. When the two sound modes are far apart (this occurs at large q) the slow mode may overlap with the central Rayleigh peak and the fast modes of adjacent spectral orders may overlap with one another, requiring different free spectral ranges to be used in order to resolve the two modes. In this situation, only one data point is contributed to the dispersion relation by each Brillouin spectrum, further extending the time required to collect a dataset like the one in Fig. 5.10. In total, thirty to forty satisfactory spectra are needed to compile a detailed dispersion relation.

A spectrum was considered 'satisfactory' if enough data had been collected to ensure that the Brillouin peaks are of sufficient intensity to be clearly distinguished from the background noise. This is only possible if optimal alignment of the Fabry-Perot interferometer can be preserved for a long enough period – in some cases as much as two hours. If the DAS-10 stabilisation unit is unable to maintain alignment then the finesse deteriorates rapidly and the Brillouin peaks disappear into the background. The spectrum can sometimes be recovered manually if the drift is noticed soon enough, but this requires considerable skill (and to some extent luck) and is often not possible (see Sec. 3.2.2.3). There are several causes of this loss of alignment which are particularly problematic when studying colloidal suspensions. Sudden pulses of intense elastic scattering from dust particles can make the DAS-10 lose its lock on the Rayleigh peak, and unfortunately dust particles are very difficult to remove from colloids – one of the factors which make them challenging subjects for Brillouin spectroscopy. Electromagnetic noise pulses from nearby electronic devices have a similar effect, as do vibrations caused by mechanical disturbances in and around the lab. The long collection times required by colloidal samples also increase the likelihood of the interferometer mirrors requiring adjustments outside the limits of the piezo stacks, which causes the DAS-10 to lose the spectrum completely unless the problem is spotted immediately and rectified by using the 'Align' potentiometers to 'walk' the mirrors back into the controllable range (see Sec. 3.2.2.3).

Roughly half of the attempts to collect a satisfactory spectrum were affected by one or more of these problems, meaning that the timescale for obtaining a detailed dispersion

relation like Fig. 5.10 is on the order of a month. Unfortunately, this is rather close to the limit imposed on the useful lifetime of a colloidal sample by the yellowing effect discussed in Sec. 5.2.3. Every effort was therefore made to ensure that measurements were completed in the shortest time possible, but even so the spectra were of significantly lower quality towards the end of the experiment. This meant that further work on the sample (either to repeat measurements or to study a different volume fraction) was not possible.

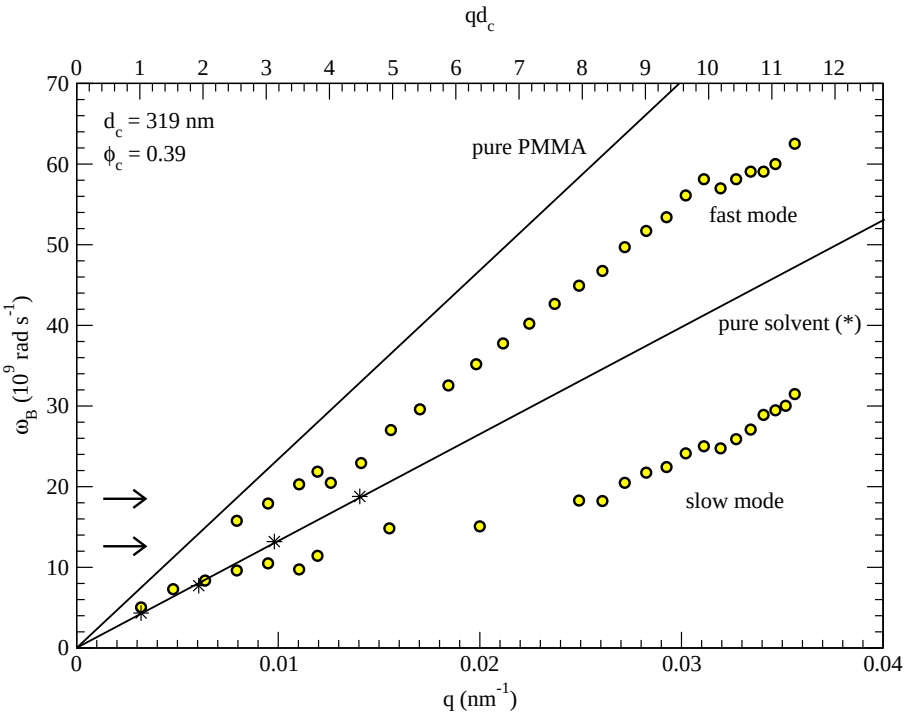

Figure 5.10: Dispersion relations for fast and slow modes in the $\phi_c = 0.39$ ASM36 colloid ($d_c = 319\,\mathrm{nm}$). The arrows at the left-hand side correspond to the frequencies of the first two peaks in the scattering amplitude of longitudinal acoustic waves incident on a single colloidal sphere [124] (see text). Uncertainties in q are negligible, as discussed in Sec. 3.2.2.1. Compare with the dispersion relation for an almost identical colloid from Ref. [123], reproduced in Fig. 5.4 above.

5.3.2.1 Discussion of ASM36 ($d_c = 319\,\mathrm{nm}$) dispersion relation

Fig. 5.10 shows the dispersion relations of the two sound modes measured in the $\phi_c = 0.39$ ASM36 colloidal suspension ($d_c = 319\,\mathrm{nm}$) – results of the experiments discussed in the previous section. Peak positions were measured to better than $\pm 0.1\,\mathrm{GHz}$ using the

`grace` program as described in Sec. 3.3.2. The dispersion relation of the pure solvent was also measured, and is included in the figure along with that of the PMMA from which the colloidal spheres are made. The PMMA data is taken from Ref. [123] and was obtained by measuring the velocity of short-wavelength hypersonic sound waves propagating in the cores of the spheres. Axes displaying the values of both q and qd_c are shown to enable comparison with dispersion for different sphere sizes. Uncertainties in q and hence qd_c are small enough to be neglected, as discussed in Sec. 3.2.2.1. The two arrows at the bottom left-hand side of the figure mark the frequencies at which scattering of longitudinal acoustic waves from a single colloidal sphere was calculated to be maximal by the authors of Ref. [123], the significance of which will be discussed below.

The transition from one to two sound modes at $q = 0.008\,\mathrm{nm}^{-1}$ and dispersion of each at higher q can clearly be seen from Fig. 5.10. For $q < 0.008\,\mathrm{nm}^{-1}$ the single mode propagates with frequencies indistinguishable from those in the pure solvent. The slow mode propagates with frequencies lower than the solvent at the same q, and the fast mode is intermediate between the solvent and solid PMMA. All of these features are the same as those identified in the original publications, discussed in some detail in Sec. 5.1.2.

In fact the dispersion relation shown in Fig. 5.10 is in almost every respect very similar to the dispersion relation of the nearly identical $d_c = 340\,\mathrm{nm}$, $\phi_c = 0.38$ colloid from Ref. [123], reproduced in Fig. 5.4 above. Comparing the two figures, we see that the second mode emerges at the same q, the shapes of the slow mode dispersion curves are the same, and the fast mode dispersion curves both soften towards the frequency of sound in the pure solvent at large q.

The main difference between the original and new dispersion relations is quantitative: the peak frequencies of both modes are approximately 30% higher for the data presented here. This is a similar result to the findings of the comparison presented in Sec. 5.3.1.2, which concluded that this disparity is due to the fact that a different dispersion medium was used in the earlier work.

Other differences which may be noted in comparing Fig. 5.4 (reproduced from Ref. [123]) and Fig. 5.10 are the properties of the gaps in the dispersion relation of the fast mode,

and a lack of data points for the slow mode at intermediate values of q. The following sections aim to address these issues.

Gaps in the fast mode dispersion relation

Distinct frequency gaps were apparent in the dispersion relation of the fast mode in the earlier work. These were discussed in Sec. 5.1.2.3 and shown by theory to correspond to the frequencies of single-sphere resonances for scattering of sound waves [124, 125]. The first gap (lowest frequency) occurred with the emergence of the second mode, and this gap is indeed evident at $q = 0.008\,\mathrm{nm}^{-1}$ in the new data plotted in Fig. 5.10. The second gap in the earlier dataset (Fig. 5.4) is at an angular frequency of $20 \times 10^9\,\mathrm{rad\ s}^{-1}$ and while no well-defined second gap in the fast mode is present in Fig. 5.10, there is a departure from linearity at ($q \approx 0.013\,\mathrm{nm}^{-1}$, $\omega_B \approx 20 \times 10^9\,\mathrm{rad\ s}^{-1}$) which may be a related effect. The two arrows at the bottom left-hand side of Fig. 5.10 denote the frequencies of these resonances (taken from Ref. [123]), which are the cause of the gaps as discussed in Sec. 5.1.2.3 (if sound is scattered strongly at a given frequency it is unable to propagate, resulting in a gap at that frequency). Although the calculation of these resonances was for a different dispersion medium (the Exxon group used a mixture of carbon disulfide and dodecane rather than *cis*-decalin/tetralin), the corresponding features in the new dataset seem to occur at very similar frequencies. Is it possible that the single-sphere resonances – which depend strongly on the material properties of the colloidal sphere – do not depend strongly on the velocity of sound in the surrounding fluid, which was found to be quite different in the two solvents (see Sec. 5.3.1.2)?

Difficulty detecting the slow mode at intermediate q: moving to five-pass

The reader may have noticed the paucity of data points for the slow mode at intermediate q in Fig. 5.10 ($0.012\,\mathrm{nm}^{-1} < q < 0.025\,\mathrm{nm}^{-1}$). Despite repeated attempts, the lower-frequency Brillouin peak could not be resolved using the interferometer in the triple-pass configuration, although the fast mode remained strong and well-defined throughout this range of scattering vectors. This was rather surprising. Why should one of the peaks 'disappear' and then return at higher q? No mention of such an effect was made in the earlier publications (Refs. [109, 123, 32]) summarised in Sec. 5.1.2.

The absence of the slow mode from these triple-pass spectra was investigated by changing the interferometer to the five-pass configuration, which provides much-improved contrast thereby enabling weaker spectral features to be detected (see Sec. 3.1.3). A comparison of three-pass and five-pass spectra from the same colloid at identical scattering vectors is shown in Fig. 5.11. The improvement in the resolution of the lower-frequency mode on moving to five-pass operation is marked, although this is at the expense of a lower signal-to-noise ratio as discussed in Sec. 5.3.1.1. The increased finesse of the central Rayleigh peak (i.e. it is narrower) allows the slow mode to be observed at frequency shifts down to just above 1 GHz, whereas the limit for three-pass operation is around 3 GHz.

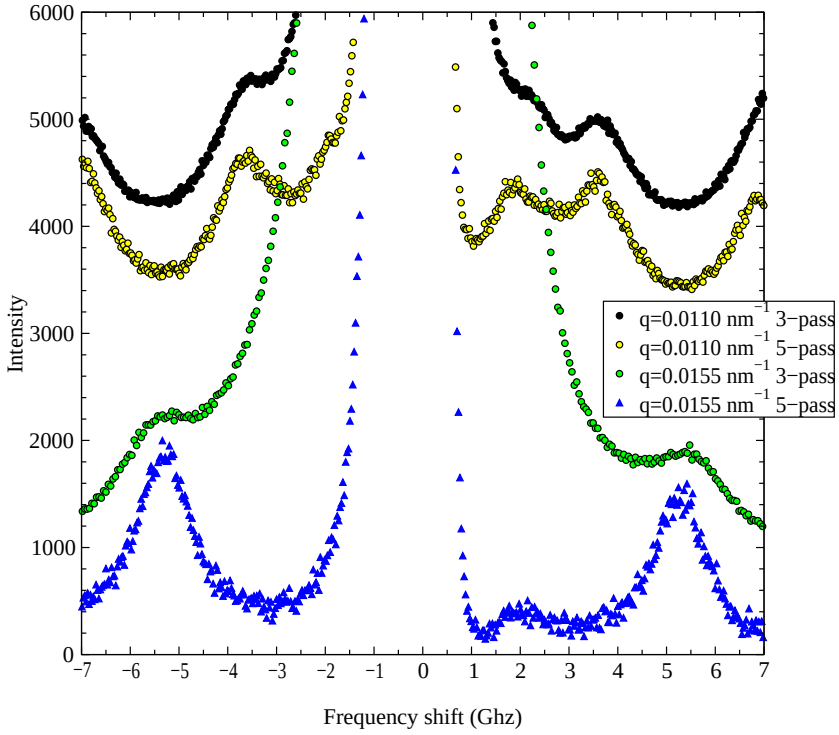

Figure 5.11: Comparison of triple-pass and five-pass spectra for the ASM36 ($d_c = 319\,\text{nm}$, $\phi_c = 0.39$) colloid at two scattering vectors. Note the lower frequencies which are accessible due to the much-improved contrast of the five-pass configuration. The FSR of the interferometer was such that the fast mode peaks in the bottom spectrum overlap, and the high-frequency sides of adjacent orders are visible in the top two spectra.

Might it be the case that the disappearance of the slow mode at intermediate q is simply due to the inability of a triple-pass interferometer to resolve the peak at low frequencies? The five-pass $q = 0.0155\,\text{nm}^{-1}$ spectrum (the bottom dataset in Fig. 5.11)

shows that although the low-frequency peak is present (at 2.2 GHz) it is extremely weak compared to the intensity of the fast mode, and is only just distinguishable from the background noise. This dramatic reduction in slow-mode intensity is therefore not an artefact of triple-pass operation, and remains unexplained. In fact the effect was also observed in the smaller colloid (ASM25) studied in the following section, and will be further discussed in Sec. 5.3.4 after the presentation of these results.

The few data points for the low-frequency mode in the $0.012\,\mathrm{nm}^{-1} < q < 0.025\,\mathrm{nm}^{-1}$ range in Fig. 5.10 were measured using the interferometer in this new five-pass configuration. The reduction in transmitted intensity resulted in longer count times being required (typically two hours per spectrum), and the anomalous weakness of the slow mode meant that several spectra had to be recorded in order to obtain each satisfactory dataset. It was not therefore possible to collect as many data points in this range of q as were obtained for the rest of the dispersion relation.

The dispersion relation of colloid ASM36: summary of findings

This first attempt to confirm the existence and dispersion relation of a second longitudinal sound mode in a hard-sphere colloidal suspension has been extremely successful. All of the qualitative features noted in the original research occur in the new work, with any quantitative discrepancies able to be explained by the different dispersion media of the two colloids. An anomalous weakening of the slow mode was observed at intermediate q – an effect not reported in the literature.

The dispersion relation of the ASM36 ($d_c = 319\,\mathrm{nm}$) colloid was only measured at one volume fraction, but rather than spend more time comparing results with the earlier work by looking at other ϕ_c, it was decided to extend the program of research to look at a suspension of much smaller spheres than have been studied before, in order to see whether the trends discussed above continue to hold at smaller d_c. On a more prosaic level, this was a sensible choice due to the experimental problems posed by yellowing of the ASM36 sample which had occurred by the time the measurements required to compile Fig. 5.10 were completed.

5.3.3 Dispersion in colloid ASM25: very small spheres ($d_c = 186\,\mathrm{nm}$)

The pioneering work on hypersound propagation in hard-sphere colloids by the Exxon group led by David Weitz and Ping Sheng looked at only two sizes of colloidal spheres: $d_c = 340\,\mathrm{nm}$ and $d_c = 650\,\mathrm{nm}$ (Refs. [109, 123, 32], summarised in Sec. 5.1.2). The aim of the previous section was to reproduce their results by obtaining the dispersion relation for an almost identical colloidal suspension. The success of this attempt both confirmed the findings of the earlier work and established the suitability of the new spectrometer at Edinburgh for Brillouin scattering studies of complex fluids.

A natural next step was to move to look at a system which had not been studied previously, such as a monodisperse suspension of spheres with a very different diameter. The smallest polymer-coated PMMA particles available from stock had a core diameter $d_c = 186\,\mathrm{nm}$, roughly half that of the smallest colloid for which a dispersion relation had been measured before. Would the second sound mode be observed in a suspension of these much smaller spheres? If so, will the dispersion relation match those of the larger particles (Fig. 5.5) when scaled by d_c to allow comparison of the different sizes?

An additional motivation for obtaining the dispersion relation for a suspension of different sphere diameter was the possibility of combining this colloid with the one studied in the previous section (ASM36) to form a binary colloidal suspension, which could then be studied using Brillouin spectroscopy. This will be discussed in Sec. 5.4 below.

Roughly 50 ml of a colloid with core diameter $d_c = 186\,\mathrm{nm}$ (designated 'ASM25', with a hard-sphere diameter $d = 216\,\mathrm{nm}$) was washed as described in Sec. 5.2.1 to obtain an index-matched suspension, the core volume fraction of which was set to $\phi_c = 0.34$, close to the concentration studied for ASM36 ($\phi_c = 0.39$) above. The hard-sphere volume fraction ϕ corresponding to $\phi_c = 0.34$ is $\phi = 0.51$, which is in the coexistence region of the hard-sphere phase diagram (see Sec. 5.1.1). The sample therefore tended to crystallise after about a week, so had to be redispersed each morning as described in Sec. 5.3.2 in order to ensure complete disorder. Approximately 20 ml of this colloid was sealed in a 15 mm diameter cylindrical glass cell by wrapping PTFE tape around the cap.

Brillouin spectra were recorded with the Fabry-Perot interferometer in the high-contrast

five-pass configuration, with a laser wavelength of 514.5 nm at a power of 200 mW. The FSR was set to roughly 20 GHz for most spectra, but reduced to about 10 GHz when attempting to resolve the slow mode at low frequencies. The best index-match was found to be at 14 °C, at which temperature all experiments were therefore performed. Scattering angles between 25 ° and 150 ° were obtained as discussed in Sec. 3.2.2.1, corresponding to $0.0079\,\mathrm{nm}^{-1} \leq q \leq 0.0353\,\mathrm{nm}^{-1}$ (calculated assuming $n = 1.495$, the refractive index of the colloidal particles) and $1.5 \leq qd_c \leq 6.6$. Collection times were similar to those required for the five-pass measurements made on the ASM36 colloid, with a satisfactory spectrum typically requiring data to be accumulated for about two hours. A similar proportion of spectra also had to be rejected due to weak Brillouin peaks and/or loss of alignment for any of the reasons discussed in Sec. 5.3.2. Two sound modes were observed, the dispersion relations of which are shown in Fig. 5.12 below.

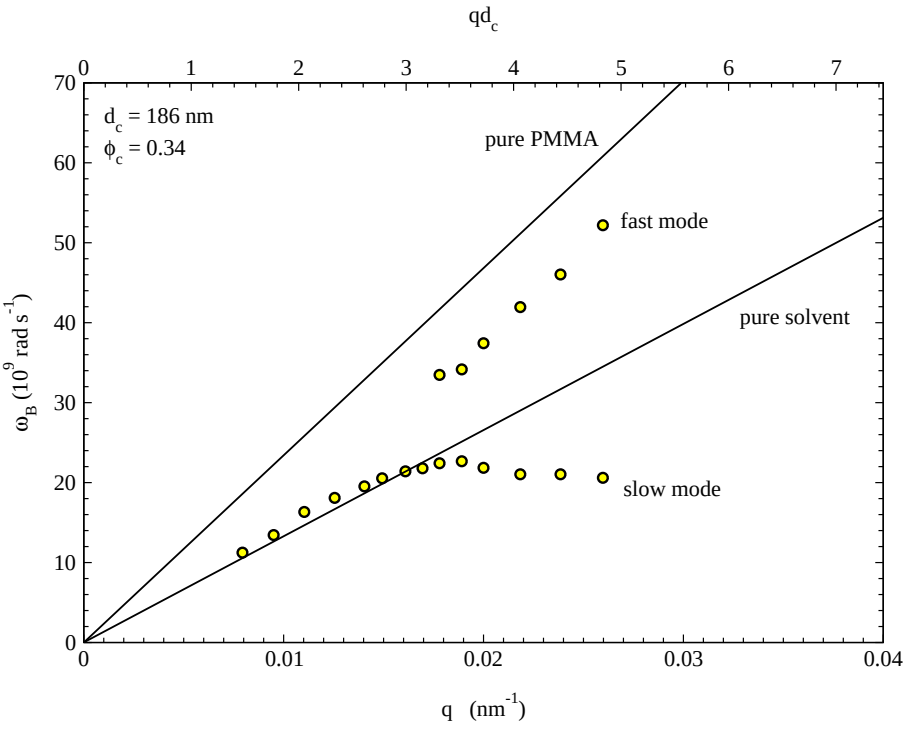

Figure 5.12: Dispersion relations for the fast and slow sound modes in the ASM25 ($d_c = 186\,\mathrm{nm}$) colloid at a core volume fraction $\phi_c = 0.34$. Data for the pure solvent was measured as discussed in Sec. 5.3.2 and the line for pure solid PMMA is taken from Ref. [123]. Spectra were recorded at larger q, but the slow mode was not visible and the high-frequency peaks belonging to adjacent orders overlapped preventing determination of the fast mode frequency.

5.3.3.1 Discussion of ASM25 results

Fig. 5.12 shows the dispersion relation for the $\phi_c = 0.34$, $d_c = 186\,\text{nm}$ ASM25 colloidal suspension. Peak frequencies were measured using the `grace` program as described in Sec. 3.3.2, incurring an uncertainty of not more than $\pm 0.1\,\text{GHz}$. Data for the pure solvent (measured in Sec. 5.3.2) and pure solid PMMA (taken from Ref. [123]) are included in the figure to facilitate comparison with dispersion relations for other particle sizes (Figs. 5.4 and 5.10). Axes labelled with both q and qd_c are provided for the same purpose. Uncertainties in q and hence qd_c are negligible throughout the range of scattering angles studied, as discussed in Sec. 3.2.2.1 above.

The trends apparent in Fig. 5.12 are in qualitative agreement with both the results for the larger colloid presented in Sec. 5.3.2 and the earlier findings of the Exxon group discussed in Sec. 5.1.2. At low q only one sound mode is present, and propagates with a frequency almost unchanged from the peak in the pure solvent. Above a certain value of q, this single mode splits into two; a fast mode with a velocity intermediate between that of the pure solvent and pure solid PMMA, and a slow mode whose velocity drops below that of the solvent.

Detailed quantitative comparisons between the dispersion relation for the ASM25 colloid and those for other sphere diameters require both ω_B and q axes to be multiplied by d_c to produce a scaled dispersion curve like the one reproduced from Ref. [123] in Fig. 5.5 above. This will shortly be carried out in Sec. 5.3.3.2, but for now we may note that the second sound mode emerges at $qd_c \approx 3$ for the ASM25 ($d_c = 186\,\text{nm}$) colloid, compared to $qd_c \approx 2$ for ASM36 ($d_c = 319\,\text{nm}$ – see Fig. 5.10). The width of the frequency gap between the emergent fast mode and the lower-frequency mode at the same q ($\approx 0.018\,\text{nm}^{-1}$) in Fig. 5.12 appears to be somewhat larger than that observed in ASM36. This difference grows with increasing q in the two-mode part of the ASM25 dispersion relation, so that the modes are separated by a greater frequency than was the case in the larger colloid. This agrees with the observation (discussed in Sec. 5.3.1.3 and Ref. [123]) that the splitting between modes varies inversely with sphere diameter.

Data was not recorded at very low q ($< 0.0079\,\text{nm}^{-1}$) because the previous section's

results on the larger colloid confirmed Ye *et al*'s observation that the low-q single sound mode simply follows the dispersion relation of the pure solvent. The limited time available experimental time was focused rather on attempting to obtain data at higher q, in the two-mode region of the dispersion relation. However the reader may have noticed that the highest q-values in Fig. 5.12 are not as large as those achieved for the previous colloid (ASM36, Fig. 5.10). Spectra were recorded for ASM25 at $q > 0.026\,\mathrm{nm}^{-1}$ but neither peak position was able to be measured. The slow mode was too weak to be detected, even by reducing the FSR of the interferometer and accumulating data for many hours. This behaviour is reminiscent of the 'disappearing' slow mode observed in the larger colloid (Sec. 5.3.2.1), but this time the effect occurs at larger scattering vectors, and the mode does not reappear with increasing q (at least not in the range accessible using light with a wavelength of 514.5 nm). This anomalous weakening of the slow mode will be discussed in Sec. 5.3.4 below. Fast mode frequencies at $q > 0.026\,\mathrm{nm}^{-1}$ were not able to be measured due to overlap with the peaks belonging to adjacent orders. This situation could have been rectified by changing to a larger free spectral range, but after spending a great deal of time focusing on attempts to detect the slow mode at small FSR, the colloid was too yellowed to permit the required spectra to be resolved.

Before proceeding to compare the d_c-scaled dispersion relations for colloids ASM36 and ASM25, let us look briefly at a subset of the data accumulated by the experiments described above, which shows in detail the crossover from the low-q single-mode régime to the existence of fast and slow sound modes at larger scattering vectors in the $d_c = 186\,\mathrm{nm}$ suspension.

Emergence of the slow mode with increasing q

During the experiments on the ASM25 colloid ($d_c = 186\,\mathrm{nm}$, $\phi_c = 0.34$) described in the previous section, particular attention was paid to the form of the spectrum around the scattering vectors at which the two-mode behaviour develops out of the low-q single-mode dispersion relation. No spectra and very little comment on the emergence of the second mode were presented by the authors of the earlier publications (Refs. [109, 123, 32]), hence it was decided to collect data at very closely spaced scattering vectors in

order to determine the shape of the peaks in this transitional region. A sequence of spectra across the range $0.0126\,\mathrm{nm}^{-1} \leq q \leq 0.0218\,\mathrm{nm}^{-1}$ (corresponding to $2.3 \leq qd_c \leq 4.1$) is shown in Fig. 5.13, nicely illustrating the emergence of the second sound mode as the scattering angle is increased.

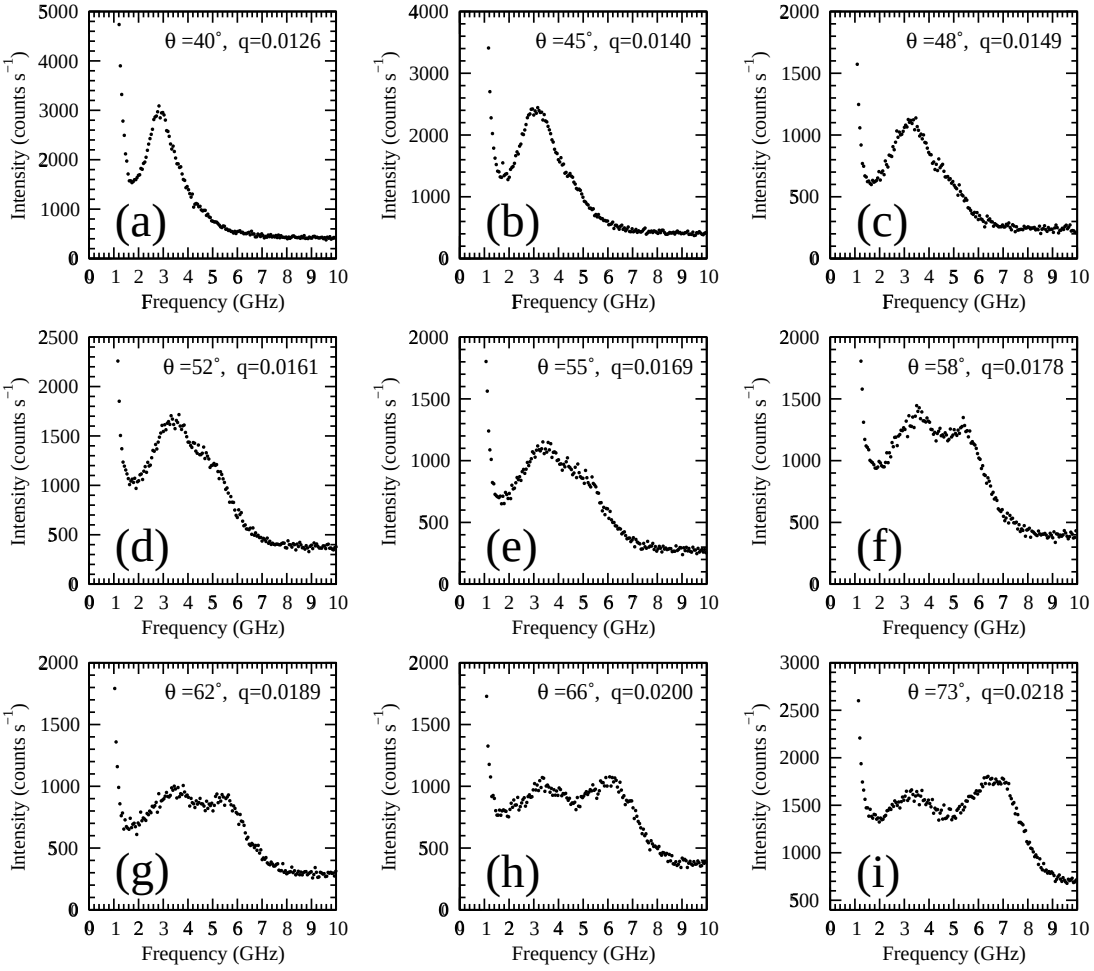

Figure 5.13: Sequence of spectra from the ASM25 colloidal suspension ($d_c = 186\,\mathrm{nm}$, $\phi_c = 0.34$) showing the emergence of the slow sound mode with increasing q. Spectra have been scaled to similar fast mode peak heights in order to facilitate comparison of the peak shapes. Note that the units of q are nm^{-1} for all graphs in the figure.

Fig. 5.13 provides some extra insight into the transition from one to two sound modes, which until now has been described simply by plotting the peak positions to give a dispersion relation. We can now see the gradual progression from a single Lorentzian peak at low q to a single peak with a distinct shoulder (graphs (c) and (d) in the figure), which then develops and shifts in frequency until two overlapping peaks create a highly

asymmetric composite (graphs (e) and (f)); finally the two peaks move far enough apart in frequency to be resolved as two distinct sound modes (graph (i)). As can be seen from the dispersion relation (Fig. 5.12), further increasing q beyond the narrow range explored in Fig. 5.13 results in the modes moving even further apart.

5.3.3.2 Scaled dispersion relations for ASM36 and ASM25

The best way of comparing the behaviour of the two different colloids for which dispersion relations have been presented above is to scale both datasets by the core diameter d_c and plot them together on one graph. This was the approach taken by the authors of the first publications on Brillouin scattering from hard-sphere colloids, who found that – barring a few minor differences – scaled dispersion relations for different sizes of colloids were qualitatively and quantitatively very similar across a wide range of volume fractions.

Fig. 5.14 shows the dispersion relations presented above for the ASM36 and ASM25 colloids, with both axes scaled by d_c in order to allow quantitative comparisons to be made between the two sphere sizes. Note the slightly unusual units on the y-axis, used only in order to allow the figure to be compared easily with the scaled dispersion relation published by the Exxon group, which is reproduced in Fig. 5.5 above.

Starting at low qd_c, we see that both colloids support only one sound mode for $qd_c < 2.5$. The scaled angular frequencies of these single modes in the two different systems are identical, and as was shown by Figs. 5.10 and 5.12 this frequency is equal to that of the sound mode in the pure solvent at the same q. Exactly the same behaviour was observed in the original publications (see Sec. 5.1.2).

Moving up in qd_c, Fig. 5.5 shows that the second sound mode appears in the dispersion relations at slightly different qd_c for the two different sizes of colloids. The first data point for the second mode in the larger colloid (ASM36) occurs at $qd_c = 2.5$, but the fast mode does not emerge until $qd_c = 3.3$ in the smaller diameter ASM25 sample. Looking at the scaled dispersion relation from Ref. [123] (Fig. 5.5 above), we see that the qd_c-value of the first data point for the fast mode is similarly indistinct, varying from $qd_c = 2.3$ to $qd_c = 3.2$ for the different sizes and volume fractions. This variation

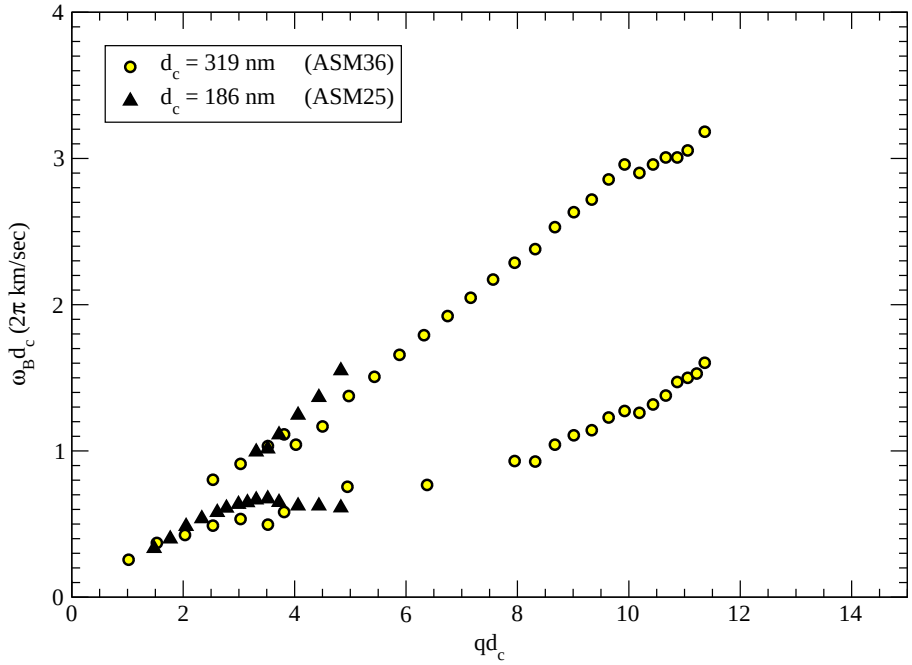

Figure 5.14: Scaled dispersion relations for both ASM36 ($d_c = 186\,\mathrm{nm}$, $\phi_c = 0.39$) and ASM25 ($d_c = 186\,\mathrm{nm}$, $\phi_c = 0.34$) colloids. Compare with the corresponding figure in Ref. [123], reproduced in Fig. 5.5 above.

was not mentioned by the authors of the earlier work; on the contrary, they state that "the splitting of the two modes occurs at the same point, $qd_c \approx \pi$, for both data sets" [123]. As no patterns are apparent in this variation either for the new data of Fig. 5.14 or the earlier publications, it seems likely that the relatively small differences in the qd_c at which the second mode emerges are simply due to the difficulty in defining a criterion for the existence or otherwise of the new peak. As shown by the sequence of spectra in Fig. 5.13, its emergence is a gradual process, hence the point at which one considers the second mode to be distinct depends to some extent on the judgement of the investigator, and also on the signal-to-noise ratio of the spectrum. The size of the frequency gap between the two modes at the point of splitting appears to be equal (within experimental uncertainty) for the two colloids in Fig. 5.14, which agrees with the earlier data reproduced in Fig. 5.5.

Above $qd_c \approx \pi$ the dispersion of the two modes in Fig. 5.14 is qualitatively similar, the only difference being that the fast mode in the smaller colloid (ASM25) increases in angular frequency with increasing qd_c at a greater rate than in ASM36. This is consistent with the findings of the Exxon group, who observed that the separation

between modes varies inversely with sphere diameter (this was discussed in Sec. 5.3.1.3 above). The ASM25 ($d_c = 186\,\text{nm}$) data is the first evidence for the continuation of this trend at smaller sphere diameters than those studied in the earlier publications ($d_c = 340\,\text{nm}$ and $650\,\text{nm}$).

As stated in Sec. 5.3.3.1, the slow mode was too weak to be detected in the ASM25 colloid at $qd_c > 4.8$, which explains the lack of data points for the mode above this value in Fig. 5.14. This is very close to the qd_c at which the slow mode 'disappeared' in the triple-pass measurements on ASM36 (Sec. 5.3.2.1) and was only just detectable on moving to five-pass, resulting in the paucity of slow mode data points at intermediate qd_c in the figure. The anomalous weakening of the low-frequency mode in both colloids will be discussed in more detail in the following section.

In summary, the scaled dispersion relation shown in Fig. 5.14 agrees in almost every respect with the findings of Ye *et al* [109,123,32] – the only earlier study of the two sound modes revealed by Brillouin scattering in hard-sphere colloidal suspensions. The work presented above showed that their results for a $d_c = 340\,\text{nm}$ colloid were reproducible in a $d_c = 319\,\text{nm}$ sample (ASM36), and extension of the research to look at spheres of roughly half the smallest diameter studied previously ($d_c = 186\,\text{nm}$ – ASM25) showed that all of the trends identified for the larger colloids remain valid for much smaller colloidal particles. The most interesting new effect which was observed in the experiments on ASM36 and ASM25 was the aforementioned anomalous reduction in slow-mode intensity for intermediate values of the scattering vector. The following section discusses this phenomenon and attempts to offer an explanation for the disappearance and subsequent re-emergence of the slow mode with increasing qd_c in the dispersion relations of both colloids studied above.

5.3.4 Anomalous weakening of the slow mode

The only completely new effect which has been revealed by the experiments on monodisperse hard-sphere colloids discussed above is the 'disappearance' of the slow mode which was observed at intermediate qd_c in both samples ASM36 and ASM25. This anomalous weakening of the low-frequency mode intensity has not been reported previously, hence merits some discussion here. Note that the intensity of the fast mode was not observed

to change much as a function of q, hence the relative heights of the two peaks are a good indication of the extent to which the slow-mode intensity varies.

The phenomenon was first observed in the triple-pass spectra for colloid ASM36 ($d_c = 319\,\mathrm{nm}$, $\phi_c = 0.39$) obtained during measurement of the dispersion relation discussed in Sec. 5.3.2. The first sign of weakening in the slow-mode intensity with increasing q began at $qd_c = 4.02$. By $qd_c = 4.94$ it had disappeared completely, not returning until $qd_c = 7.91$. At first it was thought that this disappearance might be due to the slow mode moving to frequencies lower than could be resolved with the interferometer in the triple-pass configuration, but this hypothesis was disproved upon upgrading to five-pass operation. As can be seen from Fig. 5.11, the lower-frequency mode which was absent at $q = 0.0155\,\mathrm{nm}^{-1}$ in three-pass is detectable – but very weak – in five-pass due to the improved finesse and contrast. Above $qd_c = 7.91$ both modes are of equal intensity. It is possible that the slow mode re-emerges at $qd_c < 7.91$ and that the reason for its absence from spectra in the range $4.94 < qd_c < 7.91$ is the poor finesse afforded by three-pass interferometry – it was not possible to measure five-pass spectra in this range due to yellowing of the sample (see Sec. 5.2.3).

The effect was also observed in the ASM25 ($d_c = 186\,\mathrm{nm}$, $\phi_c = 0.34$) colloid studied in Sec. 5.3.3. Note that all of the spectra obtained for this sample were collected with the interferometer operating in the five-pass configuration. A weakened slow mode can already be seen at $q = 0.0218\,\mathrm{nm}^{-1}$ in graph (i) of Fig. 5.13, corresponding to $qd_c = 4.05$. By $qd_c = 5.19$ the low-frequency mode is almost too weak to be distinguished from the background noise, a situation which persists up to the highest q accessible with $\lambda = 514.5\,\mathrm{nm}$ light ($qd_c = 6.53$).

The onset of anomalous weakening in the slow-mode intensity thus occurs in both colloids at $qd_c \approx 4$, and by $qd_c \approx 5$ it has all but disappeared. The main difference in the behaviour of the slow mode in the two samples is that it re-emerges by $qd_c = 7.91$ in the larger ASM36, whereas it remains very weak even at the highest q probed in the smaller colloid. However the maximum q obtainable for ASM25 corresponds to $qd_c = 6.53$, so it is possible that the peak might regain intensity if higher qd_c could be achieved.

Attempts were made to quantify this variation in slow-mode intensity as a function of

qd_c, but unfortunately this proved to be impossible due to the day-to-day variations in Fabry-Perot interferometer alignment, quality of index-match, signal-to-noise ratio and other practical considerations which make comparison of absolute intensities between Brillouin spectra extremely difficult. Description of the anomalous effect therefore remains at the qualitative level presented above.

5.3.4.1 Why does the slow mode disappear?

What could be the origin of this disappearance (and subsequent reappearance in the case of ASM36) of the slow mode with increasing scattering vector? Why does it occur at very similar values of the dimensionless quantity qd_c in the two sizes of colloids discussed above? Why was the effect not seen in the earlier experiments on almost identical suspensions summarised in Sec. 5.1.2?

One possible explanation which has been suggested is that the extinction of the slow mode might be due to a minimum in the form factor $P(qR)$ for elastic scattering of light from the colloidal spheres, where R is the hard-sphere radius. The form factor describes the variation of the elastic scattering amplitude with q, and may be calculated analytically for the idealised case of an isolated optically homogeneous[‖] sphere [144]. Fig. 5.15 is a plot of this $P(qR)$ with an alternative x-axis provided which relates the conventional qR representation to qd_c in order to compare with the results for ASM36 above. The conversion was calculated using the relationship

$$qd_c = 2qR - \frac{2t\,qR}{R} \tag{5.6}$$

with $t = 15\,\text{nm}$ the thickness of the polymer layer around each ASM36 sphere of hard-sphere radius $R = 175\,\text{nm}$.

Note the minima which occur in the scattering amplitude at $qR = 4.49$ and 7.73 in Fig. 5.15, which are the result of destructive interference at certain scattering angles. These values of qR correspond to $qd_c = 8.22$ and 14.16 for the ASM36 colloid and $qd_c = 7.73$, 13.31 for ASM25, calculated using Eq. 5.6. For a dilute suspension of homogeneous solid spheres, we would therefore expect to see a deep minimum in the elastic scattering amplitude at these scattering vectors. In fact this is one of the methods used

[‖]Such that the refractive index is constant throughout the volume of the sphere.

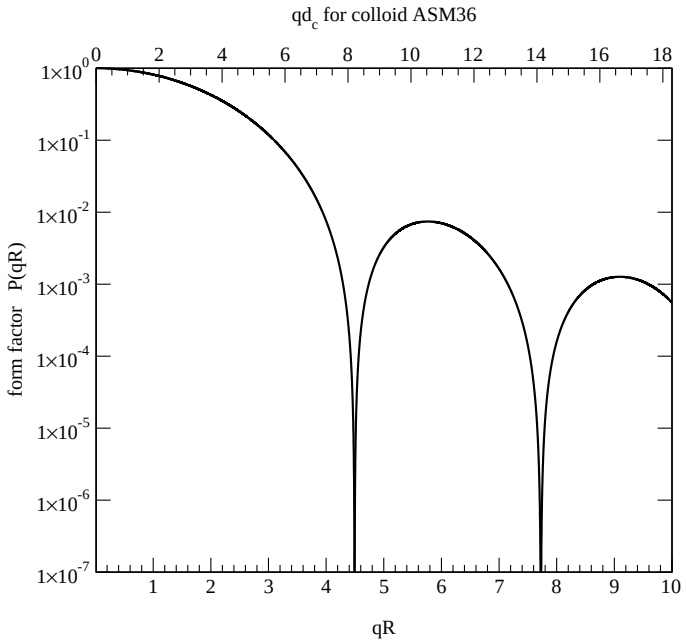

Figure 5.15: Theoretical form factor for elastic scattering of light from a single homogeneous sphere. Note the minima due to destructive interference at $qR = 4.49$ *and* 7.73*; elastic scattering is extinguished for a perfect hard sphere at these wavevectors.*

to characterise a colloidal suspension; measuring $P(qR)$ and noting the position of the first scattering minimum allows the hard-sphere radius R to be determined very accurately.

There is a significant conceptual difficulty with the suggestion that a minimum in elastic light scattering is responsible for reducing the intensity of a Brillouin peak, which is by definition the result of *inelastic* scattering. This point was unable to be resolved by recourse to the literature, and requires further consideration.

Another problem with the hypothesis that the minimum in scattering at $qR = 4.49$ may be responsible for extinguishing the slow mode is that the effect occurs at the wrong qd_c. The first minimum at $qR = 4.49$ corresponds to $qd_c = 8.22$ for ASM36 and 7.73 for ASM25, yet the anomalous weakening of the slow-mode intensity occurs in the ranges $4.02 \leq qd_c \leq 7.91$ for ASM36 and $4.05 \leq qd_c \leq 6.53$ for ASM25 (see above). This information is summarised in Table 5.2 below.

This would seem to be a strong indication that the minimum in elastic scattering is not responsible for the disappearing slow mode. It is however possible for the minimum to be moved to lower qR by any departures from the idealised properties of the spheres

Colloid	Start of effect	Weakest point	Re-emergence	1st min. in $P(qd_c)$
ASM36	4.02	4.94	7.91	8.22
ASM25	4.05	5.19	not by 6.53	7.73

Table 5.2: Values of qd_c at which the anomalous weakening of slow-mode intensity occurs in both colloids studied above, compared with the position of the first minimum in the elastic scattering amplitude for a single sphere.

which were assumed in the calculation of the curve in Fig. 5.15. Polydispersity, changes in temperature, and optical heterogeneity of the particles due to the polymer coating are all capable of shifting the minimum [121], but it is hard to imagine a perturbation sufficient to move qd_c at minimum near to the values at which the slow mode is weakest (see Table 5.2).

Measuring $P(qR)$ for colloids ASM36 and ASM25 using static light scattering (SLS) would have been sufficient to determine whether or not the minimum in elastic scattering corresponds to the disappearance of the slow mode, but this was not possible due to unavailability of equipment and ageing of the samples. Alternatively, selecting a value of qd_c at which the slow mode is weak and changing the temperature would be an effective test of the conjecture, as this should move the form factor minimum and – if it is related to the slow mode – hence cause the peak to reappear. Again this was not possible to implement due to yellowing of the colloids. Performing one of these tests on a new sample in which the variation of the slow-mode intensity with q is known should therefore be a priority for future work on hard-sphere colloidal suspensions.

Another possible origin of the anomalous weakening in the slow-mode intensity was suggested by Prof. John Page of the University of Manitoba, who has been using ultrasonic techniques to investigate sound propagation in colloids at much lower frequencies than those probed by Brillouin spectroscopy (see e.g. ref. [145]). He thinks it highly likely that the effect is due to some property of the polymer layer which coats each colloidal sphere in the sterically-stabilised suspensions used in the experiments reported here [146]. This seems reasonable: the slow mode is a wave which propagates at the interface between the spheres and the solvent, so the presence of a layer of polymer on one side of this boundary may well modify its behaviour in some qd_c-dependent way. Recall (see Sec. 5.1.2) that the group who first discovered the slow mode in colloidal

suspensions [109, 123, 32] assumed that the polymer coating is acoustically identical to the bulk solvent – this was their motivation for choosing to work in terms of the core diameter d_c and the core volume fraction ϕ_c rather than the hard-sphere equivalents. Might this be an over-simplification? If the polymer layer does affect the intensity of the slow mode, why was the effect not observed in the earlier work?

Unfortunately, we have insufficient information to comment further on this possibility. Until more experiments can be performed – perhaps investigating the effect of changing the acoustic properties of the polymer coating – the suggestion that the disappearance of the slow mode may be related to the properties of the thin layer surrounding each particle remains interesting but untested.

In conclusion, we have seen that the intensity of the slow mode weakens across a broad range of qd_c in both sizes of colloid studied, but no convincing explanation of this phenomenon has been established. Two ideas were discussed, but the first (the minimum in the form factor) seems unlikely to be correct, while the second (some property of the polymer layer) is a plausible but unsubstantiated hypothesis. A great deal of further work is clearly required in order to reveal more about this intriguing but puzzling phenomenon.

5.3.5 Summary of results for monodisperse colloids

Before moving on to look briefly at the propagation of hypersound in polydisperse colloids (in the form of binary colloids) let us summarise the findings of the work on monodisperse suspensions presented in the preceding sections.

In Sec. 5.3.1 we saw that preliminary measurements in two different sizes of colloids yielded results in excellent qualitative agreement with the earlier publications summarised in Sec. 5.1.2. Quantitative disagreements were suggested to be due to the fact that different dispersion media were used in the two sets of experiments.

Sec. 5.3.2 provided the first reproduction of the dispersion relation in a sample almost identical to one of the colloids studied by the Exxon group. Excellent qualitative and quantitative agreement was found between the new and old results. An anomalous weakening in the intensity of the slow mode was observed at intermediate scattering

vectors.

The trends in high-frequency sound propagation established for $d_c = 340\,\text{nm}$ and $650\,\text{nm}$ colloidal suspensions were then shown in Sec. 5.3.3 to be valid for much smaller spheres with $d_c = 186\,\text{nm}$. The reduction in slow-mode intensity observed in the larger colloid was again apparent..

Finally, this weakening of the slow mode was discussed in Sec. 5.3.4 and found to occur at similar qd_c in the two colloids. No convincing explanation for the effect was presented, but two possibilities were introduced.

5.4 More than one particle size: a binary colloid

All of the experiments on hard-sphere colloids reported to date (both here and elsewhere) have looked only at monodisperse suspensions; that is ones in which the colloidal spheres are all the same size. An original aim of this research program was to examine for the first time the effect of *polydispersity* on the propagation of high-frequency sound in these systems. We have seen in the preceding section that the core diameter d_c plays a very important part in determining the sound modes which exist in a monodisperse colloid; if spheres with different d_c are present, will these relationships still hold or will we see new effects due to this polydispersity?

The simplest polydisperse suspension contains particles of just two different sizes and is therefore called a *binary colloid*. A binary colloid with well-defined volume fraction and particle sizes may be prepared by mixing two monodisperse suspensions like the ones studied in the previous section, hence it was decided to focus on these systems rather than any more complicated mixtures of particle sizes.

Unfortunately there was insufficient time available to complete any detailed survey of hypersound propagation in a binary colloid, the reasons for which will be discussed below. Preliminary experiments were however performed, the results of which merit presentation and discussion.

Recall that before progressing to the measurement of full dispersion relations for monodis-

perse suspensions, spectra for two different sizes of colloids ($d_{c_1} = 194\,\text{nm}$ and $d_{c_2} = 620\,\text{nm}$) were collected (see Sec. 5.3.1). Just after these measurements, the two colloids were combined to form a binary suspension in order to see what features might be observed in the Brillouin spectrum of the new sample. The total hard-sphere volume fraction of the binary colloid was $\phi' = 0.40$, comprised of equal ($\phi = 0.20$) volume fractions of the individual components. In terms of the core volume fraction – which is more relevant in determining the sound propagation characteristics of the suspension (see Sec. 5.1.2) – the total $\phi'_c = 0.30$ for the binary mixture, with $\phi_c = 0.13$ of the smaller spheres and $\phi_c = 0.17$ of the larger ones.

Brillouin spectra were recorded using the interferometer in the triple-pass configuration, since the upgrade to five-pass had not been implemented at the time of these experiments. The usual laser wavelength of 514.5 nm was used at a power of 200 mW, and the scattering angle was $90 \pm 0.5\,^\circ$ giving a scattering vector $q = 0.0258 \pm 0.0001\,\text{nm}^{-1}$. The index-match of the composite appeared to be significantly less satisfactory than that of the individual monodisperse colloids, hence spectra had to be accumulated for roughly two hours in order to obtain a good enough signal-to-noise ratio. Several spectra were obtained, the best of which is displayed in Fig. 5.16 below along with relevant data for the monodisperse components for the purpose of comparison.

Perhaps the most notable feature of the spectrum for the binary colloid in Fig. 5.16 is its similarity to the $\phi_c = 0.13$ spectrum of the small component. The peak frequency, shape and intensity (neither spectrum is scaled and the same accumulation times were used) are all almost identical. The only difference is that there is a weak slow mode in the binary colloid at 4 GHz but no such feature in the monodisperse suspension; $\phi_c = 0.13$ is below the threshold ($\phi_c \approx 0.20$) for the propagation of the slow mode. There is also similarity between the binary colloid spectrum and the $\phi_c = 0.17$ spectrum for the larger component: although the main peak frequencies are slightly different, the hint of a slow mode in the $d_{c_2} = 620\,\text{nm}$ monodisperse colloid appears to be at a frequency close to the corresponding peak in the binary suspension. The spectrum for the more concentrated small component ($\phi_c = 0.26$) bears little resemblance to the binary colloid dataset. When comparing these spectra it must be remembered that the value of qd_c (which is key in determining the propagation characteristics of the sound modes) is different for each component of the binary colloid at a given q. For this sample, the

90° scattering angle results in $qd_{c_1} = 5.0$ for the smaller spheres and $qd_{c_2} = 16.0$ for the larger particles. Both components are therefore above $qd_c \approx \pi$ where the second sound mode was found to emerge in the previous section (see e.g. Fig. 5.14).

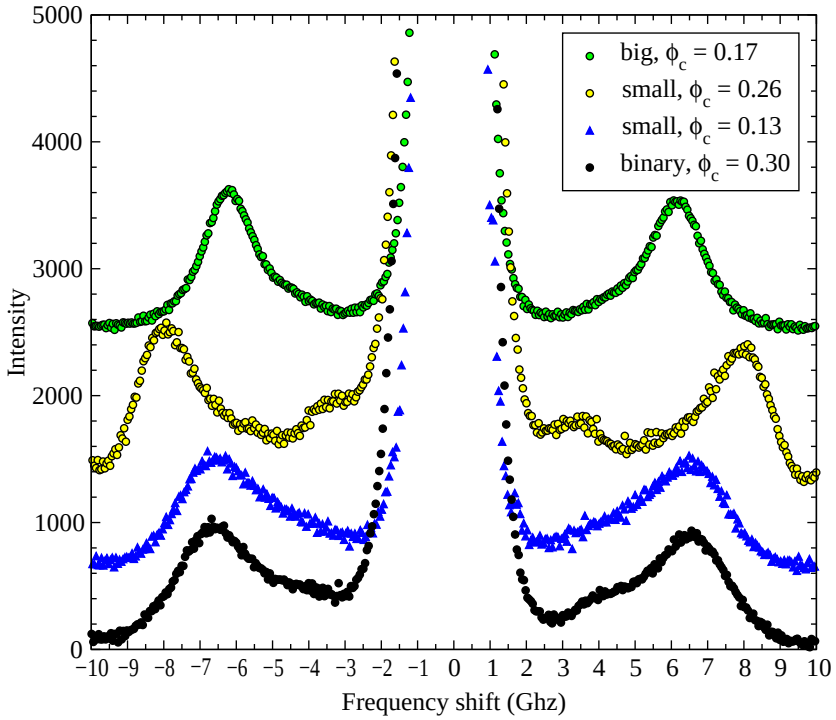

Figure 5.16: Brillouin spectrum of a binary colloidal fluid compared with spectra for the individual components in monodisperse suspension. The binary colloid has a total core volume fraction $\phi_c' = 0.30$ *comprising* $\phi_c = 0.13$ *of the smaller* ($d_{c_1} = 194\,\mathrm{nm}$) *spheres and* $\phi_c = 0.17$ *of the larger* ($d_{c_2} = 620\,\mathrm{nm}$) *ones. Spectra have been displaced but not scaled to facilitate comparison.*

Do these similarities tell us anything about mechanisms of sound propagation in the binary colloid? It is hard to draw any conclusions from a single dataset, but one interesting feature is apparent. Although the volume fractions of the individual components are both below the $\phi_c \approx 0.2$ limit for the existence of the second sound mode, a weak slow-mode peak *is* present in the binary suspension. This suggests that the slow mode must propagate between spheres of different sizes, as the volume fraction of each component is too low to allow same-size spheres to be close enough together for the interfacial excitation to hop from one to another (see Sec. 5.1.2.1 for a discussion of this propagation mechanism). If the individual volume fractions *were* greater than 0.2, would we see two slow modes at different frequencies, corresponding to interfacial waves around the two different sizes of spheres?

After completing the measurements of dispersion relations in the two monodisperse colloids discussed in Sec. 5.3 it was decided to attempt a similar study of dispersion in a binary colloid. Many parameters may be varied in the composition of a binary suspension: the size ratio of spheres, the total volume fraction, and the ratio of the volume fractions of the two components.

The most sensible choice for the sizes of spheres was deemed to be simply to combine the two colloids (ASM36 and ASM25) studied in Sec. 5.3 so that dispersion relations of the individual components would be available for comparison with results from the mixture. In order to allow the volume fractions of each component to be greater than the threshold ($\phi_c \approx 0.2$ – this was not the case for the binary colloid discussed above), the total volume fraction should be made as high as possible. An arbitrary choice was made to use equal core volume fractions of each component.

A binary colloid matching these criteria was prepared with fresh supplies of ASM36 ($d_c = 319\,\mathrm{nm}$) and ASM25 ($d_c = 186\,\mathrm{nm}$) from stock, as the samples studied previously had become too yellowed to be of further use. Each monodisperse component was washed and calibrated following the methods described in Sec. 5.2 to produce index-matched suspensions with equal core volume fractions. These were then combined to obtain the desired binary colloidal suspension.

Unfortunately, the length of this preparation procedure (more than a month) and the fact that the index-match deteriorated upon mixing meant that it was not possible to obtain satisfactory Brillouin spectra from this sample, despite five-pass interferometry and very long collection times. Problems caused by too much yellowing due to the passage of time and the poor index-match were not able to be overcome despite a great deal of effort, and no data can be presented for this binary colloid.

Time limitations prevented further attempts at obtaining the dispersion relation of a binary suspension, hence the dataset in Fig. 5.16 remains the sole product of this investigation into sound propagation in binary colloids.

In the opinion of Prof. Ping Sheng – who worked on the theory explaining the two-mode dispersion relation in hard-sphere colloids (Refs. [124, 125]) – the Brillouin spectrum of a binary colloidal suspension is almost certain to be more than just a superposi-

tion of spectra for the individual components [143]. The existence of the slow mode in the binary colloid of Fig. 5.16 supports this view. The failure to expand on this tantalising first glimpse of the second mode in a binary suspension is frustrating, and further research on these systems should be a priority of future work using the Brillouin spectrometer at Edinburgh. New physics is almost certain to be discovered, which may provide a valuable insight into the effect of polydispersity on the propagation of high-frequency sound in random media.

5.5 Discussion

The first aim of the work presented in this chapter was to show that the new Brillouin spectrometer at Edinburgh (described in Chapter 3) could be used to study the propagation of high-frequency sound in hard-sphere colloidal suspensions. Preliminary studies at fixed scattering angle (Sec. 5.3.1) were very encouraging – the second sound mode revealed by the only previous work in the field was observed at the expected scattering vectors and volume fractions, and the quality of the spectra was significantly improved compared to the earlier experiments.

After the success of this initial survey, our next priority was to attempt to reproduce the dispersion relation measured by the Exxon group for the two sound modes which they discovered in a mid-sized colloidal suspension ($d_c = 340\,\mathrm{nm}$). Despite the fact that the second ("slow") mode was first observed more than a decade ago, no confirmation of its existence or variation with scattering vector has been reported. The results presented in Sec. 5.3.2 remedy this situation – quantitative and qualitative agreement with the original publications was established by measuring the full dispersion relation of both sound modes in an almost identical sample.

Following this valuable first reproduction of the two-mode dispersion relation in a hard-sphere colloid, the research was extended by looking at a suspension of spheres approximately twice as small as any studied previously, with core diameter $d_c = 186\,\mathrm{nm}$. The results reported in Sec. 5.3.3 showed that all of the findings of the earlier work remain valid for the smaller spheres when expressed in dimensionless units scaled by d_c. This means that the parameter-free theory summarised in Sec. 5.1.2.2 is able to accurately

predict the behaviour of colloidal suspensions of particles with core diameters ranging from 186 nm to 640 nm. This is strong evidence in support of the hypothesis (discussed in Sec. 5.1.2.1) that the slow mode is an interfacial wave and the fast mode propagates through both solid and liquid phases.

An anomalous weakening in the slow-mode intensity in the range $4 \leq qd_c \leq 8$, which has not been seen before, was observed in both colloids for which dispersion relations were obtained. This was described in Sec. 5.3.4, but unfortunately no convincing explanation of the effect is available at present.

Finally, a preliminary study of a binary colloidal fluid showed that a slow mode is able to propagate despite the fact that each component of the mixture is below the threshold volume fraction for the existence of the excitation in monodisperse suspensions. This proves that the spectrum of a binary colloid is more than just a superposition of spectra for its components, and suggests that new discoveries are highly likely to result from further study of polydisperse suspensions using Brillouin spectroscopy.

The original aims of developing an instrument capable of measuring Brillouin scattering in a colloidal suspension, then using the apparatus to make a useful contribution to the understanding of high-frequency sound propagation in these systems have therefore been achieved. The success of the experiments reported in this chapter will hopefully be the first stage in a wide program of research on colloids using Brillouin spectroscopy. Many colloidal systems exhibit behaviour which may affect the Brillouin spectrum, but remain completely unexplored using the technique.

Perhaps the most exciting avenue for future research would be to use the technique to attempt to detect the existence of acoustic bandgaps in colloidal crystals. These have been predicted to arise at hypersonic frequencies due to the periodic structure of the material [147, 148, 149, 110] and should in principle be observable using Brillouin spectroscopy in the same way that gaps in the fast mode were seen in hard-sphere colloidal fluids (see Sec. 5.1.2.3). Acoustic bandgaps have never been observed at such high frequencies, but arrays of larger particles have been shown to exhibit gaps at lower frequencies [111, 146]. Interestingly given the system studied here, calculations show that PMMA spheres are too soft to produce true omnidirectional phononic bandgaps – the acoustic mismatch between particles and solvent is not large enough [110]. Crys-

talline arrays of $d = 500\,\text{nm}$ silica spheres in water are however predicted to scatter sound waves sufficiently strongly to open up acoustic bandgaps at frequencies of a few GHz [149]. A Brillouin scattering experiment aimed at detecting these gaps would be extremely challenging; single colloidal crystals of sufficient size are very difficult to manufacture and preserve, adding to the already considerable problems encountered during the work on colloidal fluids discussed in this chapter. The highly unusual acoustic and thermal properties exhibited by phononic bandgap materials mean that such an effort would certainly be worthwhile.

Many different types of soft condensed matter seem likely to show novel behaviour if studied using Brillouin spectroscopy. For example, it would be very interesting to measure the dispersion relation of a colloidal glass, then encourage crystallisation by shearing the sample and repeat the measurement. The only difference between the two datasets would be the existence of order in the crystal – how would this affect the propagation of the two sound modes? The time-dependent structure of colloidal gels should also be detectable with Brillouin scattering. There are many other examples of complex fluids with structuring on lengthscales similar to the wavelength of the sound waves probed by Brillouin scattering, most of which have never been investigated using the technique. It seems safe to assume that new physics – like the surprising second sound mode in hard-sphere colloids – is waiting to be discovered.

Chapter 6

Conclusions

This chapter will draw together the conclusions of the three areas of original research presented in this thesis, and will highlight some of the most promising avenues for future work in each field.

6.1 Development of a Brillouin spectrometer

A Brillouin spectrometer suitable for the study of soft condensed matter was designed and constructed. Scattering vector, temperature and pressure could all be varied across ranges at least as wide as those reported for any Brillouin scattering experiment in the literature. Optical and mechanical stability were sufficient to allow the Fabry-Perot interferometer to be operated in the five-pass configuration, and electronic stabilisation enabled the alignment of the system to be maintained almost indefinitely, allowing the scattering from challenging systems such as colloidal suspensions to be collected for long enough to obtain satisfactory Brillouin spectra.

Automated data analysis routines were developed which allow calibrated spectra to be obtained from raw data in a few seconds, and accurate methods of measuring peak positions and widths were implemented using numerical fitting algorithms.

Brillouin spectra collected for a variety of samples under a wide range of conditions all compared very favourably with literature data whenever this was available.

6.1.1 Further work

The apparatus described above has been shown to be capable of matching the performance of any comparable instrument, hence attempts to improve the facility should focus on developing more sophisticated data analysis techniques.

A routine allowing the true spectrum of the source to be extracted by deconvolution of the instrumental response function of the interferometer could be implemented, allowing sound absorption coefficients to be measured from the Brillouin peak width. This would also enable the analytical expression for the spectrum (with or without a relaxation term) to be fitted to experimental data in order to extract more information. In particular, the ability to measure structural or thermal relaxation times using this method would be an important advance.

6.2 Anomalous hydrodynamic behaviour in cooled aqueous solutions

A detailed Brillouin scattering study of cooled aqueous methanol solutions revealed an unexpected sharp increase in sound velocity and maximum sound absorption at low temperatures for $x_m < 0.7$. Precursors to this behaviour occur at the same temperatures in supercooled pure water. Neutron and x-ray diffraction experiments both provide strong evidence for the existence of a hydrogen-bonded water network in these solutions, relatively unperturbed compared to the pure liquid. It was therefore suggested that the anomalous effects observed in the methanol–water mixtures result from the presence of microscopic water-rich regions. The trends seen in pure water are extended to lower temperatures in the solutions due to suppression of freezing by the solvated species.

Very similar behaviour was observed in every one of a variety of other aqueous solutions surveyed, however the effects appear to be moved to higher temperatures when the non-aqueous component forms a glass or freezes at temperatures greater than the freezing point of water.

The same increase in sound velocity and maximum in absorption were reported in a detailed publication on the glass transition in aqueous LiCl, and shown to be due to the MCT α relaxation passing through the window of frequencies probed by Brillouin spectroscopy. It has also very recently been proposed that the unique thermodynamic properties of supercooled pure water are caused by the approach to a glass transition, which would explain why precursors of the same hydrodynamic anomalies are present in pure water in the limited range of temperatures accessible in the supercooled régime.

Building on the hypothesis that molecular-scale segregation (proved by neutron diffraction to exist at concentrations as high as $x_m = 0.7$ at room temperature) allows the distinctive properties of supercooled pure water to be observed in the Brillouin spectrum of methanol–water solutions, it was suggested that the increase in sound velocity towards solid-like values and maximum in sound absorption may be due to pre-glassy dynamics of the water network. This would explain both the similar temperatures at which the effects occur in different aqueous solutions, and the fact that the maximum absorption is around $-45\,^{\circ}\mathrm{C}$ in the mixtures – the temperature at which either a maximum or a divergence is predicted to exist in supercooled pure water. If this idea is correct, the presence of solutes therefore allows the behaviour of pure water to be detected in the forbidden region of the phase diagram, below the line of homogeneous nucleation.

Perhaps the most convincing support for this hypothesis from techniques other than Brillouin spectroscopy is the discovery (during preliminary analysis of the neutron diffraction data presented here) that the water network in a 50/50 methanol–water mixture tends towards a glassy solid rather than a crystal when cooled to $-35\,^{\circ}\mathrm{C}$.

6.2.1 Further work

The novelty and potential importance of the hypothesis discussed above are sufficient motivation for extending this research in a number of ways – the following ideas are some of the most promising.

Completion of detailed analysis on the neutron diffraction experiments at low temperature should be a priority. This would provide a lot of additional data on how

the properties of water in the solution change with cooling, and based on preliminary results seems likely to support the picture developed from Brillouin scattering.

The wealth of information obtained by neutron scattering means that any further experiments would be very valuable. The effect of lower temperatures on methanol–water mixtures could be probed, or other aqueous solutions tested to establish whether the water network is preserved as in aqueous methanol.

Measurements of viscosity on cooling aqueous solutions will establish whether the mixtures themselves approach a glass transition, or may show signatures of water's glassy behaviour at the frequencies probed by Brillouin scattering.

It would also be interesting to use ultrasonic techniques to see if the anomalous hydrodynamic behaviour in aqueous solutions occurs at lower frequencies (MHz rather than GHz). No such data has been reported for temperatures significantly below room temperature.

6.3 High-frequency sound propagation in colloids

The newly developed Brillouin spectrometer was used to confirm (for the first time) and extend the findings of an earlier discovery of a second longitudinal sound mode propagating at hypersonic frequencies in monodisperse hard-sphere colloidal suspensions.

The dispersion relation of a colloid almost identical to one studied previously was obtained and found to be in excellent qualitative and quantitative agreement with the data in the literature. Two sound modes were observed at $\phi_c > 0.2$ and $qd_c > \pi$: a fast mode which propagates in both solid and fluid phases, and a slow mode identified with an interfacial wave at the boundary between particle and solvent, which hops from one sphere to another via an exponentially decaying tail in the fluid.

A suspension of much smaller spheres was then investigated and found to have a very similar two-mode dispersion relation. When scaled by the particle diameter, datasets for the two sizes of spheres were found to coincide, as predicted by the multiple scattering

theory developed by the authors of the original work.

The main new effect which was observed in both colloids was a dramatic weakening of the slow mode intensity at intermediate scattering vectors. No convincing explanation for this behaviour has yet been established.

Other new findings relate to the different dispersion medium used in the earlier experiments. The change in solvent sound velocity was observed to have a significant effect on Brillouin peak frequencies, but did not seem to change the location of the single sphere resonances which result in bandgaps in the dispersion relation of the fast mode.

Finally, preliminary experiments showed that the Brillouin spectrum of a binary colloidal fluid is not simply a superposition of the spectra of its monodisperse components. The slow interfacial mode appears to propagate between spheres of different sizes, suggesting that further studies of hypersound propagation in polydisperse colloids are almost certain to result in the discovery of new phenomena.

6.3.1 Further work

In addition to this work on binary colloids, the success of the experiments on hard-sphere colloidal suspensions opens up many possibilities for future work using Brillouin spectroscopy to look for new physics in complex fluids.

Further investigation of the 'disappearing' slow mode would be interesting. Using static light scattering to probe a sample which exhibits the effect would establish whether or not the extinction of the mode is related to minima in the form factor for elastic scattering. Changing the properties of the particle-solvent interface by using different dispersion media or altering the polymer coating might also shed some light on this anomalous behaviour.

Exploring methods of avoiding light-induced yellowing in the PMMA colloids used here would be useful. This discolouration severely limits the useful lifetime of samples for the purposes of Brillouin spectroscopy, and was a serious problem throughout the experiments performed during this research.

The wealth of exciting potential applications of Brillouin spectroscopy in the study of other complex fluids was discussed in the conclusion of Chapter 5. Perhaps the most interesting possibility would be to search for the acoustic bandgaps predicted by theory to exist at hypersonic frequencies in colloidal crystals, but which have not yet been observed.

List of Figures

Bibliography

[1] J. W. S. Rayleigh, Philos. Mag. **12**, 813 (1881).

[2] A. Einstein, Ann. Physik. **33**, 1275 (1910).

[3] R. Figgins, *Inelastic light scattering in liquids: Brillouin scattering*, Contemp. Phys. **12** (3), 283 (1971).

[4] L. Brillouin, Compt. Rend. **158**, 1331 (1914).

[5] R. S. Krishnan, *Brillouin scattering*, in *The Raman effect* (A. Anderson, editor), volume 1, chapter 6, (pp. 343–404) (Marcel Dekker, New York, 1971).

[6] L. D. Landau, E. M. Lifshitz and L. P. Pitaevskiĭ, *Electrodynamics of continuous media* (Pergamon, Oxford, 1984), 2nd edition.

[7] P. A. Fleury and J. P. Boon, *Brillouin scattering in simple liquids: Argon and Neon*, Phys. Rev. **186** (1), 244 (1969).

[8] L. D. Landau and E. M. Lifshitz, *Fluid mechanics* (Pergamon, Oxford, 1987), 2nd edition.

[9] D. R. Lide (editor), *CRC Handbook of Chemistry and Physics* (CRC Press, Boca Raton, 1995), 76th edition.

[10] H. E. Stanley, *Phase transitions and critical phenomena* (Clarendon Press, Oxford, 1971).

[11] K. F. Herzfeld and T. A. Litovitz, *Absorption and dispersion of ultrasonic waves* (Academic Press, New York, 1959).

[12] W. A. B. Evans and J. G. Powles, *The interpretation of hypersonic and ultrasonic 'velocities' in fluids*, J. Phys. A **7** (15), 1944 (1974).

[13] B. J. Berne and R. Pecora, *Dynamic light scattering* (Wiley, New York, 1976).

[14] J. P. Boon and S. Yip, *Molecular hydrodynamics* (McGraw-Hill, New York, 1980).

[15] R. D. Mountain, *Spectral distribution of scattered light in a simple fluid*, Rev. Mod. Phys. **38** (1), 205 (1966).

[16] E. W. Swokowski, *Calculus* (PWS-Kent, 1991), 5th edition.

[17] P. A. Fleury and J. P. Boon, *Laser light scattering in fluid systems*, Adv. Chem. Phys. **24**, 1 (1973).

[18] R. A. Smith, *Lasers and light scattering*, Contemp. Phys. **12** (6), 523 (1971).

[19] R. D. Mountain, *Thermal relaxation and Brillouin scattering in liquids*, J. Res. Natl. Bur. Stand. **70A**, 207 (1966).

[20] W. S. Gornall, G. I. A. Stegeman, V. P. Stoicheff, R. H. Stolen and V. Volterra, *Identification of a new spectral component in Brillouin scattering of liquids*, Phys. Rev. Lett. **17** (6), 297 (1966).

[21] W. H. Nichols and E. F. Carome, *Light scattering from a multiply relaxing fluid*, J. Chem. Phys. **49** (3), 1000 (1968).

[22] N. J. Tao, G. Li and H. Z. Cummins, *Brillouin-scattering study of the liquid-glass transition in supercooled aqueous lithium chloride solutions: Generalized hydrodynamics and mode-coupling analyses*, Phys. Rev. B **43** (7), 5815 (1991).

[23] P. G. Debenedetti and F. H. Stillinger, *Supercooled liquids and the glass transition*, Nature **410**, 259 (2001).

[24] C. Dreyfus, M. J. Lebon, H. Z. Cummins, J. Toulouse, B. Bonello and R. M. Pick, *Brillouin scattering in salol: Determining T_c of the mode coupling theory*, Phys. Rev. Lett. **69** (25), 3666 (1992).

[25] M. Elmroth, L. Börjesson and L. M. Torell, *Observation of a dynamic anomaly in the liquid-glass transformation range by Brillouin scattering*, Phys. Rev. Lett **68** (1), 79 (1992).

[26] W. M. Du, G. Li, H. Z. Cummins, M. Fuchs, J. Toulouse and L. A. Knauss, *Light-scattering study of the liquid-glass transition in propylene carbonate*, Phys. Rev. E **49** (3), 2192 (1994).

[27] Y. Yang and K. A. Nelson, *Impulsive stimulated light scattered from glass-forming liquids. II. Salol relaxation dynamics, nonergodicity parameter, and testing of mode coupling theory*, J. Chem. Phys. **103** (18), 7732 (1995).

[28] J. G. Dil, *Brillouin scattering in condensed matter*, Rep. Prog. Phys. **45**, 285 (1982).

[29] J. A. Marqusee and J. M. Deutch, *Brillouin light scattering from polymer gels*, J. Chem. Phys. **75** (11), 5239 (1981).

[30] F. Mallamace, N. Micali, C. Vasi, R. Bansil, S. Pajevic and F. Sciortino, *Brillouin scattering from polymers and gels*, Macromol. Symp. **79**, 179 (1994).

[31] P. Zhao and J. J. Vanderwal, *Brillouin scattering study of gelatin gel*, Polymer Gels and Networks **5**, 23 (1997).

[32] Ling Ye, Jing Liu, Ping Sheng, J. S. Huang and D. A. Weitz, *Sound propagation in colloidal systems*, J. de Phys. IV (pp. 183–196) (1993), supplement to J. de Phys. II, vol. 3.

[33] B. Loppinet, R. Sigel, A. Larsen, G. Fytas, D. Vlassopoulos and G. Liu, *Structure and dynamics in dense suspensions of micellar nanocolloids*, Langmuir **16**, 6480 (2000).

[34] Y. Liao, N. A. Clark and P. S. Pershan, *Brillouin scattering from smectic liquid crystals*, Phys. Rev. Lett. **30** (14), 639 (1973).

[35] C. Grammes, J. K. Krüger, K.-P. Bohn, J. Baller, C. Fischer, C. Schorr, D. Rogez and P. Alnot, *Universal relaxation behavior of classical liquid crystals at hypersonic frequencies*, Phys. Rev. E **51** (1), 430 (1995).

[36] R. D. Guenther, *Modern optics* (Wiley, New York, 1990).

[37] G. Hernandez, *Fabry-Perot interferometers* (Cambridge University Press, 1986).

[38] J. M. Vaughan, *The Fabry-Perot interferometer. History, theory, practice and applications* (Adam Hilger, Bristol, 1989).

[39] M. Born and E. Wolf, *Principles of optics* (Cambridge University Press, 1999), 7th edition.

[40] J. F. James and R. S. Sternberg, *The design of optical spectrometers* (Chapman and Hall, London, 1969).

[41] J. R. Sandercock, *Some recent developments in Brillouin scattering*, RCA Rev. **36**, 89 (1975).

[42] Burleigh Instruments Inc., New York, *Fabry-Perot instruction manual*.

[43] J. Hecht, *The laser guidebook* (TAB Books, Blue Ridge Summit PA, 1992), 2nd edition.

[44] P. Sassi, G. Paliani and R. S. Cataliotti, *Brillouin spectra and vibrational-translational energy exchange in liquid acetonitrile*, J. Chem. Phys. **108** (24), 10197 (1998).

[45] H. Vass, *Instrumentation for advanced optical spectroscopies under extreme conditions*, MSc thesis, University of Edinburgh (2002).

[46] R. T. Harley, *Optical alignment of a multipass Fabry-Perot Brillouin scattering spectrometer*, J. Phys. E: Sci. Instrum. **12**, 255 (1979).

[47] C. Tanford, *The hydrophobic effect: formation of micelles and biological membranes* (Krieger, Florida, 1991), 2nd edition.

[48] P. Ball, *H_2O: A biography of water* (Phoenix, London, 2000).

[49] S. Dixit, W. C. K. Poon and J. Crain, *Hydration of methanol in aqueous solutions: A Raman spectroscopic study*, J. Phys.: Cond. Matt. **12**, L323 (2000).

[50] G. Onori, *Adiabatic compressibility and structure of aqueous solutions of methyl-alcohol*, J. Chem. Phys. **87** (2), 1251 (1987).

[51] G. Onori, *Adiabatic compressibility and structure of aqueous solutions of ethyl alcohol*, J. Chem. Phys. **89** (7), 4325 (1988).

[52] M. D'Angelo, G. Onori and A. Santucci, *Self-association of monohydric alcohols in water: Compressibility and infrared absorption measurements*, J. Chem. Phys. **100** (4), 3107 (1994).

[53] O. Conde, J. Teixeira and P. Papon, *Analysis of sound velocity in supercooled H_2O, D_2O, and water-ethanol mixtures*, J. Chem. Phys. **76** (7), 3747 (1982).

[54] F. J. Bermejo, R. Ramirez, J. L. Martinez, C. Prieto, F. Ballatan and M. Garcia-Hernandez, *Hypersonic relaxation in liquid methanol*, J. Phys.: Cond. Matt. **3**, 569 (1991).

[55] P. G. Debenedetti, *Metastable Liquids: Concepts and Principles* (Princeton University Press, 1996).

[56] J. T. Fourkas, D. Kivelson, U. Mohanty and K. A. Nelson (editors), *Supercooled liquids* (ACS symposium series, 1997).

[57] O. Mishima and H. E. Stanley, *The relationship between liquid, supercooled and glassy water*, Nature **396**, 329 (1998).

[58] R. Bergman and J. Swenson, *Dynamics of supercooled water in confined geometry*, Nature **403**, 283 (2000).

[59] R. J. Speedy and C. A. Angell, *Isothermal compressibility of supercooled water and evidence for a thermodynamic singularity at -45°*C, J. Chem. Phys. **65**, 851 (1976).

[60] C. A. Angell, in *Water: a comprehensive treatise* (ed. F. Franks), volume 7 (Plenum, New York, 1982).

[61] R. J. Speedy, *Stability-limit conjecture. An interpretation of the properties of water*, J. Phys. Chem. **86**, 982 (1982).

[62] P. G. Debenedetti, *One substance, two liquids?*, Nature **392**, 127 (1998).

[63] S. Sastry, P. G. Debenedetti, F. Sciortino and H. E. Stanley, *Singularity-free interpretation of the thermodynamics of supercooled water*, Phys. Rev. E **53** (6), 6144 (1996).

[64] S. Sastry, *Going strong or falling apart?*, Nature **398**, 467 (1999).

[65] F. W. Sciortino, P. Gallo, P. Tartaglia and S. Chen, *Supercooled water and the kinetic glass transition*, Phys. Rev. E **54** (6), 6331 (1996).

[66] C. A. Angell, *Formation of glasses from liquids and biopolymers*, Science **267**, 1924 (1995).

[67] W. Götze and L. Sjogren, *Relaxation processes in supercooled liquids*, Rep. Prog. Phys. **55** (3), 241 (1992).

[68] A. P. Sokolov, J. Hurst and D. Quitmann, *Dynamics of supercooled water: mode-coupling theory approach*, Phys. Rev. B **51** (18), 12865 (1995).

[69] M. C. Bellissent-Funel, S. Longeville, J. M. Zanotti and S. H. Chen, *Experimental observation of the α relaxation in supercooled water*, Phys. Rev. Lett. **85** (17), 3644 (2000).

[70] P. H. Poole, F. Sciortino, U. Essman and H. E. Stanley, *Phase behavior of metastable water*, Nature **360**, 324 (1992).

[71] H. E. Stanley, S. V. Buldyrev, O. Mishima, M. R. Sadr-Lahijany, A. Scala and F. W. Starr, *Unsolved mysteries of water in its liquid and glassy phases*, J. Phys.: Cond. Matt. **12**, A403 (2000).

[72] Y. Katayama, T. Mizutani, W. Utsumi, O. Shimomura, M. Yamakata and K. Funakoshi, *A first-order liquid-liquid phase transition in phosphorus*, Nature **403**, 170 (2000).

[73] H. Tanaka, *General view of a liquid-liquid phase transition*, Phys. Rev. E **62** (5), 6968 (2000).

[74] G. Franzese, G. Malescio, A. Skibinsky, S. V. Buldyrev and H. E. Stanley, *Generic mechanism for generating a liquid-liquid phase transition*, Nature **409**, 692 (2001).

[75] O. Mishima and H. E. Stanley, *Decompression-induced melting of ice IV and the liquid-liquid transition in water*, Nature **392**, 164 (1998).

[76] M.-C. Bellissent-Funel, *Is there a liquid-liquid phase transition in supercooled water?*, Europhys. Lett. **42** (2), 161 (1998).

[77] A. K. Soper and M. A. Ricci, *Structures of high-density and low-density water*, Phys. Rev. Lett. **84** (13), 2881 (2000).

[78] N. Micali, S. Trusso, C. Vasi, D. Blaudez and F. Mallamace, *Dynamical properties of water-methanol solutions studied by depolarised Rayleigh scattering*, Phys. Rev. E **54** (2), 1720 (1996).

[79] A. S. Kertes and C. J. King, *Extraction chemistry of low molecular weight aliphatic alcohols*, Chem. Rev. **87**, 687 (1987).

[80] D. T. Bowron, J. L. Finney and A. K. Soper, *Strucural investigation of solute–solute interactions in aqueous soulutions of tertiary butanol*, J. Phys. Chem. B **102**, 3551 (1998).

[81] S. Dixit, *Molecular models of hydration in methanol-water mixtures*, Ph.D. thesis, University of Edinburgh (2002).

[82] T. Takamuku, T. Yamaguchi, M. Asato, M. Matsumoto and N. Nishi, *Structure of clusters in methanol-water binary solutions studied by mass spectrometry and x-ray diffraction*, Z. Naturforsch. **55** (a), 513 (2000).

[83] T. Sato, A. Chiba and R. Nozaki, *Hydrophobic hydration and molecular association in methanol–water mixtures studied by microwave dielectric analysis*, J. Chem. Phys. **112** (6), 2924 (2000).

[84] S. Dixit, J. Crain, W. C. K. Poon, J. L. Finney and A. K. Soper, *Molecular segregation observed in a concentrated alcohol–water solution*, Nature **416**, 829 (2002).

[85] A. K. Soper and J. L. Finney, *Hydration of methanol in aqueous solution*, Phys. Rev. Lett. **71** (26), 4346 (1993).

[86] N. Crampton, *An optical spectroscopic study of alcohol–water mixtures: alcohol demixing and aggregation*, Master's thesis, University of Edinburgh (2001).

[87] S. S. N. Murthy, *Detailed study of ice clathrate relaxation: Evidence for the existence of clathrate structures in some water-alcohol mixtures*, J. Phys. Chem. A **103**, 7927 (1999).

[88] K. Takaizumi and T. Wakabayashi, *The freezing process in methanol-, ethanol- and propanol-water systems as revealed by differential scanning calorimetry*, J. Soln. Chem. **26** (10), 927 (1997).

[89] D. R. Lide (editor), *CRC handbook of chemistry and physics* (CRC press, Boca Raton, 2001), 81st edition.

[90] C. A. Angell, *Supercooled water*, Annu. Rev. Phys. Chem. **34**, 593 (1983).

[91] G. Maisano, P. Migliardo, F. Aliotta, C. Vasi, F. Wanderlingh and G. D'Arrigo, *Evidence of anomalous acoustic behavior from Brillouin scattering in supercooled water*, Phys. Rev. Lett. **52** (12), 1025 (1984).

[92] A. Cunsolo and M. Nardone, *Velocity dispersion and viscous relaxation in supercooled water*, J. Chem. Phys. **105** (10), 3911 (1996).

[93] A. Ozawa and A. Minamisawa, *Concentration of ultrasonic-velocity invariant with respect to temperature observed in alcohol-water mixtures*, Jpn. J. Appl. Phys. **37** (5), 2799 (1998).

[94] S. Magazù, G. Maisano, D. Majolino, F. Mallamace, P. Migliardo, F. Aliotta and C. Vasi, *Relaxation process in deeply supercooled water by Mandelstam-Brillouin scattering*, J. Phys. Chem. **93**, 942 (1989).

[95] T. Yamaguchi, *New horizons in hydrogen bonded clusters in solution*, Pure Appl. Chem. **71** (9), 1741 (1999).

[96] M. A. Roberts, private communication (2001).

[97] T. Yamaguchi, private communication (2001).

[98] J. L. Finney, private communication (2001).

[99] P. A. Egelstaff, *An introduction to the liquid state* (Clarendon Press, Oxford, 1994), 2nd edition.

[100] A. K. Soper, *The quest for the structure of water and aqueous solutions*, J. Phys.: Cond. Matt. **9**, 2717 (1997).

[101] A. K. Soper, *Empirical potential Monte Carlo simulation of fluid structure*, Chem. Phys. **202**, 295 (1996).

[102] J. L. Finney, D. T. Bowron and A. K. Soper, *The structure of aqueous solutions of tertiary butanol*, J. Phys.: Cond. Matt. **12**, A123 (2000).

[103] D. T. Bowron and J. L. Finney, *Concentration and temperature dependence of hydrophobic association: a SANS study*, Technical report, Institut von Laue - Langevin (1997), experiment 6-02-151.

[104] D. T. Bowron and J. L. Finney, *Concentration and temperature dependence of hydrophobic association: a small angle scattering study*, Technical report, Institut von Laue - Langevin (1999), experiment 6-02-173.

[105] D. T. Bowron, J. L. Finney and P. A. Timmins, *Very long range structural correlations in aqueous solutions of tertiary butanol* (1998), unpublished.

[106] M. Grimsditch, R. Bhadra and L. M. Torell, *Shear waves through the glass-liquid transformation*, Phys. Rev. Lett. **62** (22), 2616 (1989).

[107] M. Cutroni, P. Migliardo, A. Piccolo and C. Alba-Simionesco, *The dynamic glass transition of a 'fragile' molecular liquid in the megahertz domain*, J. Phys.: Cond. Matt. **6**, 5283 (1994).

[108] A. Aouadi, C. Dreyfus, M. Massot, R. M. Pick, T. Berger, W. Steffen, A. Patkowski and C. Alba-Simionesco, *Light scattering study of the liquid-glass transition of meta-toluidine*, J. Chem. Phys. **112** (22), 9860 (2000).

[109] Jing Liu, Ling Ye, D. A. Weitz and Ping Sheng, *Novel acoustic excitations in suspensions of hard-sphere colloids*, Phys. Rev. Lett. **65** (20), 2602 (1990).

[110] I. E. Psarobas, A. Modinos, R. Sainidou and N. Stefanou, *Acoustic properties of colloidal crystals*, Phys. Rev. B **65**, 064307 (2002).

[111] Z. Liu, Z. Zhang, Y. Mao, Y. Y. Zhu, Z. Yang, C. T. Chan and Ping Sheng, *Locally resonant sonic materials*, Science **289**, 1734 (2000).

[112] W. W. Wood and J. D. Jacobson, *Preliminary results from a recalculation of the Monte Carlo equation of state of hard spheres*, J. Chem. Phys. **27**, 1207 (1957).

[113] W. G. Hoover and F. H. Ree, *Melting transition and communal entropy of hard spheres*, J. Chem. Phys. **49** (8), 3609 (1968).

[114] S.-E. Phan, W. B. Russel, Z. Cheng, J. Zhu, P. M. Chaikin, J. H. Dunsmuir and R. H. Ottewill, *Phase transition, equation of state, and limiting shear viscosities of hard sphere dispersions*, Phys. Rev. E **54** (6), 6633 (1996).

[115] J. Israelachvili, *Intermolecular and surface forces* (Academic Press, London, 1991).

[116] L. A. Galloway, *Phase behaviour of colloid-micelle mixtures*, Ph.D. thesis, University of Edinburgh (2001).

[117] P. N. Pusey and W. van Megen, *Phase behaviour of concentrated suspensions of nearly hard spheres*, Nature **320**, 340 (1986).

[118] L. Antl, J. Goodwin, R. Hill, R. Ottewill, S. Owens, S. Papworth and J. Waters, *The preparation of poly(methyl methacrylate) latices in non-aqueous media*, Colloids and Surfaces **17** (1), 67 (1986).

[119] C. Pathmamanoharan, C. Slob and H. Lekkerkerker, *Preparation of polymethylmethacrylate lattices in non-polar media*, Coll. Polymer Sci. **267** (5), 448 (1989).

[120] A. B. Schofield, private communication (2002).

[121] D. J. Fairhurst, *Polydispersity in colloidal phase transitions*, Ph.D. thesis, University of Edinburgh (1999).

[122] V. C. Martelozzo, *Crystallisation and phase separation in colloidal systems*, Ph.D. thesis, University of Edinburgh (2001).

[123] Ling Ye, Jing Liu, Ping Sheng and D. A. Weitz, *Sound propagation in suspensions of solid spheres*, Phys. Rev. E **48** (4), 2805 (1993).

[124] Xiaodun Jing, Ping Sheng and Minyao Zhou, *Theory of acoustic excitations in colloidal suspensions*, Phys. Rev. Lett. **66** (9), 1240 (1991).

[125] Xiaodun Jing, Ping Sheng and Minyao Zhou, *Acoustic and electromagnetic quasimodes in dispersed random media*, Phys. Rev. A **46** (10), 6513 (1992).

[126] Ping Sheng, *Introduction to wave scattering, localisation and mesoscopic phenomena* (Academic Press, London, 1995).

[127] L. Schwartz and T. J. Plona, *Ultrasonic propagation in close-packed disordered suspensions*, J. Appl. Phys. **55** (11), 3971 (1984).

[128] L. Schwartz and D. L. Johnson, *Long-wavelength acoustic propagation in ordered and disordered suspensions*, Phys. Rev. B **30** (8), 4302 (1984).

[129] K. Attenborough, *Acoustical characteristics of porous materials*, Phys. Rep. **82** (3), 179 (1982), review section of Physics Letters.

[130] Z. Hashin, *The elastic moduli of heterogeneous materials*, J. Appl. Mech. **29**, 143 (1962).

[131] R. Stoneley, *Elastic waves at the surface of separation of two solids*, Proc. Roy. Soc. London Series A **106**, 416 (1924).

[132] L. M. Brekhovskikh, *Waves in layered media* (Academic Press, New York, 1980).

[133] C. F. Bohren and D. R. Huffman, *Absorption and scattering of light by small particles* (Wiley-Interscience, New York, 1983).

[134] Ping Sheng (editor), *Scattering and localization of classical waves in random media* (World Scientific, Singapore, 1990).

[135] E. N. Economou, *Green's functions in quantum physics* (Springer-Verlag, New York, 1983), 2nd edition.

[136] D. O. Riese and G. H. Wegdam, *Sound propagation in suspensions of colloidal spheres with viscous coupling*, Phys. Rev. Lett. **82** (8), 1676 (1999).

[137] R. S. Penciu, G. Fytas, E. N. Economou, W. Steffen and S. N. Yannopoulos, *Acoustic excitations in suspensions of soft colloids*, Phys. Rev. Lett. **85** (21), 4622 (2000).

[138] W. Schaertl and H. Sillescu, *Brownian dynamics of polydisperse colloidal hard spheres: equilibrium structures and random close packings*, J. Stat. Phys. **77** (5-6), 1007 (1994).

[139] R. S. Longhurst, *Geometrical and physical optics* (Longmans, Green and Co, 1957).

[140] S. Paulin and B. Ackerson, *Observation of a phase transition in the sedimentation velocity of hard spheres*, Phys. Rev. Lett. **64** (22), 2663 (1990).

[141] M. D. Eldridge, P. A. Madden, P. N. Pusey and P. Bartlett, *Binary hard-sphere mixtures: a comparison between computer simulation and experiment*, Mol. Phys. **84** (2), 395 (1995).

[142] E. H. Rodd, *Chemistry of carbon compounds*, volume 3B (Elsevier, 1956).

[143] Ping Sheng, private communication (1999).

[144] P. N. Pusey and W. van Megen, *Detection of small polydispersities by photon correlation spectroscopy*, J Chem Phys **80** (8), 3513 (1984).

[145] J. H. Page, I. P. Jones, H. P. Schriemer, M. L. Cowan, Ping Sheng and D. A. Weitz, *Diffusive transport of acoustic waves in strongly scattering media*, Physica B **263-264**, 37 (1999).

[146] J. H. Page, private communication (2002).

[147] M. Kafesaki and E. N. Economou, *Interpretation of the band-structure results for elastic and acoustic waves by analogy with the LCAO approach*, Phys. Rev. B **52** (18), 13317 (1995).

[148] M. Kafesaki and E. N. Economou, *Multiple-scattering theory for three-dimensional periodic acoustic composites*, Phys. Rev. B **60** (17), 11993 (1999).

[149] R. Sprik and G. H. Wegdam, *Acoustic band gaps in composites of solids and viscous liquids*, Solid State Commun. **106** (2), 77 (1998).